Università degli Studi di Trieste

Dipartimento di Ingegneria e Architettura
XXXII ciclo del Dottorato di Ricerca in Ingegneria Industriale
e dell'Informazione

Experimental and numerical study of planing hulls in waves

Tesi di Dottorato in Architettura Navale (ING-IND/01)

Dottorando
Riccardo Vasco Pigazzini

Supervisore
Ing. Amedeo Migali
Co-Supervisore
Prof. Alberto Francescutto

A.A. 2019/2020

To my parents, Louis and Nadia

Abstract

The work presented in this thesis has been carried out as part of the SOPHYA (Seakeeping Of Planing Hull YAchts) project. The research and development project is aimed at the investigation of the performances of planing pleasure-boats in terms of sea-kindliness, safety and powering in mild weather conditions. This investigation is pursued via three complementary approaches: model scale experiments,sea trials and numerical simulations.

This thesis is mainly focused on the study of planing hulls seakeeping, in particular, a large part of this work has been dedicated to experimental investigations and data analysis both in model and full scale. The results of towing tank tests have been then used as reference data for CFD simulations with the aim of to develop a reliable computational framework for seakeeping simulations of planing hulls.

A novel experimental work has been carried out in order to investigate nonlinear behavior of planing hulls in regular waves and the effects of geometrical parameters, speed and wave steepness on higher harmonic response of hull motions and accelerations. An extensive analysis of the second and third harmonic response of motion and accelerations is presented, adding valuable results to the Naples Systematic Series data set and providing detailed benchmark data for future computational studies.

Full scale calm water and seakeeping trials have been carefully planned and executed, the yacht has been fully instrumented and a wave buoy has been used for directional sea state measurement. An innovative integrated analysis method of on-board and wave measurements has been developed in order to improve full scale transfer functions estimation. The effect of wave directional distribution models on the estimated transfer functions has been investigated. The results show a remarkable agreement with model scale experimental results.

Planing hull calm water and seakeeping simulations have been performed using open source CFD code. An open source fully automated pre-processing procedure has been developed to drastically reduce time-to simulations. The procedure generate a mesh refined ad-hoc for planing hull simulations and a ready-to-run case folder using OpenFOAM built-in and custom tools.

Calm water simulations showed an underestimation of the running trim angle and resistance at high speeds. Seakeeping simulations however showed much better agreement with experimental results in terms of motion transfer functions. New simulation tools have been implemented for the specific case of reproducing towing tank conditions, such as virtual accelerometers and new restraint capabilities that are more faithful of the real towing arm restraint conditions. The tested simulation framework has been used to investigate the effect of hull form variations on seakeeping performances of eight alternative hulls. Experimental results on the best performing hull alternative show comparable results with simulations.

Sommario

Il lavoro presentato nella presente tesi è stato svolto nell'ambito del progetto SOPHYA (Seakeeping Of Planing Hull YAchts). Il progetto di ricerca e sviluppo è finalizzato all'indagine delle prestazioni imbarcazioni plananti da diporto in termini di tenuta al mare, sicurezza e propulsione in condizioni di mare medie. Questa indagine è stata condotta attraverso tre approcci complementari: esperimenti in scala modello, prove in mare e simulazioni numeriche.

La tesi si concentra principalmente sulla tenuta al mare degli scafi plananti, in particolare, buona parte del lavoro è stata dedicata allo studio sperimentale e all'analisi dei dati delle prove su modello e scala reale. I risultati sono stati utilizzati come dati di riferimento per le simulazioni CFD al fine di sviluppare un procedura affidabile per le simulazioni di scafi plananti su onda.

È stato condotta un'indagine sperimentale estensiva sullo studio del comportamento non lineare di scafi plananti in onde regolari e l'effetti dei parametri geometrici dello scafo, della velocità e della pendenza dell'onda sulla risposta ultra armonica dei moti e delle accelerazioni. Ilcontributo principale dello studio è rappresentato dall'ampia analisi della seconda e terza risposta armonica del moto e delle accelerazioni. I risultati rappresentano inoltre un notevole contributo ai dati della serie sistematica di Napoli e forniscono un riferimento dettagliato per futuri studi computazionali.

Le prove di tenuta al mare al vero sono state pianificate ed eseguite, lo yacht è stato completamente strumentato e una boa ondametrica è stata utilizzata per la misurazione direzionale dello stato del mare. È stato sviluppato un metodo innovativo di analisi integrata delle misure di moti a bordo e d'onda al fine di migliorare la stima delle funzioni di trasferimento in scala reale ed è stato investigato l'effetto dei modelli di distribuzione direzionale dell'onda sul risultato. Le funzioni di trasferimento al vero ottenute con l'analisi integrata proposta sono confrontabili con quelle in scala modello.

Sono state eseguite simulazioni in acqua calma e di seakeeping di uno scafo planante utilizzando un codice open source basato su foam-extend. In seguito è stata sviluppata una procedura di preprocessing automatizzata che riduce drasticamente i tempi di pre-simulazione. Questa procedura genera una griglia raffinata ad-hoc per simulazioni di idrodinamica navale e prepara una cartella del caso da simulare pronta per l'uso. La procedura utilizza strumenti di generazione griglie compresi in openFOAM ed altri svilupati appositamente. Le simulazioni di acqua calma hanno mostrato una una sottostima dell'assetto in corsa e della resistenza alle alte velocità, tuttavia le simulazioni di seakeeping mostrano risultati molto più fedeli ai dati sperimentali in termini di funzioni di trasferimento. Sono inoltre stati implementati nuovi strumenti per le simulazioni che debbano riprodurre fedelmente le condizioni della vasca navale, come accelerometri virtuali e nuove condizioni cinematiche più fedeli al reale fissaggio del braccio di rimorchio.

I solutori e gli strumenti sviluppati sono stati in seguito utilizzati per studiare l'effetto delle variazioni della forma dello scafo sulle prestazioni di tenuta del mare di otto diverse varianti. I risultati sperimentali dello scafo con le migliori prestazioni sono comparabili con quelli ottenuti dalle simulazioni.

Contents

List of papers

Journal papers

Pigazzini, R., Contento, G., Martini, S., Puzzer, T., Morgut, M. and Mola, A., 2018. VIV analysis of a single elastically-mounted 2D cylinder: Parameter Identification of a single-degree-of-freedom multi-frequency model. *Journal of Fluids and Structures*, 78, pp.299-313.

Pigazzini, R., Contento, G., Martini, S., Morgut, M. and Puzzer, T., 2018. An investigation on VIV of a single 2D elastically-mounted cylinder with different mass ratios. *Journal of Marine Science and Technology*, pp.1-14.

Conference papers

Pigazzini, R., Puzzer, T., Martini, S., Morgut, M., Contento, G., Gatin, I., Vukčević, V., Jasak, H., Begovich, E., Caldarella, S. and Migali, A., 2018. Experimental and Numerical Prediction of the Hydrodynamic Performances of a 65 ft Planing Hull in Calm Water. In *Technology and Science for the Ships of the Future: Proceedings of NAV 2018: 19th International Conference on Ship & Maritime Research* (Vol. 1, pp. 480-487). IOS Press.

Martini, S., Pigazzini, R., Puzzer, T., Morgut, M. and Contento, G., 2018, June. Numerical Investigation of 2D Vortex Induced and Wake Induced Vibrations of Two Circular Cylinders in Tandem Arrangement. In *Technology and Science for the Ships of the Future: Proceedings of NAV 2018: 19th International Conference on Ship & Maritime Research* (Vol. 1, p. 348). IOS Press.

Puzzer, T., Pigazzini, R.V., Contento, G., Morgut, M. and Martini, S., 2018. An open-source fully-automated pre-processing procedure for planing hull CFD simulations. In *23th Symposium on Theory and Practice of Shipbuilding SORTA 2018* (Vol. 1, No. 1, pp. 1-8).

De Santis, M., Migali, A., Pigazzini, R., Puzzer, T., Martini, S., Morgut, M., ... & Brunetti, F. (2018). Case Study: Sea Trials on a 65 ft Planing Hull in Waves. In *Full Scale Ship Performance Conference* (pp. 141-146). The Royal Institution of Naval Architects.

Puzzer, T., Pigazzini, R., Davison, S., Morgut, M. and Contento, G., 2019, July. Full-Scale Seakeeping Trials: An Integrated Analysis of Sea State and On-Board Data. In *The 29th International Ocean and Polar Engineering Conference*. International Society of Offshore and Polar Engineers.

Preface and motivation

This thesis is submitted in partial fulfillment of the requirements for the degree Doctor of Philosophy at the University of Trieste.

The global recreational boating market is growing considerably in recent years, among different boat types, motor yachts make up almost 90% of the global market share [1]. The comfort and efficiency of a motor yacht are important factors for new hull designs that have to stand out of the increasing competition. Apart from on board facilities, the comfort of a pleasure craft is tightly related to its sea-going capabilities, seakeeping being one of the most important one.

Current seakeeping prediction methods used in the design of new hulls result from studies on conventional displacement hulls and are less suited to planing hull crafts. Planing crafts response at sea are governed by more complex hydrodynamic phenomena respect to displacement ships, better planing hull design tools are therefore needed for more accurate seakeeping predictions.

The experimental and numerical study presented in this thesis is part of the research project SOPHYA (Seakeeping Of Planing Hull YAchts) and it is aimed at the investigation of the seakeeping of planing pleasure crafts in a seaway and the development of a computational tools for seakeeping simulations. The correlation between full scale and predicted seakeeping performances is investigated via model scale experiments and full scale sea trials. Model scale experimental results are then used as reference data in order to develop a reliable computational framework for seakeeping simulations of planing hulls.

The prediction method based on the proposed computational framework show good agreement to experimental data and it has been used to study the effect of hullform variations on seakeeping performances. The comparison with experimental data on a new hull model show encouraging results.

In this thesis, the research on the seakeeping of a planing hull has been conducted on a 65 foot yacht hull built by Monte Carlo Yachts, the industrial partner of the research project. As part of the research on the topic, specific seakeeping model experiments have been carried out also on two Naples Systematic Series hulls.

The research work presented in this thesis has been carried out at the HyMO*Lab* (HYdrodynamics and MetOcean Laboratory), headed by professor Giorgio Contento. The Laboratory is located in the department of Architecture and Engineering of the University of Trieste.

Model experiments have been carried out at the towing tank facility of the University of Naples "Federico II". My Ph.D. project, lasted from october 2016 to december 2019, has been supervised by Amedeo Migali Ph.D. and Prof. Alberto Francescutto.

Structure of the thesis

The present work is divided into three main chapters, covering the experimental and numerical assesment of the seakeeeping of a planing hull yacht. The present thesis is structured as follows:

Introduction An short historical background on the birth and evolution of planing crafts is presented, from early military applications to modern sport motor and sailboats. A chronological review of the experimental and computational-based research on the subject of planing hulls is presented. The review cover some of the most relevant studies made from early experiments on planing surfaces, to calm water and seakeeping experiments on planing hulls, full scale testing and the latest works based on computational fluid dynamics methods.

Model experiments An extensive description of the experimental work done on calm water and regular waves model tests is presented. The methods and tools used for the model experiments on the reference hull, as well as the data analysis are presented. Moreover, a novel investigation on the nonlinear seakeeping behaviour of systematic series of planing hull is also presented in detail.

Full scale sea trials The process of planning, executing and analysis of full scale seakeeping trials of a pleasure planing hull yacht is presented. A novel integrated approach for the analysis of data from on-board and sea state measurements is presented in detail. Full scale calm water and seakeeping results are compared with the reference model data.

Numerical simulations CFD simulations of calm water and regular waves seakeeping of the reference planing hull are presented and results are compared with experimental data. An open-source automatic grid generation procedure that significantly reduce the time-to-simulation is described. The process of selecting a better performing hull variant based on seakeeping capabilities is shown, along with the comparison of the results with experimental data.

Conclusions The conclusions on the work carried out in this thesis are provided , the important contributions in each of the main topics are higlighted. Finally, in light of the precious experimental data gathered during this work, some recommendations on future work are proposed.

Chapter 1

Introduction

1.1 Historical background

The high speed hull concept was born in the end of the nineteenth century as a military vessel, and its primary objective was to be able to attack larger ships swiftly and escape thanks to the high speed and maneuverability. The first high speed vessels started out as torpedo boats, initially built to carry spar or towed torpedoes, as in the case of the Norwegian warship HNoMS *Rap* "quick", built by John Thornycroft in Chiswick, England, around the year 1872. The *Rap* was 18.2m, weighted 7 tons and and the 100 Hp steam engine allowed speeds up to 14.5 knots, making it one of the fastest vessel of the time. Since the self-propelled torpedo introduced by Whitehead 1868 was clearly a superior method of delivering the warhead to the enemy ship hull, *Rap* was never fitted with spars and was later outfitted with launch racks for delivering self-propelled torpedoes in 1879. The first torpedo boat designed to carry such self-propelled torpedos was the HMS *Lightning*, also built by Thornycroft and enterd service in 1876. The *Lightning* was a much larger (26m, 33 ton) vessel and its top speed was 18.5 knots, thanks to its two 460 Hp steam engines.

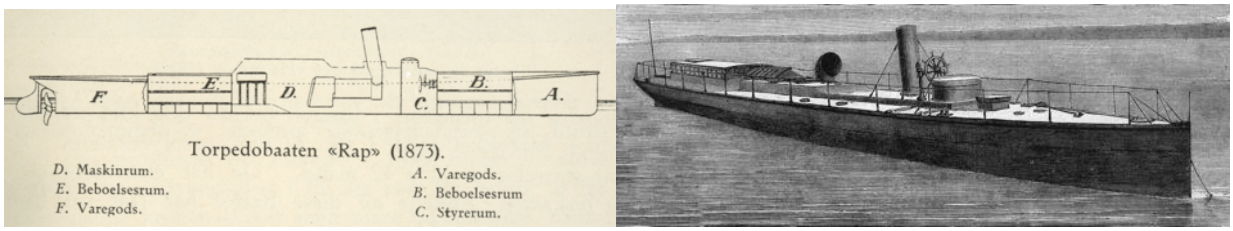

(a) HNoMS *Rap* [2]

(b) HMS *Lightning* [3]

Figure 1.1: Illustration of early torpedo boats

The steam engine quickly became the limiting factor for higher speeds as they were bulky and heavy, the next step towards modern high speed crafts came with the invention of the steam turbine by Sir Charles Parsons in 1884. Parsons himself developed the famous turbine-powered *Turbinia*, and thanks to the superior power-to weight ratio of the steam turbine the 32 m ship

was able to sail at a remarkable speed of 34.5 knots in 1897 (Fig. 1.2).

Figure 1.2: Turbinia at speed at the Queen Victoria's Diamond Jubilee Naval Review in 1897

The adoption of the smaller internal combustion engine allowed for a further step forward in terms of vessel speed. The new engine allowed for smaller and faster motor torpedo boats (MTB), they rapidly became part of navy fleets between WWI and WWII. This new class of high speed boats were capable to cruise at 30 to 50 knots, although being only 15 to 30 meters in length thanks to the adoption of the hard chine planing hull (Fig.1.3). The V shaped hard chine planing hulls allowed the boats to exploit the hydrodynamic lift to plane at very high speed with less resistance but suffered from poor seakeeping abilities respect displacement hulls. After WWII, lots of MTB were decommissioned due to the maintenance, running costs and because of the poor seakeeping abilities. Post WWII period saw the adoption of planing hull combatant ships by numerous navies as patrol crafts, fast missile crafts etc. [4], in particular, the US developed multiple small fast crafts to be used in the rivers and and along the coasts of southeast Asia during the Vietnam war.

Figure 1.3: Motoscafo armato silurante "MAS", Italian Navy motor torpedo boat

Aside the developement of military vessels, fast boats were used for racing as soon as the early XX century, with the birth of the first first annual international award for motorboat racing, the Harmsworth Cup, or Harmsworth Trophy. The first winner was a 40 foot steel powerboat piloted by a Dorothy Levitt, with a speed of 19.2 knots. By 1911, the first V-bottom planing hull reached speeds in excess of 40 knots, one decade later the 50 knots barrier was broken and by 1931 the Harmsworth Cup winner traveled at over 70 knots. The search for higher speed culminated with jet engine powered hydroplanes capable of extremely high speed, in 1955 Donald Campbell's *Bluebird K7* hydroplane travelled at over 180 knots and by 1964 he reached 240 knots on Lake Dumbleyung. The fastest speed recorded on water belongs to Ken Warby's *Spirit of Australia* (Fig.1.4a), a hydroplane like *Bluebird K7* that broke the 500 km/h barrier in 1978 on Blowering Dam in New South Wales, Australia.

(a) Spirit of Australia hydroplane (b) VOR 60 ocean sailing yacht

Figure 1.4: Planing sport boats

Planing hulls have revolutionized not only motorboat design, planing sailing boats started to

appear in Australia as soon as 1892, with the first 18 foot skiff by Mark Foy, capable of planing downwind. In 1928, Uffa Fox introduced the International 14 in regattas and the planing dinghy that won almost all the regattas that participated in that year. The planing hull design has been later developed by other designers, and by 1970 *Dribbly Mk3* became the fist sailing vessel able to windward planing. With the advent of new boat building materials such as composite fibres, by the '90s 18 foot skiffs were capable of planing at over 30 knots downwind. Around the same time, 60 foot planing sailboats (Fig .1.4b)revolutionized ocean racing in the Withbread race, proving to be faster than much bigger sailing boats in the fleet in the downwind leg of the southern thanks to the higher planing speed.

1.2 The seakeeping of planing hull yachts

Recently, planing hulls became quite common in leisure motor boats and luxury yachts, but the hull geometry remained almost the same as the early motor torpedo boat and with it the issues regarding its seakeeping abilities. Apart from the general hull design guidelines for seakeeping [5, 6], only minor hull design enhancements have been introduced in the design of planing hull pleasure yacht, such as warped hull bottom and double chine to mitigate wave impacts and the adoption of lifting strakes, flaps and interceptors in order to increase lift and enhance running attitude.

Today, the design of luxury yacht is more focused on finding solutions to enhance seakeeping and efficiency instead of increasing cruise speeds. Advances in technology allowed the adoption of different active systems in order to decrease motions and accelerations on board using gyroscopic and fin stabilizers. In general, in depth studies of the seakeeping performances of planing yachts are rarely carried out because of the high cost and time effort.

1.3 Literature review

In this section, a brief review of the relevant experimental works on the subject of planing hulls is presented. In particular, the review is divided by topic, and the literature is ordered chronologically in order to highlight the development of the studies on the subject.

1.3.1 Experiments on planing surfaces

The first studies addressing the problem of planing surfaces made by Von Karman [7] and Wagner [8] around 1930 are considered the first steps toward the mathematical modeling of the forces involving simple planing surfaces. The main application of those studies was the understanding of the seaplanes's floats hydrodynamics during take off and landing. Further relevant experimental investigations on flat planing surfaces have been carried out by Sottorf [9, 10], Sambraus [11], Locke [12] and Sedov [13]. Later studies in the matter of seaplane floats started focusing on simple V-shaped planing surfaces, Shoemaker [14] towing tank tests with V-shaped surfaces having different deadrise angles contributed the field of float design with numerical data on the resistance, center of pressure, and wetted length of a planing surface at different load, speed, and trim angle. Later studies by Sottorf [15] refined the study of seaplanes float with a systematic study of families of floats with varying l length/beam ratio and deadrise angle known as standard DVL floats, aimed at the best utilization on any airplane. The study of the of simple flat and V-shaped surfaces in unsymmetrical planing condition by Savitsky [16] show for the first time the effect of yaw and roll on the hydrodynamics of a planing surface.

1.3.2 Experiments on planing hulls in calm water

The first studies of systematic planing hull models were carried out at the United States experimental basin in 1941 by prof. Kenneth S.M. Davidson, of the Stevens Institute of Technology. [17]. The 20 single-chine EMB Series 50 hulls series was created by varying both beam-draft ratio and displacement-lenght ratio and was tested at three different displacements and trim angle.

Since the EMB Series 50 models were only 40 inches long and laminar flow was present along the hull, together with the fact that the choice of dimensional ratios were unsuitable for the study of planing hulls, Clement and Blount [18] later tested a new systematic series in order to address those shortcomings. Five planing boat models of different length-beam ratio and different loads and LCG locations were tested, the systematic series was designated TMB Series 62. The TMB Series 62 will be later extended by Keuning in 1982 [19], adding five new model with doubled (25 degree) deadrise angle and in 1993 [20] adding another four models having 30 degree deadrise angle and revisiting all the data analysis of the systematic series.

Although the work of Fridsma [21] on a series of prismatic hulls is mainly focused and known for the investigation on the seakeeping performances, its first published report in 1969 presented also calm water results of all the models. Both the resistance, trim and sinkage were measured for speeds up to 20 fps. The tests were conducted in the Davidson Laboratory using a free trim and sinkage resistance restraint system. Sixteen model configurations (A-P) were tested, deadrise angle, lenght-beam ratio and displacement values were varied systematically. Porpoising limits and adimensional mean wetted length were reported in the calm water results plots

In 1974 Hubble [22, 23] published the NSRDC Series 65, the parent hull is a scale model of the AG(EH) hydrofoil hull. The series was developed through a systematic variation of length-beam, length-draft and beam-draft ratios of seven models. Resistance characteristics of the Series hulls were obtained utilizing a captive model technique that allowed only heave motion. In addition, a modified Series 62 hull has been tested, using the conventional free to trim and sink towing technique in a different tank.

The NTUA systematic Series, published by Grigoropoulos in 1999 [24, 25] provided calm water data for a double chine, wide transom hull form with warped planing surface. The Series consists of five models with five different length-beam ratios, each tested at six displacements,including very light ones.

In 2005, Kowalyshyn and Metcalf published the USCG systematic series [26, 27], resistance experiments were performed on models based on the United States Coast Guard 47-foot Motor Lifeboat (MLB) hull form. The series includes three models with varying length-beam ratios and one model with transom dead-rise angle variation. Resistance tests were carried out varying displacement and location of the centre of gravity on all four models, each one having different combination of length-beam and beam-depth ratio. The models were towed with a restraining system that allowed free pitch, heave, and roll. The objective was to investigate the influence of geometrical ratios, transom deadrise angle, longitudinal center of gravity (LCG) and displacement on the resistance and running attitude.

Taunton [28] presented a planing hull series inspired at the modern design practice used to build high speed military and para-military interceptor crafts and powerboats.The single-chine warped parent hull (C) was modified varying in L/B ratio in order to abtain three additional models (A,B,D). Two additional models having one and two transverse steps are designated C1 and C2. The model were tested using a restraining system that allowed free trim and sinkage to very high speeds.

Begovich et al. [29] tested a series of hard chine planing hullforms consisting in three warped and one monohedral hulls. The models were fitted with transparent bottom surfaces in order to visualize the flow and accurately assess the wetted surface. mean wetted length, wetted surface of pressure area, mean wetted length of whisker spray and wetted surface of whisker spray are reported, along the resistance, running trim and sinkage. Resistance of warped hullfoarms is found to be higher than the monohedral counterpart, but lower trim values makes warped hullforms better in terms of riding attitude, eliminating the need of appendages in order to control excessive running trim.

More recently, De Luca and Pensa [30] published a the Naples systematic series of hard chine warped hulls (NSS).The hulls were designed and tested at the naval division of the Dipartimento di Ingegneria Industriale (DII) of the Università degli Studi di Napoli “Federico II”. The parent hull (C1), designed taking into account the use of interceptors, is characterized by deadrise angles constantly growing from astern to forward. The NSS is composed of five models, the four models derived from C1, were developed by scaling depth and breadth so that homothetic forms of transversal sections are maintained. Both length-beam and length-displacement ratios are increased as the scaling factor diminishes but the hull coefficients are constant throughout the models. All models were tested with and without interceptors at two different loading conditions having zero or one degree static trim angle.

1.3.3 Experiments on the seakeeping of planing hulls

The first systematic experimental studies on planing hull performances in rough water were carried out by Fridsma [21, 31]. He presented both calm water, regular and irregular wave data of a family of simple prismatic (constant deadrise) hulls. In particular, in the first experiments [21], the prismatic hulls were tested in calm water and regular waves with the goal of highlighting the effects of lenght-beam, deadrise and loading on added resistance, motions and accelerations. Three deadrise angles, two lenght-beam ratios, two loading conditions and two running trim angles were tested with six different wavelengths. Heave and pitch responses are presented as non dimensional transfer functions, using wave height and slope respectively. In addition to the motion response in regular waves phase lead or lag of motions is also plotted. Linearity plots were also shown where the nonlinearity of heave, pitch and added resistance with the wave amplitude is highlighed.

The second part of Fridsma's insvestigation [31], extended later by Zarnik and Turner [32] dealt with the responses in irregular waves. The same models used for regular waves were used with the addition of a model with warped bow surfaces in order to investigate the effect of section shape and bow warp. The magnitude of all maxima and minima of the motions and the positive acceleration peaks were sampled and underwent a statistical analysis. It was found that motion response was represented well by a distorted Rayleigh distribution, where accelerations followed a simple exponential distribution instead. The parameters of the distributions are the presented in tabular form.

Taunton [33] presented the results of seakeeping of eight models in irregular head waves at three different speeds . The wave spectra used were based on previous wave buoy measurements near the Isle of Wight. Throughout the tests, seven different wave spectra were tested, although two of them were the most common and the ones tested for every hull. The test matrix consisted in a total of 41 hull and wave spectra combinations. Results of heave and pitch maxima and minima, as well as acceleration data were presented as statistical distributions.

Begovic et al. [34] studied effect of hull warping on heave, pitch and accelerations in regular waves. A small systematic series of three warped and a monohedral hull has been tested in regular waves and the Response Amplitude Operators (RAOs) of heave, pitch and acceleration are compared. It has been found tha although significant geometrical differences were were present between hullforms, motion responses were within 10–20%. The biggest differences were encountered in the acceleration response at higher speeds, where the warped hullforms showed up to 50% decrease in acceleration response. A comparison of the monohedral and warped hull in irregular waves [35] using JONSWAP spectrum has also been carried out. Pitch and heave RMS and mean of both models are reported, along with relative statistical distributions fitted to wave, pitch and heave data.

1.3.4 Full scale testing

One of the first and most known study on full scale data of planing hulls in waves is the work published by Allen and Jones [36]. They measured pressure, strain and accelerations on different high speed vessels in waves, two of which were conventional planing hulls. The aim of the study was to develop a simplified model for predicting the hull bottom impact pressure and provide boat designers an equivalent uniform static pressure for the scantling of hull structural components.

Kallio [37] compared the motions and accelerations recorded during Seakeeping trials on a ram wing planing craft and a conventional planing craft. The conventional planing hull was tested in head, bow and stern quartering and following sea at speeds up to 60 knots. The mostly unidirectional sea state had 0.7 m significant wave height. Significant double amplitudes of motions and accelerations were measured using a stabilized platform and accelerometer respectively. The seastate was recorded by means of a USCG wave buoy.

Ooms [38] carried out full scale data from two similar fast rescue vessels. The accelerations and motions measurements on both ships were carried out simultaneously. The focus of the work was to compare RMS and peak values of accelerations in the wheelhouse and bow sections of both hulls. All the measurements, including pitch, speed and course were sampled at 30Hz and analized using 10Hz lowpass filter. The tests were carried out at speeds ranging from 12 to 30 knots, the helmsman was not allowed to change route and/or speed. In the real world, this is not the case, see [39, 40], but the full scale tests were designed to be as close as possible to the towing tank tests.

Akers [41] performed sea trials with a planing hull with the aim of validate the results obtained with a planing hull simulator. The tests were conducted with a 25-foot commercial utility boat. Accelerations and motions were measured using two three-axis accelerometers and a inertial measurement unit (IMU). The tests were carried out in calm water and in the wake generated by a passing boat. In addition to acceleration and motions, both wave and wake of the wavemaking boat were measured using wavebuoy and videocamera respectively. A summary of the maxima and minima of pitch and vertical acceleration are given in tabular form along with some timeseries plots of the same variables on selected runs.

Garme and Rosén [42] presented full-scale trials results of a swedish marine medical evacuation high speed craft. The study was focused on the characteristics of slamming impacts and the validation of the proposed numerical method. The Storebro SB90E used in the tests was 9.5 m long, had a displacement of 6.5 tonnes and speeds varying from 10 to 40 knots. They measured motions with a 15Hz Inertial measurement unit (IMU)and vertical accelerations with 2kHz accelerometers. The craft was also equipped with 2kHz pressure transducers, shear and strain gauges in order to record pressure peaks and structural response. Although the high sampling rate, it was found that it was sometimes too low to capture pressure peaks. The tests were performed for head ($\mu = 180°$) and bow sea ($\mu = 180°$). Interestingly, it has been found that in bow seas presents higher impact pressure and lower impact acceleration respect to head seas.

Mørch and Hermundstad [43] presented results of accelerations, pressures, strain and deflection measurements on a planing pleasure craft in waves. The aim of the study was to gain a better understanding of slamming loads and structural response of a planing craft at sea. The Nidelv 610 craft used in the sea trials is 6.1 m long and has a displacement of 1550 Kg. Sea state was measured by a single accelerometer on a PVC float, where all on-board measurements were sampled at 750 Hz and filtered through moving average. It was found that although a large safety margin is used in the DNV rules, design pressures were easily exceeded during tests.

Keuning [44] published the results of an extensive research program on three 55 meter long monohull Patrol Boat concepts. The aim of the study was to gain insight on the aspects that most impact the craft operability at sea and try to evaluate their limit values of motions and accelerations in order to ensure safe operation of the ship. Hull design was the main variable

explored in the research in order to evaluate three radically different bow geometries. The tested ships motion and accelerations were recorded during a large number of runs while performing their usual tasks under real circumstances at sea. Other than the usual sea state and motion measurements, the throttle position has been recorded in order to detect voluntary crew speed reductions.

Townsend [45] performed full scale sekeeping tests on a Royal National Lifeboat Institution (RNLI) Atlantic 75 rigid inflatable boat (RIB) in order to study the influence of speed, ballast, wave height, encounter frequency, and tube pressure on RIB motions.

Recently, Prini et al. [46] published the results of full scale tests on a RNLI Severn class all-weather lifeboat. Strain gauges, accelerometers and rate gyros have been used to sample structural strain, accelerations and rigid motion. Accelerations and strain, subject to sudden variations, were sampled at 2048Hz, rigid body motions at 256 Hz. The sea state was measured by a Datawell GPS wave buoy. Results of the tests were analysed both in time domain using statistical indicators and in frequency domain in order to compute Response Amplitude Operators of the vertical bending moment. Results were compared with the results from a marine structural analysis software.

Camilleri et al. [47] carried out Full-scale trials on a 9.6m high-speed marine target autonomous planing craft. The aim of the tests was to investigate the characteristics of slamming impacts and its effect on motions and structural response. An extensive set of experimental data on accelerations, pressure and strain of the hull at sea has been presented. Accelerations and strain have been measured at the helm and bow, water pressure in more than 20 places on the hull and global hull deflections were measured using linear position sensors. Instead of simply reporting the results plots and tables he data analysis method used is reported in full. The pressure peaks are fitted to Weibull and Generalized Pareto statistical models using a least squares parameter identification technique. A strong correlation between pressure and structural strain is observed, and larger values have been recorded at high speed in moderate seas instead of at moderate speed in high sea states. It is also found that ISO standards and DNV rules underpredict slamming pressure, LR rules instaed overestimate it although being closer to the observed values.

1.3.5 CFD of planing hulls

One of the first to study the hydrodynamics of high speed planing hulls using computational fluid dynamics was Caponneto [48, 49]. In his study he used the finite volume Reynolds Averaged Navier-Stokes (RANS) solver Comet to perform steady state simulations of two prismatic hulls. The results were compared with the Savitsky [50] method and showed good agreements. Simulations of 3 trim angles and 3 sinkages were carried out in order to estimate the running attitude of the design hull via quadratic interpolation.

A step forward in the simulation of planing hull has been presented by Azcueta [51], showing results of quasi-steady and unsteady simulations of a prismatic hull in both calm water and regular waves. The Comet 6-DOF body motion module [52] was used to compute hull dynamics. The seakeeping results showed good agreement with model data from Katayama [53]. Caponneto et al.[54] also performed the same simulations using a different approach for the hull motion, where rigid body motion were computed with a fortran script through an estimation of the forces and moments based on previous timestep values. Thornhill et al.[55] presented captive, 1-DOF and 2-DOF simulations of a planing hull performed using the commecially avalaible Fluent®CFD code.

The results were compared with experimental data [56] and results using the Savitsky method. The single and 2-DOF results showed an excessive pressure estimation that lead to a reduced estimation of the hull resistance due to the different equilibrium attitude.

More recently, Brizzolara et al. [57] simulated the planing surface experiments by Cambliss [58] and concluded that CFD results performs better than widely used semi-empirical methods such as the ones proposed by Savitsky or Shuford [59]. Predictions based on CFD simulations showed error of around 5% for the lift and 10% drag force. Later, Brizzolara et al. [60] implemented an external routine to the CFD solver for assessing the runnning attitude of a planing hull. The routine was based on the theory of Savitsky and it was found that a allowed for a faster convergence respect to the built-in 2-DOF solver. The same author also presented simulations on patially ventilated planing hulls [61] Yousefi et al. [62] reviewed the existing techniques for hydrodynamic analysis of planing hulls, including commercial CFD software. Fu et al. [63] presented a comprehensive collection of CFD simulations of planing hulls in calm water, regular and irregular waves using both CFDShip-Iowa [64] and Numerical Flow Analysis (NFA) [65] to predict the hydrodynamic forces and moments, accelerations, motions and impact pressures. Gaggero et. al [66] presented the results of CFD simulation on a Series 62 parent hull using OpenFOAM [67], an open-source CFD tool. The results showed good agreement with the experimental measurements of the hull resistance, lift and drag. Except for low speed, the maximum drag and lift error is about 5%, although lift shows a lower average error. De Luca et al. [68] presented an extended Verification and Validation (V& V) study of CFD simulations on three models of the Naples Systematic Series of warped planing hulls. Pennino et al. [69] presented comparison between the three-dimensional pressure distribution on a planing hull bottom obtained with CFD simulation using CD-Adapco®STAR CCM+®code and and empyrical method. Comparison between CFD and experimental results for trim and sinkage values is also presented. The error on the resistance was within 10%, whereas errors for trim and sinkage and trim were higher, due to the fact that the code takes into account different pressure areas. Recently, more advanced planing hulls have been studied using CFD techniques, De Marco et al. [70] presented an extensive comparison between URANS and LES simulations of a stepped hull, computational results showed that the overset mesh technique leads to better attitude estimation than morphing mesh methods. In addition, the ventilated step region flow is carefully analysed by means of LES simulations and compared to experimental results. Seakeeping simulations of two-stepped planing hull in regular waves has also been carried out by Niazmand et al.[71] and compared the results with a fast analytical model.

Chapter 2

Model experiments

2.1 Introduction

Model scale resistance and seakeeping tests were an important milestone for the SOPHYA project. The experimental campaign included resistance, seakeeping and self propulsion experiments. In particular, seakeeping experiments were conducted using regular and irregular waves, though in this work, only regular waves results will be discussed. Results of the model experimental data, both in calm water in terms of hull running attitude and resistance and regular waves in terms of motion and acceleration transfer functions will be used as reference data for numerical simulation results and compared to full scale data. The experimental campaign was carried out at the the Towing Tank facility of the Department of Industrial Engineering of the Università degli Studi di Napoli "Federico II" under the supervision of Prof. Begovic. The towing tank (see fig. 2.1) is 136.0 m in length, 9.0 m wide and 4 m deep and it is equipped with a wave maker at the far end, capable of generating both regular and irregular waves.

The tests were carried out on a 1:6.5 scale fibre glass model of the original Yacht, a Monte Carlo Yachts 65, the main dimensions of the yacht and the tested model are reported in tab. 2.1.

Load Case 1	**Full Scale**	**Model Scale**
Length overall LOA (m)	18.158	2.794
Breadth overall BOA (m)	5.145	0.792
Waterline Length LWL (m)	16.1577	2.4825
Waterline Breadth BWL (m)	4.7977	0.7375
Depth T (m)	1.2126	0.1836
Displacement Δ (t, kg)	40.587	143.61

Table 2.1: Model details

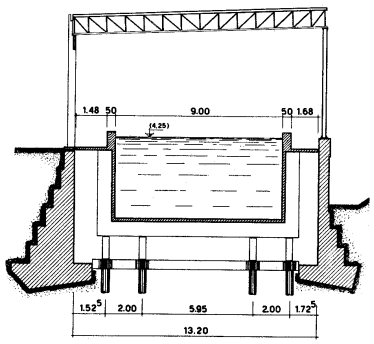

(a) Transversal Section

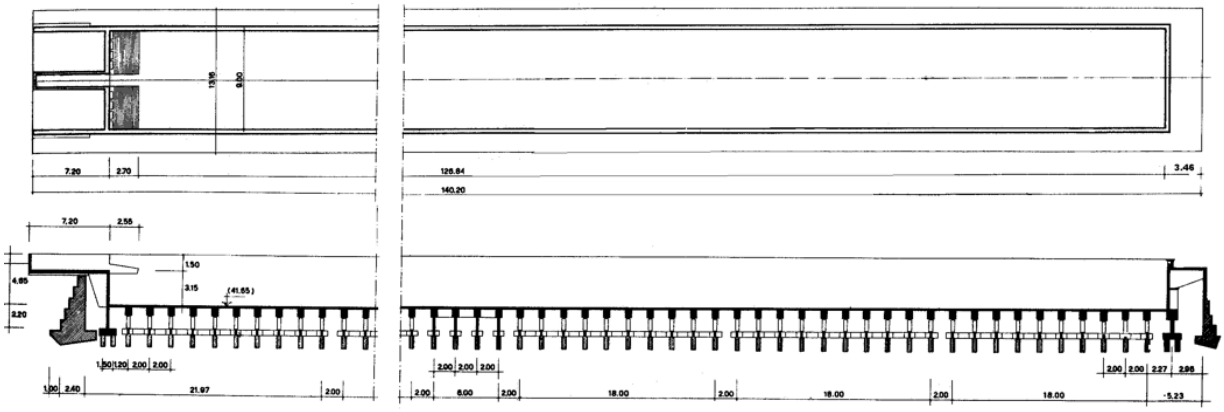

(b) Plan and longitudinal section

Figure 2.1: Naples DII Towing Tank

2.2 Calm water tests

Calm water tests are meant to collect reference data for calm water resistance in free trim and sinkage conditions. The calm water experiment program is based on the speed range provided by the shipyard and are reported in table 2.2.

The calm water tests are conducted for four different loading conditions but only the design loading condition (Loading Condition 1) is tested for all the speeds. Loading conditions 2 to 4 will be tested at a reduced speed range that should include 18 and 25 knots (ship speed), the two design cruise speeds. The two design speeds are also the ones used for the seakeeping tests in the next part of model tests.

Turbulence stimulators are not used in this experiments as the lowest test speed is 2.421 m/s, corresponding to a Reynolds number of $6.76 \cdot 10^6$, far more than the critical value of $3.5 \cdot 10^5$.

Ship (Kn)		12	15	18	22	25	28	30	32
Model (m/s)	LC 1	2.421	3.026	3.632	4.439	5.044	5.648	6.052	6.455
	LC 2			3.632		5.044	5.648		
	LC 3			3.632		5.044	5.648		
	LC 4			3.632		5.044	5.648		

Table 2.2: Calm water experimental program

2.2.1 Experimental setup

Before the model was ready to be tested, it had to be measured, marked and sensor must be mounted. The first step is to mark the waterlines on the hull, made by using a felt pen fixed on the gantry of a model milling machine (fig.2.2). The alignment of the gantry to the mill bed ensures high horizontal precision and the fine worm screw-operated vertical arm on which the pen pivots ensure an accurate vertical spacing. The waterline are needed once the hull is into the water in order to check that the desired design trim and depth has been achieved.

(a) Model on the mill bed

(b) Tracing waterlines

Figure 2.2: Tracing waterlines on the model hull

Next, the bare hull is weighted along with all the instrumentation, and the required ballast weights are collected in order to achieve the desired weight. The text step is to find the bare model center of gravity coordinates using the intertial balance and a longitudinal weight rack (fig.2.3). The longitudinal position of the center of gravity (LCG) is found by translating the model on the balance so that it is horizontal, at this point the pivot point of the balance is at LCG. Next the vertical position of the center of gravity (VCG) is found using the weight rack mounted on the inertial balance. The VCG is found by measuring the vertical distance between the pivot point

and the center of gravity ΔZ_G:

$$\Delta Z_G = \frac{m\Delta x\, cot(\theta)}{m + M} \tag{2.1}$$

where m is the mass placed over one of the weight rack screw at a Δx distance from the center one, θ is the measured trim angle and M is the hull weight. Multiple measurements of Δx and θ are made in order to reduce the error. Baallast weight distribution are then computed so that the ballasted model center of gravity is in the desired position.

(a) Inetrial balance (b) Weight rack

Figure 2.3: Center of gravity and inertia measurement apparatus

Once the ballasting is done, the inertial balance is used to check the result. Target weight, LCG and VCG are different for every loading condition and are listed in tab.

	LC1	LC2	LC3	LC4
Δ (kg)	143.51	143.51	143.51	129.36
LCG (m)	1.038	1.079	0.989	1.037
VCG (m)	0.302	0.302	0.302	0.287

Table 2.3: Weight and center of gravity for different loading conditions

Once the model is in the water,it is checked that the model floats the waterline previously traced for the design loading condition. At this point only minor transversal ballast adjusments is made in order to null a small heel due to the hull construction weight asymmetry. The actual model is then adequately restrained to the towing carriage so that both trim and sinkage are allowed during the run. For yaw and sway restraining, two longitudinal carbon fibre rods are fitted at the bow and stern, whose are free to slide between two vertical rods fixed on the carriage and aligned with the towing tank (fig.2.4). The hull is then connected to a vertical sliding arm via a cardan joint that allows rotation along the transversal axis (pitch). Roll motion is restrained

since the rotation axis of the two carbon sticks aft and forward of the boat and the longitudinal rotation axis of the cardanic joint at the centre are parallel but do not coincide (cardanic joint is placed lower on the inner deck).

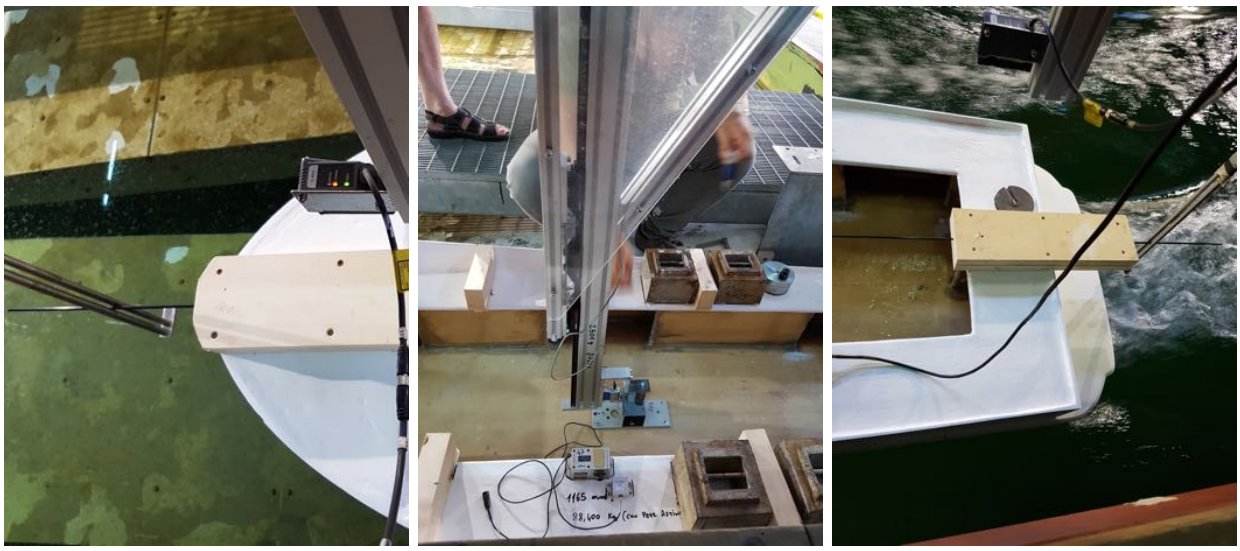

(a) Bow restraint (b) Towing arm (c) Aft restraint

Figure 2.4: Model restraint setup

The towing point has been placed as near as possible to the center of gravity of the hull ballasted for the loading condition 1. The towing point is fixed for all four loading conditions and its coordinates are reported in tab. 2.4, it is used as the reference point for vertical displacements and initial draft $z_{fs,0}$ (fig.2.5).

X_{TOW}	1043	mm
Y_{TOW}	0	mm
Z_{TOW}	270	mm

Table 2.4: Towing point coordinates.

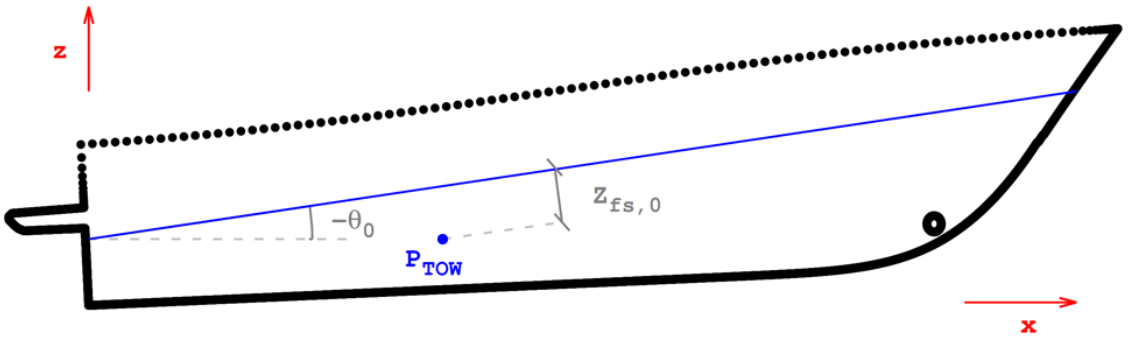

Figure 2.5: Initial towing point immersion $Z_{fs,0}$ and initial trim θ_0.

2.2.2 Measurement system

The measurement system for calm water is very simple since it is required only to measure running trim, sinkage and resistance (horizontal towing force). Running trim and sinkage are measured using two Keyance IL-600CMOS CMOS analog laser distance sensors, one placed at 2.436 m and a second one at 0.176 m distance from the transom stern. From the measured vertical distances sinkage and trim were derived by simple coordinate transformations The resistance is measured using an S-beam load cell that connects the sliding arm to the cardan joint, ensuring that only horizontal force is measured. In fig. 2.6, a detailed picture of both laser and load cell sensor is shown.

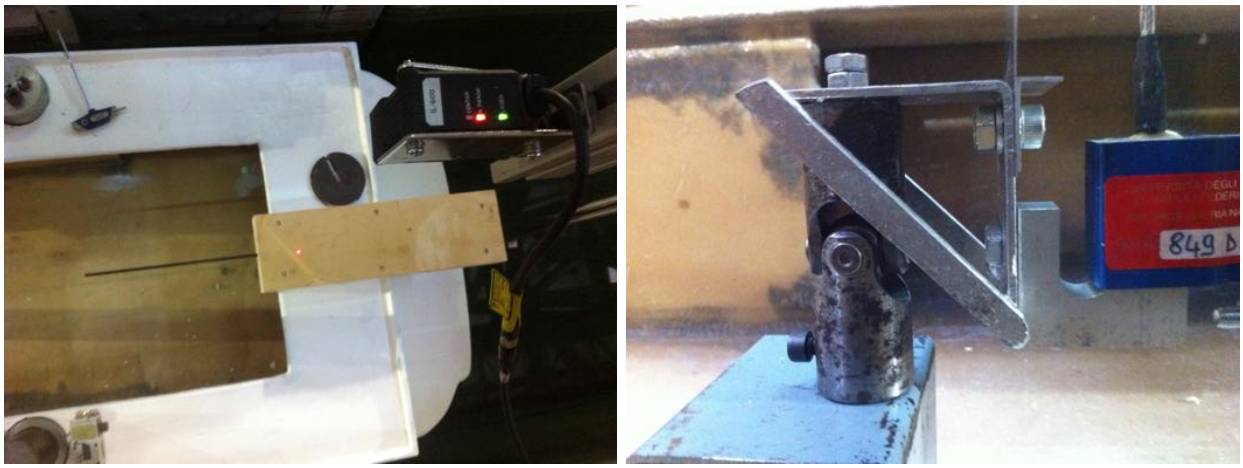

(a) Stern laser sensor (b) Load cell

Figure 2.6: Calm water measurement system

The sampling rate used is not constant throughout the whole speed range, the lower towing speeds (up to 4.439 m/s) are sampled at 500 Hz, while sampling rate is increased to 5 kHz for higher speeds.

2.2.3 Experimental procedure

The experiments were carried out one speed per run, wave damper on the towing tank were fully rise in order to reduce the waiting times between run. Ultrasonic wave probes were used to monitor residual waves prior to every run, along with visual observation of the water surface. The data is collected by the acquisition system using an ad-hoc LabView®interface and is exported as .xls file.

Before every run, the acquisition is started with the towing carriage being stationary. The data from the load cell and laser pointers is used as offset values for that specific run and flagged with "1". During the run, once the carriage is at the desired speed, a preliminary data windowing was applied manually by the operator, tagging the data with "2". Later in the data analysis process, the tagged data has been used to plot preliminary results and to inspect the relevant timeseries. Next, both zero-speed and steady forward speed windows have been resized after visual observation of the time series, in order to select the cleanest data possible.

2.2.4 Data analysis

The data analysis has been carried out using MATLAB®scripts developed with the aim of delivering benchmark results for CFD simualtions as well as serving as comparison for full scale data. In the folowing section the method used to analyse raw data collected during the towing tests is explained.

Trim and Sinkage values

Trim and sinkage values are not result of a direct measurement, as in the case of resistance and carriage speed. They have to be computed from the two measurements from the laser sensors by means of trigonometry calculations explained in the following points:

First approximation

The first approximation values for trim and sinkage were calculated using the assumption that:
- The laser sensors are pointing on two co-planar plates.
- The plates move perpendicular to the laser beams.

- **Trim**
  Trim has been calculated using the following equation:

$$\theta = \frac{180}{\pi} \arctan\left(\frac{(h_1 - h_{1,0}) - (h_2 - h_{2,0})}{L_{LAS}}\right) + \theta_0 \tag{2.2}$$

  Where:

  - h_1: bow plate height measured by laser

- h_2: aft plate height measured by laser
- $h_{1,0}$: bow plate height measured by laser at zero speed
- $h_{2,0}$: aft plate height measured by laser at zero speed
- L_{LAS}: horizontal distance between the two vertical positions
- θ_0: Static trim

- **Sinkage**
  Sinkage is evaluated at the towing point and it is computed using the following equation:

$$\Delta T = -((h_2 - h_{2,0}) + L_A \tan(\theta)) + T_0 \tag{2.3}$$

  Where:

  - L_A: horizontal distance between the towing point and aft laser sensor
  - X_{TOW}: towing point longitudinal coordinate
  - T_0: Static immersion at X_{TOW}

As an example, fig. 2.7 shows the trim and spray formation difference between design speed (18 kn) and 25 kn.

(a) V=3.632 m/s (b) V=5.649 m/s

Figure 2.7: Calm water tests

Corrected Trim and Sinkage

Corrected values of trim and sinkage are calculated in order to take into account that both the assumption made for first approximation are not met in the experiments. In fact, the plates were mounted on the after and fore deck of the model, whose are at different heights (see Fig.2.8) and the model had a non-zero static trim angle.

The corrected values are computed as:

- **Trim**
  In order to take into account both plate heights and static trim, the corrected trim value

has been calculated using the following equation:

$$\theta = \arctan\left(\frac{(h_1 - h_{1,0}) - (h_2 - h_{2,zero}) - (F - A)(1/\cos\theta - 1/\cos\theta_0) + L\tan\theta_0}{L_{LAS}}\right) \quad (2.4)$$

Where:

- F: vertical distance between towing point and bow laser plate

- A: vertical distance between towing point and aft laser plate Since the corrected trim equation is implicit, the first approximation trim value has been used as the initial value in the *while* loop.

- **Sinkage**
  The sinkage value has been also corrected using the following equation:

$$\Delta T = (h_2 - h_{2,0}) - A(1/\cos\theta - 1/\cos\theta_0) + L_A(\tan\theta - \tan\theta_0) \quad (2.5)$$

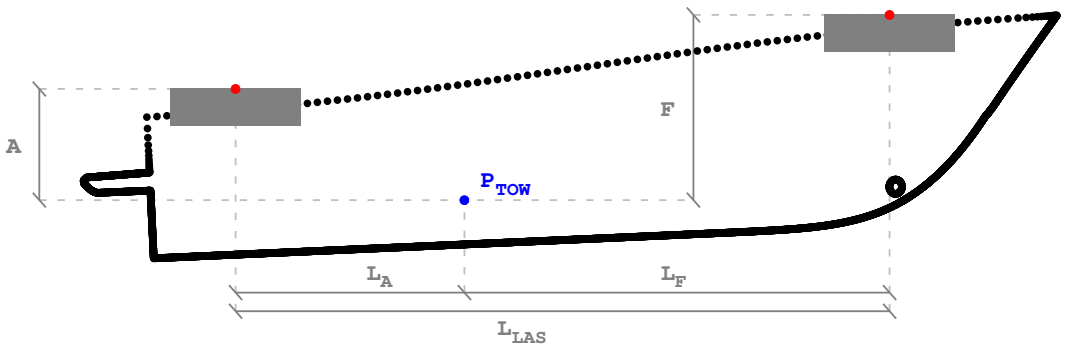

Figure 2.8: Laser plates and torwing point position

Both corrected trim and sinkage values have been computed using the average value along with the maximum and minimum values of the windowed time series.

Carriage rail curvature correction

After the first look at the sinkage data, it was clear that a very low frequency trend was present. The data showed reduced noise but with remarkable differences inside the time window where speed and resistance were steady. In order to investigate the presence of rail curvature that could affect the measurement of heave, a slow run (0.25 m/s) was performed without a hull attached. The carriage was equipped with three ultrasonic wave gauges and the run was performed after a long pause. The ultrasonic sensors output represent the distance between an horizontal reference surface (still water) and the carriage platform, ultimately indicating any carriage rail deviation respect to the water surface.

The results of the run is plotted in fig.2.9, the three ultrasonic sensor output show a 6 millimeter vertical deviation along 100 meters of run length. The signal also shows the presence of a standing wave only marginally affected by wave dampers, the wave amplitude is zero at the center of the tank (60m) and grows towards the end. The slow carriage speed allowed to measure the actual rail curvature, isolating the effect due to the low frequency standing waves, that affects the measure but it is not correlated to the rail curvature.

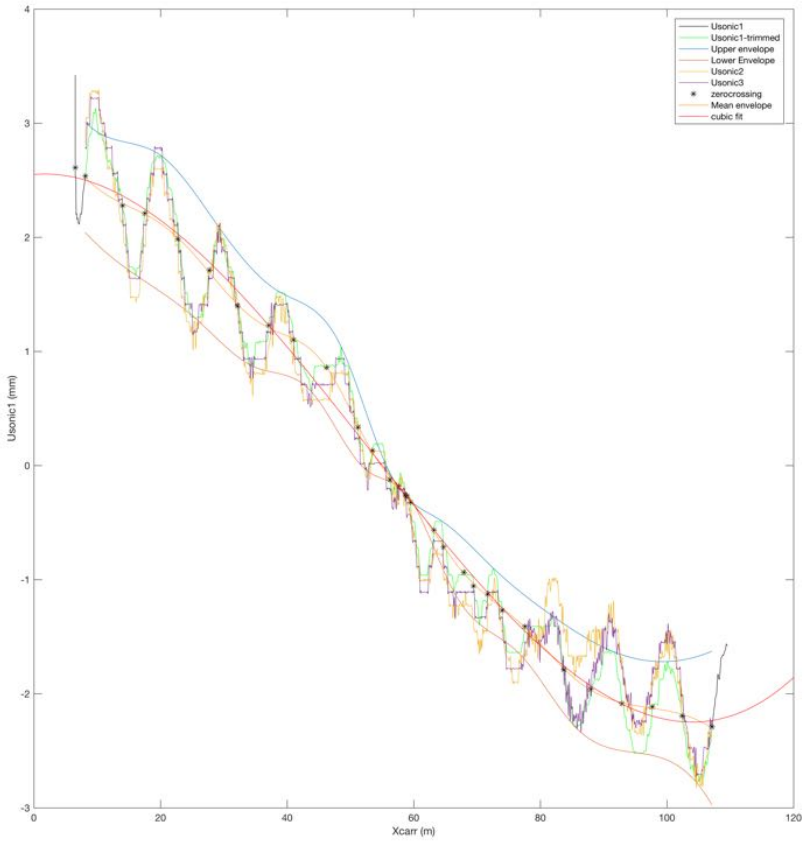

Figure 2.9: Carriage rail correction experiment

In order to extract the mean rail deviation, first the two signal envelopes are computed using two splines. The intersection between ultrasonic signals and the average line between the envelope have been marked as "zero crossing". The cubic fit of the "zero crossing" points has been used as the rail curvature correction for heave measurements.

This experiment has been carried out one year later during another experimental campaign, but the correction has been applied to all previous results.

An example of the sinkage timeseries is shown in fig. 2.10, it clearly shows the detrend effect

of the rail curvature correction.

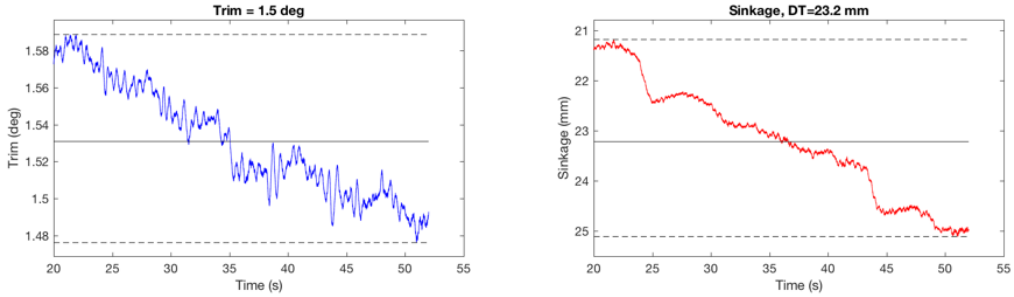

(a) Original results

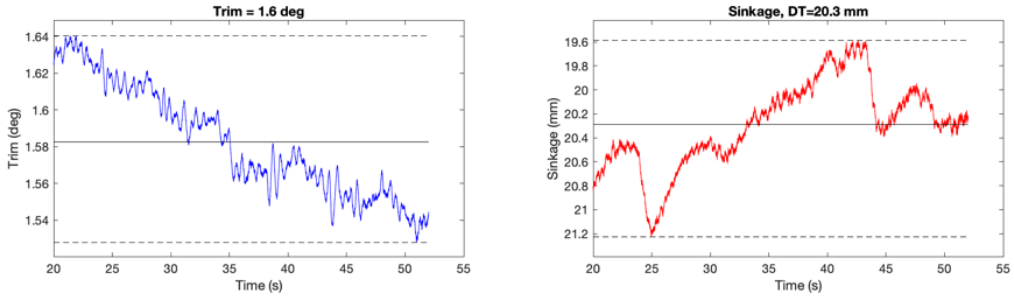

(b) Corrected results

Figure 2.10: Rail curvature heave detrend

Carriage speed

Carriage speed shows a fairly good signal with reduced noise. Isolated very high peaks are found here and there, possibly related to small discontinuities in the rails of the towing system. Outliers points are rejected using a 3σ threshold in order to avoid affecting mean and standard deviation too much. Rejected outliers are marked in red in the top-left plot of fig.2.11.

Mean value $\overline{V}_{carr}$ is represented by solid black line and dashed lines are confidence intervals delimited by $\overline{V}_{carr} \pm 2\sigma$.

Resistance

Resistance values do not present significant outliers, so raw data has been analyzed. Mean value and confidence intervals (double standard deviation) are represented as in the case of carriage speed time series.

Results format

The results of the calm water test data analysis are plotted case by case, both time series and average values are plotted in order to check any possible error in the analysis procedure (fig. 2.11).

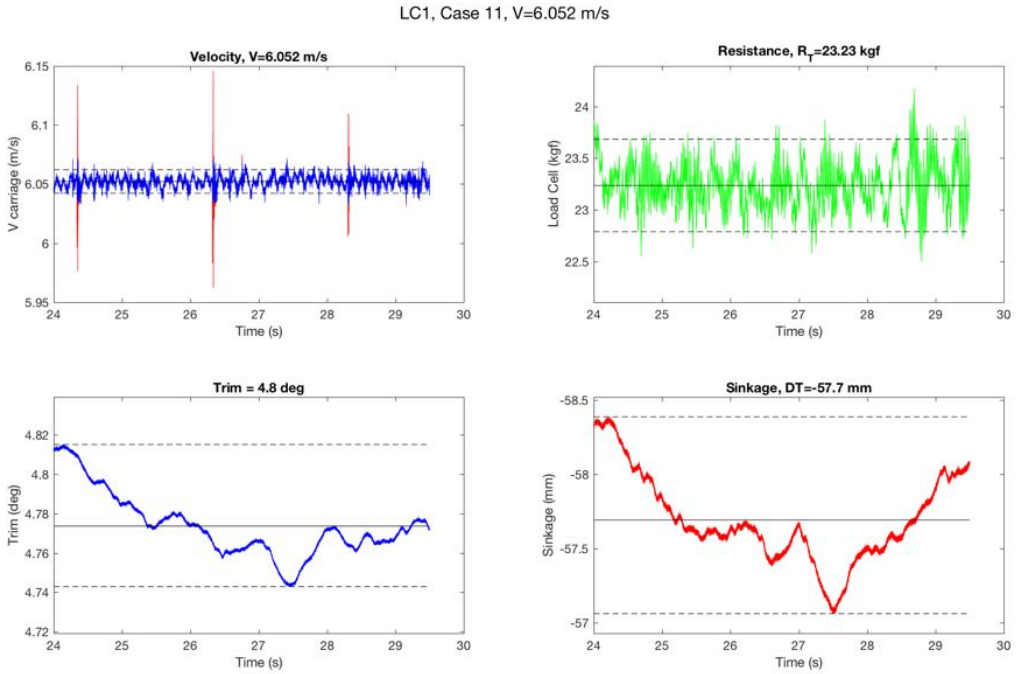

Figure 2.11: Results time series example

A summary of the results is also written to a text file, structured in such a way that it should be easily readable and simple to import in post-processing scripts.

2.2.5 Results

The results of the calm water experiments are plotted in fig.2.12, resistance (F_{TOW}) trim and sinkage are plotted for every tested loading condition and speed. With reference to tab. 2.3, it can be observed that, as expected, the dynamic trim for the LC1 case stays between LC2 (higher LCG, lower trim) and LC3 (lower LCG, higher trim) cases. The lower displacement LC4 case shows slightly decreased dynamic trim. Dynamic trim for LC1 shows a maximum value of 4.8 degrees for 5.648 m/s.

Sinkage comparison follows essentially what it has been observed for the case of trim, the main difference is that there is no maximum value. Sinkage is always reducing as speed increases, as the hydrodynamic lift grows with the speed.

Resistance values for LC1 case show that as the trim value reach its maximum, also the total resistance does. As expected, the lower displacement LC4 case shows less resistance respect to the other cases. The LC3 case resistance is close to the LC1 case, although higher trim angles. The low-trim LC2 case shows higher resistance values at higher speeds instead.

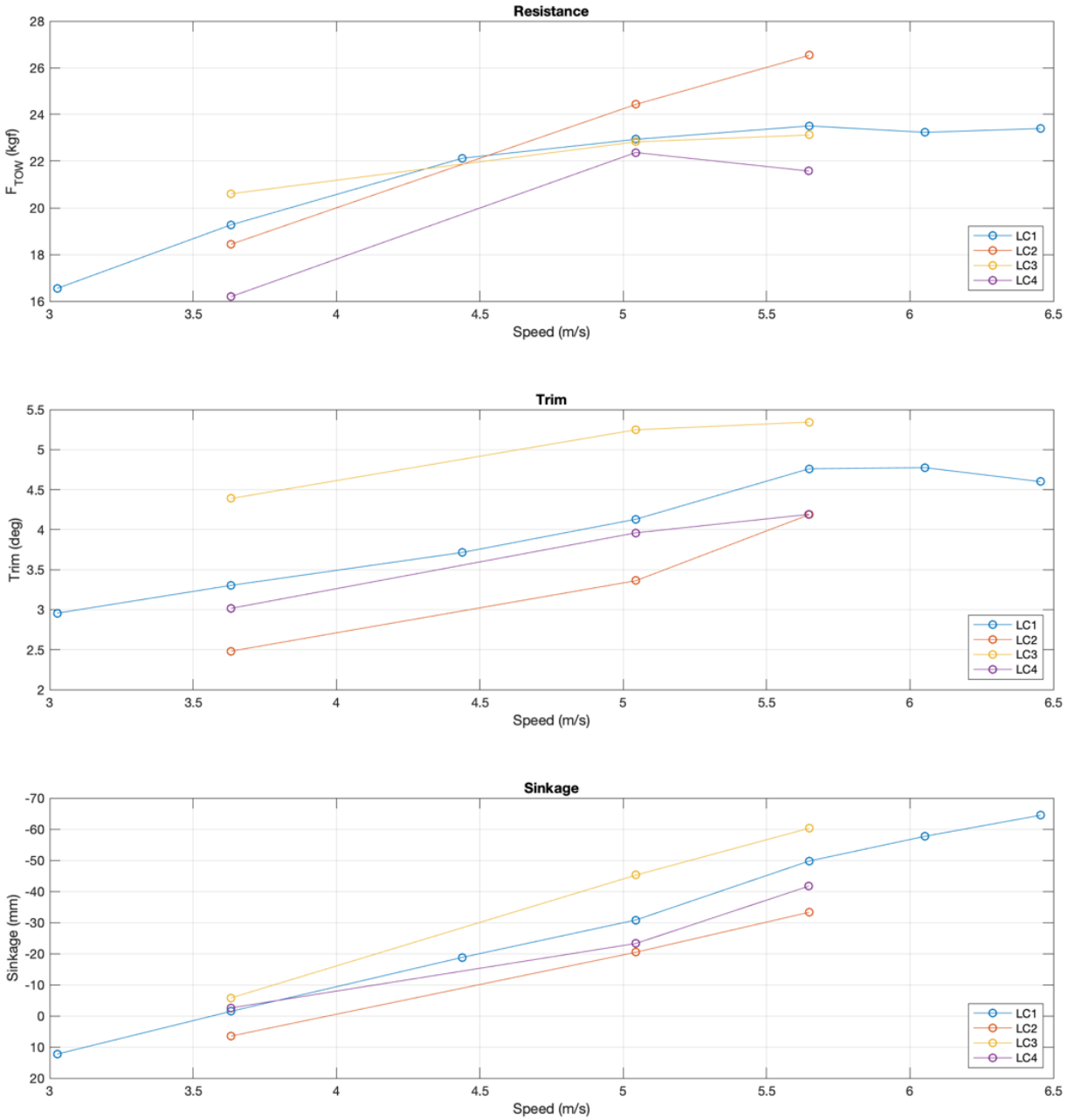

Figure 2.12: Calm water results

2.3 Seakeeping tests

Regular waves seakeeping tests are part of the core of the research as they provide reference data for seakeeping trials and simulations. In particular, the main goal of model scale seakeeping tests in regular waves is to obtain motion and acceleration response over a range of wave frequencies. The model motion and acceleration response characteristics are usually summarized by the so called transfer functions (TF). Transfer functions from regular wave experiments will be compared with the full scale and simulated ones.

2.3.1 Experimental setup

Since model motions are the main subject of the experiments, the model moments of inertia have to be taken in to account. The full scale boat structures and equipment has been taken into account in the calculation of the Yacht (target) moments of inertia. In particular, assumptions on fill level of the tanks are reported in Tab. 2.5. Only tanks fluid weights are taken into account for the computation of the moments of inertia, without free surface effects.

Item	fill level
Fuel Tanks	70%
Fresh water tanks	20%
Black water tanks	10%
Grey water tanks	10%
Boiler	0%

Table 2.5: Tank fill levels

The calculations on the reference loading condition (LC1) resulted in two target values, one for pitching and one for transversal moment of inertia in terms of ratio between radius of gyration and waterline length and breadth respectively. The dimensional target values in model scale are reported in tab. 2.6.

The moments of inertia of the bare hull are first measured using the inertial balance, the ballast are then moved symmetrically forward/backwards in order to match the target value without affecting the centre of gravity.

The inertial balance is able to oscillate the model around the pivot point around any axis thanks to a cardan joint, this allows the measurement of both transveral and longitudanal oscillations. The hull is oscillated on the balance and the oscillation periods are measured real time thanks to a three axis accelerometer mounted on the oscillating structure above the pivot point on the balance support assembly (Fig.2.13(a)). The periods are measured for a 10-15 oscillation moving window until the standard deviation is below 10^{-3} using a LabView®interface on a laptop connected to the acquisition system (Fig.2.13(b)). Measurements of transversal moment of inertia, although not necessary, were carried out upon the commissioner request. In order to avoid possible coupling between transversal and longitudinal oscillations, also pure longitudinal and transversal oscillations have been analysed for the respective moment of inertia.

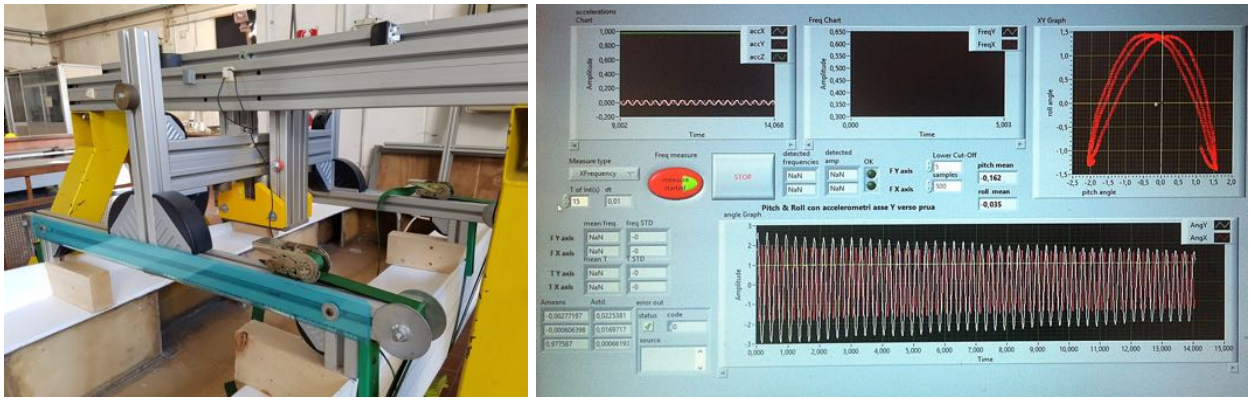

(a) Inertial balance pivot/accelerometer

(b) Measuring oscillation periods

Figure 2.13: Inertial balance measurements

The model moment of inertia are then computed since the position of the centre of gravity and the inertia of the balance support are known. It turned out that the bare hull had a larger moment of inertia than expected due to manufacturing aspects, probably because of the detail of the bow thruster tunnel that required a lot of fiberglass to be shaped. The measured model roll (I_{xx}) and pitch (I_{yy}) moments of inertia are listed in tab. 2.6 along with the target values.

	LC1	LC2	LC3	LC4	Target
I_{xx} $(kg \cdot m^2)$	12.859	11.251	12.859	11.251	10.004
I_{yy} $(kg \cdot m^2)$	67.331	68.891	73.728	68.891	61.051

Table 2.6: Model moments of inertia

The seakeeping tests have been carried out using the same towing arm and restraining setup as the calm water tests. The vertical positioning of the vertical guide rods at the bow is more of an issue in this tests because of it has to allow the full bow movement range without interfering with the water surface of the incoming waves. A trade-off position is found for every combination of speed and wave frequency (Tab. 2.7).

2.3.2 Measurement system

The measurement system for the regular waves seakeeping tests differ from the case of calm water by having two additional measurements, namely wave profile and accelerations. The incoming wave profile generated has been measured using a Baumer UNDK 30U6103 ultrasonic probe fixed to the carriage in front of the model. Accelerations are measured by means of two Cross Bow CXL04GP3-R-AL thee-axis MEMS accelerometers, one at the same horizontal position of the center of gravity and the other on the bow at 2.285m from the transom stern. The sampling rate is set 5 kHz for all the tests.

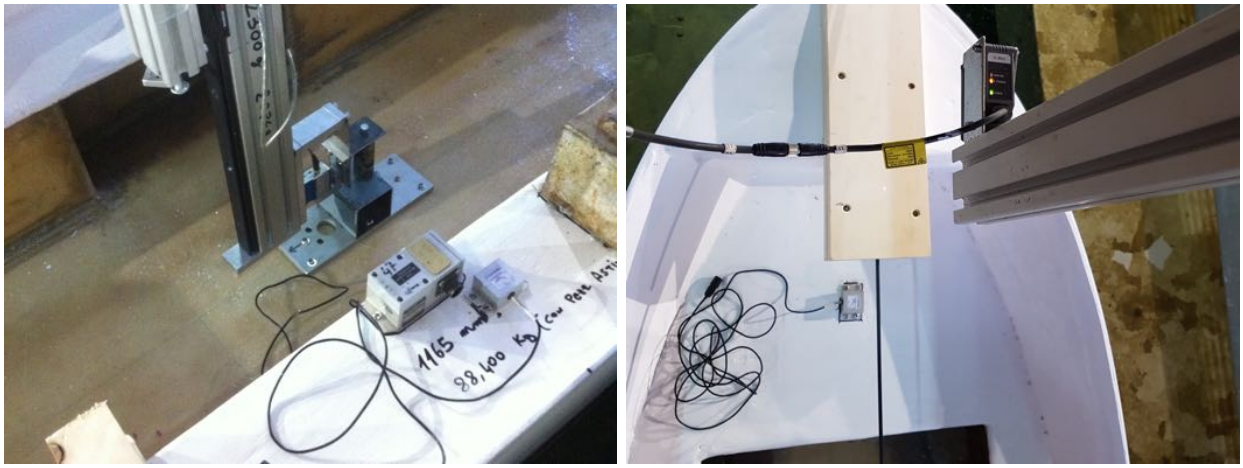

(a) Center of gravity accelerometer (b) Bow accelerometer

Figure 2.14: On board accelerometers

2.3.3 Experimental procedure

The regular waves seakeeping tests program comprised of a set of nine wave frequencies, all having the same steepness (H/λ) of 1/100. All the loading conditions were tested for all nine wave frequencies at the design speed of 3.632 m/s (18 kn), loading condition 1 has also been tested at 5.044 m/s (25 kn). The seakeeping experimental program is summarized in tab. 2.7.

V=3.632 m/s	Wave frequency (Hz)								
LC1	0.319	0.364	0.425	0.464	0.51	0.567	0.637	0.728	0.85
LC2	0.319	0.364	0.425	0.464	0.51	0.567	0.637	0.728	0.85
LC3	0.319	0.364	0.425	0.464	0.51	0.567	0.637	0.728	0.85
LC4	0.319	0.364	0.425	0.464	0.51	0.567	0.637	0.728	0.85
V=5.044 m/s	Wave frequency (Hz)								
LC1	0.319	0.364	0.425	0.464	0.51	0.567	0.637	0.728	0.85

Table 2.7: Seakeeping tests program

Due to equipment malfunction, data for the LC1 case has been found to be unusable, the model has been re-tested in the LC1 configuration 1 year later, results that will be plotted refer to the re-tested model.

2.3.4 Data analysis

Raw sampled data from the acquisition system of the Naples towing tank is presented in form of excel spreadsheets. Data is imported in Matlab in a large matrix having the data from different sensors stored in different matrix columns. Data is the filtered using the fifth order Butterworh filter, the passband edge frequency is set at 45 Hz and stopband edge frequency at 160 Hz. In Fig. 2.15, the Butterworh filter frequency response is shown along the original and filtered timeseries. The acceleration spectrum used in figure has been normalized in order to show the peaks that are inside the passband.

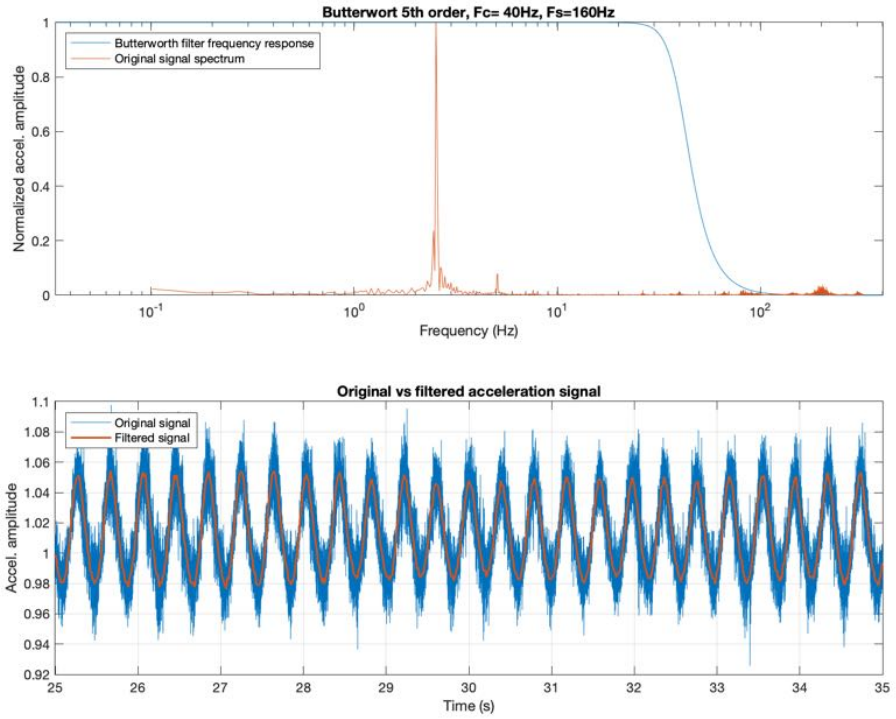

Figure 2.15: Data filtering example

The carriage rail correction has been applied to the ultrasonic and laser sensors as well in order to detrend the heave and wave measurement. The pitch is calculated using the corrected trim formulation shown in the calm water section.

As a first step, preliminary windows are set by visual observation of the data, the goal is to select an appropriate amount of wave encounter and the signal should be as steady as possible. Then, the upper and lower envelopes (blue and red lines in 2.18)of the preliminarly windowed motion time series (black line) are computed using third order splines passing through the peaks. A simple "zero crossing" detection algorithm is then used in order to find the index of the first and last crossing up point of the signal respect to the mean line, the signal is then trimmed using those

points (green line). The average line between the envelopes is then used to create a straightened, zero-mean of the the original signal(blue line).

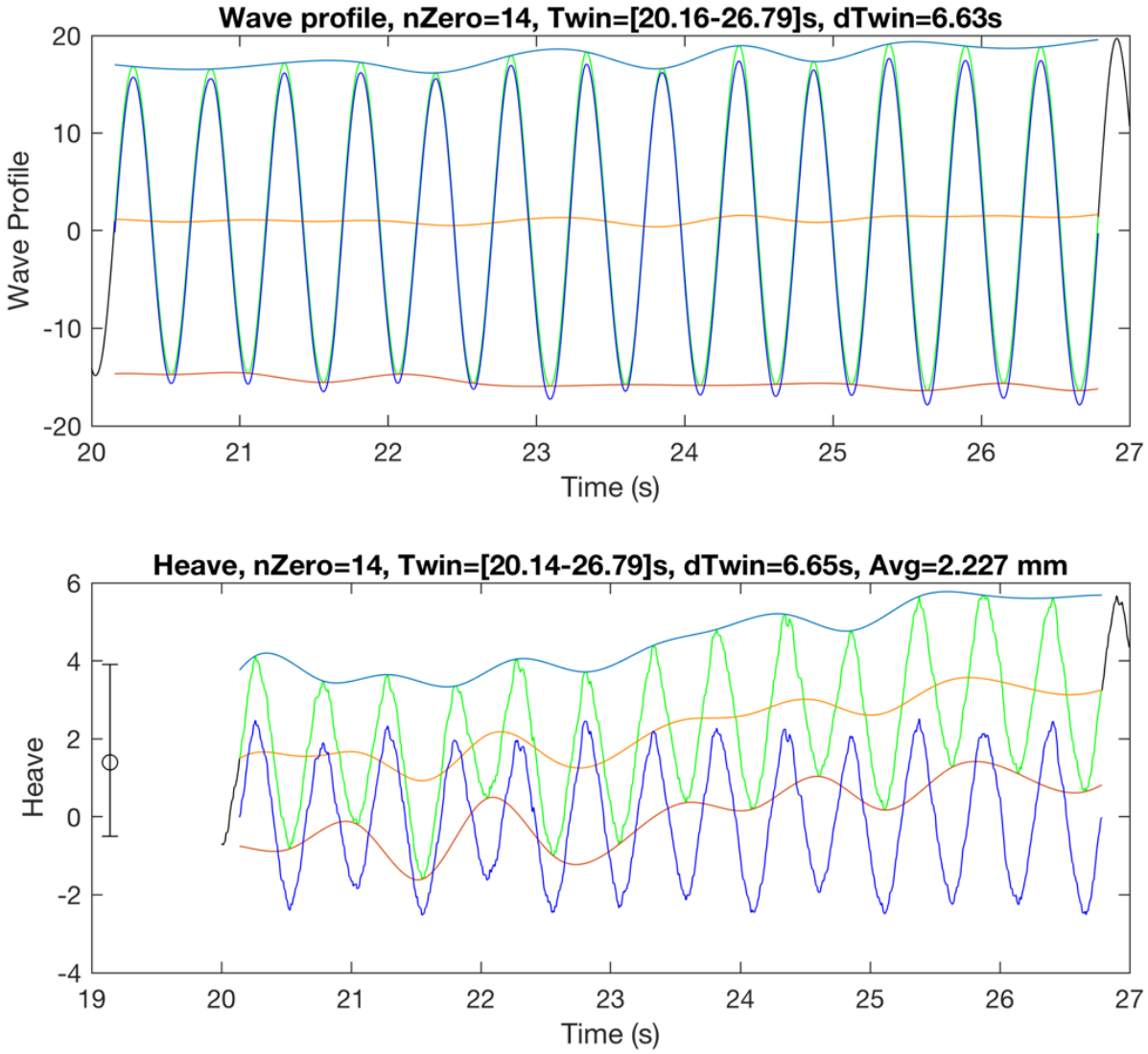

Figure 2.16: Example of wave and heave time series

The goal of this analysis is to evaluate wave and motion response characteristics in order to evaluate the model transfer functions. The wave and motion response amplitudes are valuated through the single sided amplitude spectrum, computed using MATLAB® using the built-in Fourier transform algorithm. In particular, the response amplitude is computed as the value of first harmonic amplitude of the signal's spectrum.

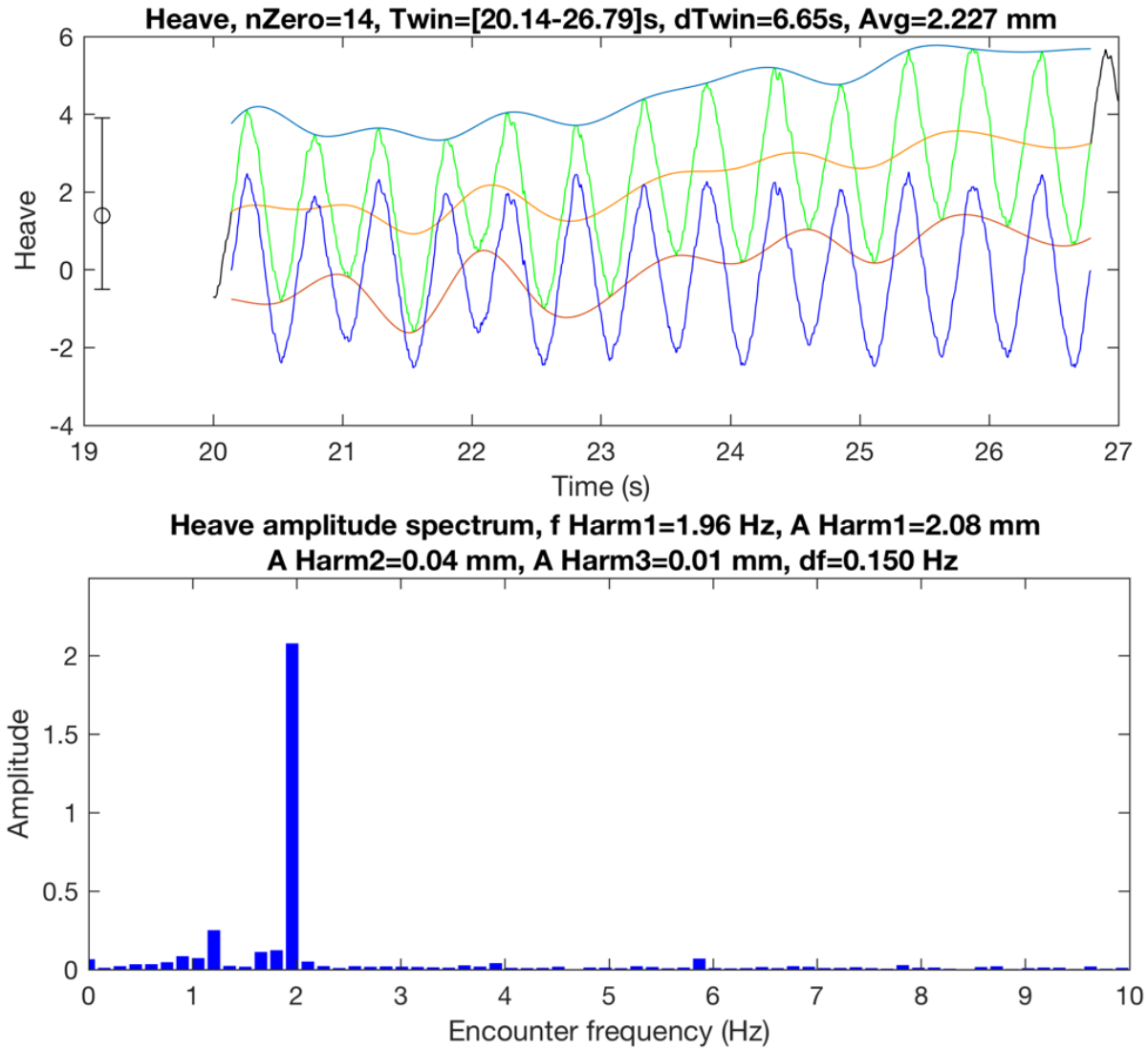

Figure 2.17: Example of heave time series and spectrum

The wavelength is an essential parameter for the evaluation of the pitch transfer functions. Since the measured frequency of waves and hull motions is in fact the encounter frequency, the first guess wavelength is computed using via the dispersion relation for deep water using the input frequency of the wave maker f_{input}:

$$\lambda = \frac{g}{f_{input}} \tag{2.6}$$

The actual wavelength is then corrected for intermediate depths via the implicit expression of the dispersion relation:

$$\lambda = \frac{g}{f_{input}} tanh\left(\frac{2\pi h}{\lambda}\right) \tag{2.7}$$

Where h is the towing tank water depth. The correction will not have an effect apart from the three lowest frequencies. At this point, the motion transfer functions can be computed, the heave transfer function is computed as the ratio between the first harmonic amplitudes of heave and wave amplitude:

$$TF_{HEAVE} = \frac{A_{heave}}{A_{wave}} \tag{2.8}$$

The pitch transfer function is computed as the ratio between the first harmonic amplitudes of pitch amplitude and wave slope:

$$TF_{PITCH} = \frac{A_{pitch}}{kA_{wave}} \tag{2.9}$$

where $k = 2\pi/\lambda$ is the wavenumber.

Acceleration transfer functions are also computed using the same method and are defined as:

$$TF_{ACC} = \frac{A_{acc}}{\omega_e^2 A_{wave}} \tag{2.10}$$

where $\omega_e = 2\pi f_e$ is the angular encounter frequency, corresponding to the first harmonic of the wave amplitude.

The gravity acceleration constant g has been evaluated using accurate absolute measurements near the towing tank position [72]. The value at the towing tank has been estimated through bilinear interpolation of the two nearest measurement. The latitude and longitude of the towing tank and the two nearest measurement laboratories was used for the interpolation since there are no significant elevation differences.

The value of g is used here in order to estimate the wavelength but it will be used later when comparing CFD and experimental resistance, since the CFD code output will be in Newton (N) and not in kilograms force, as it is the case of the load-cell. The estimated value of g at the towing tank is 9.8026 m/s, essentially the same value of the nearest two sites if rounded to the fourth decimal.

2.3.5 Results

The results of the regular waves seakeeping test data analysis are plotted case by case, both time series and their relative amplitude spectrum are plotted side by side, an example of the analysis results plots for the hull vertical motions is shown in Fig. 2.18.

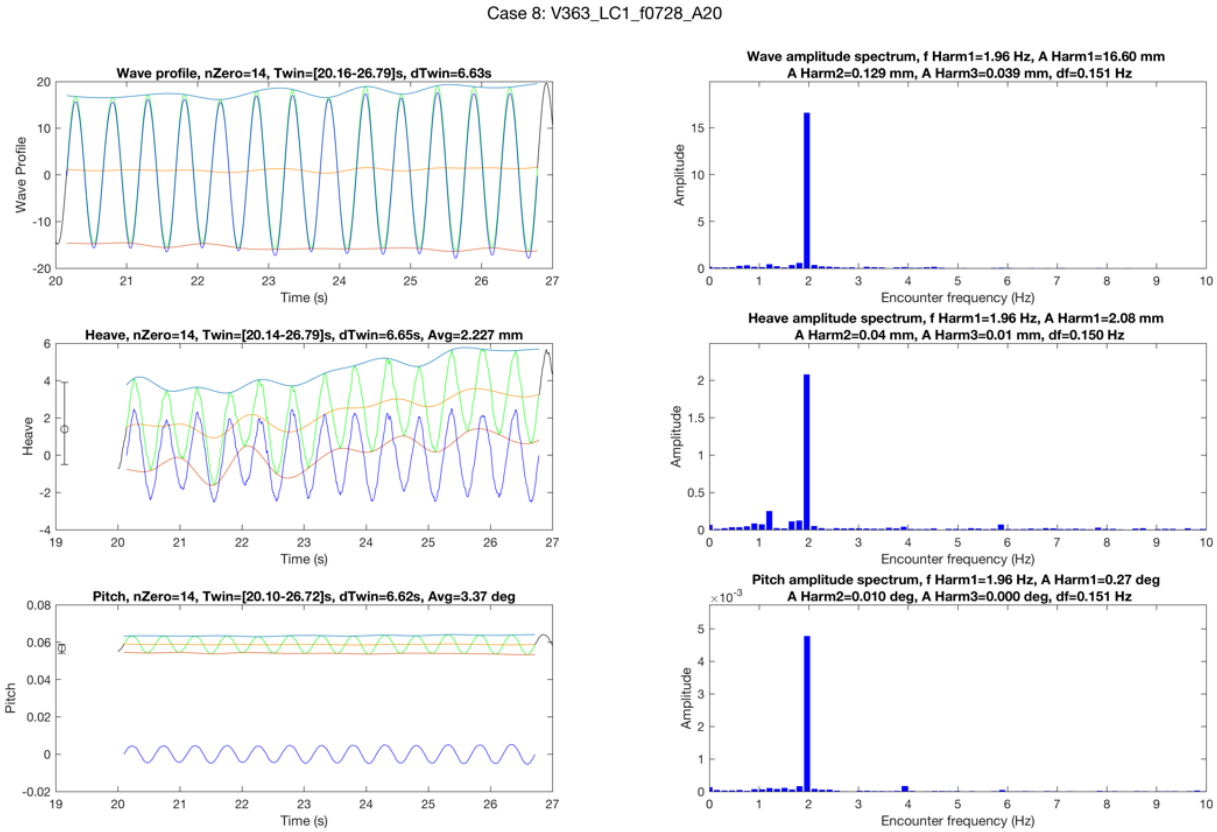

Figure 2.18: Vertical motions results example

On the left, the time series are plotted, information about the window are reported on top of each plot, along with the average value. On the right, their relative time series spectra are plotted, on top of the plots, the first harmonic frequency and amplitudes are reported. In addition second end third harmonic amplitudes are also reported.

The result plot of vertical accelerations follows the same scheme of the case of vertical motions, as it can be seen in Fig.2.18

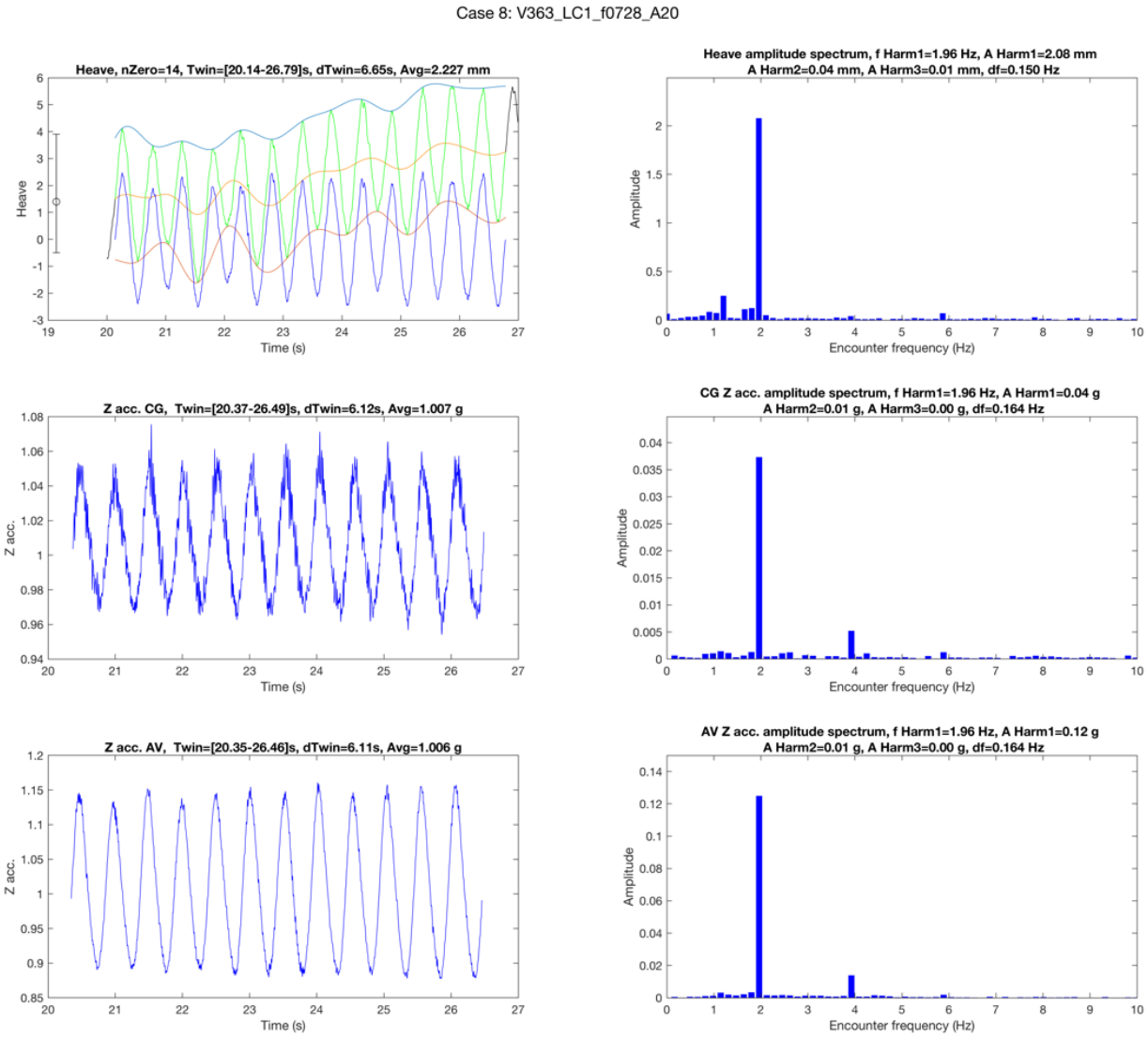

Figure 2.19: Vertical accelerations results example

As expected, in the case of vertical accelerations, the response is greater at the bow (AV) than at the center of gravity (CG), and they share the main harmonic frequency with the wave signal. Differently from the case of vertical motions, vertical accelerations show greater second and third harmonic response amplitudes. It is known that acceleration responses of high speed crafts are nonlinear (see [21] and [34] for example), but no specific analysis is carried out on the MCY65 model hull.

The presence of nonlinear effects on a set of planing hulls will be discussed in a separate section, where both hull motions and acceleration will measured and analysed with the purpose of studying the presence of higher harmonics as a function of speed, hull forms and wave characteristics of a systematic hull series.

The plots in Fig. 2.20 show the comparison of the vertical motion transfer functions relative to the four loading conditions.

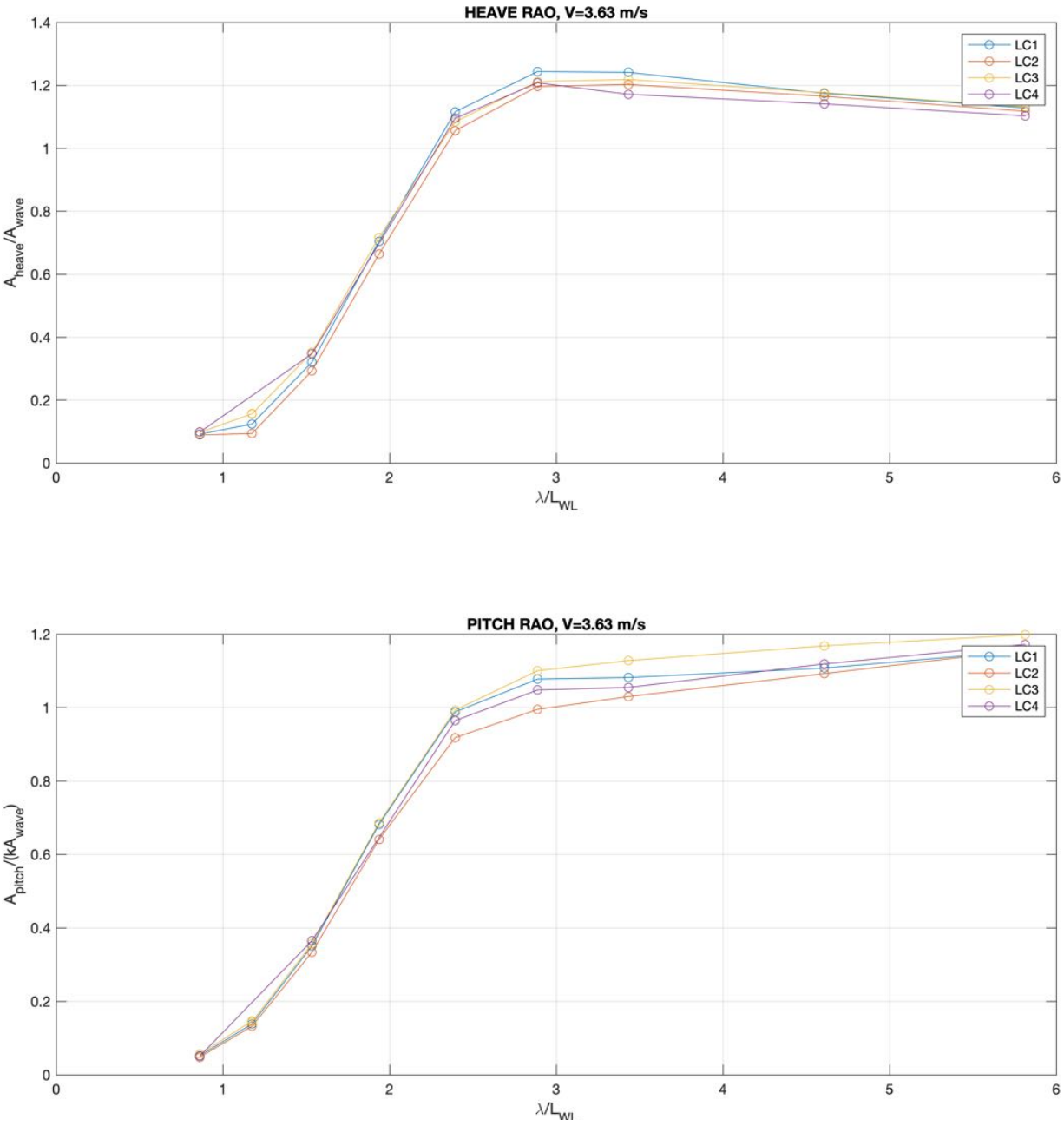

Figure 2.20: Vertical motions transfer functions comparison

It is clear that the effect of the chosen loading conditions on the heave transfer functions is visible although not important. All loading conditions show a peak in the heave response for

wavelength of about three waterline lengths. This because of the high speed of the craft is such that the critical frequency is reached for longer waves than it is the case for conventional ships. Higher static trim seems to lead to higher heave response (LC2) than the lower case (LC3) over the whole range of wave frequency tested. Loading condition 1 seems to have the highest response around the peak wavelength, it is worth remainding that this loading condition has not been tested consequently to the other three.

Pitch transfer functions also do not show large differences between loading conditions, however in this case the effect of static trim is consistent with what it is expected. Both LC1 and LC4 pitch responses amplitudes are always between the other two loading conditions, as they share the same mid-positioned centre of gravity. The more aft the center of gravity is moved (larger static trim), the higher the pitch response is, and vice versa. Differently from the heave response, no peak value is present and the highest pitch response is measured for the longest waves tested.

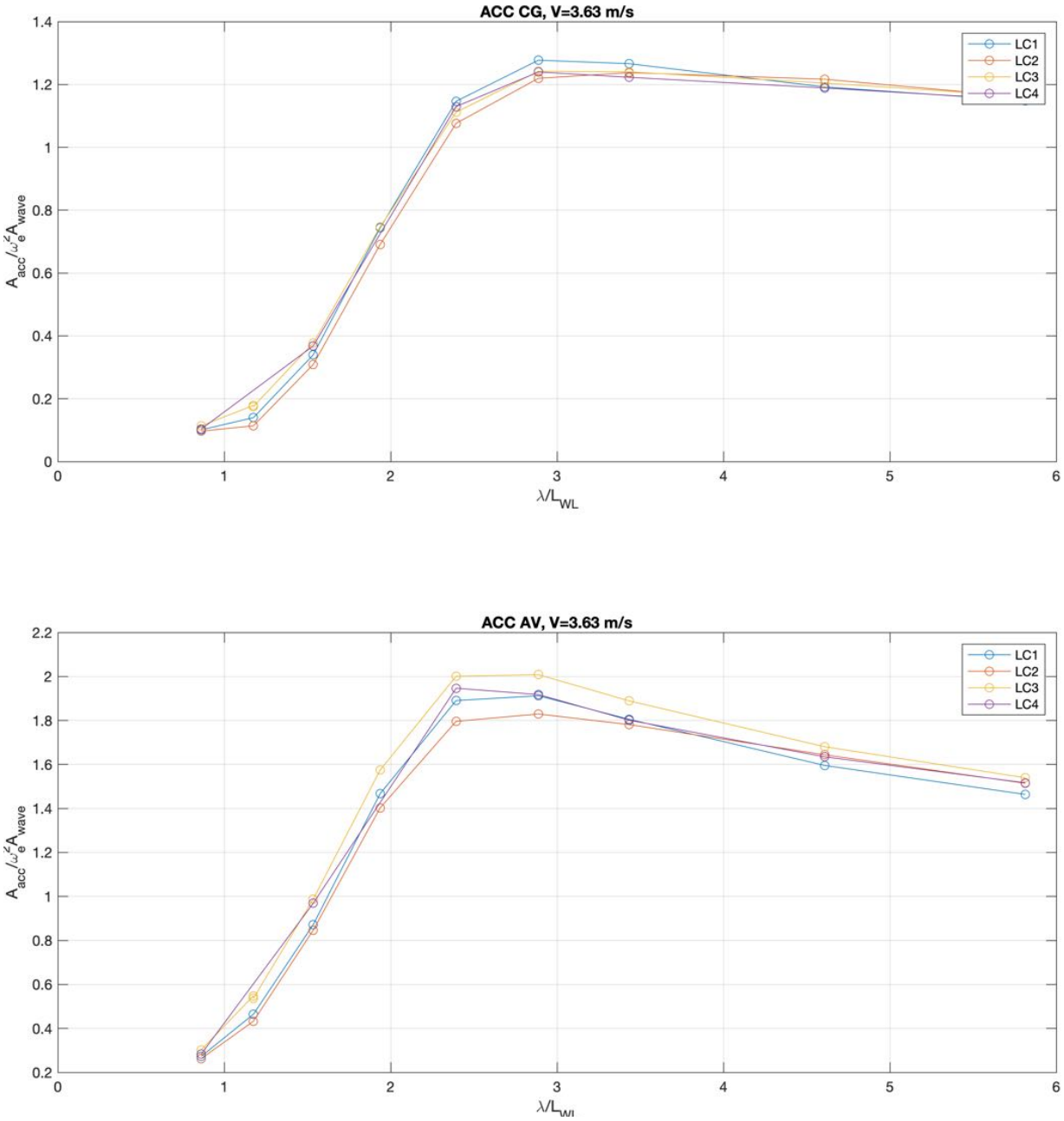

Figure 2.21: Vertical acceleration transfer functions comparison

The centre of gravity acceleration transfer functions shown in Fig. 2.21 show a very similar trend to what has been seen for the case of the heave transfer functions. Peak acceleration occurs at the same wavelength as the heave motion. In the case of the vertical acceleration at the bow, the response peak seems to be slightly shifted towards shorter wavelengths, but only the lighter configuration shows effectively higher response for smaller wavelength. In the case of bow

accelerations, the response of the mid loading conditions 1 and 4 are between the other two loading conditions for the most part of the tested wavelengths range.

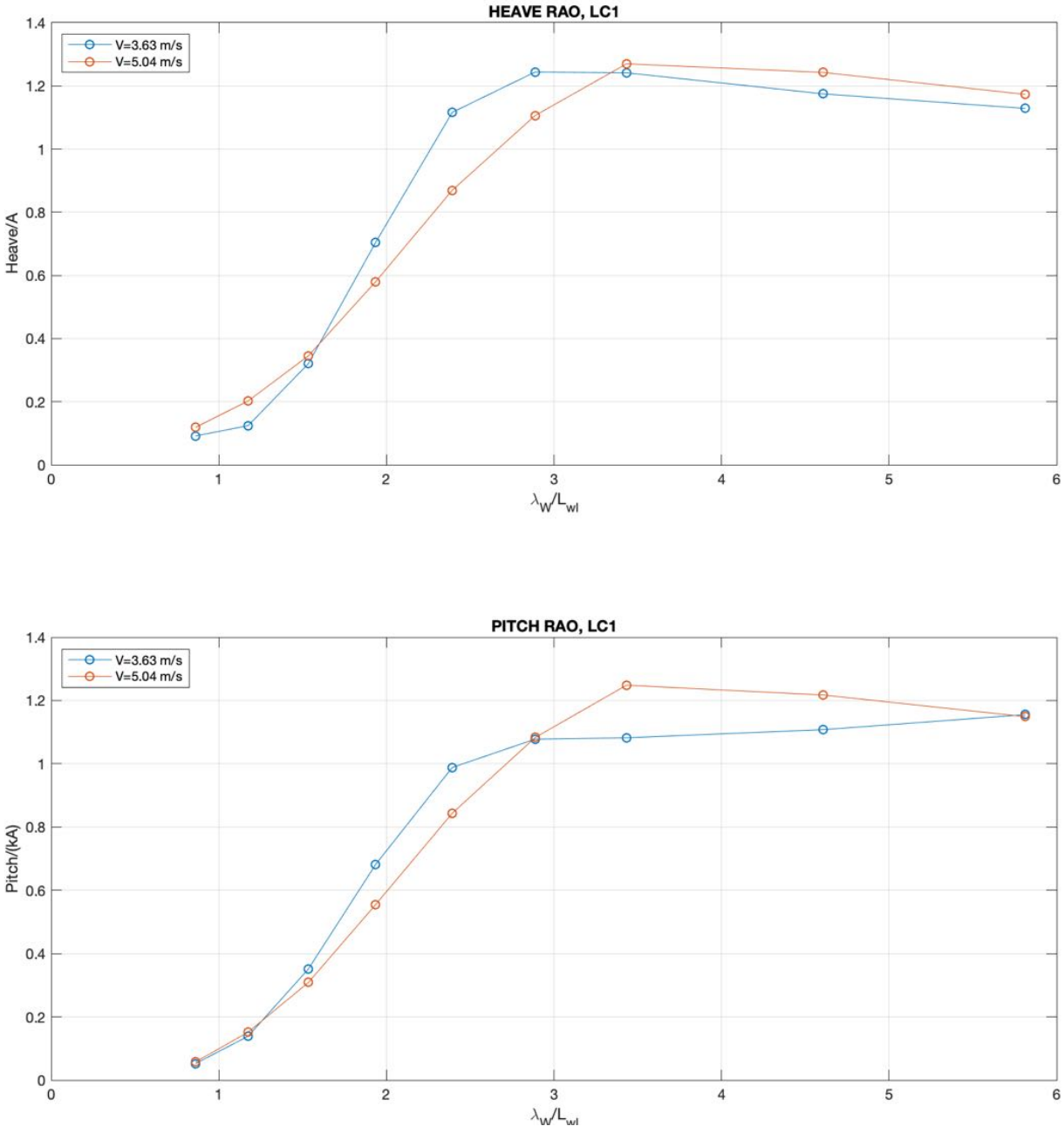

Figure 2.22: Effect of speed on vertical motion transfer functions

In Fig. 2.22, the effect of speed on the vertical motion transfer functions is highlighted. The main difference that can be noted is that the peak response of bith heave and pitch motions occur

at longer wavelengths as the speed is increased. Higher responses, especially in the case of pitch are observed after the peak. The shift in peak wavelength does not mean that the peak frequency is also shifted, in the contrary, the peak frequency remain unchanged (it is a characteristic of the hull) as the plot in Fig. 2.23 clearly shows. Being the speed higher, the same peak encounter frequency is found at the longer wavelength.

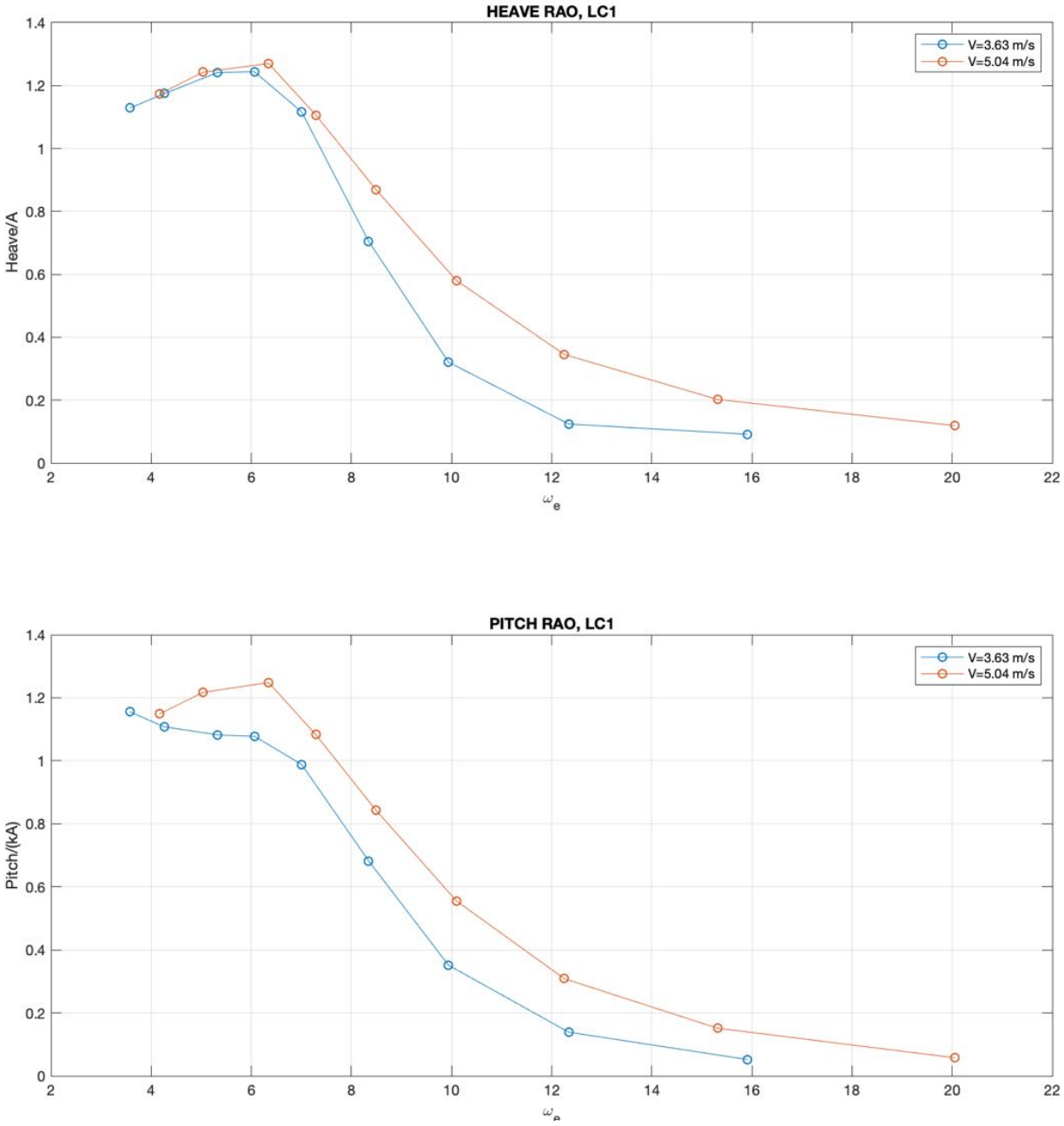

Figure 2.23: Effect of speed on vertical motion transfer functions

2.4 Nonlinear effects

2.4.1 Introduction

As the speed of a ship operating in waves increases, its seakeeping performances become more relevant to the safety and comfort on board. This is particularly true for lighter high speed crafts, that are more prone to experience larger motions and accelerations. In order to study the motions of a given hull in waves, model scale seakeeping experiments were carried out starting in the late 1960 with Fridsma [21] both in regular and irregular waves. Under the assumption that the problem of ship motions in small amplitude waves can be represented by a linear system, seakeeping characteristics of a given hull are usually described in the frequency domain by the Response Amplitude Operator (RAO) [73] or Transfer Functions (TF) [74]. Transfer Functions provide a simple yet very effective method for the estimation of the ship motion response in rough sea, given its statistical wave spectrum [74, 73]. In the particular case of fast hulls, it is known that the assumption of linear system is less appropriate, in particular, early model tests in regular waves clearly observed the dependence of TF on wave height [21].

Early experimental work on planing prismatic hulls in regular waves made by Fridsma used different wave heights to check for linearity ranges of motion response. He highlighted that accelerations are always nonlinear and nonlinearity of the vertical motions are more pronounced at resonance frequency. Other experimental studies [75] also showed linearity checks on different models, but were not focused on motion nonlinearities and their trends respect to a specific hull or wave parameter. The hull motion and acceleration nonlinearities are related to multiple concurring hydrodynamic phenomena that results in the excitation of the hull motions. The most important fact of fast craft seakeeping is that for a planing hull a small change in hull attitude can results in significant changes in waterplane area and wetted surface due to the deadrise. This directly affects added mass, restoring and damping characteristics of the hull during its motion, inducing nonlinearities in its response. In some cases, large and sudden variation of waterplane area in the bow sections due to large hull motions can results in bow flare impacts, impulsive pressure peaks that introduce further motion nonlinearities.

Nonlinearities observed during regular waves tests can be divided based on the considered response signal harmonic. First harmonic response nonlinearities (or TF nonlinearities) are present if the motion TF show different trend with increasing wave steepness or amplitude. The second harmonic response nonlinearities here discussed are the ones related to the existence (and trend) of a second harmonic component of the motion response with increasing wave steepness or amplitude. Even if the first harmonic response nonlinearities are already reported in earlier experimental research [21, 75], the same does not apply for second harmonic response nonlinearities. In general, the presence of higher harmonics in the motion response in regular waves has been described as one indicator of motion nonlinearity, but not many authors [76, 77, 78, 79, 34] showed the effect of wave characteristics on these harmonics.

The scope of the present work is to investigate nonlinearities of vertical motions and accelerations in regular waves of using a subset of the Naples Systematic Series (NSS) hulls. Both first and higher harmonics nonlinearities of vertical motions and accelerations of two different hulls in regular waves have been analysed for two different speeds. The analysis is meant to assess the presence of motion and acceleration nonlinearities and their dependence on wave steepness, speed

and slenderness ratio. In addition, the experimental data gathered during the present study adds comprehensive regular wave seakeeping results to the already published and well studied NSS dataset.

2.4.2 Experimental Setup

The two models used for the experiments are from the Naples Systematic Series (NSS), published in [30], more specifically model C1s and C2s. These models have been built as reduced scale C1 and C2 models [30] in order to fit into the instrumentation limits during seakeeping tests. In Fig. 2.24 the body plan and buttock lines of a the C1 model are shown.

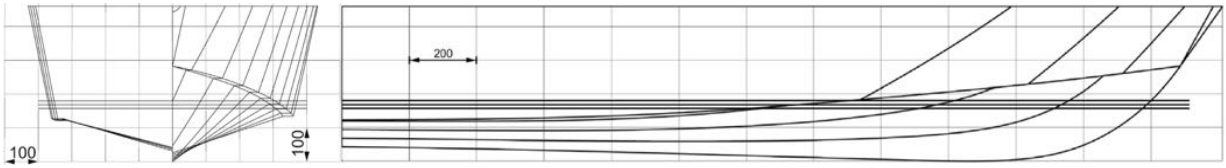

Figure 2.24: C1 Model body plan and profile

The models where tested in the Towing Tank of the Department of Industrial Engineering of the Università degli Studi di Napoli "Federico II". The tank is 136.0 m in length, 9.0 m wide 4.5 m deep; maximum speed of the carriage 10.0 m/s. For the sake of consistency, the same mass configuration used in [80] has been adopted, see Table 2.8.

Model	C1s	C2s
L_{OA} (m)	1.567	1.567
L_{WL} (m)	1.44	1.44
B_{WL} (m)	0.446	0.396
LCG (m)	0.567	0.567
Δ (kg)	26.52	20.91
Ⓜ	4.83	5.23
A_T/A_X	0.94	0.94
L_{WL}/B_{WL}	3.23	3.64
B_{WL}/T	4.12	4.12
VCG/B_{WL}	0.5	0.5
K_{44}/B_{WL}	0.4	0.4
K_{55}/L_{WL}	0.25	0.25
β_T(deg)	13.2	13.2
$\beta_{0.5}$(deg)	22.3	22.3
$\beta_{0.75}$(deg)	38.5	38.5

Table 2.8: Hulls specifications

The tests were performed at 3.5 and 4.5 m/s, corresponding to $Fr = 0.93$ and $Fr = 1.20$

($Fr_\nabla = 2.05$ to 2.74). A flap wavemaker (Fig. 2.26(b))was used to generate regular waves with frequencies ranging from 0.40 to 1.0 Hz and steepness from $H/\lambda = 1/100$ to $H/\lambda = 1/20$. Not all possible combinations have been tested, both because time and instrumentation limits. The experimental matrices in Fig. 2.25 show both nominal and measured wave frequency and steepness for both hulls and speed. Since model C1s and C2s differ only by their L_{WL}/B_{WL} ratio (C2 is 11% slimmer), differences in the hull response between the two can be regarded as effects due to the L_{WL}/B_{WL} ratio.

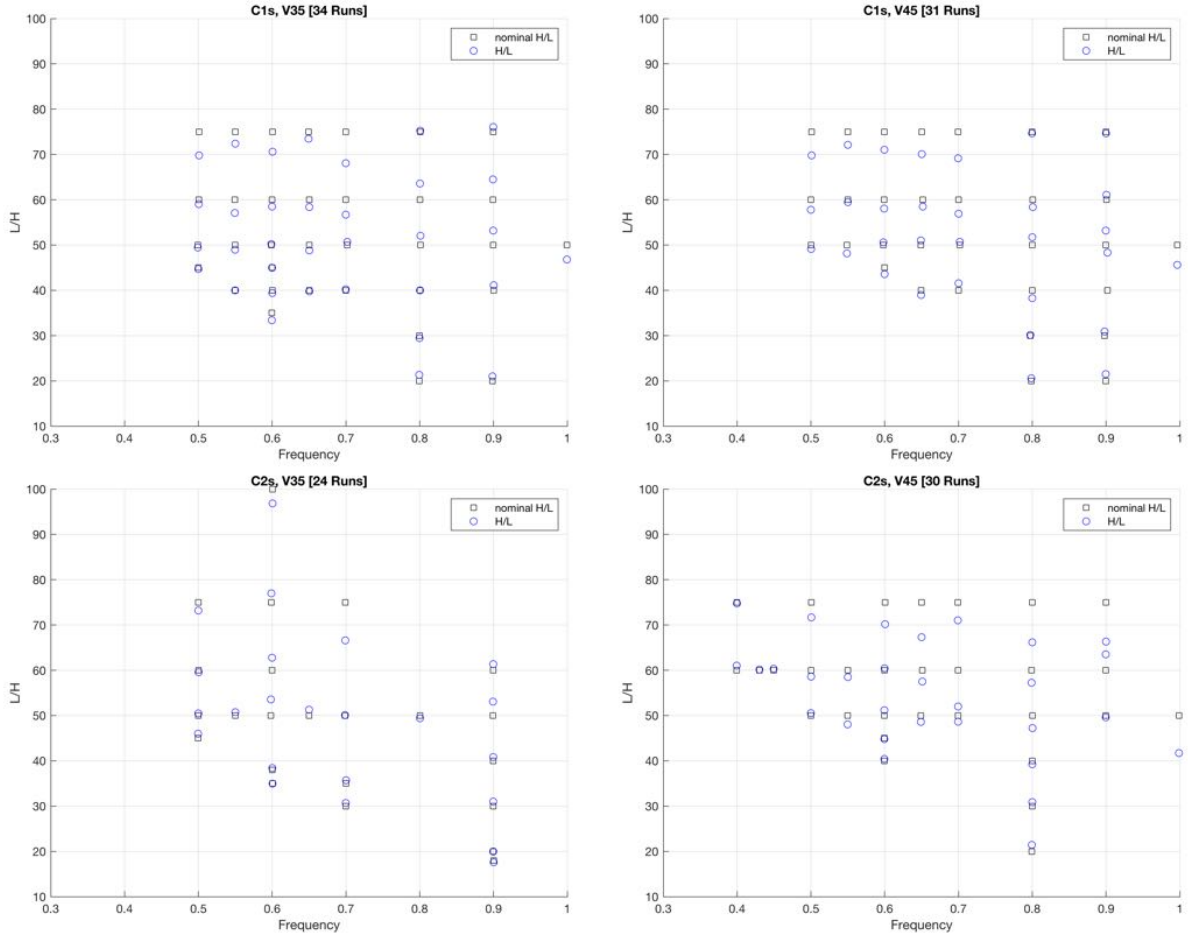

Figure 2.25: Tested combinations of wave steepness, frequency, hull and speed

The incoming wave profile generated has been measured using ACAMINA AWP-24-2 wave height gauges capacitive probes and Baumer UNDK 30U6103 ultrasonic probes. The measure from the capacitive probes (Fig. 2.26(a)) , fixed on the towing tank, has been used as a reference for wave height and frequency. The ultrasonic probes, fixed on the towing carriage were used to compute the actual encounter frequencies phase difference between wave ad motions. The calibrated capacitive probes were used to check the wave-maker transfer functions. The Qualisys Motion Capture System, a high precision optical motion tracking system fixed to the towing

carriage has been used to capture hull motions, in particular heave and pitch. Images of the two models tested for this study is shown in Fig. 2.27, notice that that the spherical refrlective marker for the motion capture system are higlighted.

(a) Towing tank wave-maker (b) Wave capacitive probes array

Figure 2.26: Wave maker and capacitive probes array

Accelerations were measured at the center of mass G and at the bow, 0.5 L_{WL} forward of center of gravity using three axis Crossbow Cross Bow CXL04GP3-R-AL MEMS accelerometers (Input Range: $\pm$ 4g, Sensitivity: 500 $\pm$ 15 mV/g, Noise: 10 mg rms and Bandwidth: DC -100 Hz).

The models were towed using an inclined hinged shaft connecting the model to a stationary vertical arm (see Fig. 2.28), yaw motion is constrained by bow and aft vertical guides(see Fig. 2.27). The height of the vertical guides has bee carefully adjusted case by case in order both to accommodate the large motions experienced by the model bow and avoid the contact with the water surface at the peak of the wave. In Fig. 2.29, snapshots of one of the tests shows the model motion during a wave encounter.

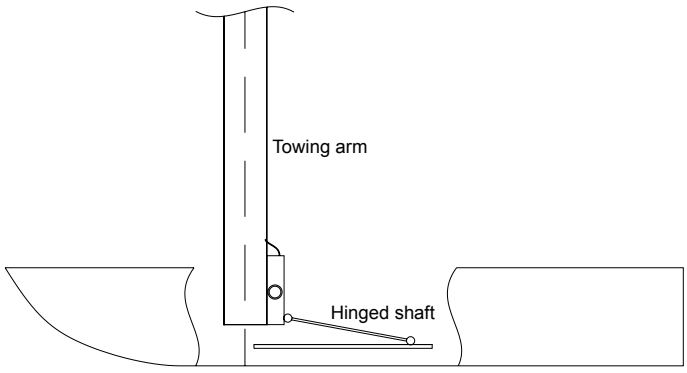

Figure 2.28: Experimental setup

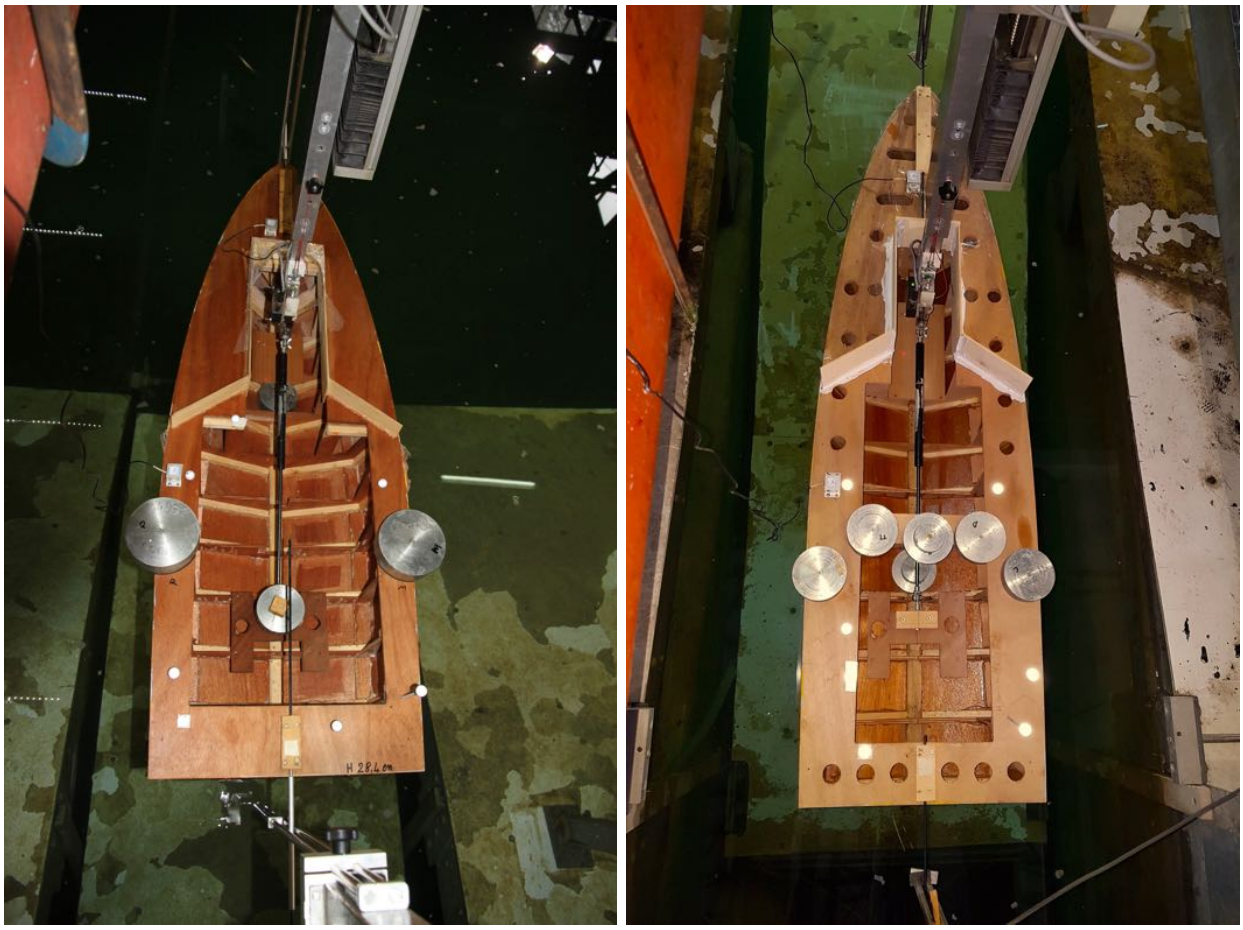

(a) NSS C1s model (b) NSS C1s model

Figure 2.27: NSS C1s and C2s models attached to the towing carriage

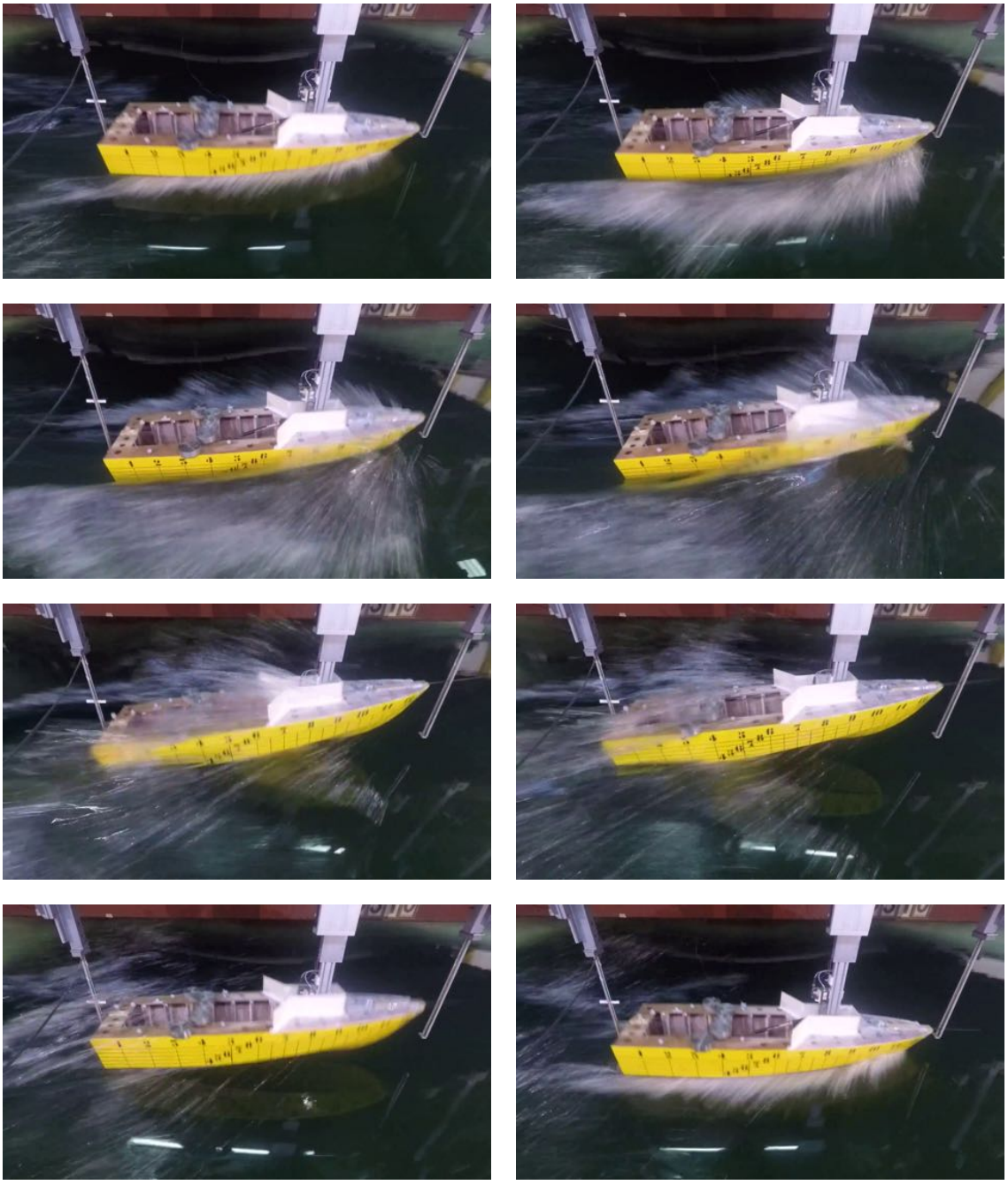

Figure 2.29: Snapshots of C2s at $v = 4.5m/s$, $H/\lambda = 1/50$ and $\lambda/L_{WL} = 3$

2.4.3 Data analysis

Towing tank and carriage mounted instruments were sampled at 500 Hz. Both motion and wave elevation data from experiments has been filtered with a fifth order Butterworth bandpass filter with lower cut-off frequency 0.1 Hz and upper cut-off frequency 160 Hz. An appropriate window of at least 10 wave encounters is set for every run, in particular, all signals are trimmed so that the start and the end of the signal are homologous points to reduce spectral leakage since the core of the analysis is done in the frequency domain via FFT.

The capacitive probes data is used to compute the wavelength λ via the implicit dispersion relation using the actual tank depth. To check the actual wave steepness H/λ, wave height H is measured in the time domain as the average trough to peak distance. The amplitude and frequency of the first and second harmonic components of both wave elevation and hull motion time series are computed via FFT as the first and second peak values of the amplitude spectrum and their respective frequency bin.

The data analysis was performed using MATLAB®, one pre-processing script imports all the data from the 119 runs and performs the data filtering, windowing and analysis. The results are then stored in a structured database and ready to be imported into the post-processing script that prints all the relevant plots for a comprehensive and clear visualization of the whole dataset.

2.4.4 Data visualization

From what has been shown in the introduction, for every hull and speed combination, hull motions have been evaluated against two variables, namely frequency and wave steepness. This lead to transfer functions that are not defined by a single curve, like they are normally plotted [74], but by a surface, having wavelength or frequency and wave steepness as the two parameters.

In order to better investigate the effects (in particular nonlinear ones) of each variable on the motion, results will be presented in form of iso-steepness and iso-frequency curves separately. The iso-steepness method is the common way transfer functions are plotted, only here multiple curves are stacked, each one referring to a different wave steepness. This method can easily highlight if there are peak frequency shifts. The iso-frequency method is meant to highlight the trends of the selected motion harmonic amplitude with wave steepness. This method allows for a clear assessment of the existence and trends of motion nonlinearities due to increasing wave steepness.

2.4.5 First harmonic nonlinearities

In this section, nonlinearities concerning the first harmonic component of the response will be discussed. The behavior of the first harmonic of the response is analysed using the usual transfer functions definition [74], defined frequency by frequency.

The use of conventional transfer functions, that normally implies motions responses to be linear, could be seen as inappropriate in this context. However, plotting a series of iso-steepness transfer functions has been chosen as an arbitrary method in order to highlight the known nonlinear effects. The fact that the curves are not perfectly overlapped implies that none of them could be used to fully characterize the hull seakeeping capabilities. The differences observed between

different transfer functions, due to a systematic variation of wave steepness, are here used for an assessment of nonlinearities.

Taking into account the amplitude of the first harmonic of heave H_1, its transfer function is defined as H_1/ζ_1, where ζ_1 is the amplitude of the first harmonic of the incident wave. The iso-steepness plots in Fig. 2.30 show heave transfer functions vs λ/L_{WL}.

Plots are presented so that in the first row are C1s hull measurements and the second row are hull C2s measurements. The first column is relative to $v = 3.5m/s$ and the second is relative to $v = 4.5m/s$.

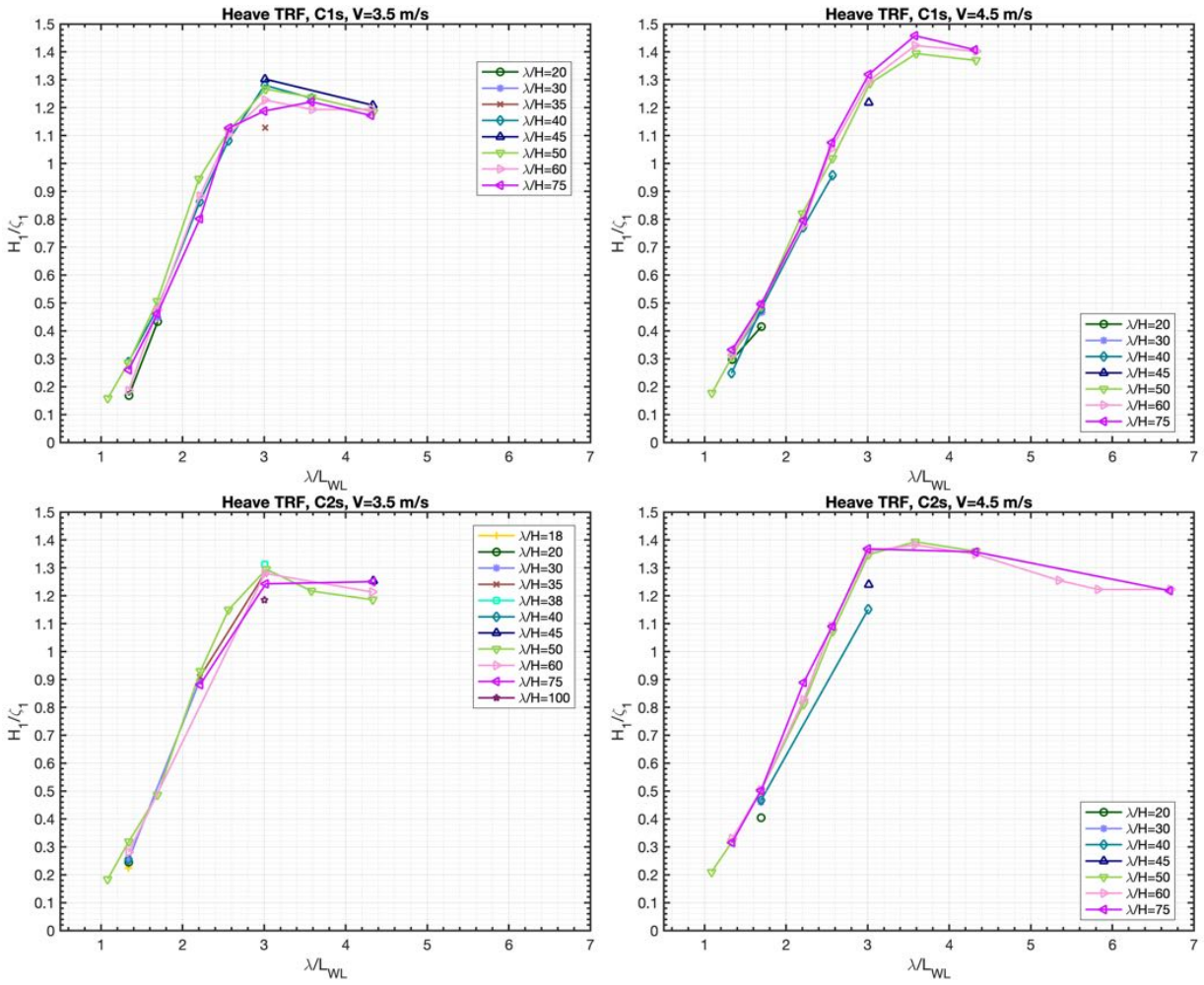

Figure 2.30: Heave transfer functions vs λ/L_{WL}

Plots in Fig. 2.30 show that the wavelength corresponding to the peak of heave response is clearly greater than the waterline length L_{WL} for both hulls and speeds tested, this is consistent with what is reported by other authors [81, 82]. In particular, the heave response peak is at $\lambda/L_{WL} = 3$ in the case of $v = 3.5m/s$ and $\lambda/L_{WL} = 3.6$ in the case of $v = 4.5m/s$, L/B ratio

seems to have no effect on the critical λ/L_{WL} ratio. For both hulls and speeds, first harmonic nonlinearities are more pronounced at the critical λ/L_{WL} ratio.

The iso-frequency plots in Fig. 2.31 show heave transfer functions respect to λ/H.

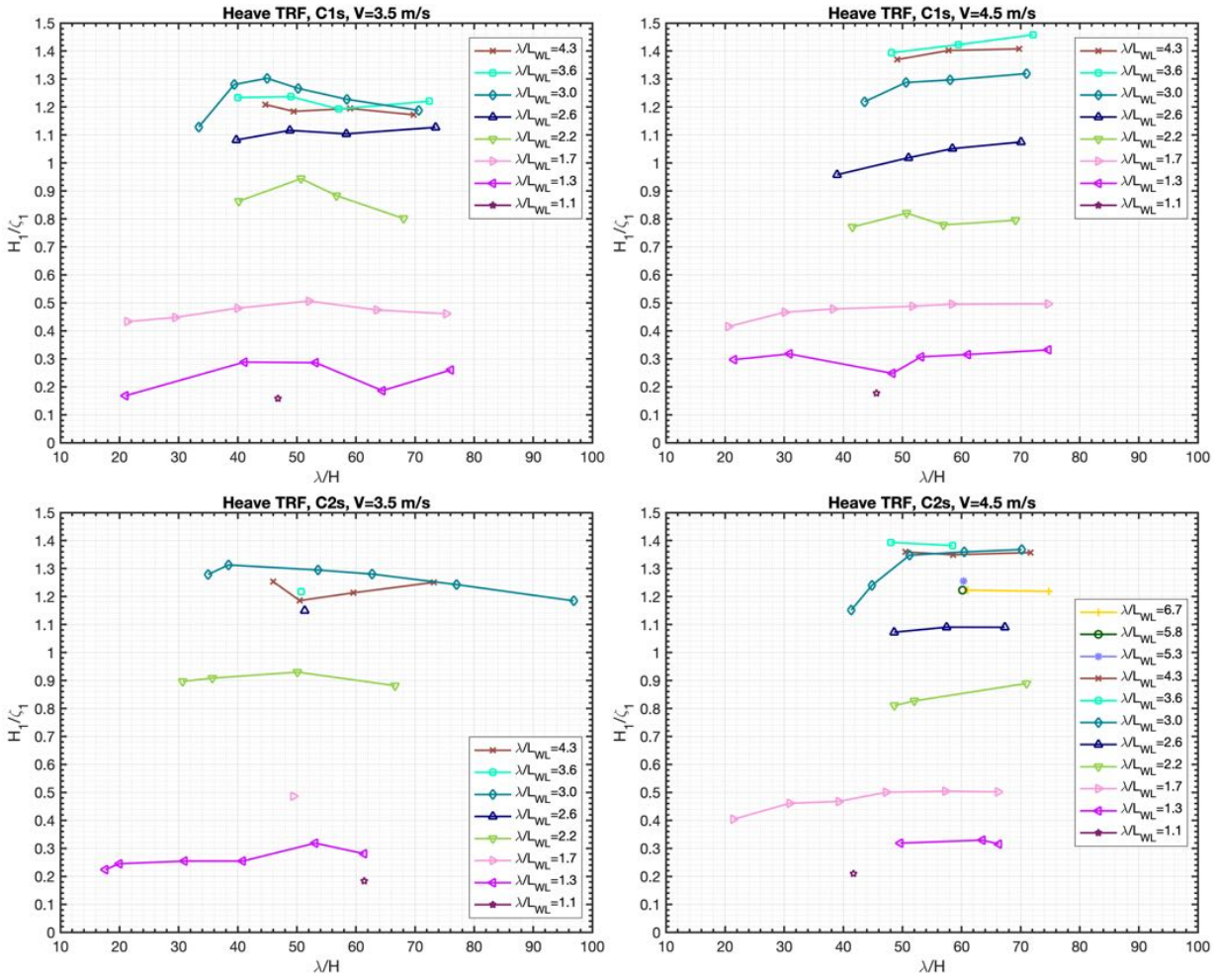

Figure 2.31: Heave transfer functions vs λ/H

Heave response shows some dependency respect to the wave steepness, in general it can be noted that the peak value is obtained for values of λ/H between 50 and 60 for $v = 3.5m/s$. For $v = 4.5m/s$ heave response peak occurs for higher values of λ/H. Heave response tends to decrease for λ/H lower than 50, for both speeds and L/B ratios.

Taking into account the amplitude of the first harmonic of the pitch angle P_1, its transfer function is defined as $P_1/k\zeta_1$, where $k = 2\pi/\lambda$ is the wavenumber of the incident wave. The iso-steepness plots in Fig. 2.32 show pitch transfer functions vs λ/L_{WL}.

Figure 2.32 shows that also in the case of pitch motion, the wavelength corresponding to the peak of pitch response is greater than the waterline length L_{WL} for all tested cases. Pitch response

peak is at $\lambda/L_{WL} = 3$ in the case of $v = 3.5m/s$, similar to heave. In the $v = 4.5m/s$ cases, the peak seems to be near $\lambda/L_{WL} = 4.6$, so for higher speeds, pitch response show a greater shift in peak response wavelength respect to heave motion.

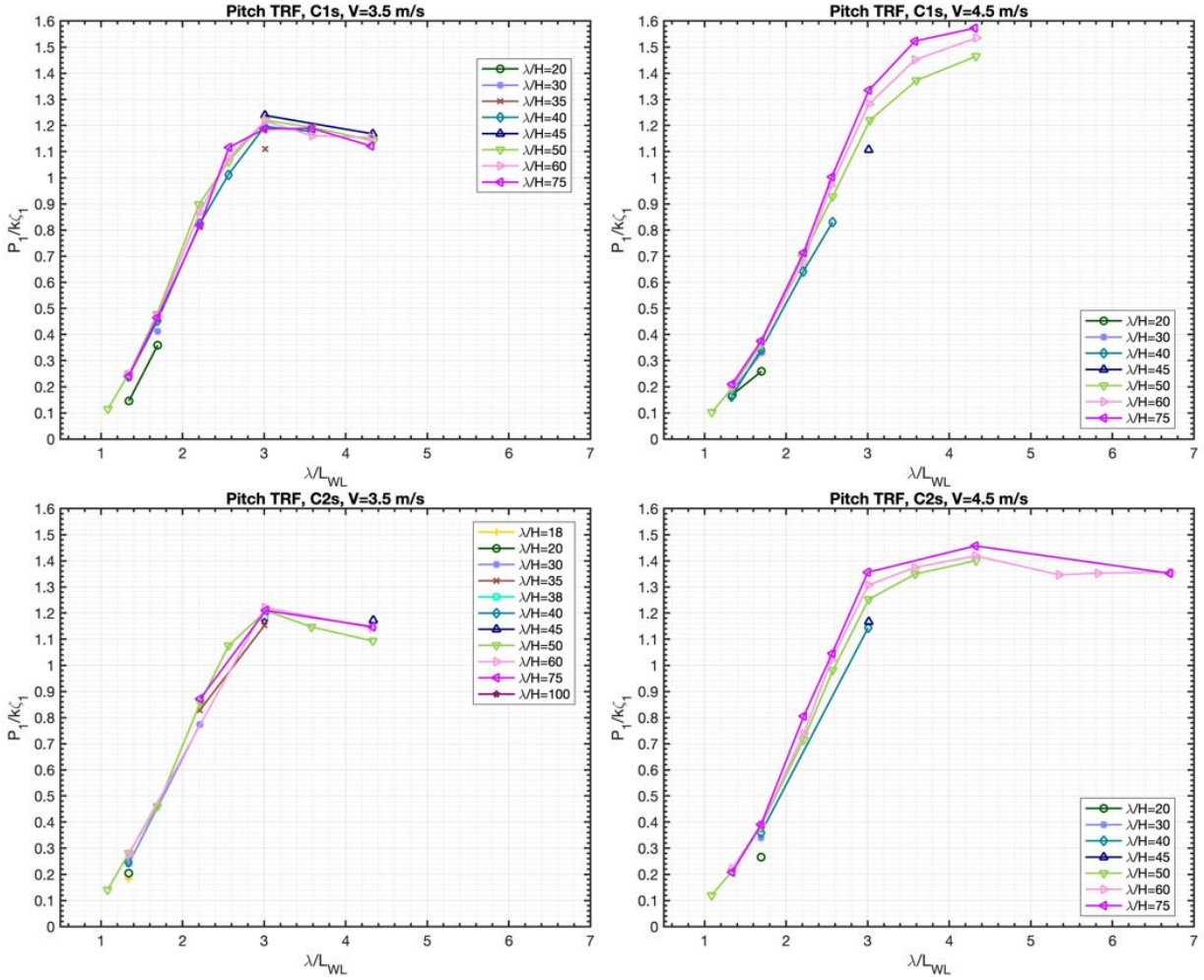

Figure 2.32: Pitch transfer functions vs λ/L_{WL}

In the iso-frequency plots in Fig. 2.33 it can be observed that variation of the pitch transfer functions respect to λ/H increases as speed increases and L/B ratio decreases. At the highest speed, pitch transfer functions dependency on wave steepness is stronger as pitch response is greater. In addition, it can be noted that the absolute peak value of the pitch response shows significant dependency on slenderness ratio only at the highest speed tested. At higher speeds, pitch response tends to grow with higher wavelengths.

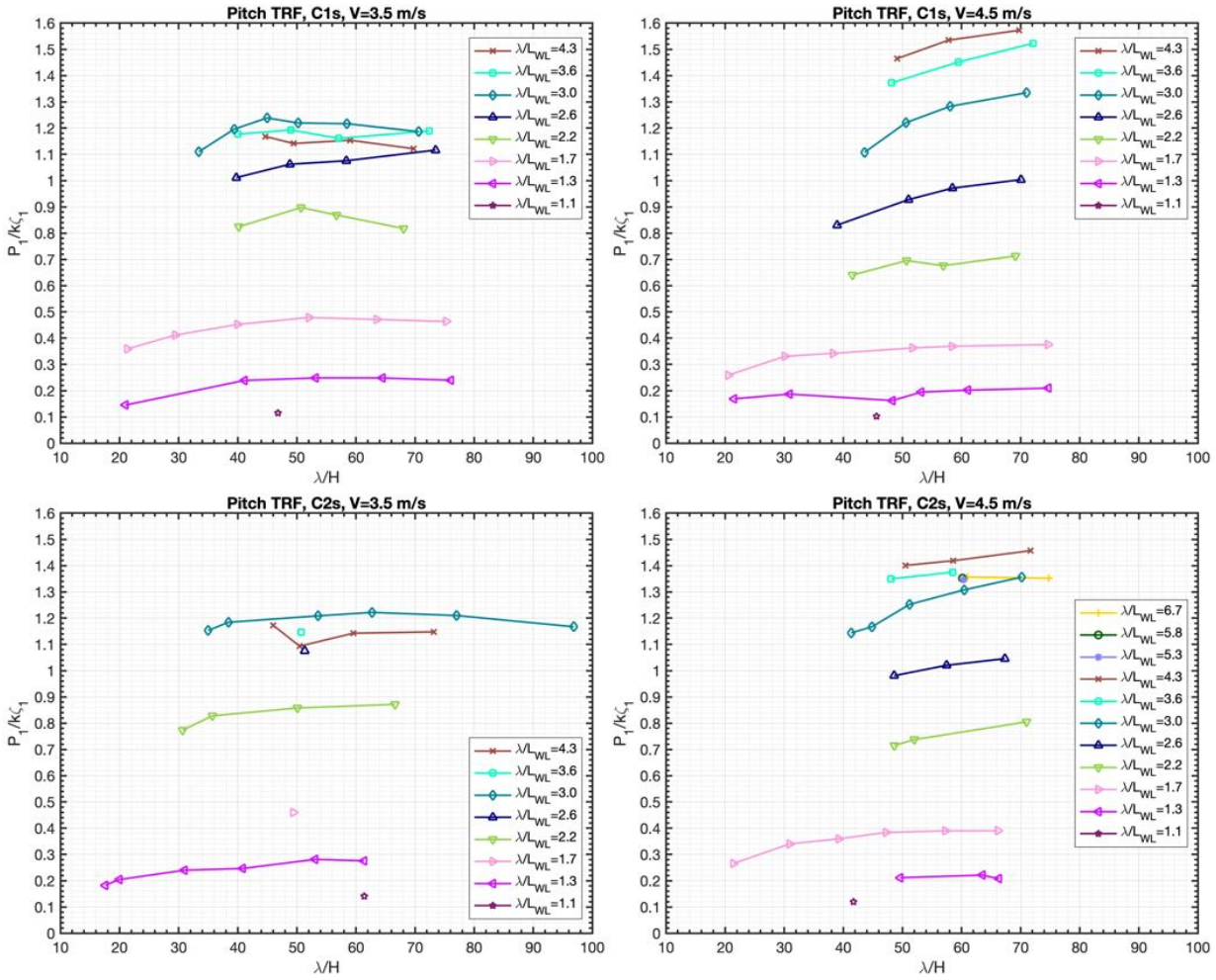

Figure 2.33: Pitch transfer function vs λ/H

Vertical acceleration measurements are also of great importance in seakeeping studies, since they are directly related to onboard comfort and operability. The transfer function of vertical acceleration has been defined as $A_1/\omega_e^2\zeta_1$, with A_1 being the amplitude of the first harmonic of the vertical acceleration and ω_e^2 the encounter angular frequency. Starting with the forward accelerometer (AV) measurements , in Fig. 2.34 vertical acceleration (AV) transfer functions are plotted against λ/L_{WL}. The transfer functions of vertical acceleration at the bow in Fig. 2.34 show a well defined peak of the response. As in the case of heave and pitch motion, peak acceleration response for $v = 3.5m/s$ occurs for wavelength ratios of about $\lambda/L_{WL} = 2$, for $v = 4.5m/s$ the peak is observed for longer waves, around $\lambda/L_{WL} = 3$.

No significant differences can be observed between the two hulls, the only parameter influencing the maximum amplitude of the first harmonic component of acceleration is speed. In general, it can be noted that peak values of vertical acceleration at the bow occur at shorter wavelength with respect to peak motions.

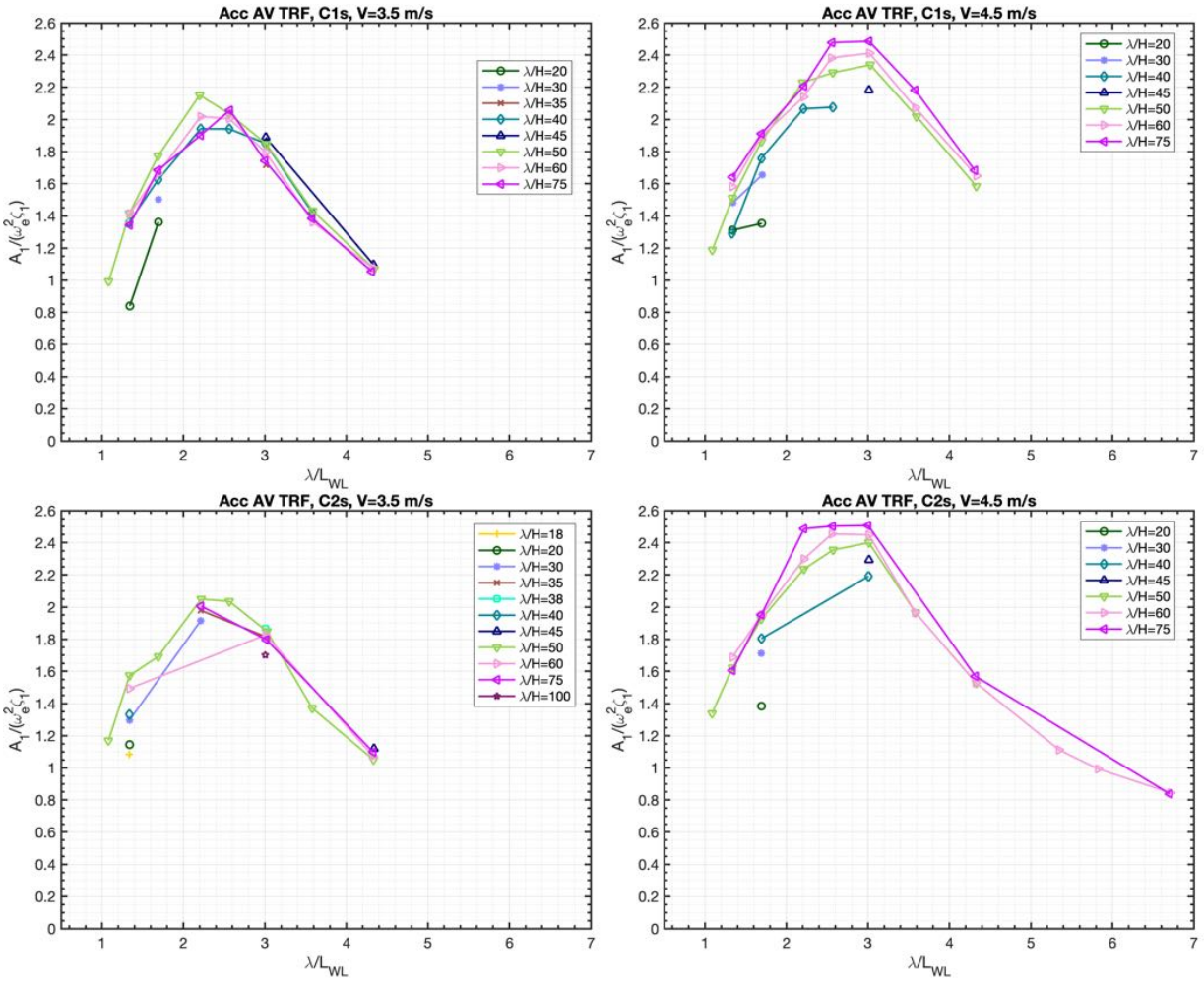

Figure 2.34: Vertical acceleration (AV) transfer functions vs λ/L_{WL}

Looking at the same data plotted in Fig. 2.35 as a function of wave steepness, it shows that maximum vertical acceleration response at $v = 3.5m/s$ occurs always around λ/H ratios of about 50. For $v = 4.5m/s$, vertical acceleration response at the bow shows stronger dependency on wave steepness respect to heave motion. As in the case of pitch motion, a stronger dependency is observed for the highest acceleration values.

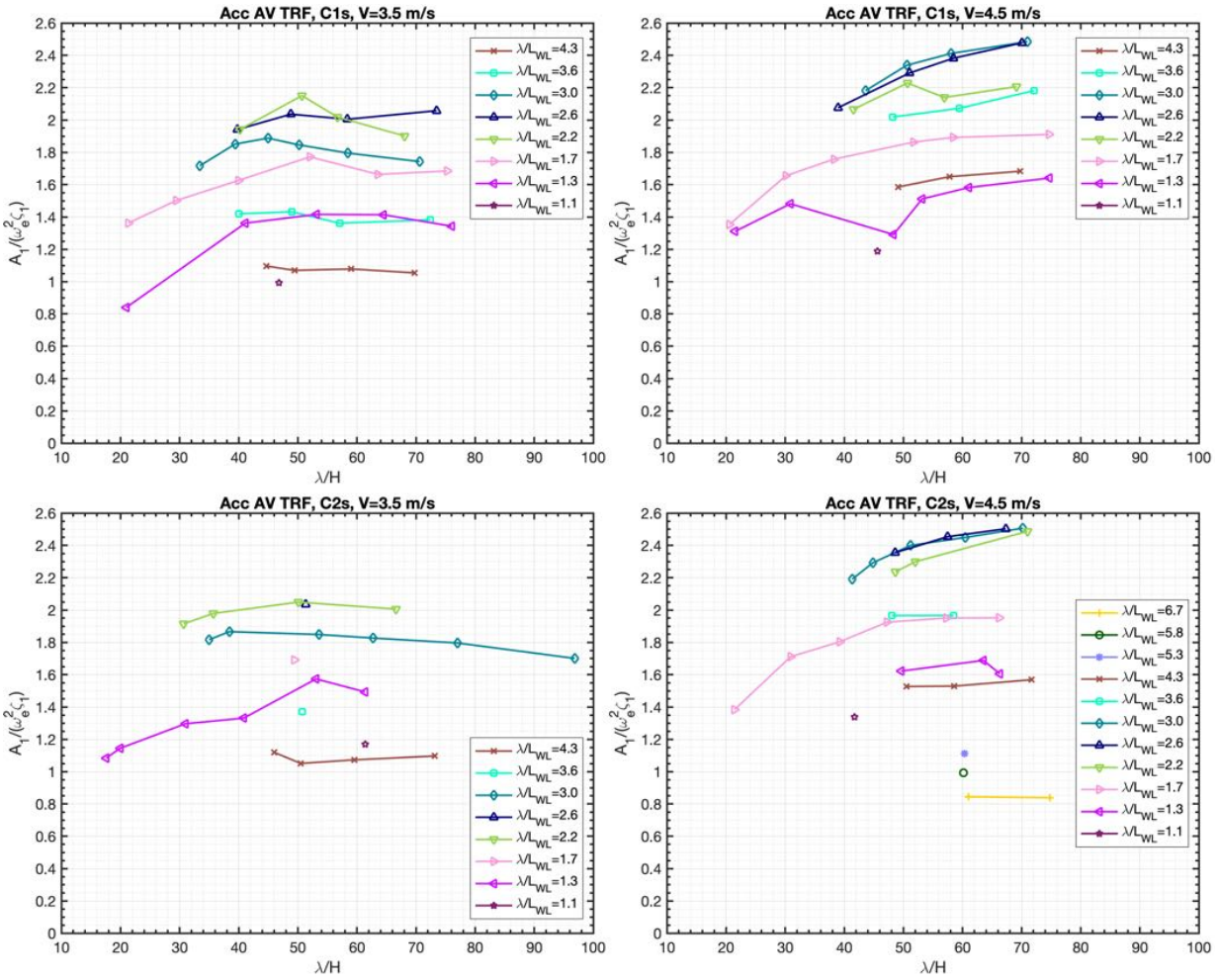

Figure 2.35: Vertical acceleration (AV) transfer functions vs λ/H

In the next figures, the data from the accelerometer placed at the center of gravity (CG) is plotted. The first harmonic component of the vertical acceleration response in the center of gravity shows a different trend with respect to the one at the bow. Starting from the iso-steepness plots, the transfer functions show a common peak wavelength ratio λ/L_{WL} around 2.5-3.0 for $v = 3.5m/s$ and 3.0 for $v = 4.5m/s$. In this case, the peak wavelength shows a weaker dependency on the speed respect to bow accelerations. Accelerations at the center of gravity show no significant nonlinearities at the peak wavelength. The slender hulls show only slightly higher peak acceleration response with respect to the broader hull.

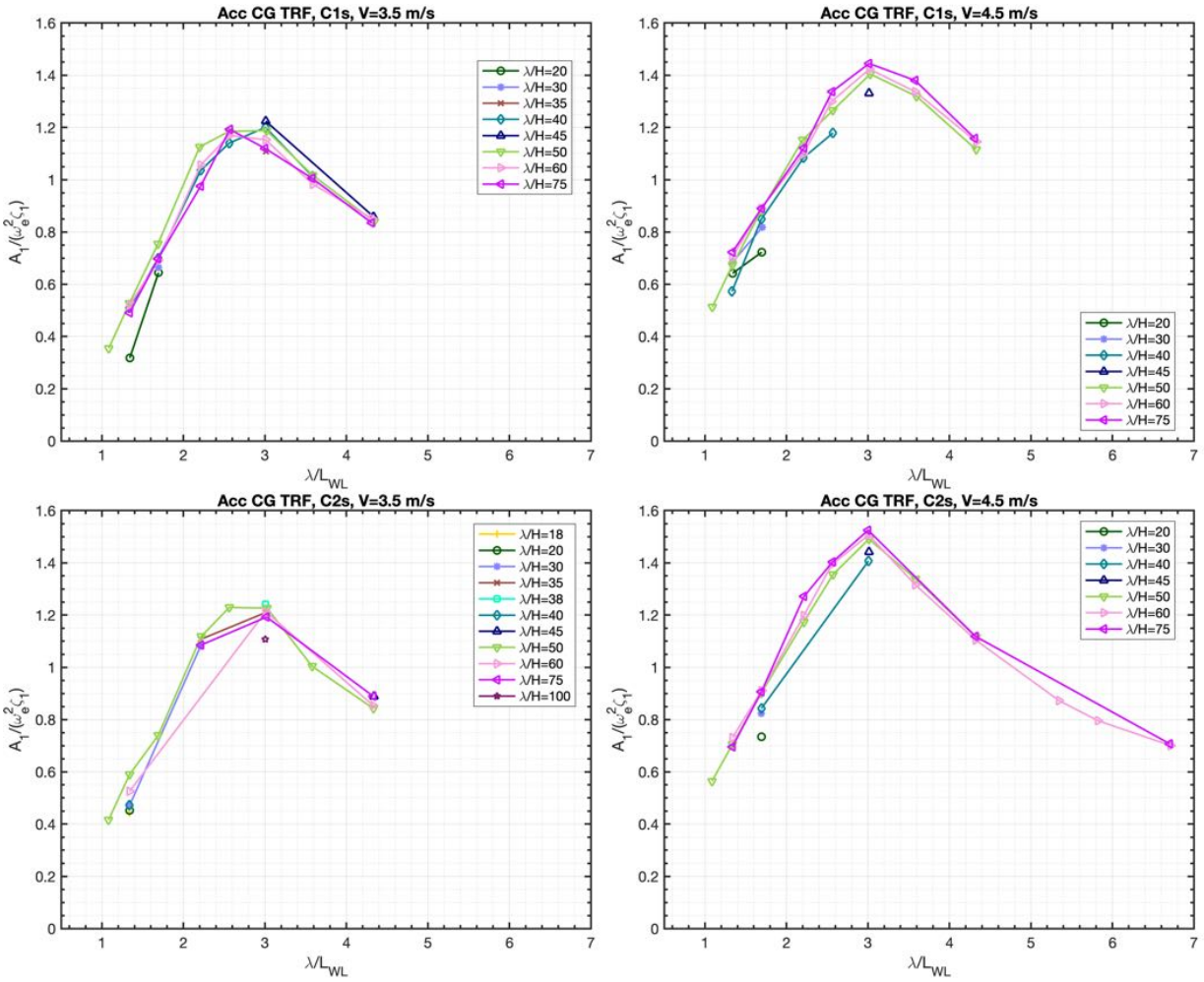

Figure 2.36: Vertical acceleration (CG) transfer functions vs λ/L_{WL}

The iso-frequency plots in Fig. 2.37 shows that for $v = 3.5m/s$ the maximum of first harmonic response values occur with λ/H ratios near 50. The dependency of the transfer function on wave steepness is visible only for values of λ/H lower than 50 in some cases. For the high speed case, the dependency on wave steepness is more marked but still limited respect to bow accelerations.

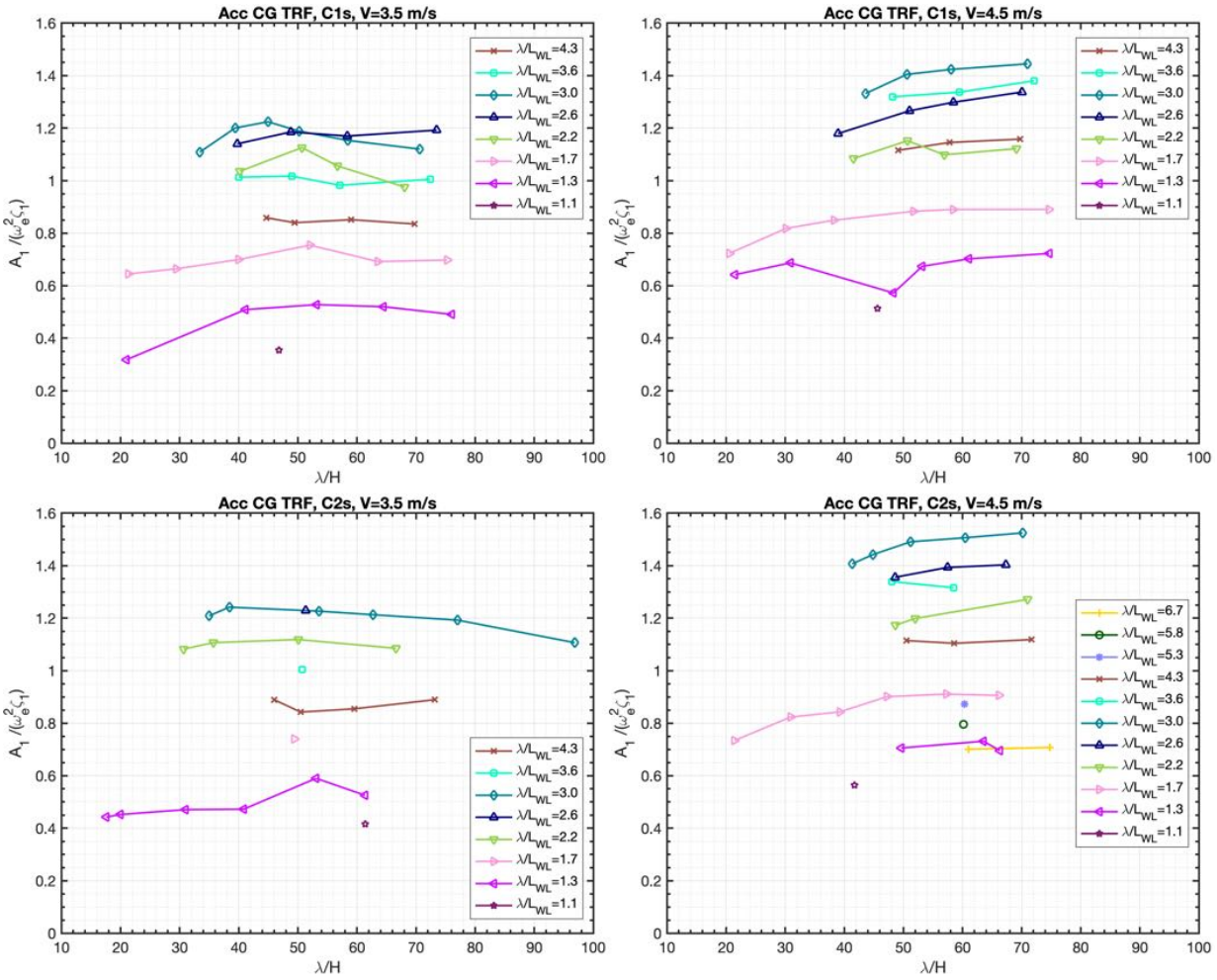

Figure 2.37: Vertical acceleration (CG) transfer functions vs λ/H

2.4.6 Second harmonic nonlinearities

In this section, nonlinearities related to the response second harmonic will be discussed. Since transfer function have been used to analyse harmonic nonlinearities, in order to be consistent, the amplitude of the second harmonic of the response will also be non dimensionalized using the first harmonic amplitude of the forcing term. Also, the same iso-steepness and iso-frequency plots will be used in this analysis. In Fig. 2.38 an example of both heave and pitch timeseries and spectra of are plotted. The second harmonic content is relevant in both cases, further harmonics are also visible.

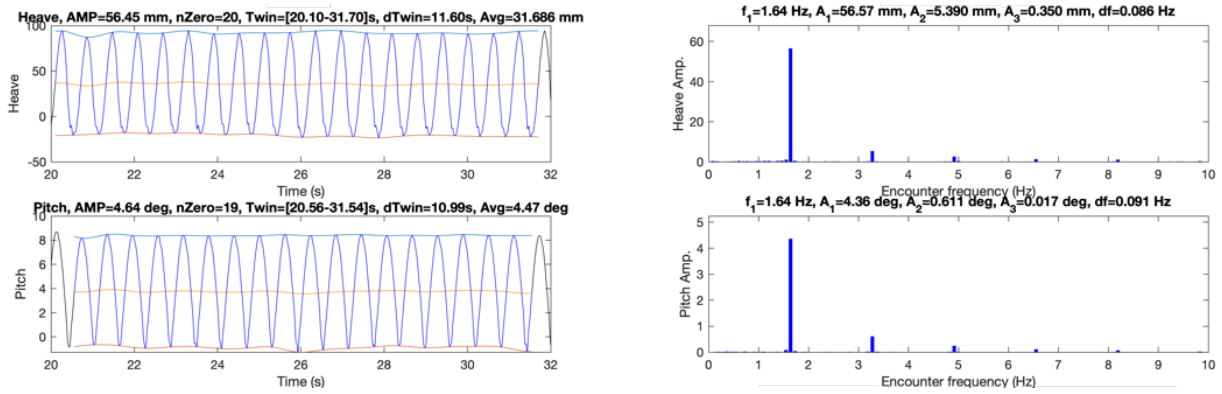

Figure 2.38: Heave and Pitch time series and amplitude spectra

In Fig. 2.39, iso-steepness plots of second harmonic response of heave show a response peak for $\lambda/L_{WL} = 3.0$, the main difference with respect to heave transfer function is that the peak wavelength is not influenced by speed. Peak values of the second harmonic amplitudes grow as the speed is higher and nonlinearities are more pronounced at the peak wavelength. Taking the $\lambda/H = 50$ case into consideration, the second harmonic amplitude is up to 8% of the first harmonic amplitude for $v = 3.5m/s$ and up to 9% for $v = 4.5m/s$. Values up to 14% of the first harmonic amplitude are seen for $\lambda/H = 50$ at higher speeds.

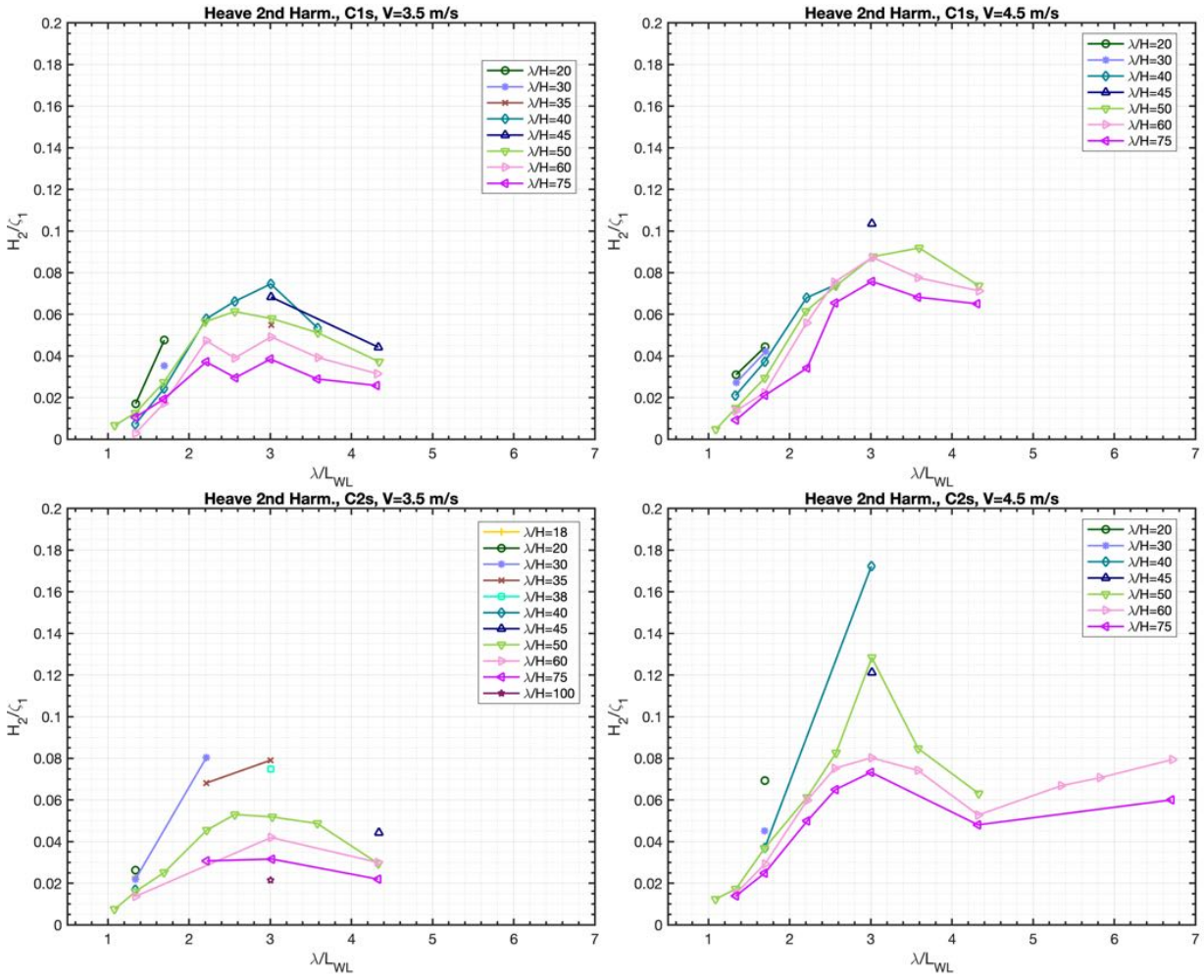

Figure 2.39: Heave second harmonic response vs λ/L_{WL}

In Fig. 2.40, iso-frequency plots of the second harmonic amplitude of heave clearly highlights the dependency on wave steepness. The second harmonic amplitudes of the heave motion increases as wave steepness and speed is increased, independently of slenderness ratio and wavelength.

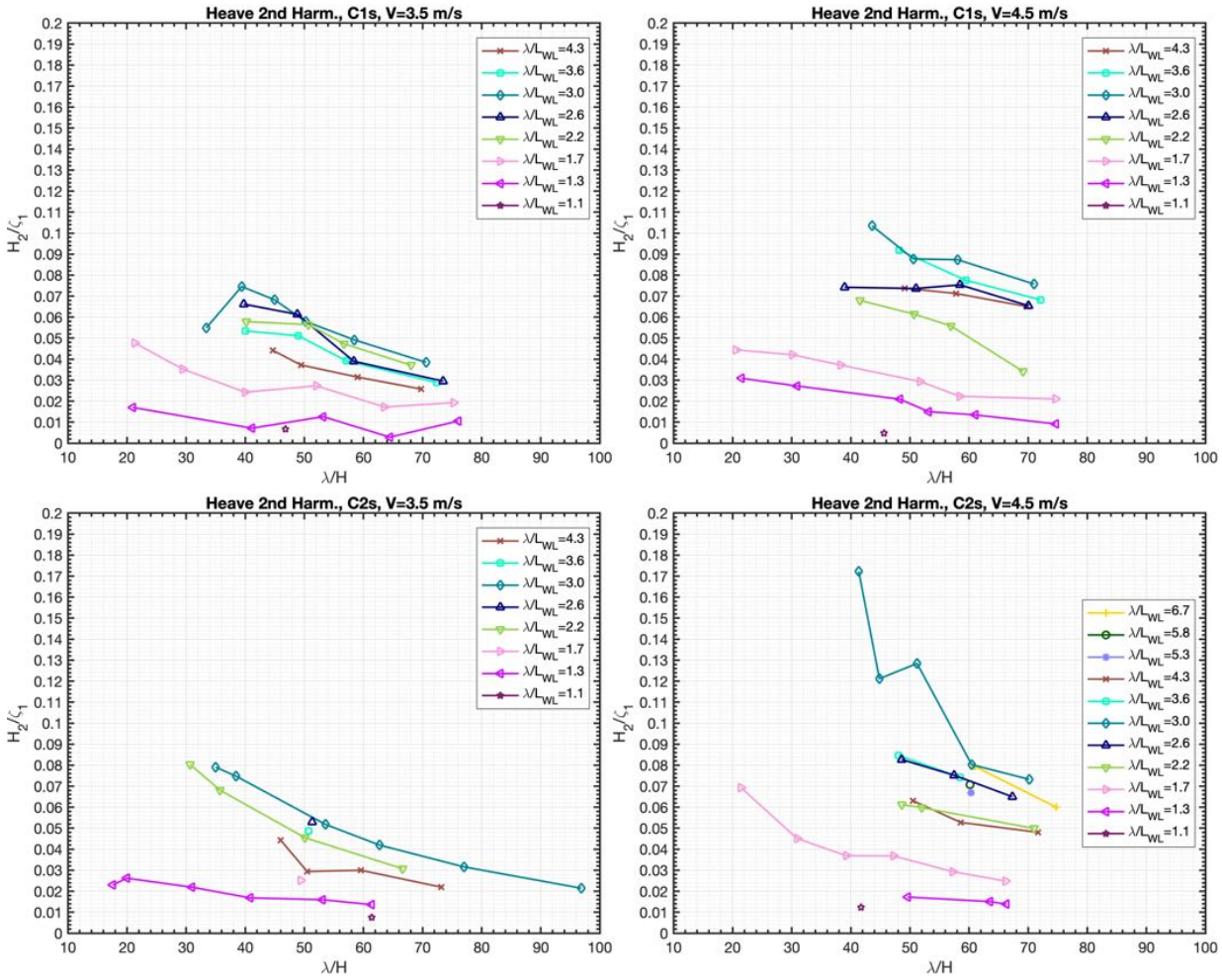

Figure 2.40: Heave second harmonic response vs λ/H

The second harmonic of the pitch motion, plotted in Fig. 2.41 shows that speed has a much larger influence on its trend with respect to the case of heave. For $v = 3.5m/s$, second harmonic amplitude of pitch peaks at $\lambda/L_{WL} = 3.0$ for most of the cases, $\lambda/H = 50$ is the only case where the peak is at $\lambda/L_{WL} = 3.6$. The higher speed plots show that the second harmonic of pitch motion response is very different from what it has been shown in the case of heave, and its maximum value is almost twice the maximum values at the lower speed. The critical wavelength of $\lambda/L_{WL} = 3.0$, apart from the $\lambda/H = 50$ case, now marks the point from where the growth of the response is somewhat attenuated and the dependency on wave steepness increases significantly. At higher speeds, the steepness does not affect the second harmonic response as much as it does at lower speeds for $\lambda/L_{WL} \leq 3.0$. For $v = 4.5m/s$ and $\lambda/L_{WL} \geq 3.0$, the broader hull shows higher second harmonic amplitude than the slimmer hull. In terms of amplitude of the second harmonic of pitch with respect to the first harmonic for the $\lambda/H = 50$ case, the results are similar to the case of heave, namely 9% at $v = 3.5m/s$ and 14% at $v = 4.5m/s$.

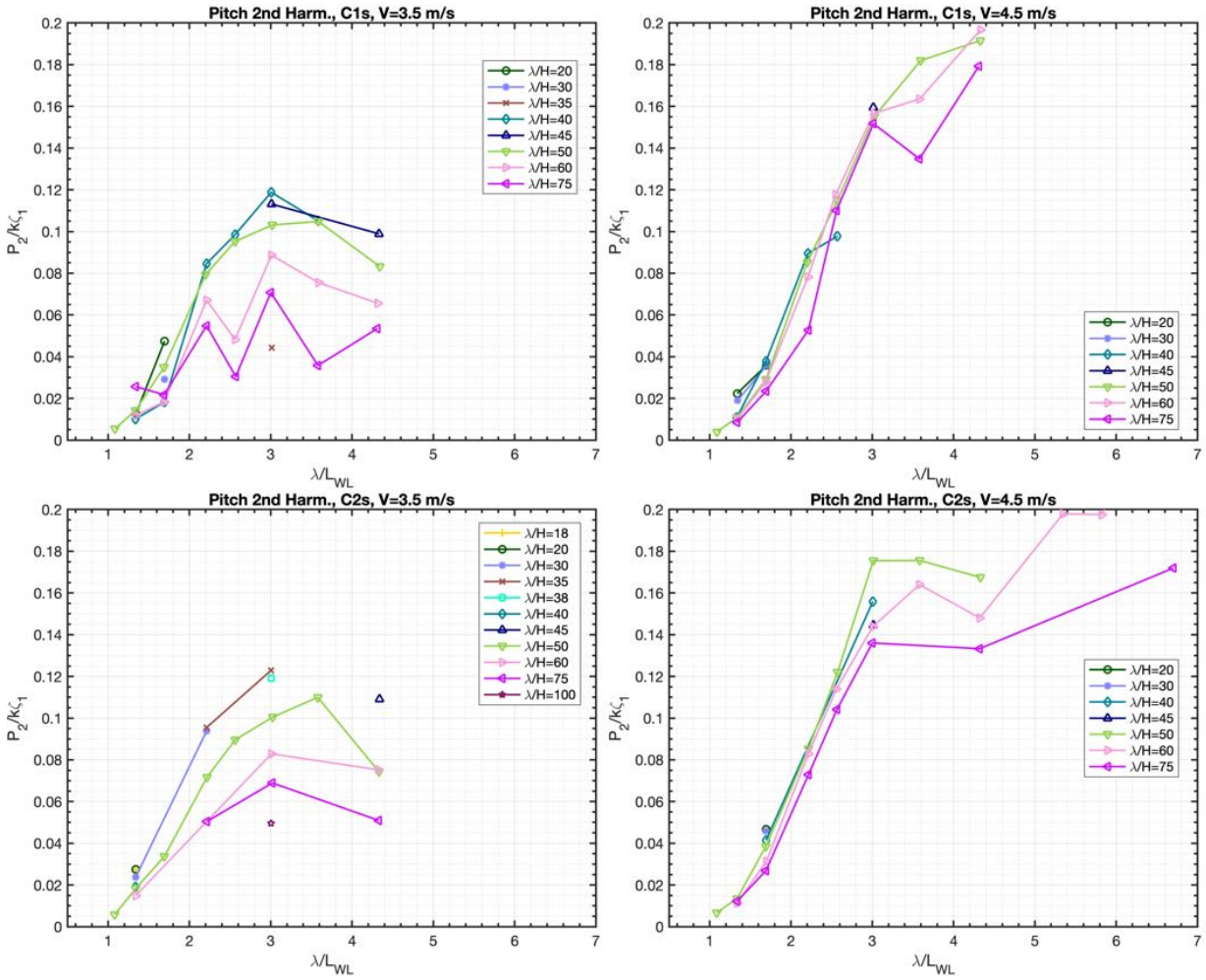

Figure 2.41: Pitch second harmonic response vs λ/L_{WL}

Figure2.42 shows that almost in all cases, the pitch second harmonic response is increasing with increasing wave steepness. In general, the higher the response, the steeper the curves of pitch response are.

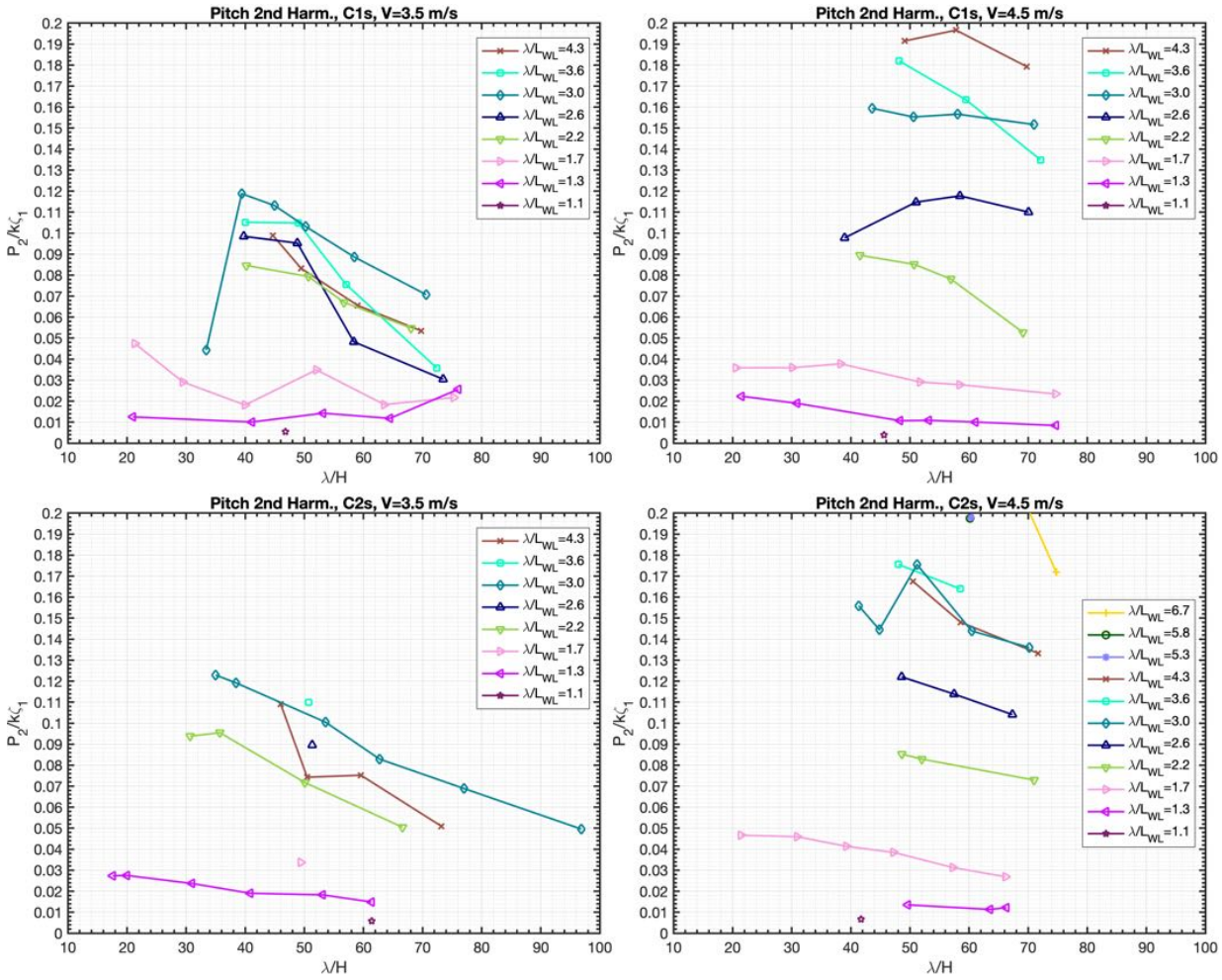

Figure 2.42: Pitch second harmonic response vs λ/H

Using the following plots, second harmonics of vertical accelerations will be discussed. Also in the case of accelerations, the amplitude of the second harmonic of the response will also be non dimensionalized using the first harmonic amplitude of the forcing term $\omega_e^2\zeta_1$. Where ω_e is the encounter angular frequency, obtained from the ultrasonic wave elevation sensor fixed to the carriage.

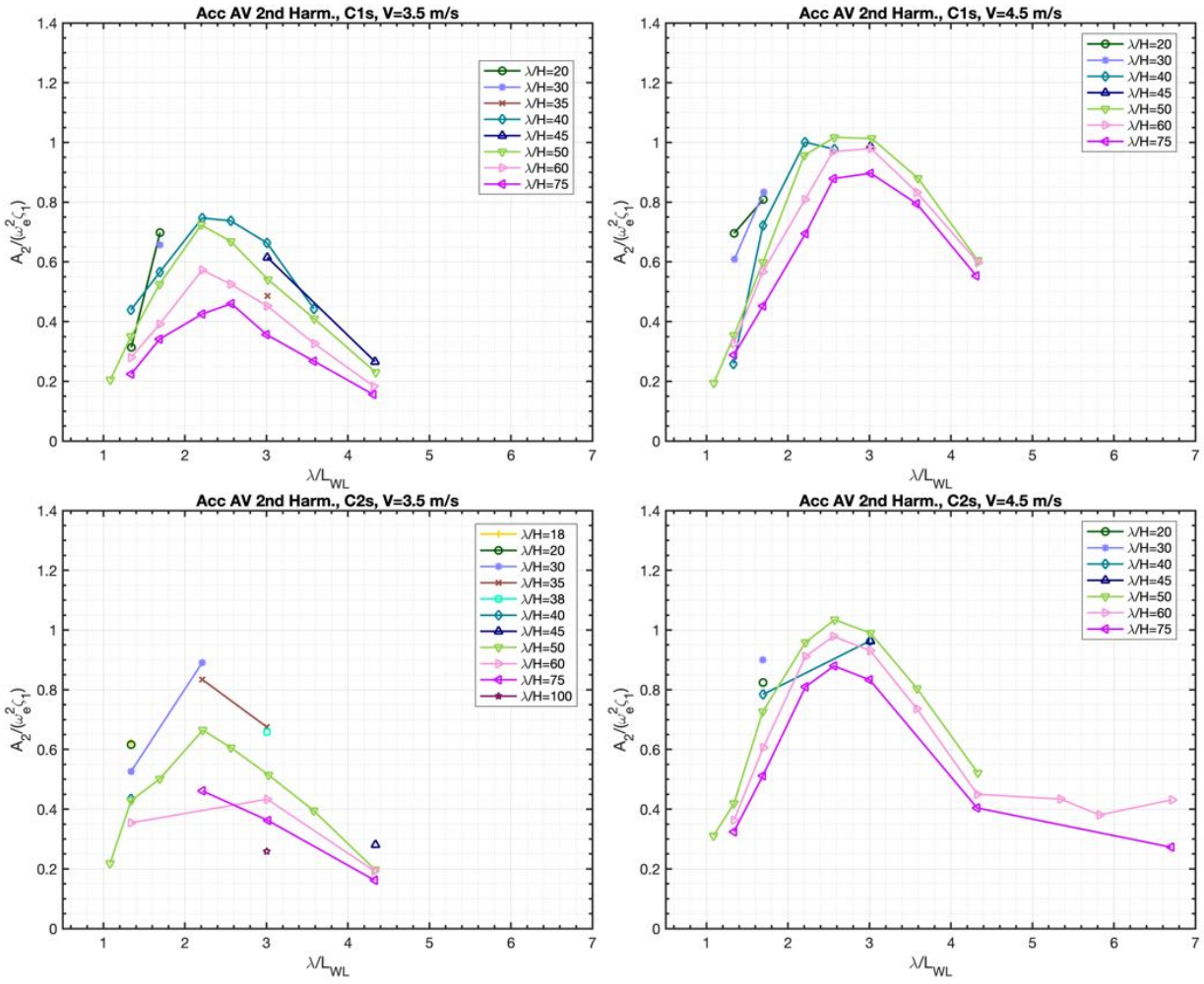

Figure 2.43: Vertical acceleration (AV) 2nd harmonic vs λ/L_{WL}

The second harmonic amplitude of the bow vertical acceleration (Fig. 2.43) shows that for $v = 3.5m/s$ the peak wavelength is $\lambda/L_{WL} = 2.0$ for both hulls, meanwhile for $v = 4.5m/s$ the peak wavelength is increased to $\lambda/L_{WL} = 3.0$ for the broader hull and $\lambda/L_{WL} = 2.6$ for the slimmer one. Taking into consideration the $\lambda/H = 50$, the amplitude of the second harmonic is 30% the amplitude of the first one for $v = 3.5m/s$ and 40% for $v = 4.5m/s$. As in the case of pitch, for $v = 4.5m/s$ the broader hull shows higher second harmonic amplitude than the slimmer hull for $\lambda/L_{WL} \geq 3.0$. The effects of wave steepness are clearly shown in Fig. 2.44, second harmonic amplitudes are higher as steepness increases, the trend is more pronounced with respect to the case of pitch motion. In particular, the effect of wave steepness is almost constant across all wavelengths.

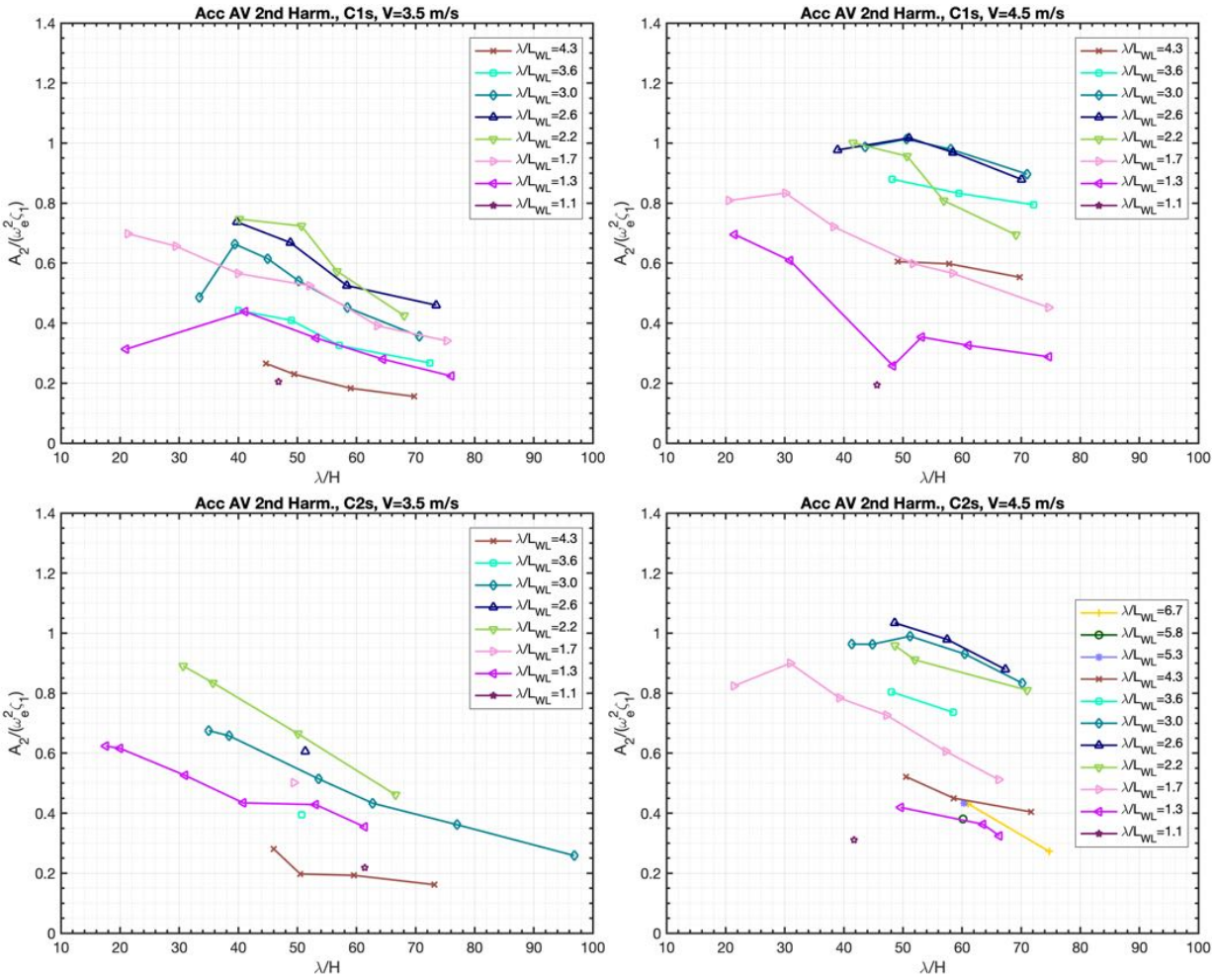

Figure 2.44: Vertical acceleration (AV) 2nd harmonic vs λ/H

Accelerations show not only a much higher second harmonic amplitude respect to motions but significant third harmonic amplitudes. The plot in Fig. 2.45 shows the time series and spectrum of the vertical acceleration at the bow and center of gravity. The amplitude of the third harmonic component is clearly relevant in this case. In Fig. 2.46, the third harmonic amplitude of vertical bow accelerations is plotted against λ/L_{WL}. It is clear that the second and third harmonic response of both hulls share a very similar trend with respect to the wavelength. The third harmonic shows increasing peak wavelength with speed but the effect of wave steepness is stronger at the peak.

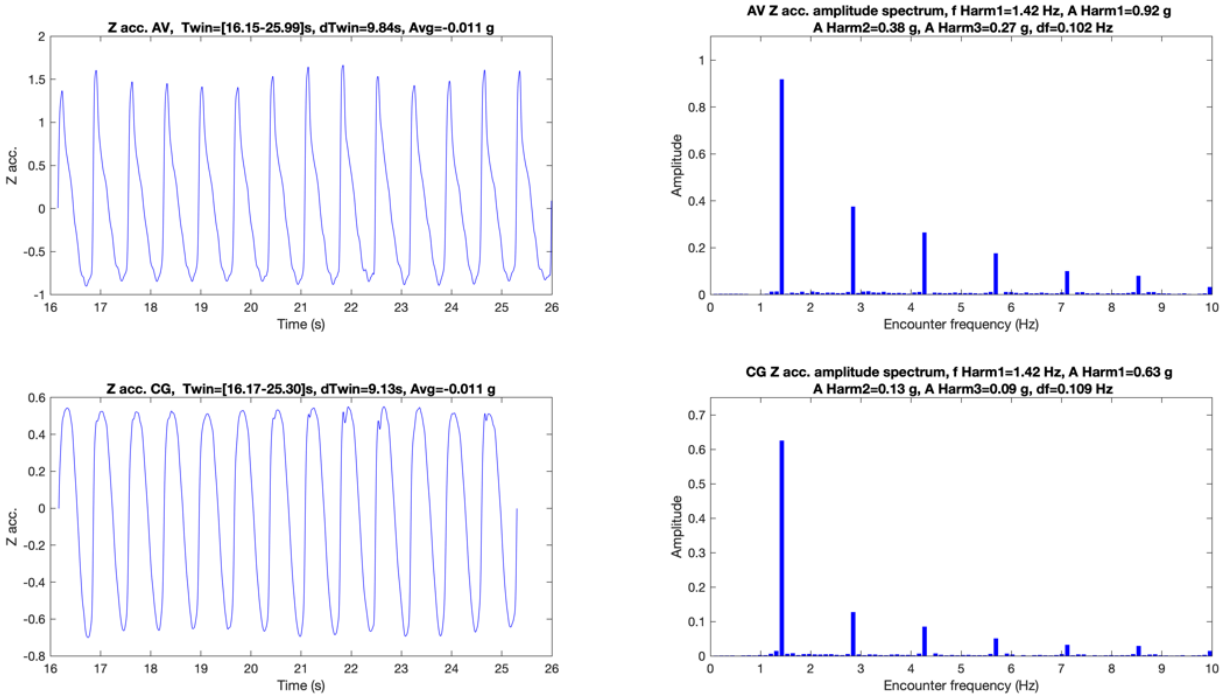

Figure 2.45: Vertical acceleration time series and their amplitude spectrum

The faster the hull, the higher the third harmonic content of the acceleration signal. Taking into consideration the $\lambda/H = 50$ case, the third harmonic amplitude is up to 16% of the first harmonic for $v = 4.5m/s$ and 23% of the first harmonic for $v = 4.5m/s$.

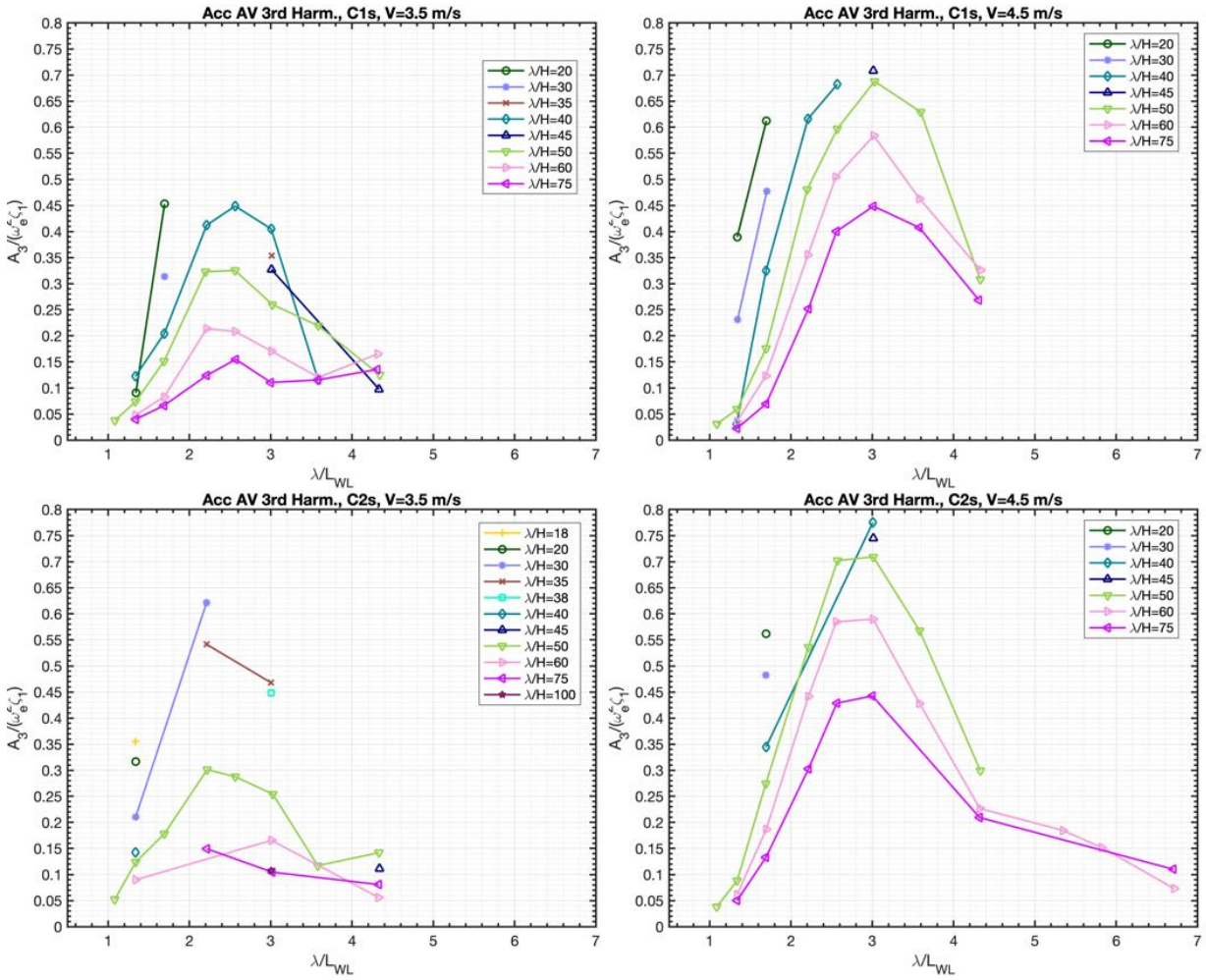

Figure 2.46: Vertical acceleration (AV) 3rd harmonic vs λ/L_{WL}

The general dependency on wave steepness is also stronger than the second harmonic, as it can be seen in Fig. 2.47. Considering the $\lambda/L_{WL} = 0.7 - 0.8$, the trend of second harmonic response of wave steepness is close to a linear function of the wave steepness, where the trend of the third harmonic response is closer to a quadratic function.

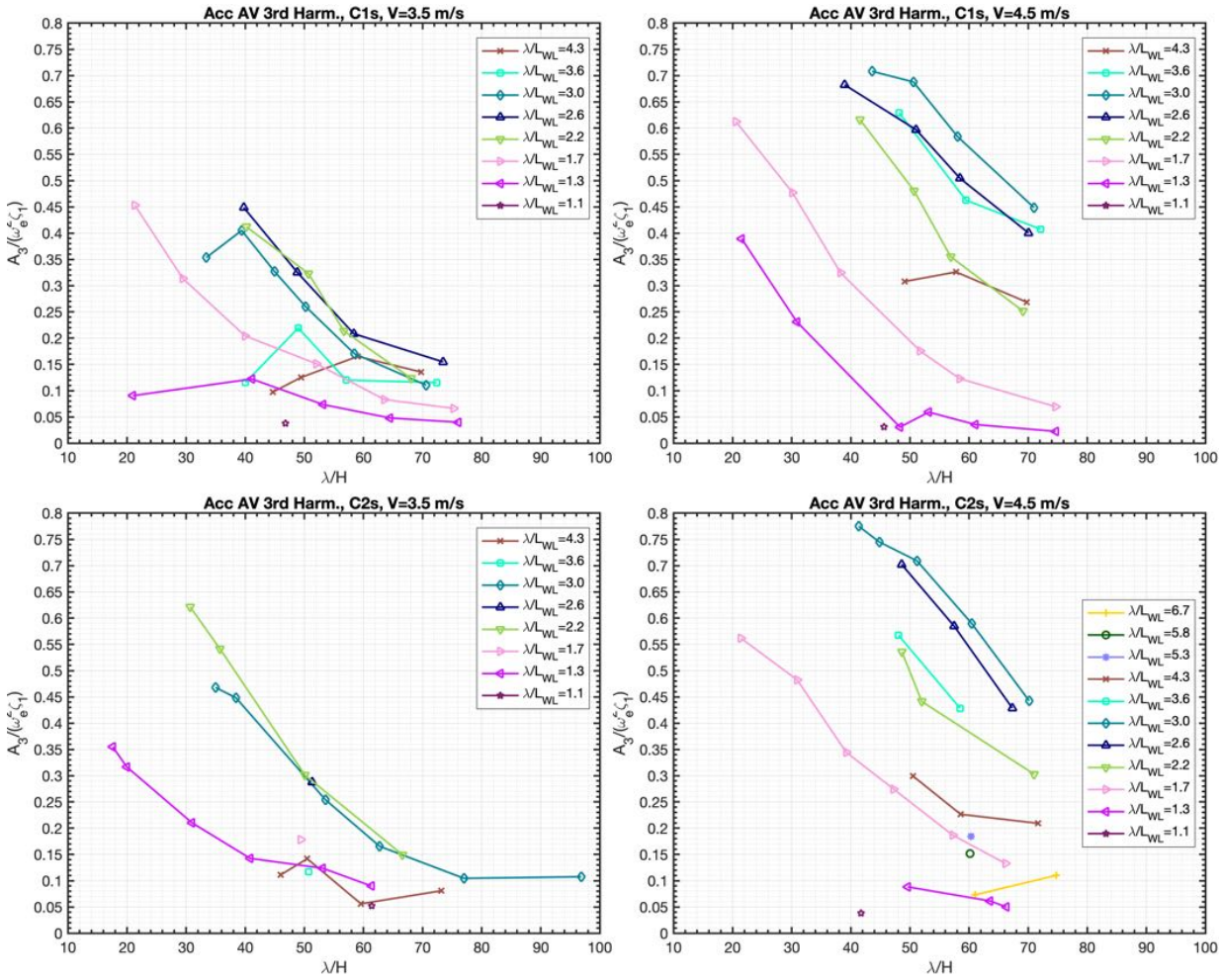

Figure 2.47: Vertical acceleration (AV) 3rd harmonic vs λ/H

Next, the iso-steepness plots of second harmonic of the vertical acceleration at the center of gravity are shown in Fig. 2.48. The trend is similar to the case of bow accelerations, apart from the lower values. The $\lambda/H = 50$ case show that the amplitude of the second harmonic response is 15% the amplitude of the first harmonic for $v = 3.5m/s$, and 25% the amplitude of the first harmonic for $v = 4.5m/s$. The broader hull shows a higher peak value for $v = 3.5m/s$, and marginally lower peak value for $v = 4.5m/s$. For $\lambda/L_{WL} \geq 3.0$ and $v = 4.5m/s$, second harmonic response is lower for the slimmer hull. Peak values also occur at the same wavelengths as the case of bow accelerations and the effect of wave steepness is stronger at the peak wavelength.

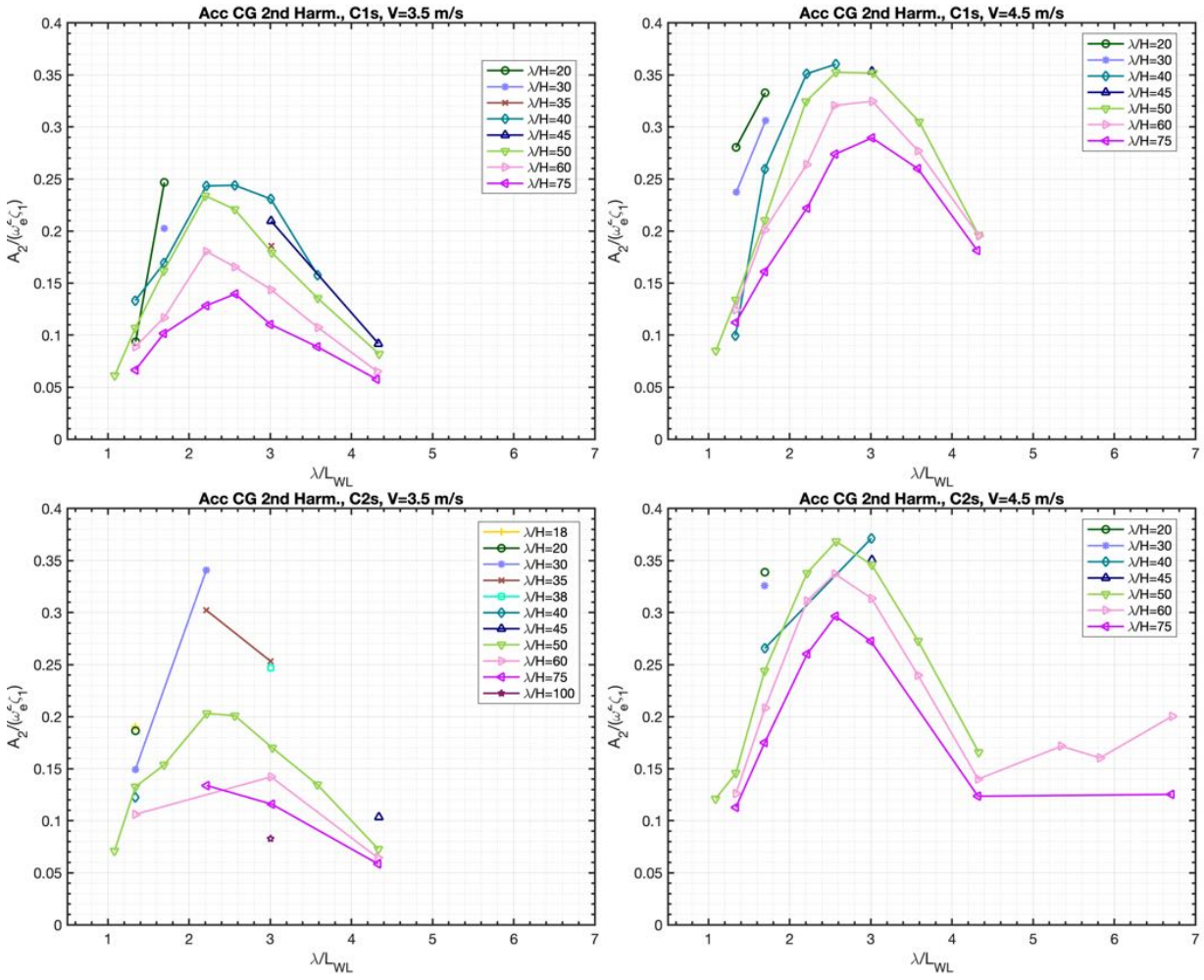

Figure 2.48: Vertical acceleration (CG) 2nd harmonic vs λ/L_{WL}

Iso-frequency plots in 2.49 show that also in this case, the second harmonic amplitude of the acceleration response grows as wave steepness increases, for every speed, wavelength and hull combinations.

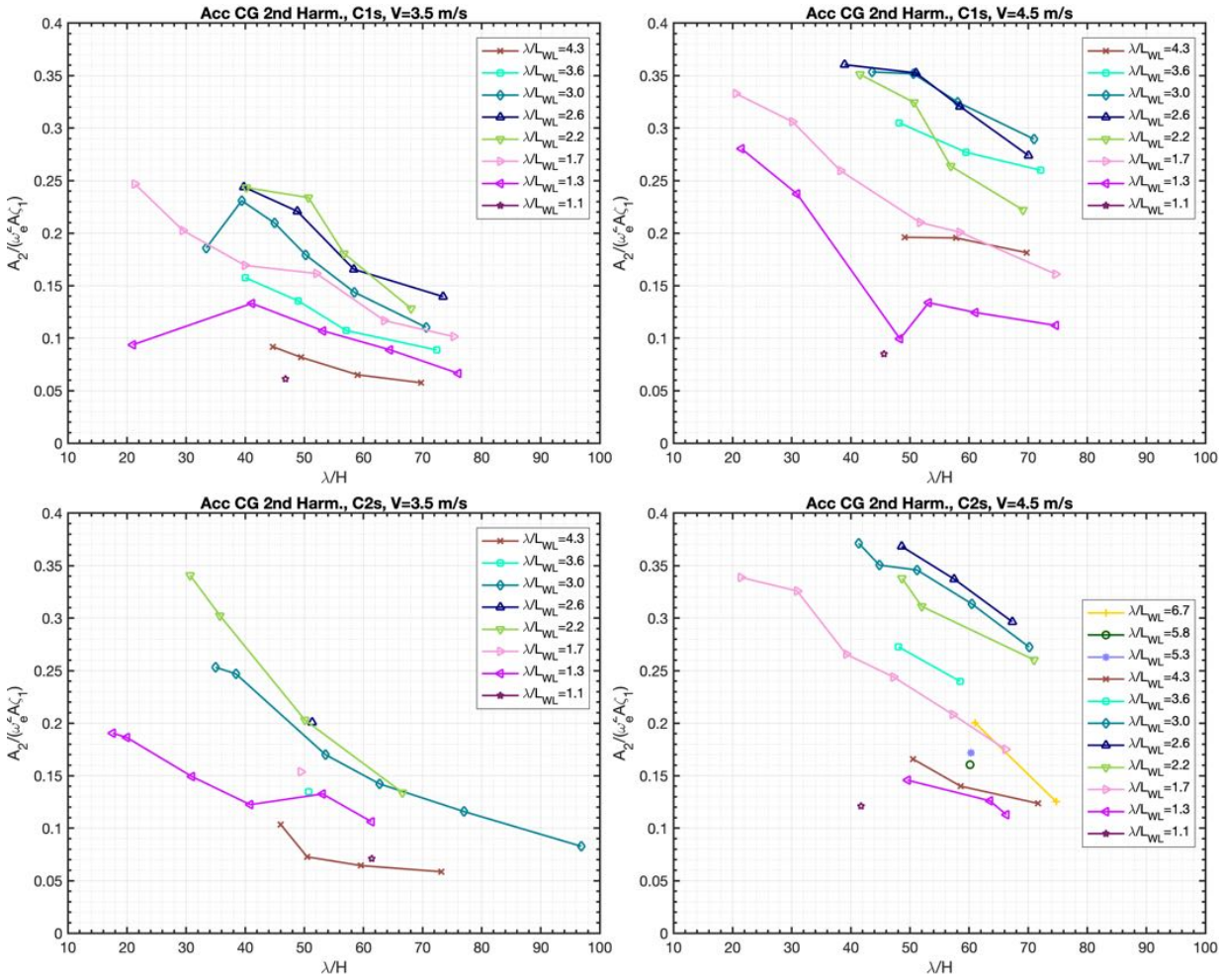

Figure 2.49: Vertical acceleration (CG) 2nd harmonic vs λ/H

Lastly, the third harmonic response of the vertical acceleration in the center of gravity as a function of wavelength shown in Fig. 2.50 shows that peak wavelengths are the same as in the case of the third harmonic response of bow vertical accelerations. The shift in peak wavelengths is still present for higher speed, independently of wave steepness and slenderness ratio. Taking the $\lambda/H = 50$ case in consideration, the amplitude of the third harmonic response is up to 8% the amplitude of the first harmonic for $v = 3.5m/s$, and 12% the amplitude of the first harmonic for $v = 4.5m/s$. The slimmer hull shows marginally higher peak values for both speeds.

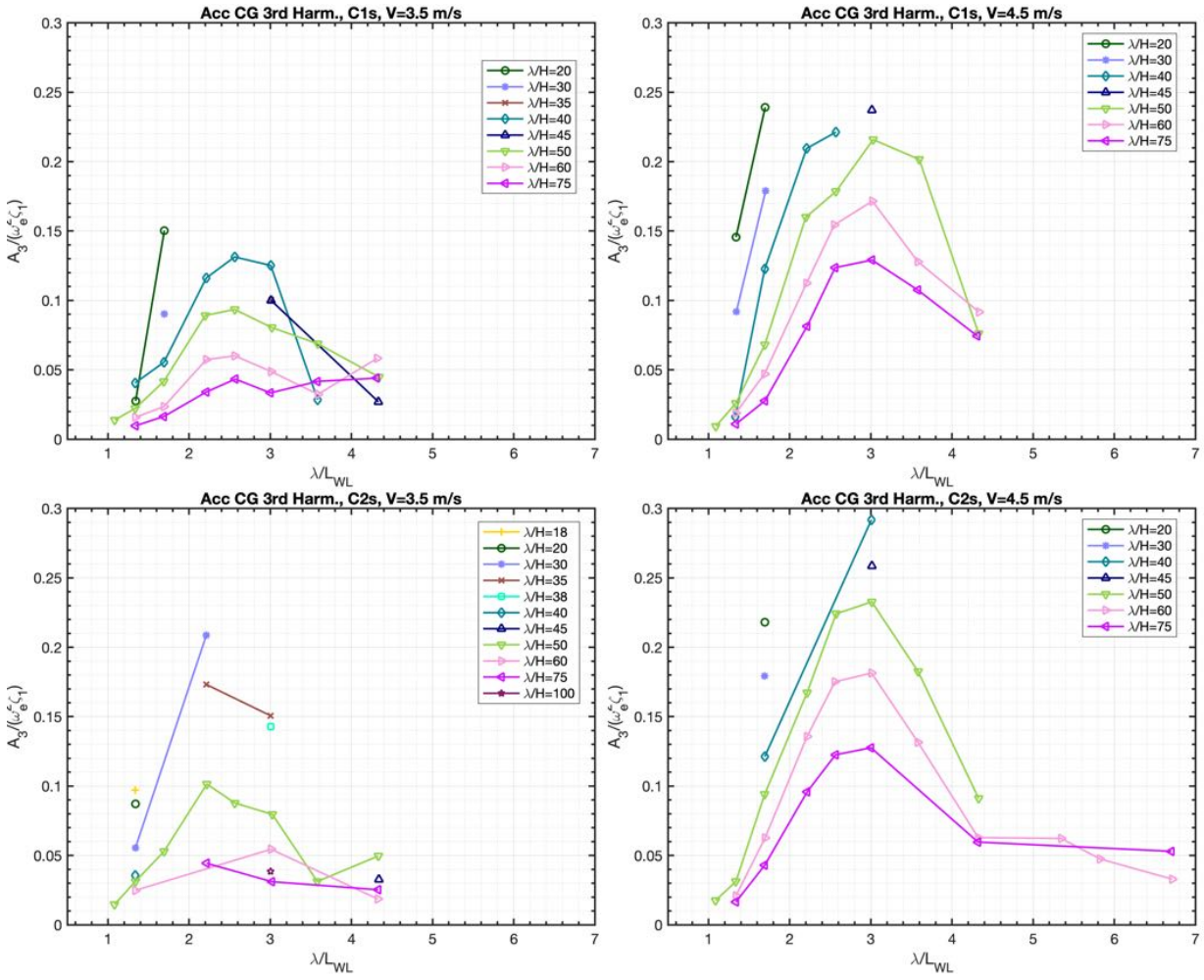

Figure 2.50: Vertical acceleration (CG) 3rd harmonic vs λ/L_{WL}

Similarly to what already shown in Fig. 2.47, also in this case a strong dependency of the third harmonic of the acceleration on wave steepness is observed in Fig. 2.51.

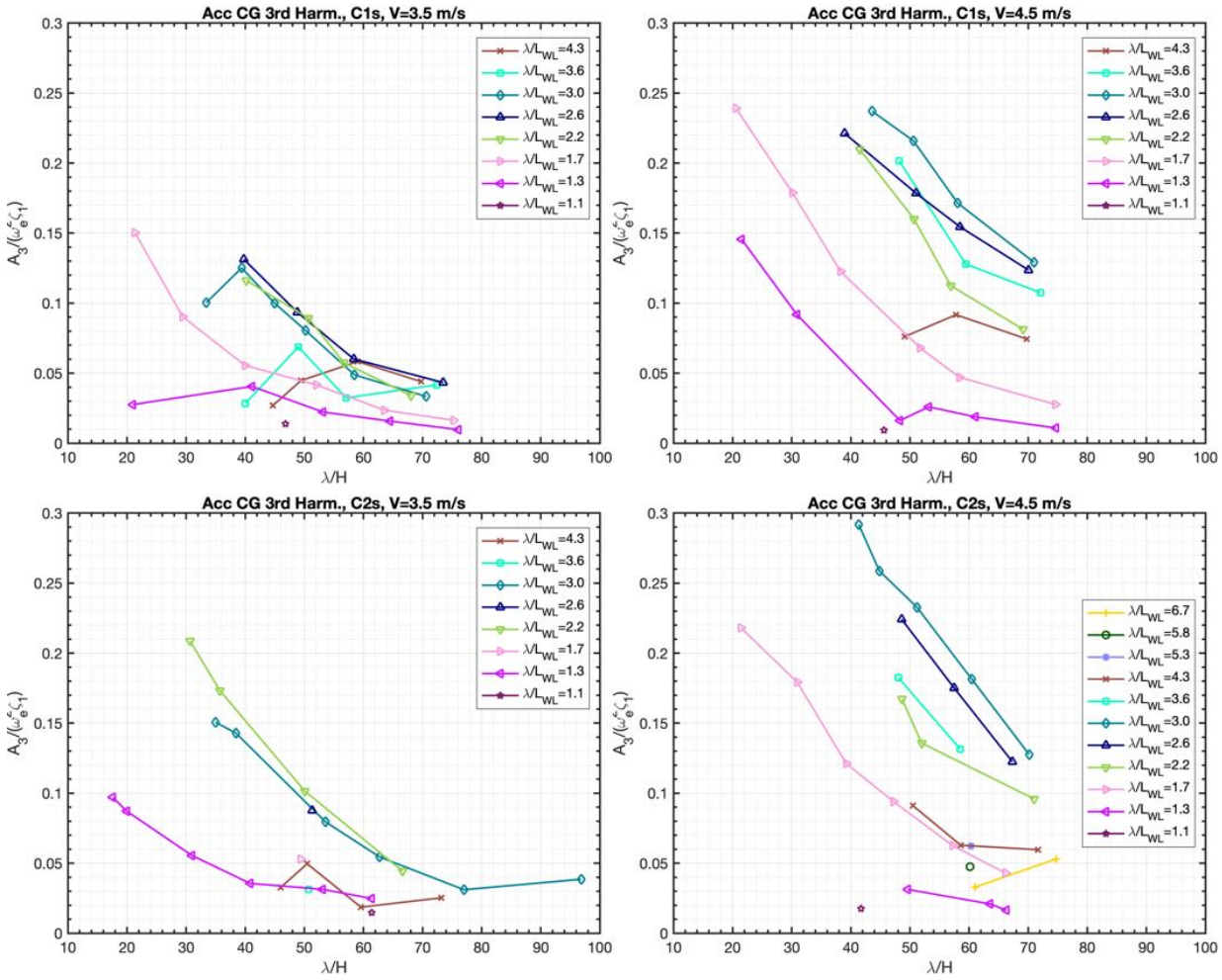

Figure 2.51: Vertical acceleration (CG) 3rd harmonic vs λ/H

2.4.7 Motion phase analysis

In order to provide the most comprehensive set of results of the present experimental investigation, the motion and acceleration phases have been also analysed. The wave elevation data from the ultrasonic sensor placed laterally respect to the model center of gravity has been used as phase reference. The signals phase difference has been computed using the phase of their main harmonic, corresponding wave encounter frequency. This method proved to be the more robust respect to the time domain approach using zero crossing time differences and it is coherent to the frequency domain analysis carried out in the analysis of the motion nonlinearities.

This analysis is also meant to investigate possible relations between the first and second harmonic nonlinearities trends and the phase of such motions relative to the incoming waves. The phase data of each response could be useful in an attempt to explain the cause of nonlinear aspects of motions and acceleration and in any case it provides a further insight in the seakeeping behavior

of this NSS subset.

The following plots will show the phase difference between the first harmonic of the wave elevation and the signal in question as a function of both wavelength and wave steepness. Given that, an increase of the phase value corresponds to an increase of the response phase lead.

In the following, motion and acceleration phases are presented using the same iso-steepness and iso-frequency plots methodology used in the previous section.

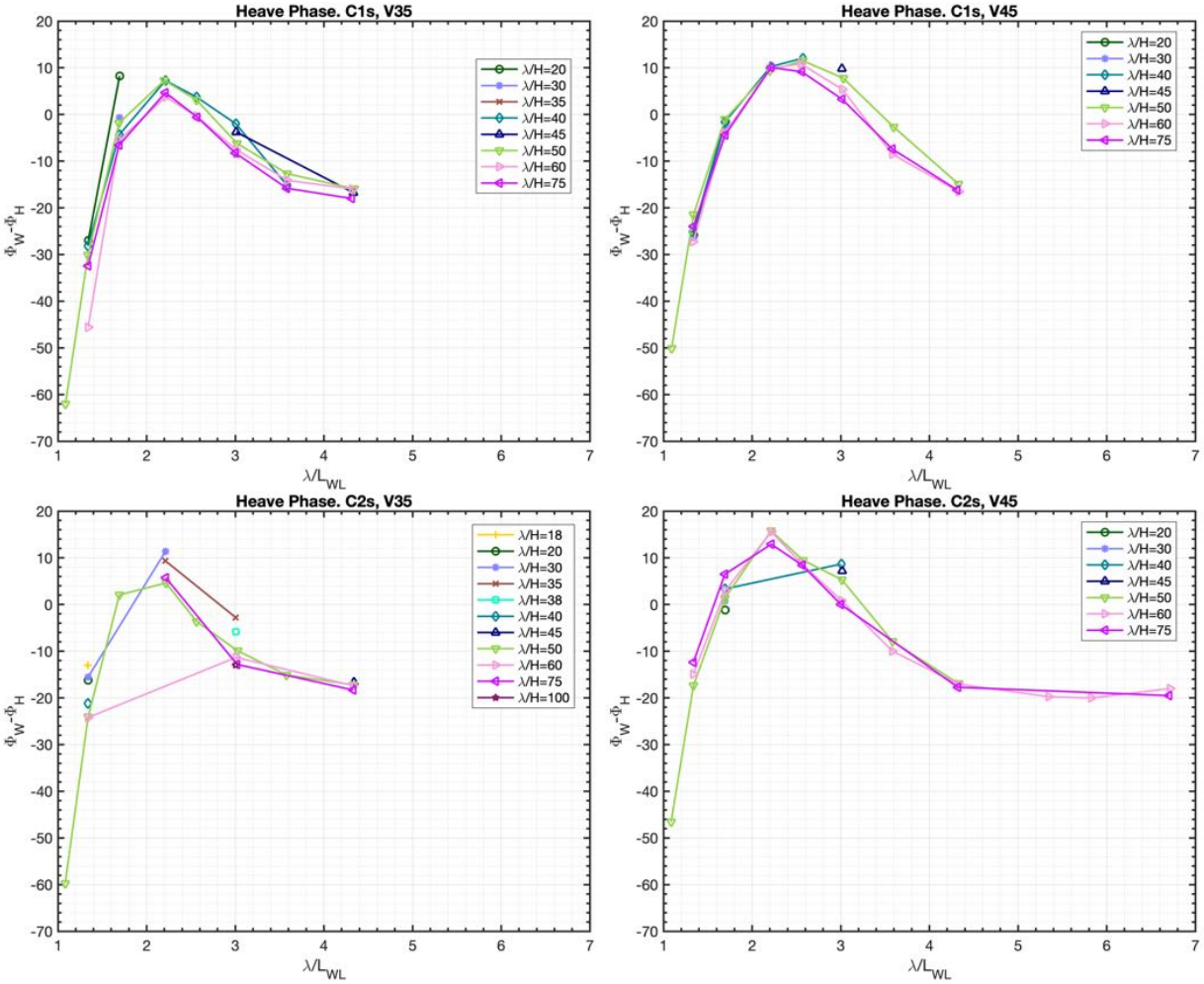

Figure 2.52: Heave phase vs λ/L_{WL}

The heave phase show a relatively smooth trend against the wavelength, starting with 20-30 degrees phase lead at shorter wavelength, reaching a maximum phase lag of around 10 degrees and back to 20 degrees lead for longer wavelength.

The maximum value of the phase is around $\lambda/L_{WL} = 2.2$ for both hulls and speed considered. Taking the $\lambda/H = 50$ case into consideration, it can be observed that in general the broader hull shows higher phase differences than the slimmer hull.

Taking into consideration Heave transfer function (see Fig. 2.30), it can be observed that the peak response occours after the phase peak (longer wavelength), where phase decreases.

Taking into consideration Heave second harmonic responses (see Fig. 2.39), it is clear that the maximum phase lag occours at slightly shorter waves respect to the maximum second harmonic response for every hull and speed combination. In any case, maximum second harmonic response occurs slightly after the phase peak, where phase is decreasing.

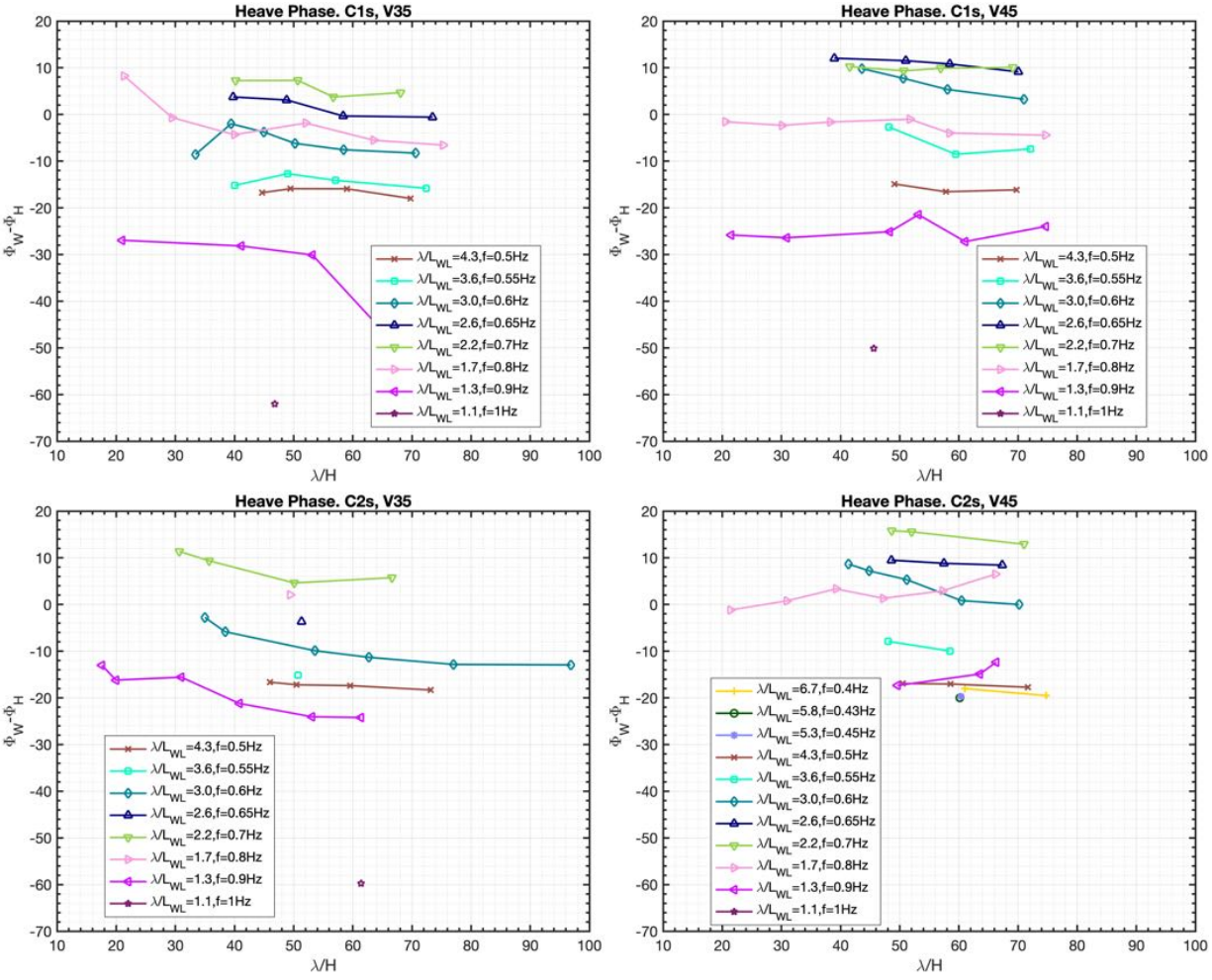

Figure 2.53: Heave phase vs λ/H

Looking at the phase results against wave steepness, no particular trend is visible across all wavelength apart from the case of $\lambda/L_{WL} = 3.0$, where phase decreases with decreasing wave steepness. This behavior is somewhat expected, meaning that the response tends to lag slightly more for steeper waves.

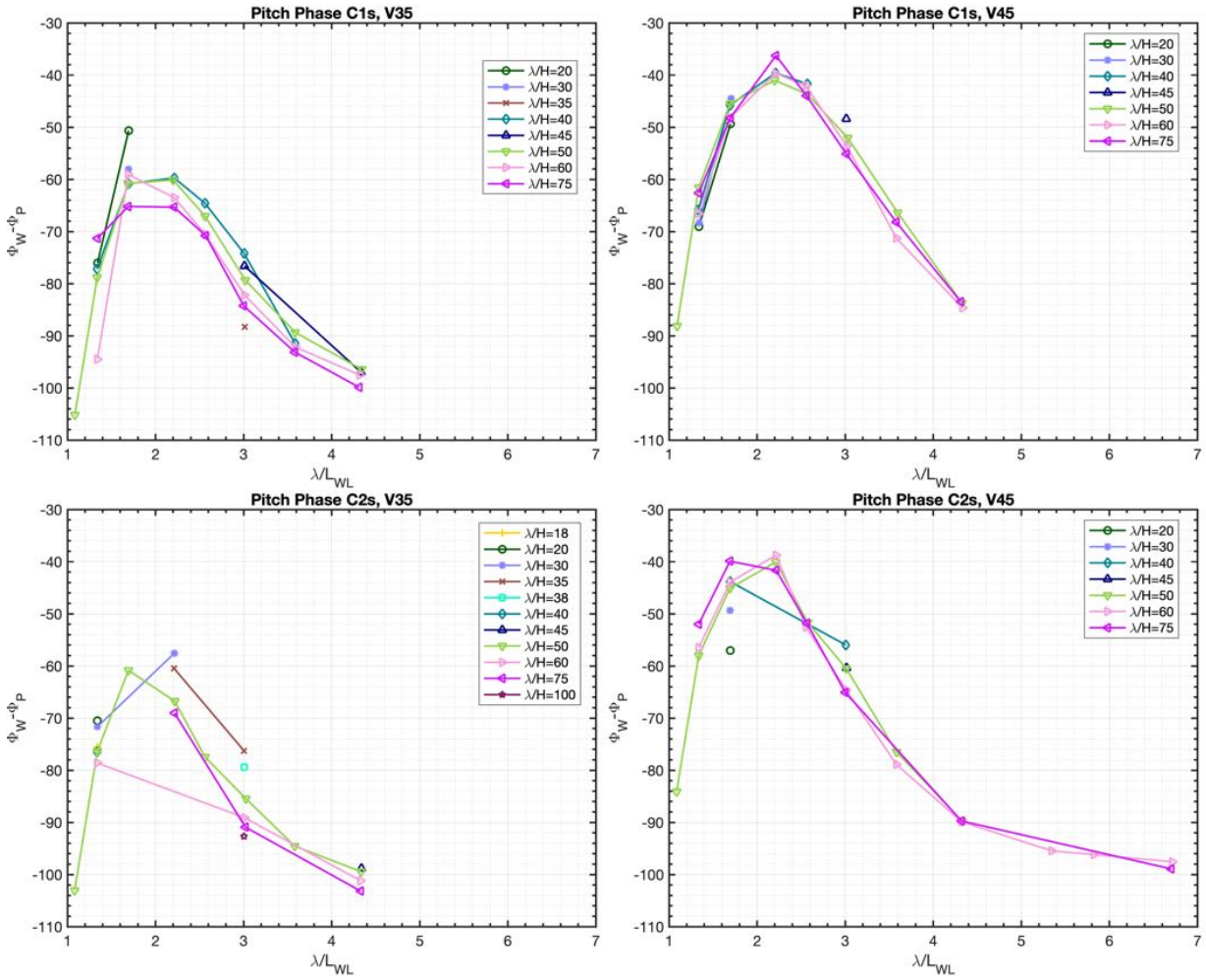

Figure 2.54: Pitch phase vs λ/L_{WL}

Pitch phase also show a smooth trend against the wavelength. As expected, pitch response is always leading wave excitation.

The maximum value of the pitch phase is around $\lambda/L_{WL} = 2.2$ for both hulls and speed considered. For the $\lambda/H = 50$ case, phase differences between hulls follows what it has been said for the case of heave motion.

Taking into consideration Pitch transfer function and econd harmonic responses (see Fig. 2.32 and 2.41), it can be observed that the peak response occours after the phase peak , as in the case of heave.

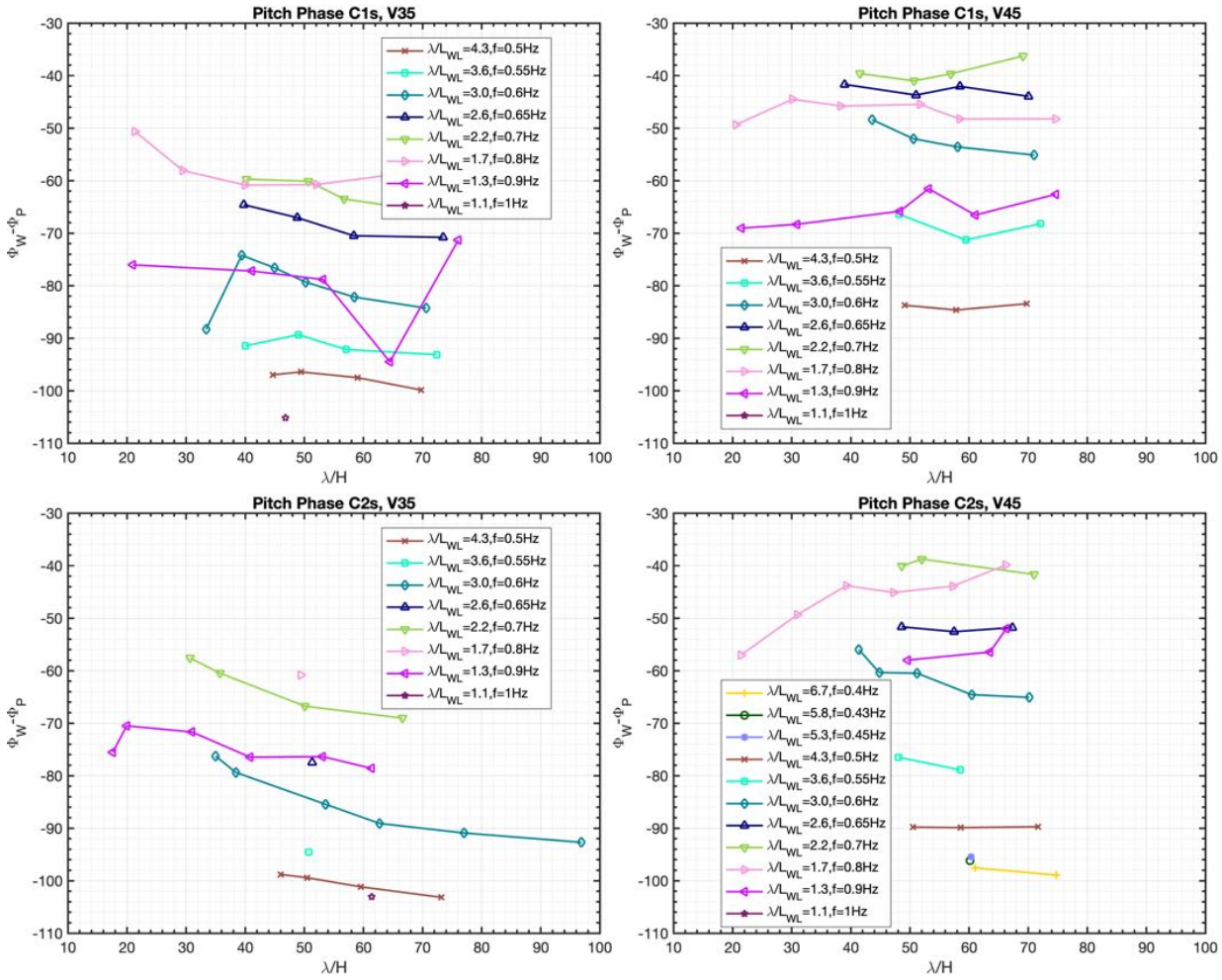

Figure 2.55: Pitch phase vs λ/H

Pitch phase shows only a slight dependence on wave steepness in the case of the lowest tested speed, as in the case of heave, otherwise no significant correlations are present.

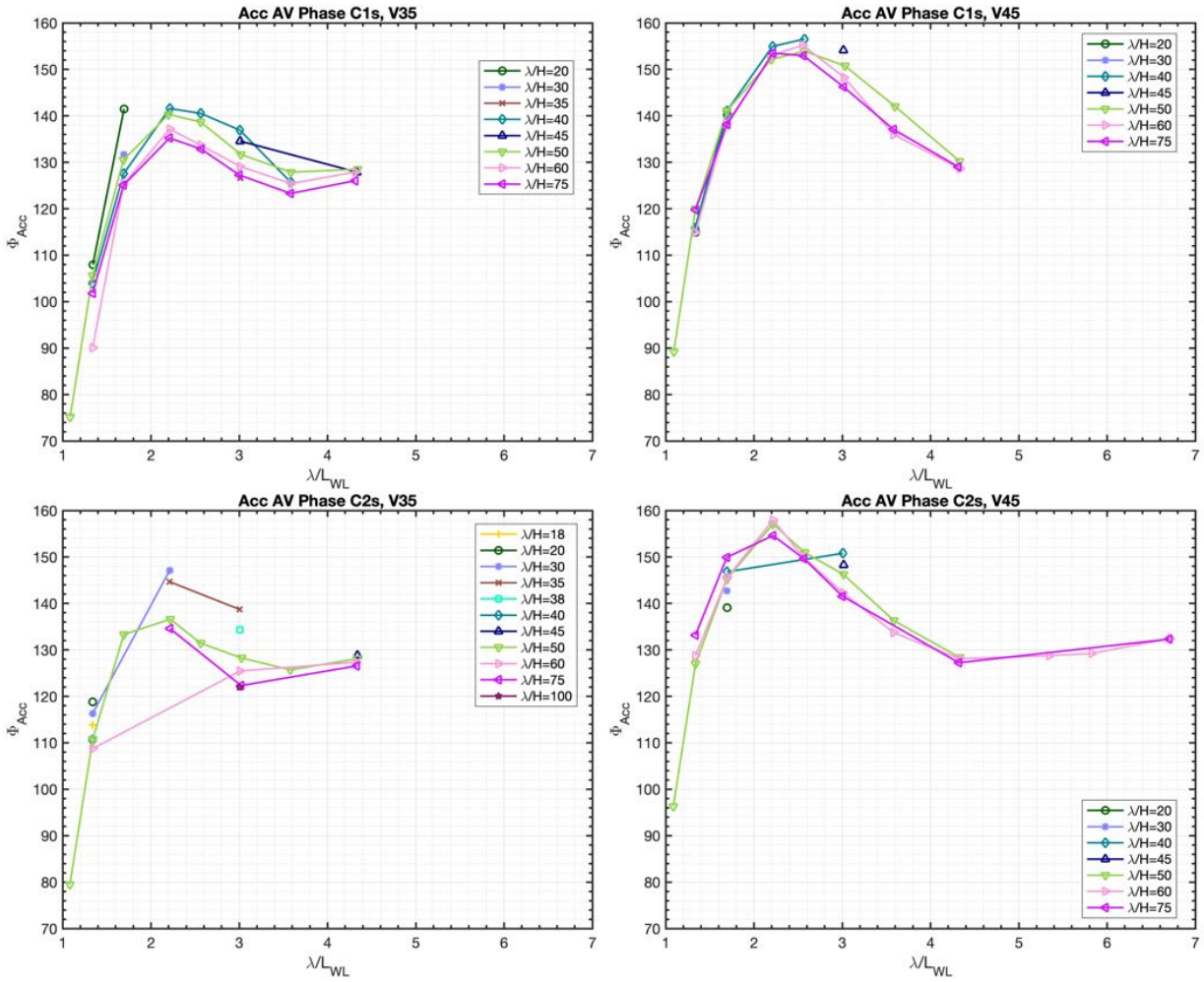

Figure 2.56: Vertical acceleration (AV) phase vs λ/L_{WL}

Also in the case of vertical accelerations at the bow, phase share the same trend against wavelengths as in the previous cases.

Absolute phase values here have no particular meaning since the reference signal (wave) is relative to the hull center of gravity, where accelerations are measured at the bow instead. This does not implies that the phase trend and differences are otherwise meaningful.

Comparing phases in Fig 2.56 with the bow vertical acceleration transfer function, second and third harmonic response (see Fig. 2.34, 2.43 and 2.46), it is interesting to note that for the low speed cases, both phase and harmonic responses (including the transfer function), share the same peak wavelength. The same is not true for the higher speed cases, where the peak responses occour at slighly higher wavelength.

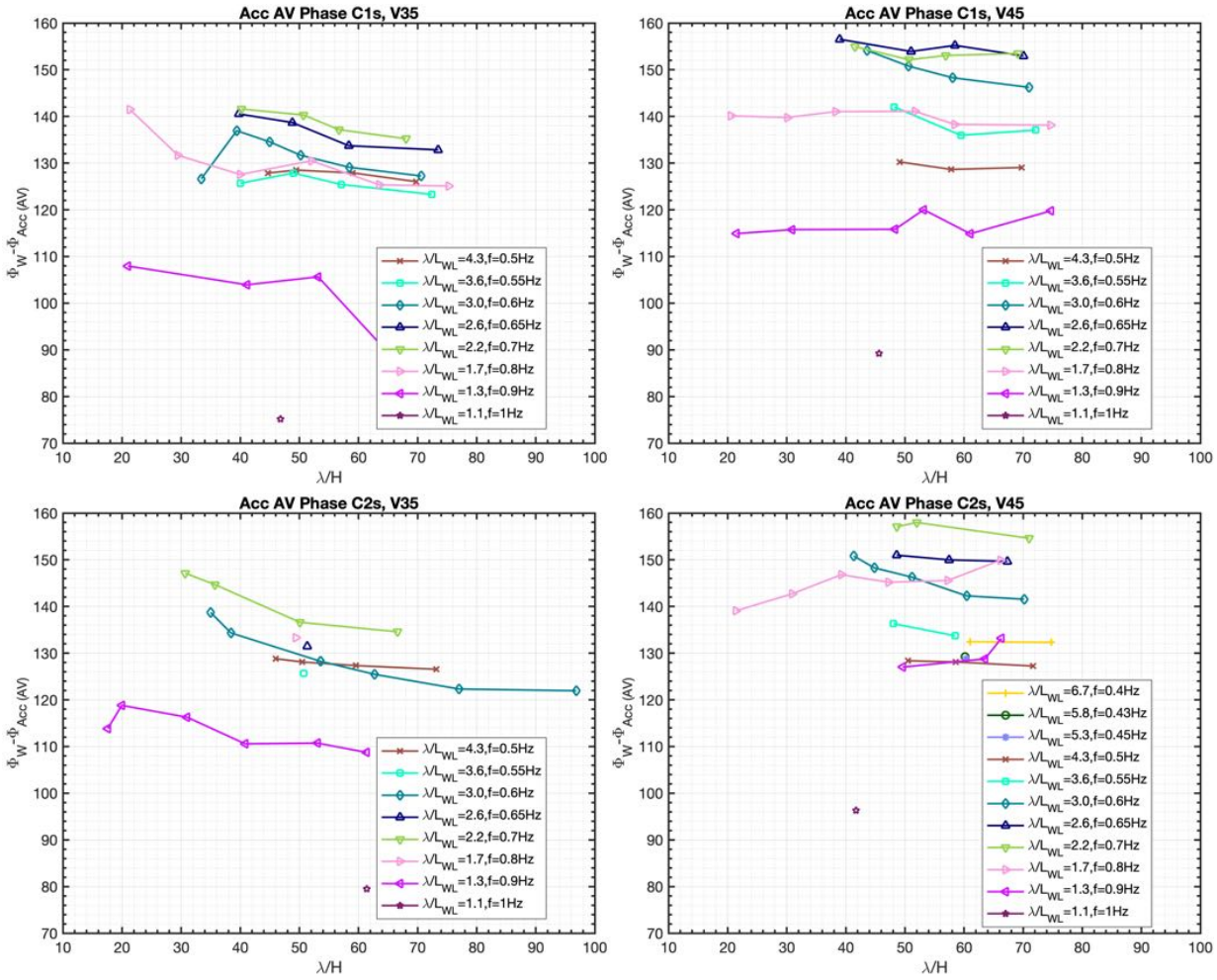

Figure 2.57: Vertical acceleration (AV) phase vs λ/H

Also in this case, only a minor phase dependency respect to wave steepness is observed at the lower speed, sharing the same characteristics as in the pitch case.

It is worth noting that although the strong dependency of the higher harmonics content on the wave steepness (see Fig. 2.44 and 2.47), phase response show little to no correlation to this phenomena.

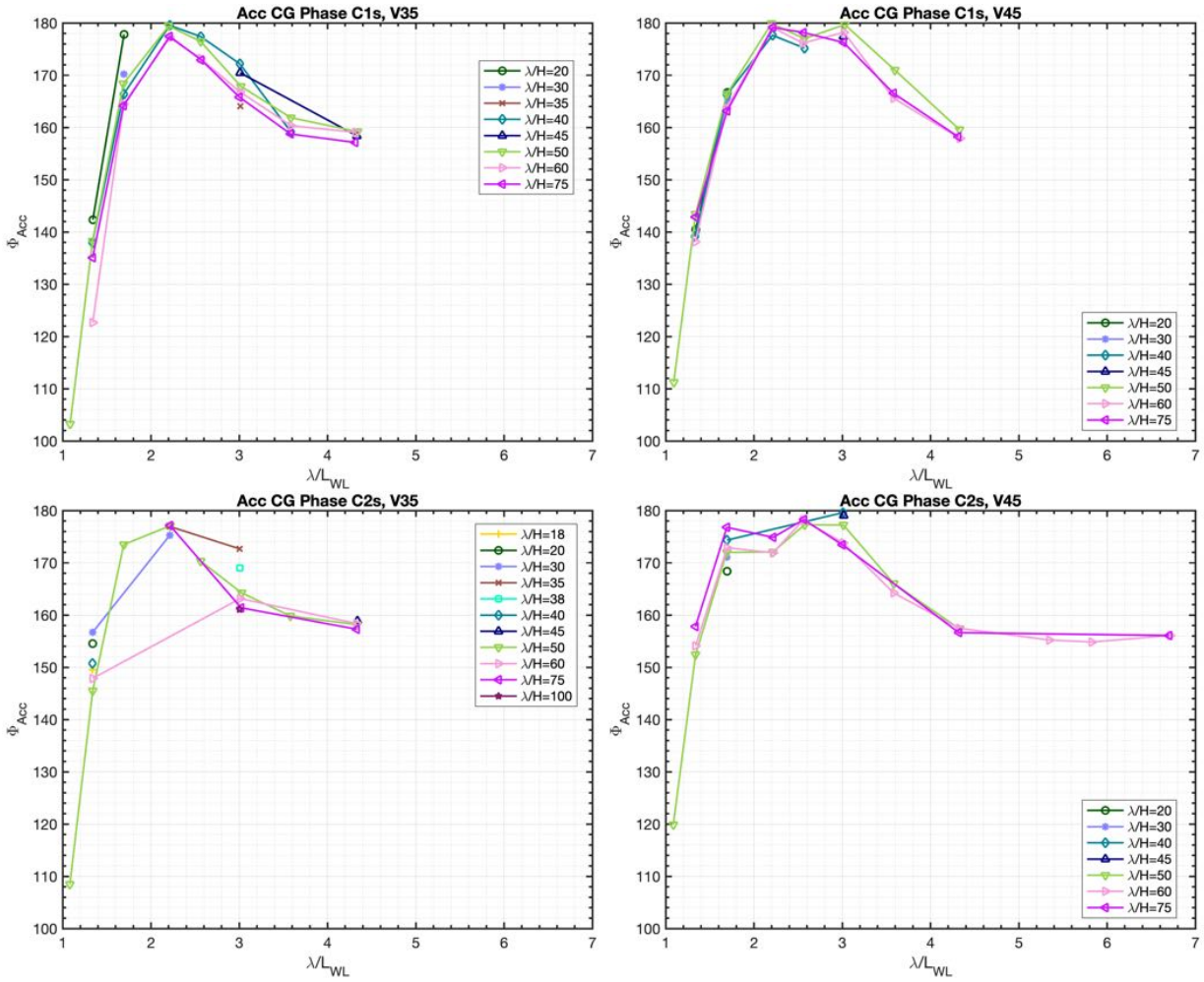

Figure 2.58: Vertical acceleration (CG) phase vs λ/L_{WL}

Despite similar phase trend respect to the other cases, center of gravity vertical acceleration phase shows a different characteristic for the highest speed cases, where peak phase value occur over a broader range of wavelength.

Comparing phases in Fig 2.58 with the center of gravity vertical acceleration second and third harmonic response (see Fig. 2.48 and 2.50), it can be observed that peak phase and higher harmonic response share the same critical wavelengths. Looking at the vertical acceleration transfer function in Fig. 2.36, the same is true for the highest speed cases, but for $v = 3.5m/s$ the peak response occours at longer wavelengths.

Also in the case of center of gravity and bow vertical accelerations, phase differences are greater in the case of the broader hull.

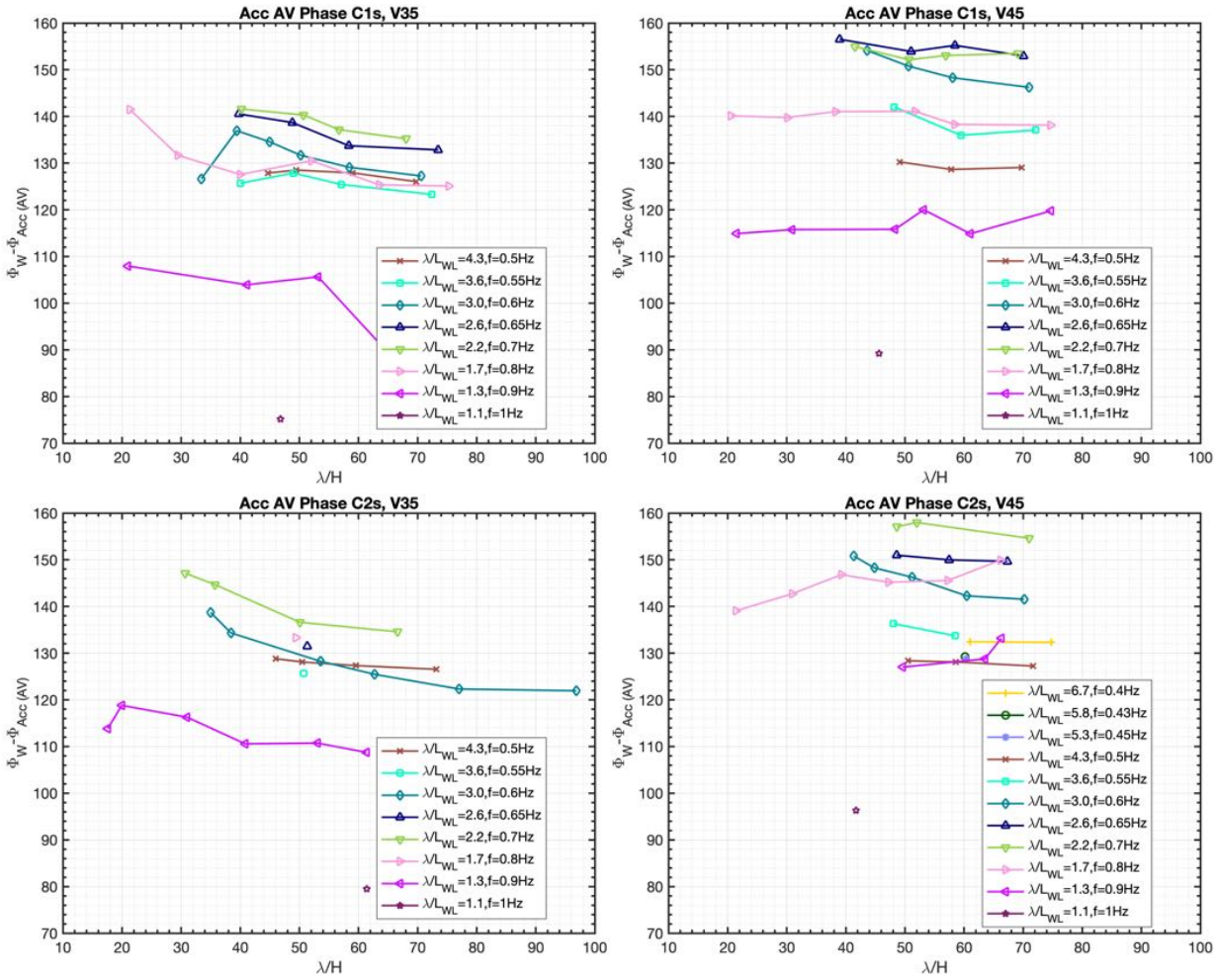

Figure 2.59: Vertical acceleration (CG) phase vs λ/H

The plot in Fig. 2.59 shows the same phase behavior as in the previous cases. Also in this case, although a strong dependency of the higher harmonics content on the wave steepness (see Fig. 2.49 and 2.51) is present, phase seems to be not correlated.

2.5 Closure

In this chapter, an extensive description of the experimental work done in the towing tank has been laid down. Both calm water and regular waves seakeeping tests carried out during the course of the SOPHYA project have been documented. It has been an important milestone in the Ph.D. program as it allowed to experience methods and issues related to the experimental hydrodynamic research. The data analysis methods learned in the process and the scripts developed have been proved very useful in the full scale sea trial data analysis later in the project. The results of the model tests data analysis have been used as a reference for full scale and computational results.

The analysis of the results of seakeeping tests in regular waves with the MCY65 model showed how the motion response for regular waves with steepness $H/\lambda = 1/100$ is not affected by nonlinear effects, but it is not the case for the vertical accelerations. The research for nonlinear behavior of high speed craft in regular waves sparked the idea to further investigate the nonlinear effects of wave steepness, speed and possibly other factors on planing hull motions in regular waves. Thanks to the collaboration of Fabio De Luca, a researcher of the University of Naples, we have been able to study the nonlinear effects of planing hull motions in regular waves using a well developed systematic series of hulls.

Experiments were planned in order to study the regular waves seakeeping performances of the hulls, in particular nonlinear motion responses in terms of transfer functions and higher harmonic response as a function of both wave frequency and steepness. The results of this work lead to an original research that contributes to the study of the seakeeping of planing hulls in waves.

The analysis of the experimental data confirmed behavior observed by other authors, such as fact that peak motion and acceleration response for planing hulls occur at longer wavelength respect to conventional hulls and that acceleration is more nonlinear with respect to motions. We observed how an additional shift in critical wavelength is present when speed is increased inside the planning regime and that the same shift is also observed in the second harmonic response, in particular for vertical accelerations.

Slenderness ratio is found to have a notable effect only on pitch motion at higher speeds, otherwise it is neutral with respect to peak values of heave and acceleration transfer functions. The effect of wave steepness on motion and acceleration transfer functions, shown through a dedicated set of plots, confirms other authors observations about the decrease of the first harmonic response with increasing steepness.

The presence of the second harmonic motion and acceleration response is also observed and its dependency on both speed and wave steepness is shown. Also in this case, the response is not affected by slenderness ratio in most cases. From the proposed analysis it is clear that increasing wave steepness and speed lead to increased second harmonic response. In addition, third harmonic response of vertical acceleration are investigated since they show significant amplitudes. In particular, it is observed that the trend of the second harmonic response with respect to wave steepness is close to a linear function and third harmonic response is closer to a quadratic one. To the author knowledge, this particular behavior has not been explicitly reported by earlier studies on the subject.

In addition, motions and acceleration response phases shows that higher harmonic content is generally associated with a higher phase lead, although phases show no particular dependency on

the wave steepness.

The above observation could give a hint on some possible physical aspects behind the nonlinear motions and accelerations observed. As motion phase lag increases, the hull-water surface relative velocity during a wave encounter will increase. This will lead to a more severe hull bottom impact, hence increase impulsive non linear hydrodynamic forces and damping (spray formation) on the hull. Those increased nonlinear forcing and damping terms could be one of the main reasons behind the nonlinerities trends observed in this study.

The main novelty of the work is represented by the focus on an extensive analysis regarding nonlinearities of a systematic series of planing hulls in regular waves. In particular the aspects concerning higher harmonics and their trends with respect to speed, wave and geometrical characteristics. The presented data is also a considerable addition to the already rich Naples Systematic Series dataset and provides a detailed benchmark case for computational studies.

Chapter 3

Full scale sea trials

3.1 Introduction

The main goal of this rare experimental investigation is to assess both calm water and seakeeeping full scale performances of the reference yacht hull. In addition, propulsion-related data is also acquired during the tests in order to be able to use such data for further research on the effects of a seaway on the yacht propulsive characteristics.

The sea trials were conducted on a 65 foot yacht built by Monte Carlo Yachts (Fig. 3.1 - `http://www.montecarloyachts.it`). The Full-scale experimental campaign is part of the SOPHYA (Seakeeping Of Planing Hull YAchts) project, aimed at assessing the performances of planing pleasure-boats in terms of sea-kindliness, safety and powering in mild weather conditions.

The sea trials that took place in the Gulf of Trieste (North Adriatic Sea) during the period December 2017 - January 2018. The experimental campaign took a total of four days of tests. Sea trials were carried out both in calm seas and in waves.

The duration of each run is around 10 min, which leads to a covered distance of 3 nm at 18 kn. Along this distance, the sea state is assumed reasonably homogeneous. Wind waves only (no swell) were present in the sea-trial area. It can be noted from Table 3.1 that the zero-crossing period (derived from the frequency-domain analysis of the free surface elevation) is generally very small, according to the geographic area and the target wind conditions. In particular *Run* 1, 4 and 5 are considered as limit conditions for the proper use of the buoy. Indeed for these specific records, log files from the wave buoy showed a non negligible number of errors. Still H_s met the project targets fairly well.

During the tests, the hull had no interceptors and trim flaps were kept in fully raised position. The design boat speed for the sea trials was 18 kn. Since a speed control system was not available, the tests were conducted at prescribed engine rpm and consequently the vessel speed varied slighty during the runs due to the waves. In table 3.1 the standard deviation of the vessel speed is reported. Fig. 3.2 shows an example of speed and course time series.

Figure 3.1: MCY 65 yacht

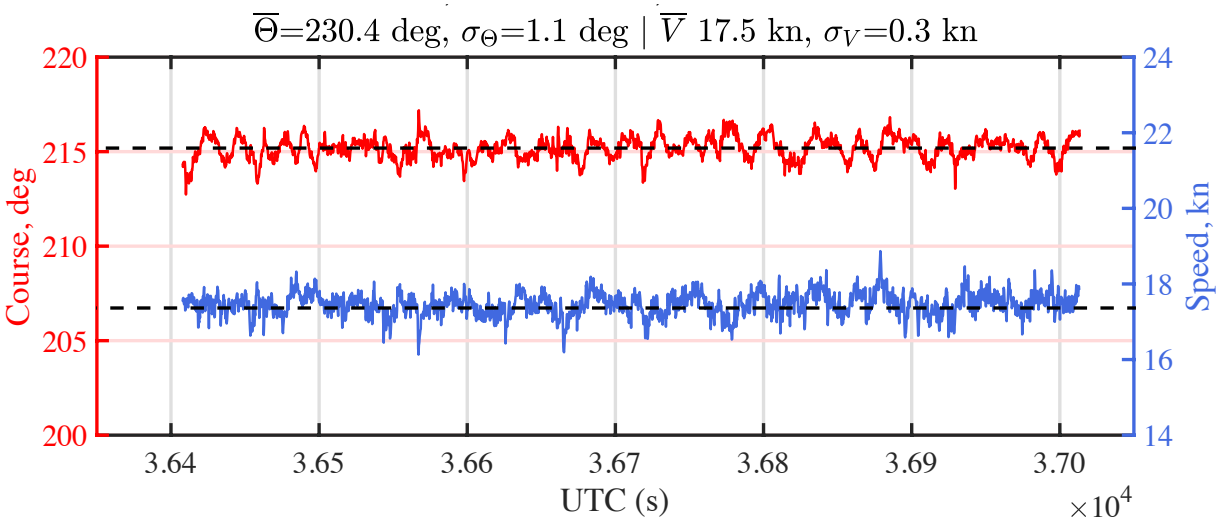

Figure 3.2: Sample time series of ship speed and course.

In accordance with the project targets, head sea conditions only were tested and analyzed. For every run, the target vessel heading was identified from the analysis of the last record available from a dedicated in-situ directional wave buoy. The target sea state of the project is here defined

as *mild weather conditions* corresponding to a significant wave height H_s of about 0.50-0.60 m. These are very low sea state conditions that may take the measurement system (buoy) to its intrinsic lower limits, in particular in the presence of short-crested sea.

	date (dd/mm/yyyy)	time (hh:mm:ss)	H_s (cm)	T_z (s)	V (kn)	σ_V (kn)
Run 1	15/12/2017	13:02-13:13	60	3.1	18.4	0.4
Run 2	16/01/2018	14:17-14:25	59	4.8	17.4	0.3
Run 3	16/01/2018	14:47-15:57	60	4.8	18.5	0.4
Run 4	18/01/2018	10:06-10:16	54	3.5	17.5	0.3
Run 5	18/01/2018	11:09-11:18	43	3.0	18.6	0.4

Table 3.1: Sea state and average boat speed during the tests.

3.2 Seakeeping trials planning

In the following section, the planning procedure used to prepare the full-scale seakeeping trials test program is explained.

The main document used for the planning of the seakeeping trials is the “Task 3" part of the “Specialist committe on Trials and Monitoring" report of the 22nd ITTC conference in Seoul [83]. The other documentation used is chapter 15 of Lloyd’s “Seakeeping: ship behaviour in rough weather" [74], where seakeeping trials are discussed.

3.2.1 Location

As discussed with the shipyard, the full-scale seakeepig trials will be carried out in the northern Adriatic Sea, just outside the Marano Lagoon. in particular the test zone will be chosen within 3 to 5 nautic miles from the fixed wavebuoy, belonging to the oceanographic division of the OGS (Istituto Nazionale di Oceanografia e di Geofisica Sperimentale) institute. This will allow the use of the data from the “DWRG1" wavebuoy as a back-up and verification of the mobile GPS wavebuoy.

In figure 3.3, the test zone is displayed, the “DWRG1" coordinates are: 45.56559° N, 13.24795° E.

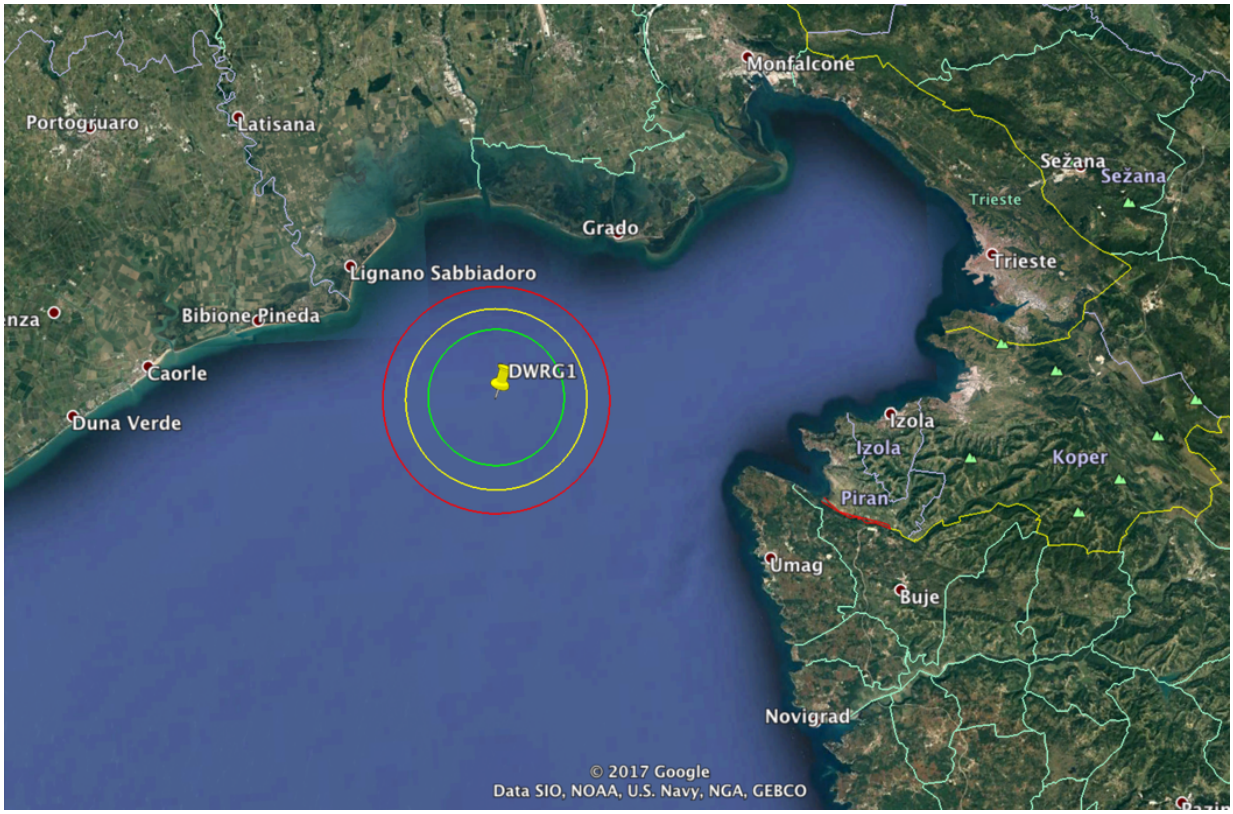

Figure 3.3: Test zone, green circle radius: 3 nm, yellow: 4 nm, red: 5 nm

3.2.2 Sea State

The days for the sea trials were selected accurately in order to match the target sea state (significant wave height H_s) by means of the high-fidelity high-resolution wind-wave forecast, run daily by the authors at HyMOLab [`http://hymolab.units.it`]. Table 3.1 summarizes the wave conditions during the tests.

In order to characterize the possible sea states during the tests and to check their compatibility with the project target sea conditions, HyMOLab has put at the disposal of the project free retrospective proprietary marine and weather data. The data has a temporal resolution of one hour, space resolution is about 10 km, the retrospective analysis span from 1979 to present on a Mediterranean scale (Mediterranean Wind Wave Model - MWM), see [84].

Figure 3.4 shows the significant wave-peak period (H_S-T_P) scatter diagrams related to four characteristic points in the Gulf of Trieste (Fig. 3.5a). The project target significant wave height is of the order of 0.5-0.6 m. It can be seen from the plots that this is a condition of high probability of occurrence in the Gulf, in particular for peak periods below 4.5-5.0 s. Limited to point P004, Figure 3.5b shows the directional distribution of significant height. From the gathered information, it can be seen that the most probable average direction of the waves with $H_S = 0.5$ m corresponds to sea from south/south-east. Based on these parameters, it was established that the tests should

be programmed in the area of interest for days with sea from $120° - 180°$, $H_S \approx 0.5$ m and $T_P \approx 4.5 - 5.0$ s.

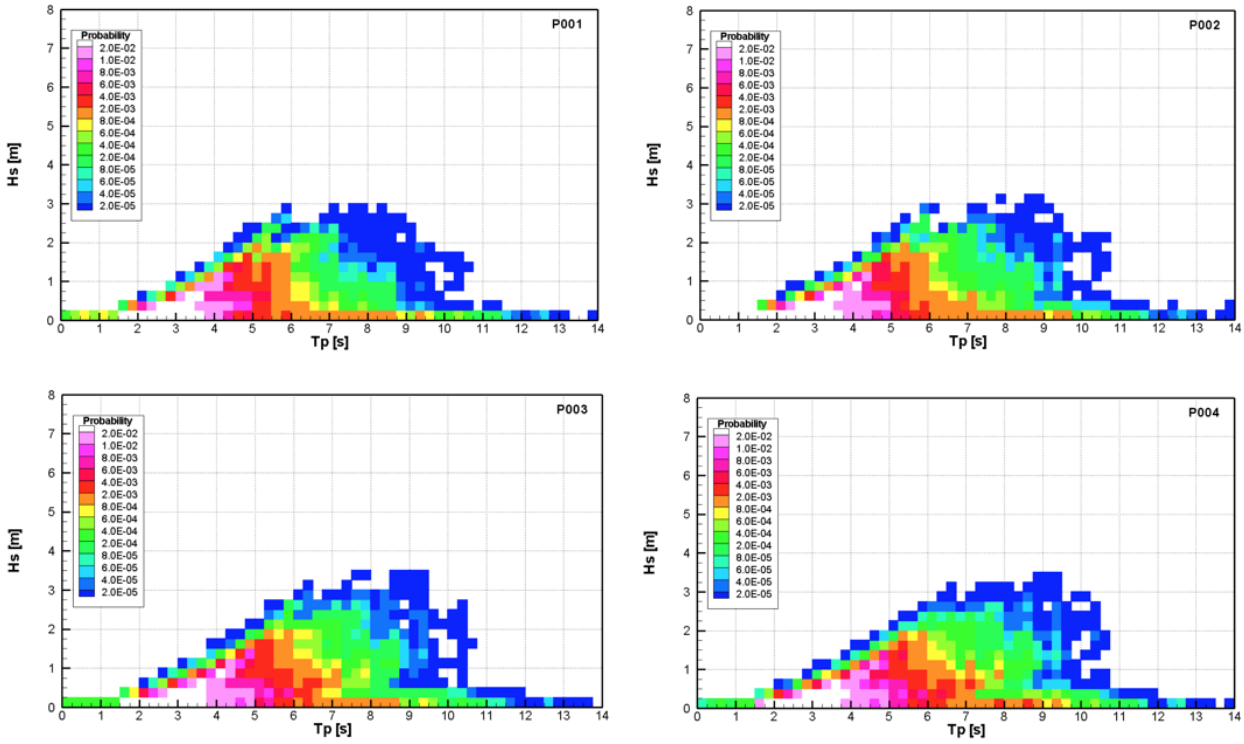

Figure 3.4: H_S-T_P scatter diagrams

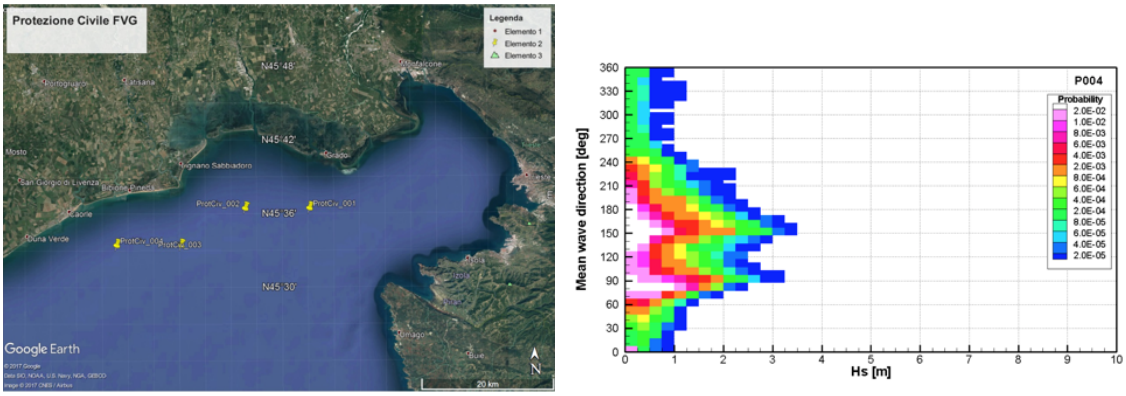

(a) POI map

(b) H_S-Direction scatter diagram

Figure 3.5: POI map and direction scatter diagram for P004

3.2.3 Standard seakeeping trial layout

Starting from the documents specified earlier, the seakeeping trials consist in a sequence of courses with specific encounter angles so that all relevant cases of wave-ship encounter are covered in one cycle, minimizing the distance of the ship from the deployed wave buoy. An example, taken from [74], regarding the sequence of courses for a trial planned for frigate at 20 knots. is shown in figure 3.6.

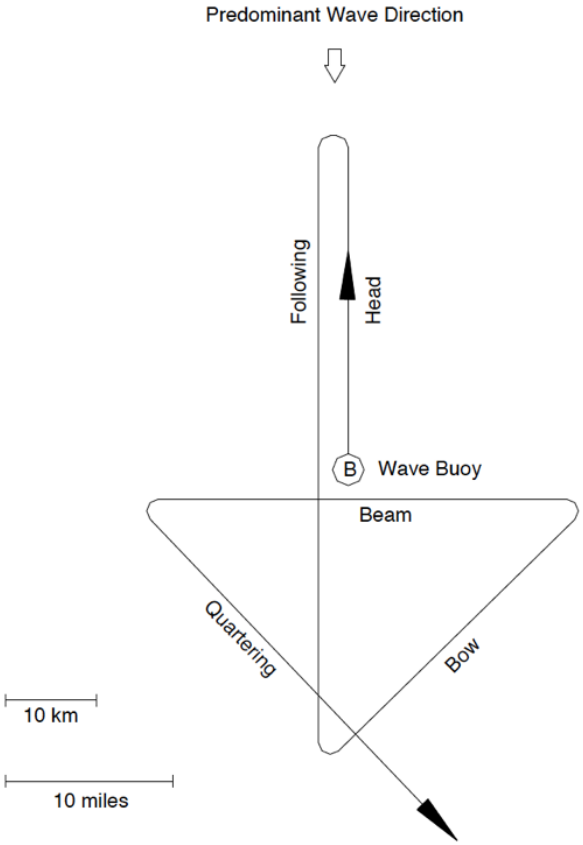

Figure 3.6: Sequence of courses for full-scale seakeeping trials, as suggested by Lloyd [74] and ITTC[83]

3.2.4 Wave buoy measurements schedule

The measurement of wave elevation will be performed using the fixed “DWRG1" wavebuoy and a second mobile wavebuoy, launched at the begininning of the tests. The Measure of the directional wave spectra is carried out by the mobile and fixed wavebuoy according to the following scheme:

- The wave buoy start sampling every half an hour, according to the UTC time (hh:00, hh:30 and so on) for a duration of 20 minutes..

- After the sampling phase, data will be analysed on the buoy itself during the 10 minutes remaining before the start of the new sampling window.

3.2.5 Environmental measurements

If possible, as suggested by the ITTC, the wind direction and speed should be measured during the tests. As a first approximation, the environmental readings onboard the fixed buoy "PALOMA" in the gulf of trieste can be used as source.

3.2.6 Requirements

The requirements for full-scale seakeeping tests can be very different depending on the particular needs of each of the parties involved (shipyard and research institution in this case). In particular, ship motions would be ideally measured in the following curses:

- Head sea ($\chi = 180°$): Head
- Following sea ($\chi = 0°$): Following
- Bow sea ($\chi = 225°$): Bow
- Beam sea ($\chi = 90°$): Beam
- quartering sea ($\chi = 315°$): Quartering

Where χ is the angle between ship heading and wave direction. In order to have a better statistical representation of the motions, ITTC guidelines suggest that a minimum of 100 wave encounters are necessary for every test run.

3.2.7 Test sequence study

The guidelines found in the literature refer to the situation in which only one wavelength buoy is present in the test area. In the case in question, as previously illustrated, there will be two buoys on the test area, one of which is fixed and one can be positioned according to the direction of the incoming sea.

The standard test route was taken into consideration in the presence of the two buoys and is shown in Fig. 3.7a. This type of route was originally designed to offer more space for trials where the wave comes from the stern and to minimize the distance from the single buoy. Furthermore, the route ends at a different point from the initial one, far from the buoy. For these reasons, this solution was considered to be inadequate to our needs. The scheme has therefore been adapted to make the circuit repeatable without the need for a transfer to the initial position at the end of the test. The adapted route is shown in Fig. 3.7b.

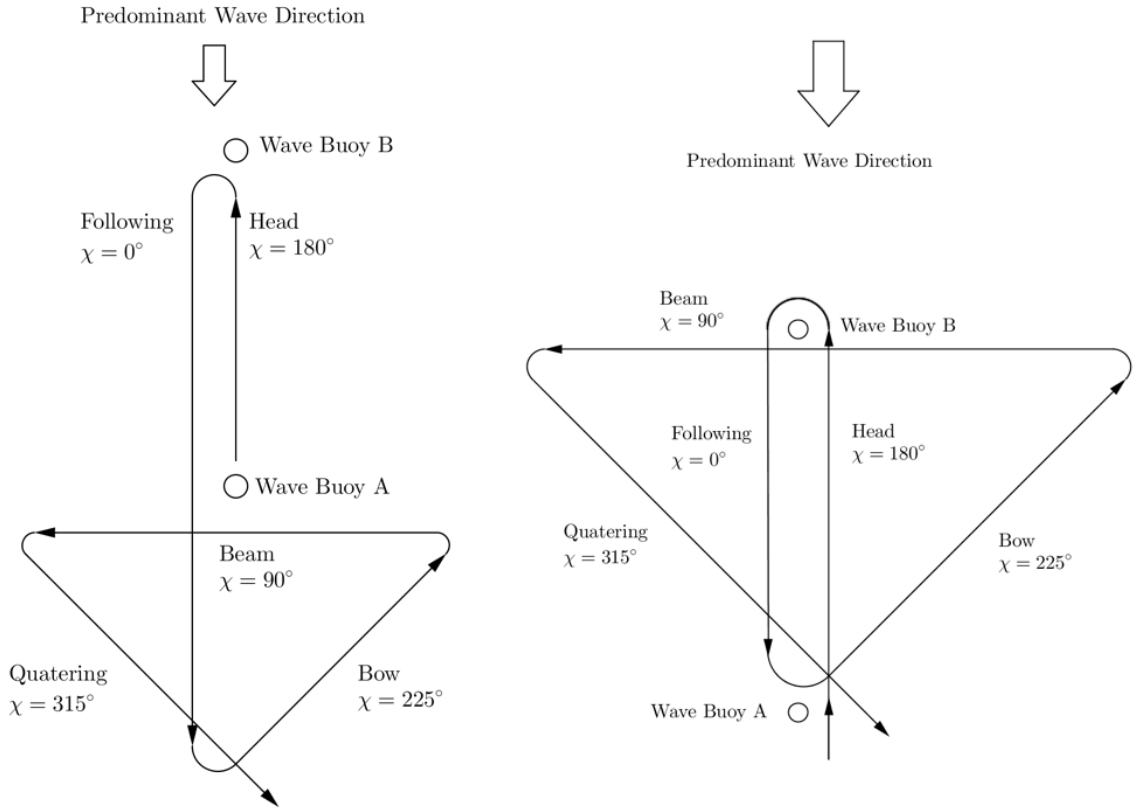

(a) Standard sequence

(b) Modified sequence

Figure 3.7: Sequences considered during planning

However, even in this case there was a flaw from the point of view of the effectiveness of the test, namely the excessive length of the beam sea course.

The solution adopted to remedy this flaw was to divide the bow sea course in two parts, the first with sea on the port side and the second on the starboard side. In this way, the length of the section with the cross beam was halved. The choice of the route therefore fell on the latter case, shown in Fig. 3.8.

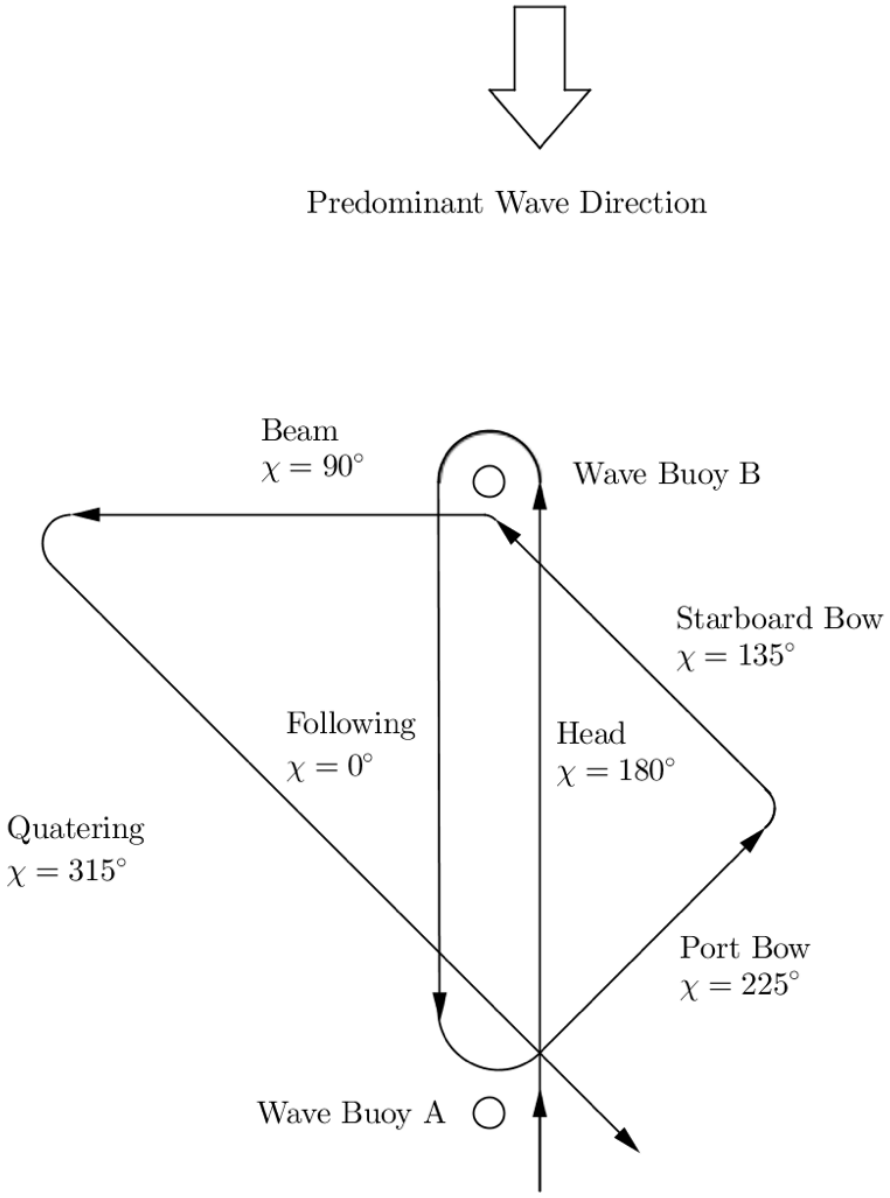

Figure 3.8: Final sequence

$V = 18$ kn	χ	**Distance between wave buoys**			
		2 nm	3 nm	4 nm	5 nm
Head	180°	175	278	381	454
Following	0°	-24	-38	-52	-66
Bow	225°	217	338	460	581
Beam	90°	75	120	164	208
Quartering	315°	7	11	16	20

Table 3.2: Number of wave encounters at $V = 18$ kn and $T_w = 4.5$ s.

$V = 25$ kn	χ	**Distance between wave buoys**			
		2 nm	3 nm	4 nm	5 nm
Head	180°	143	234	324	415
Following	0°	-42	-68	-95	-121
Bow	225°	177	280	384	488
Beam	90°	50	82	114	146
Quartering	315°	-22	-36	-49	-62

Table 3.3: Number of wave encounters at $V = 25$ kn and $T_w = 4.5$ s.

3.2.8 Wave encounters

In order to evaluate the distance between the buoys, and therefore the length of the sections of the chosen route, the number of wave-ship encounters in the various sections was assessed. The table 3.2 relating to races with speeds of 18 knots shows the number of wave matches as a function of the ship-wave angle χ and of the distance between the two wave buoys. In the same way in table 3.3, the values are reported for a speed of 25 knots.In both cases, the considered wave period is equal to 4.5 s.

It can be seen how, in the case of waves with a 4.5 second period, in the quartering sea course leg at 18 knots, the waves overtakes the boat (overtaking sea), highlighted by positive values in the number of encounters. In the case of 25 knots, the same leg has negative values and therefore the boat overtakes the waves (following sea).

The number of meetings per way was evaluated considering a margin of 60 seconds necessary to accelerate and obtain the desired speed in a stable manner.

Evaluating the the tabular results, the alternative with a distance of 2 miles was not chosen due to the fact that for most of the routes the number of encounters is well below the value recommended by the ITTC. Alternatives with 4 and 5 mile distances, on the other hand, proved to be too expensive in terms of execution time (i.e. at least 3 buoy recordings).

The choice therefore fell on the 3 miles distance as the duration of the route, calculating all the margins, is 63 minutes (at 18 kn), that is about two measurement windows of the buoy. This guarantees greater confidence in the stability of the sea state during an entire sequence.

3.2.9 Tests scheduling

Given the acquisitions time frame of the wave buoy, it was considered useful to create a test scheduling script based on the duration times of the different sequence legs.

The resulting diagram (Fig. 3.9) of this approach makes it easy to evaluate the time required for a given set of tests. Should there be any delays, the scheme simply moves to the next useful buoy acquisition window (vertical dotted lines).

The proposed scheduling consists of the following operations:

- Arrival at wave buoy (A) "DWRG1" and measuring ship motions at zero speed for the duration of a buoy acquisition window;
- Start of the head sea leg at 18 kn up to the launch position of the second mark (B), measurement of ship motions and power; [t=0:00]
- Wave buoy (B) launching ; [t=0:15]
- Measure ship motions at zero speed for the duration of a buoy acquisition window; [t=0:30]
- Return to buoy (A) at 18 kn, following sea leg; [t=1:00]
- Round trip (A-B-A) at 18 kn; [T=1: 30]
- Measure ship motions at zero speed for the duration of a buoy acquisition window; [T=2:00]
- Complete five legs of the sequence at 18 kn; [T=2:30]
- Measure ship motions at zero speed forthe remaining time of the buoy acquisition window; [T=3:40]
- Complete five legs of the sequence at 25 kn; [T=4:00]
- Departure with head sea at 25 kn up to the position of the second mark (B); [T=5:00]
- Recovery of the buoy (B); [T=5:20]
- Return to buoy (A) at 25 kn, following sea leg; [T=5:30]
- Return to the shipyard.

During measurements at zero speed, the boat will be positioned with different ship-wave angles.

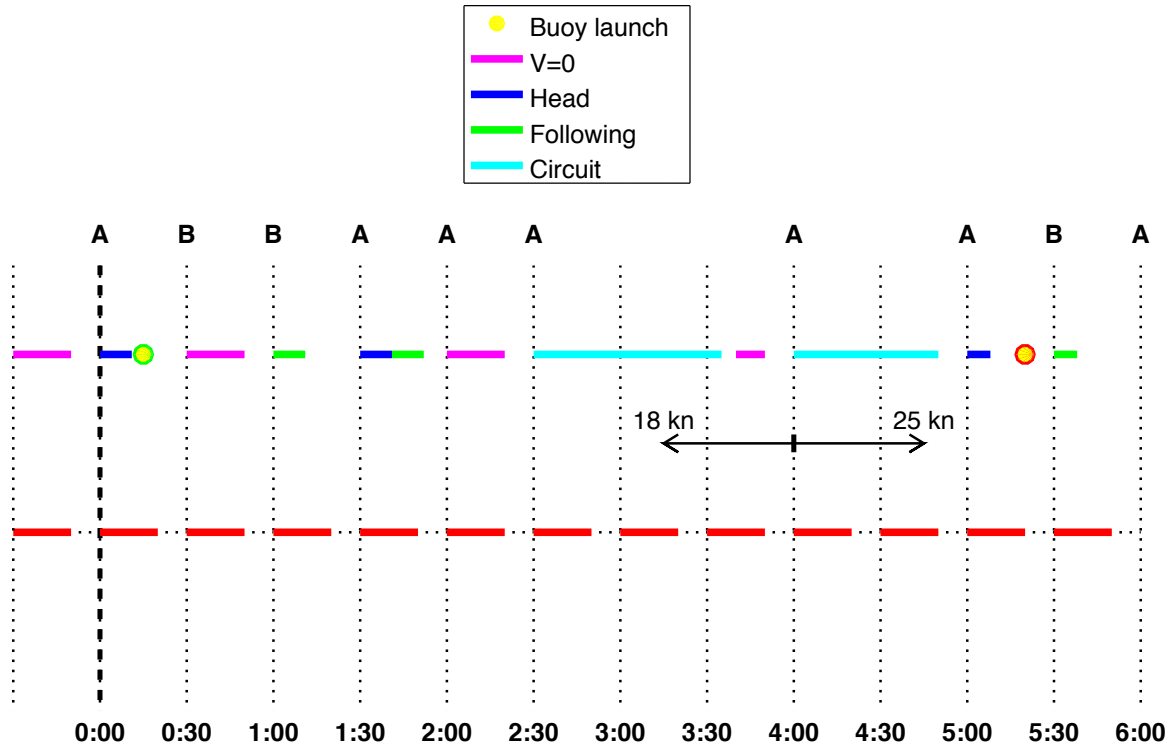

Figure 3.9: Proposed test scheduling

3.2.10 Specific tests

Since the tested yacht has an active stabilization system (seakeeper) installed, further measurements can be made in order to evaluate the effect of the apparatus.

Also in this case, some guidelines are issued by the ITTC, advising that once the test leg has been chosen, the test is divided into three parts. The first and last part in which the system is deactivated and the central part in which the system is activated. The central part is of equal duration compared to the other two.

It is important to point out that this procedure is not necessarily suitable for a fast boat with relatively short sequence legs at disposal. The reason for this method derives from the need to check that during the test the sea conditions have not changed considerably. Furthermore, in the analysis phase, the stabilization system action could be highlighted more clearly if a single time series is recorded for both on and off states.

The proposed three part procedure is also not very practical in this particular case since the apparatus in question relies on a gyroscopic stabilization using a gimballed spinning disk. This beacause the stabilizing disk can takeupwards of 20 min to reach the design RPM, and even longer to stop itself by coasting.

3.3 Sea state measurements

A directional Datawell Waverider DWR-G4 buoy (diameter = 0.4 m, weight = 170 N), moored in the sea-trial area, was used as main source of wave information. North, West and vertical (heave) displacements are measured through a GPS-based motion sensor with an accuracy of 1.0 cm in all directions and with a sampling frequency of 1.28 Hz. The GPS technology supersedes the need for calibration of accelerometer and compass based sensors and it is not affected by spinning or manual handling. One potential disadvantage is that wave wash on the GPS antenna or extreme tilting could mask the signal. This only happened sporadically and for a few seconds during the whole deployment time. As a 30 min logging windows of the time series were considered, signal masking did not represent an issue.

Wave properties expressed in directional spectral form are given as energy and mean wave direction for each frequency f_i, with $i = 1, \ldots, N_f$. In this study, $N_f = 64$, $f_1 = f_{min} = 0.025\,Hz$, $f_{N_f} = f_{max} = 0.580\,Hz$ and Δf is here defined as follows:

$$\Delta f = \begin{cases} 0.005\,Hz & \text{if } f < 0.1\,Hz \\ 0.010\,Hz & \text{if } f > 0.1\,Hz \end{cases} \tag{3.1}$$

The synthetic information derived from the buoy is summarized in the Table 3.4.

Table 3.4: Standard output of a directional wave buoy DWR.

Wave frequency	f	$[Hz]$
Spectral density	$S_\zeta(f)$	$[m^2 Hz^{-1}]$
Wave direction	$Dir(f)$	$[deg]$
Directional spread	$Spr(f)$	$[deg]$
Directional skewness	$Skew(f)$	$[-]$
Directional kurtosis	$Kurt(f)$	$[-]$

Fig. 3.10 shows a standard 1D wave spectral density $S_\zeta(f)$. In particular, this sample case refers to the *Run* 2 of Table 3.1, characterized by a very narrow-band, single-peak sea state.

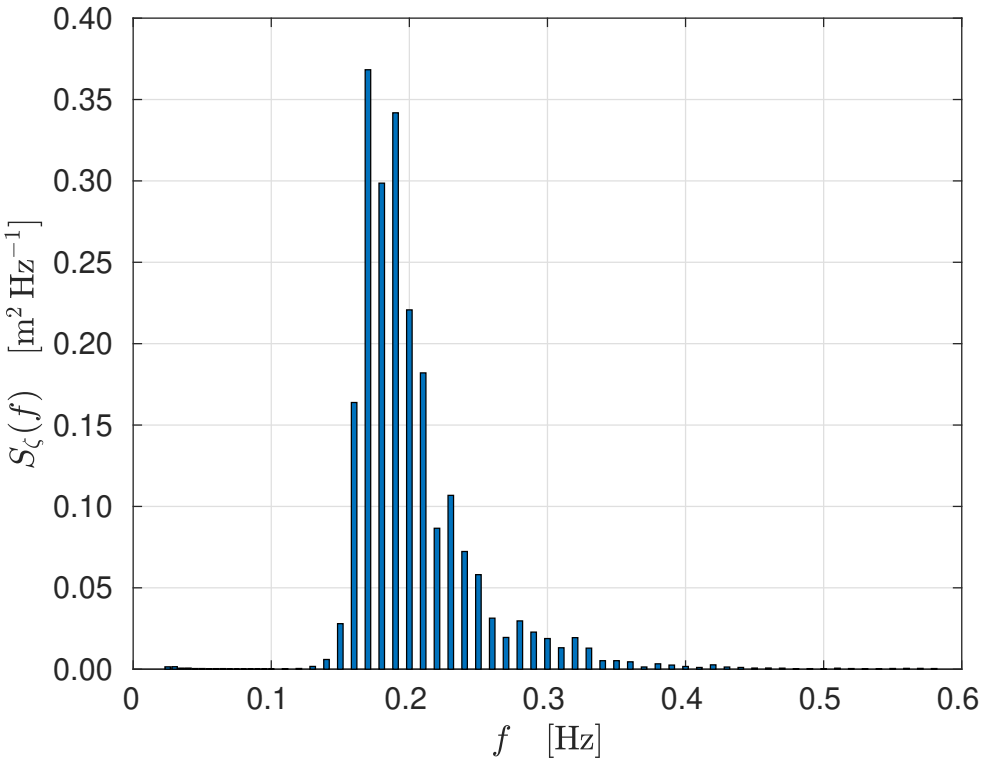

Figure 3.10: Wave power spectral density data from the wave buoy.

3.4 Loading condition measurements

The yacht loading condition is assessed every test day. Three measurements are carried out by hand. In particular, the depth of the starboard and portside aft end of the chines and the distance between the water surface and the bow end of the chine. The measured depths and distance will be used to define the actual waterplane and then the loading condition parameters computed computed using Orca3D plugin (see Fig. 3.11).

The comparison between full scale and model (scaled) displacement and longitudinal centre of gravity is shown in Tab. 3.5. It is worth noting that full scale data is subject to errors due to measurements accuracy. The waterline measurements have been carried out from a small rib using tape measure.

	full scale	model (LC1)
Displacement, kg	41748	40587
LCG, mm	6670	6742

Table 3.5: Comparison between model and full scale loading condition

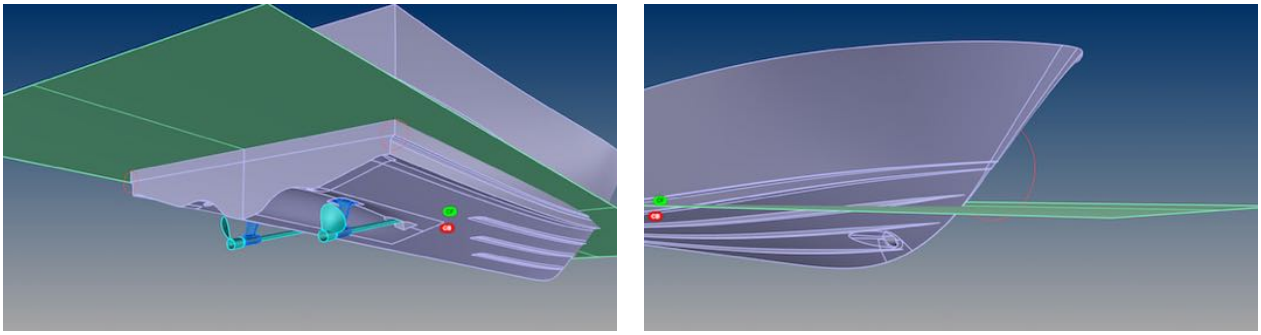

(a) Aft measurement point

(b) Bow measurement point

Figure 3.11: Actual waterline measurement spots for the loading condition assessment

3.5 Ship motions measurements

The onboard measuring system for ship motions consisted in 3 Xsens Inertial Measurement Units (IMU) and additional Global Navigation Satellite System (GNSS). The Inertial Measurement Units are able to output body orientation data using three axis MEMS accelerometers, three axis gyro and three axis magnetometer built in the case. A sensor fusion algorithm uses the data from all the sensor in order to reduce noise and improve accuracy in the output of the orientation data. In particular, IMU1 and IMU2 are Xsens MTi-G-700 have an extra SMA connector to allow a 72 channel GNSS receiver (GPS, GLONASS, BeiDou and Galileo) antenna to be attached (see Fig. 3.12a), this allows for additional synchronized position and speed tracking during the sea trials. The combined GNSS/IMU solution is tipically referred as INS (Inertial Navigation System).

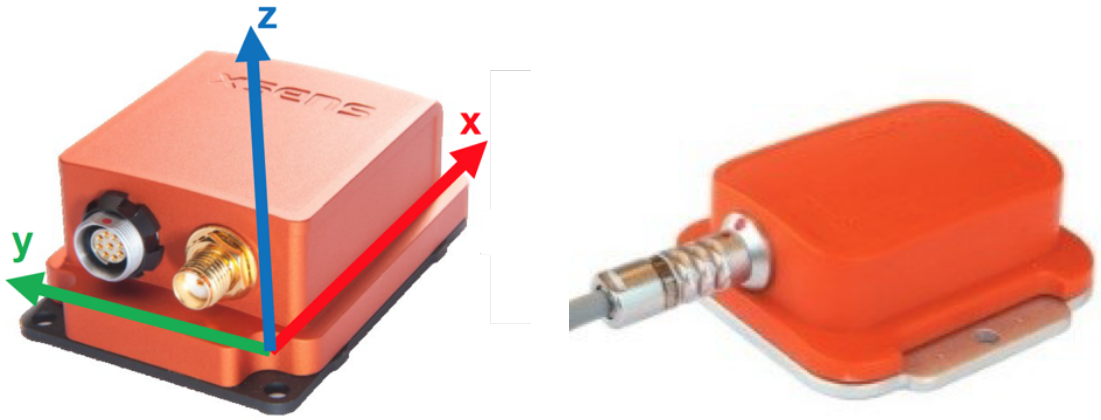

(a) Xsens MTi-G-700 Inertial measurement system (IMU1 and IMU2)

(b) Xsens MTi-300 Inertial measurement system (IMU3)

Figure 3.12: Onboard IMUs

Orientation, gyro and acceleration data from the IMUs are computed using the sensor-fixed output coordinate system seen in Fig. 3.12a. In order to be have correct roll, pitch and yaw readings, IMU1 has been carefully placed in the CG of the yacht, making sure that the sensor-fixed X axes is aligned to the yacht centerline.

The GNSS reciever of IMU1 was taped to the master bedroom portside porthole (see Fig. 3.16a), the one connected to the IMU2 to the starboard porthole in order to ensure the best satellite coverage possible. The position data from the GNSS receiver is represented in latitude and longitude in the WGS84 datum and logged using Earth Centered – Earth Fixed (ECEF) format. Another important factor is that IMU1 and IMU2 both share an UTC timestamp that is provided by their GNSS data packet, IMU3 does not.

The proprietary acquisition system of the IMU samples accelerations, rate of turn and compute Euler angles at 100 Hz whereas GNSS data are sampled at 4 Hz. The sensor fusion algorithm uses acceleration, magnetic and gyro data to interpolate latitude,longitude, speed and course data between two consecutive GNSS fix.

IMU1 was positioned at the center of gravity (CG), IMU2 at the same longitudinal position of CG but at starboard and IMU3 in the middle of the bow cabin (see Fig.3.13 for the layout).

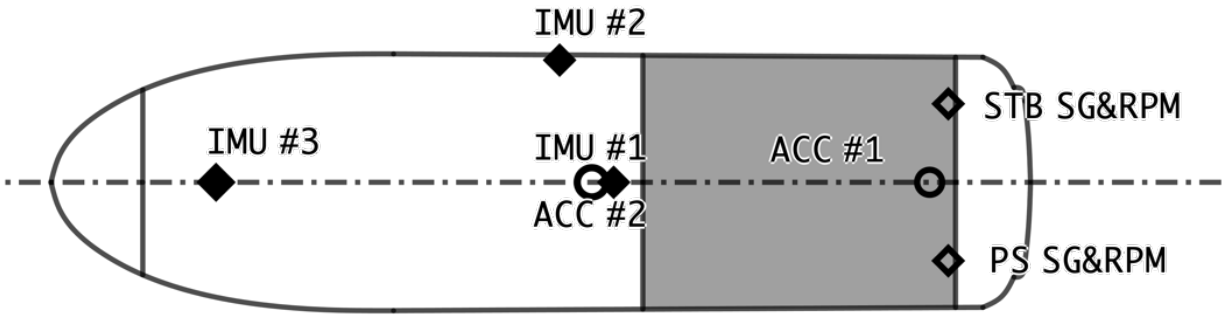

Figure 3.13: Onboard measuring systems layout

The data used in the full-scale data analysis is from IMU1 only, the most used data fields, out of the 52 avalaible are listed in table 3.6.

In Fig. 3.14, images of the onboard IMUs and accelerometers are shown.

Variable		Dim.	Variable		Dim.
`UTC_Nano`	elapsed nanoseconds	(s^{-9})	`Pitch`	Pitch	$(°)$
`UTC_Hour`	elapsed hours from 00:00	(h)	`Roll`	Roll	$(°)$
`UTC_Minute`	elapsed minutes from last hour	(min)	`Latitude`	Latitude	$(°)$
`UTC_Second`	elapsed seconds from last minute	(s)	`Longitude`	Longitude	$(°)$
`Acc_X`	raw X-axis acceleration	(m/s^2)	`Vel_X`	X-axis velocity	(m/s)
`Acc_Y`	raw X-axis acceleration	(m/s^2)	`Vel_Y`	Y-axis velocity	(m/s)
`Acc_Z`	raw X-axis acceleration	(m/s^2)	`Vel_Z`	Z-axis velocity	(m/s)

Table 3.6: Most used IMU data fields

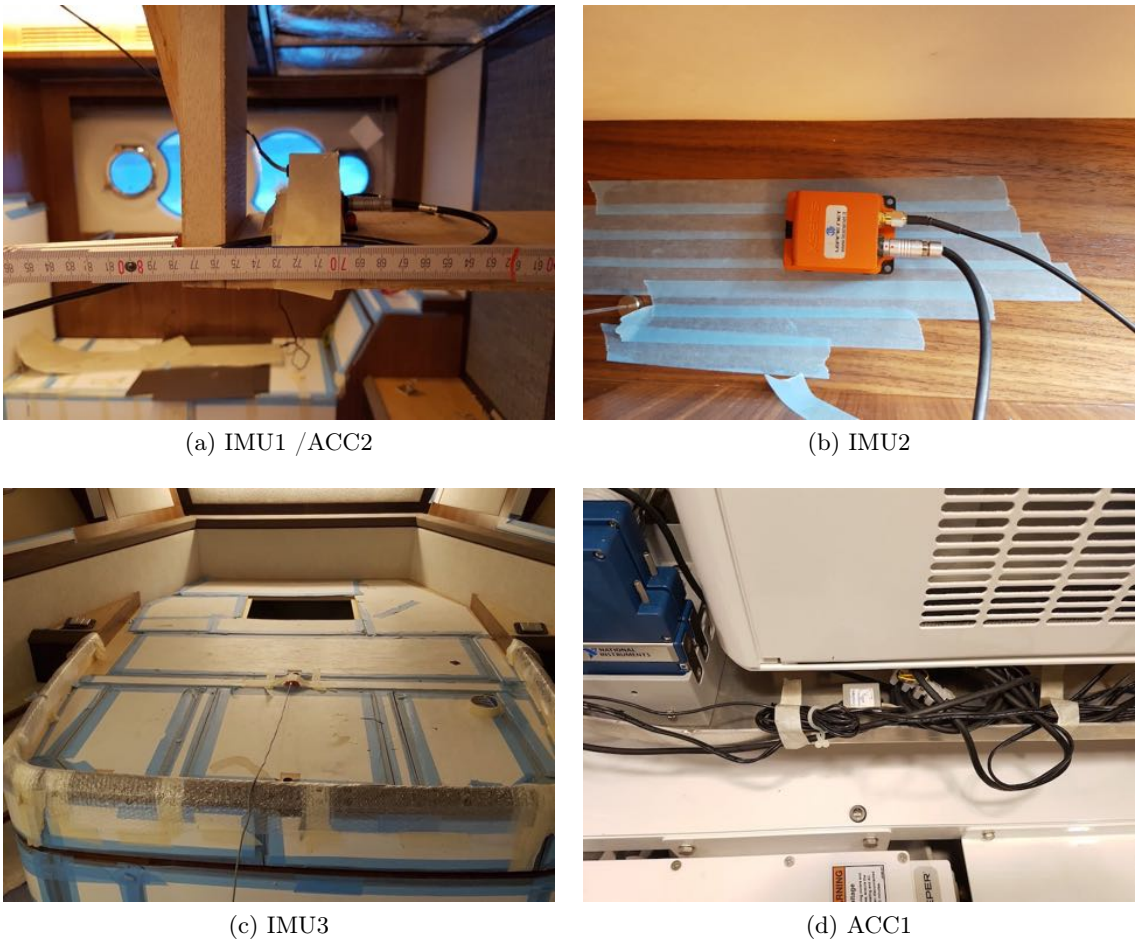

(a) IMU1 /ACC2

(b) IMU2

(c) IMU3

(d) ACC1

Figure 3.14: Motion measuring system

The positions of both onboard IMUs and accelerometers have been checked using the actual CAD model of the yacht (Fig. 3.15)and are the following:

	Item	X (mm)	X (mm)	X (mm)	Position	ID
IMU1	7003	0	60	2037	CG	07700902
IMU2	8061	-2198	59	1592	Center-STB	0770015C
IMU3	14750	0	60	1890	Bow Cabin	00301032
ACC1	3022	56	54	1509	Engine Room	-
ACC2	17003	0	43	2047	CG	-

Table 3.7: Coordinates of onboard IMUs and accelerometers

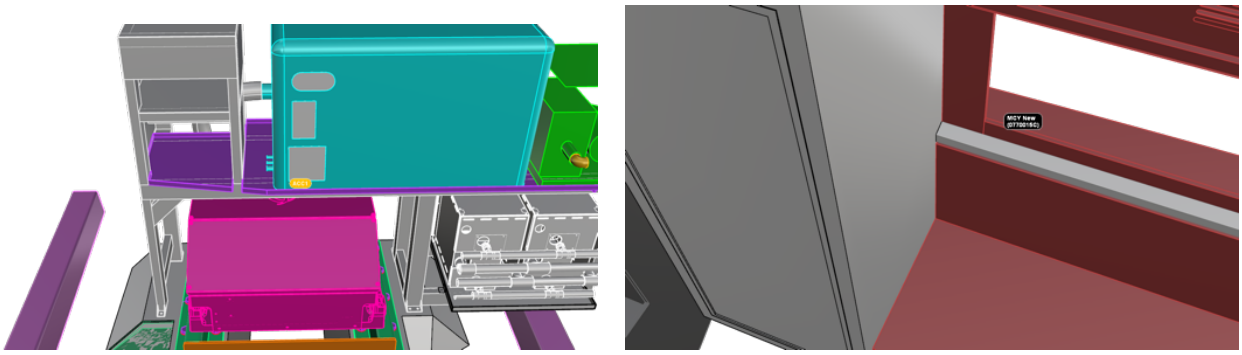

(a) ACC1 (Engine Room)

(b) IMU2 (id:0770015C) (Center-STB)

Figure 3.15: Examples of the CAD model used for the placement of the sensors

In order to place IMU1 and ACC2 in the actual yacht CG, an ad-hoc wooden structure has been fixed to the master bedroom roof as it can be seen in Fig. 3.16a. All three IMU were connected to a PC (Fig. 3.16b) in the master bedroom that managed the monitoring and logging of the data in proprietary binary files. The logging frequency is 100Hz for all three IMUs, after being processed by the sensor fusion algorithm (IMU1 and IMU2) or Kalman filter (IMU3). The log files are then exported in ASCII comma separate values for the data analysis.

(a) Wooden structure for IMU1 and ACC2 positioning

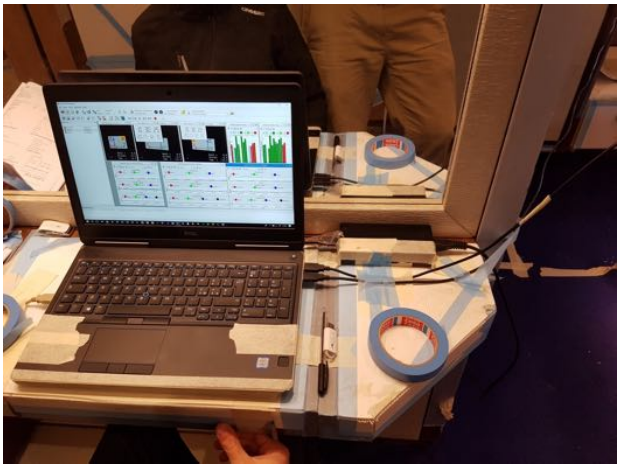

(b) PC used for IMU monitoring/acquisition

Figure 3.16: Master bedroom setup

3.6 Ship propulsion measurements

During the sea trials, one of the project goal was to not only monitor and log attitude and motion of the yacht but also the propulsion characteristics. The measure or monitoring of the propulsion onboard ships is carried out by measuring the torsional deformation and rotational speed of the propeller shaft. Once the deformation is assessed, shaft torque is computed using the shaft's mechanical properties, in particular, its shear modulus G (N/m^2):

$$G = \frac{E}{2(1+\nu)} \tag{3.2}$$

Where E is the Young's modulus and ν is the Poisson's ratio. For a circular shaft subjected to an external torque T, the angular displacement γ is:

$$\gamma = \frac{TD}{2GI_P} \tag{3.3}$$

Where I_P is the shaft section polar moment of inertia and D its outer diameter. The shaft linear strain ϵ (measured by the strain gauge) is related to the angular displacement γ and the angle respect to the shaft axis α:

$$\epsilon = \frac{\gamma sin(2\alpha)}{2} \tag{3.4}$$

In order to measure shaft strain, a set of strain gauges (rosette) are placed on the shaft surface to form a Wheatstone bridge circuit as shown in Fig. 3.17. In order to maximise the measurement resolution (measured strain), the strain gauge rosette is oriented at a 45 degree angle respect to the shaft axis. The deformation of the shaft induces a resistance change in the strain gauge bridge that is then converted to a frequency modulation ready to be transmitted. The deformation

measurements are then transmitted from the shaft to the acquisition system via a UHF radio transmitter. The receiver then convert the signal to a ±10 V analog signal fed into a Binsfeld TorqueTrak 9000 Digital Telemetry System that handle the actual measurements. The bridge input voltage is delivered from a shaft-fixed 6LR61 battery that also powers the transducer.

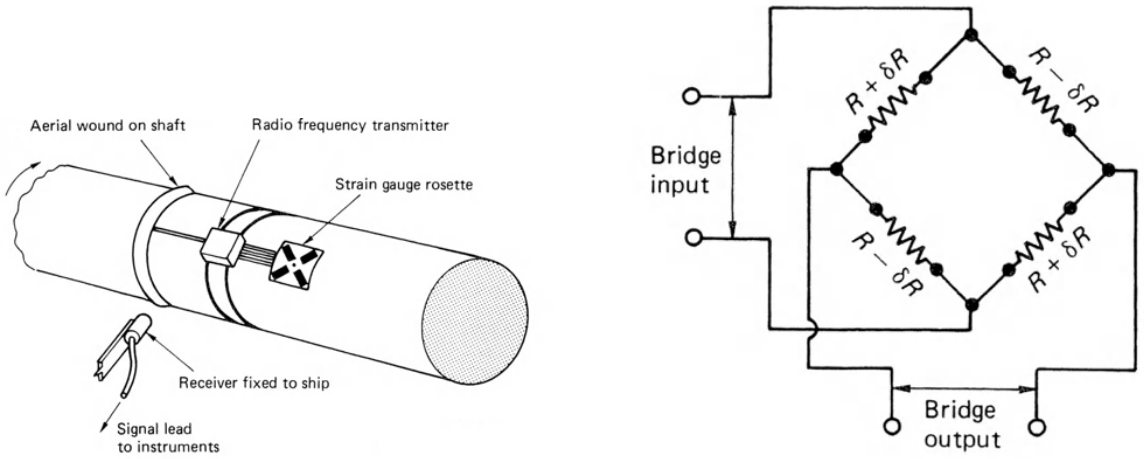

(a) Strain gauges placement

(b) Strain gauges circuit

Figure 3.17: Use of strain gauge for shaft deformation measurements, from [85]

The actual system used in the sea trials is shown in Fig. 3.18. The strain gauge rosette (yellowish patch in Fig. 3.18a) is applied to the shaft using cyanoacrilate glue and wired to the transducer, fixed to the shaft via multiple layers of insulating and glass fiber reinforced tape (see Fig. 3.18a). The battery is placed opposite to the transducer/transmitter for weight balancing.

The measurement of the angular speed of the shaft is carried out using a proximity sensor fixed to the boat and a split ring containing 12 equally spaced bolts as seen in Fig.3.18b . The proximity sensor is then aligned to the hex socket cap of the bolts in order to ensure a clear output signal. The pulse frequency of the output signal is then converted to angular frequency of the shaft.

(a) Attaching gauges rosette

(b) Completed shaft measurement system

Figure 3.18: Assembling the onboard shaft measurement system

All the measure signals are synchronized and resampled by a compact DAQ-9188 acquisition module and transmitted to a PC using a dedicated LabView monitoring framework. The signals are sampled by the acquisition module at 1kHz and later downsampled to 100Hz.

In addition to the shaft measurements, two Cross Bow CXL04GP3-R-AL three axis MEMS accelerometers are also sampled. One accelerometer is placed at the yacht's CG, directly over the IMU1 (ACC2, see Fig. 3.19a). The second accelerometer is placed in the engine room at the base of the generator set (ACC1, see Fig. 3.19b) .

(a) ACC2 accelerometer at the CG

(b) ACC1 accelerometer in the engine room

Figure 3.19: Accelerometers placement

The propulsion measurements output is a comma separate values ASCII file containing fol-

lowing the following data:

data	unit
time	(s)
shaft rotation	$(s^{-}1)$
shaft torque	(Nm)
acceleration	g$(-)$

Table 3.8: Propulsion measurement system output data

Shaft rotation and torque output is divided for starboard and portside propeller shafts, and acceleration data is divided for both accelerometers and all three components.

In order to be able to syncronize the motion database to the propulsion database, ACC2 accelerometer has been placed directly on top of the IMU1. In the post-processing phase, the raw accelerometer signal from the IMU will be compared to the signal from the ACC2 accelerometer and used to compute the delay between the timecodes of the two databases.

Both IMUs and accelerometers have been attached to the yacht structure using removable adhesive strips and tapes since the test yacht was already finished and ready for the delivery. This anchoring method not suitable for shocks and vibration specific measurements, but were adequate for our case, where rigid body motions were the main objective. Inertial forces due to heave and pitching are negligible respect to restraining forces from the adhesive strips and tapes since they are relative low frequency motion.

3.7 Integrated analysis

3.7.1 Introduction

The correlation between full scale and predicted seakeeping performances of a vessel and its validation are still open problem. In particular, the available literature on the correlation between theoretical or model scale experimental predictions and full scale results of a planing hull in waves is somewhat limited. The estimate of full scale transfer function *TF* is not common practice, especially for pleasure yachts and planing craft in general. Within the limitations of the linear approach behind the concept of *TF*, the availability of their estimates may be source of multiple benefits, such as validation of design methods and operational procedures based on the coupling between wave forecast models and ship *TF*, the so-called ship response forecast.

Among the data needed to compute *TF*, the absolute and encounter wave spectra from measurements play a fundamental role. Basic procedures for calculating the encounter frequency wave spectrum from combined sea state and ship motions measurements, generally rely on the simplifying assumption of unidirectional waves, thus neglecting at first stage the actual wave spreading or even multiple peak directional spectrum. This approximation is largely due to the difficulties in obtaining reliable directional wave spectra from full scale measurements. Still, it is acknowledged that the directional distribution is a major feature for the reliability of the final result.

As for the representation of the sea state in terms of directional wave spectrum, significant

advances in measurement techniques were made during the last two decades and a number of devices working on different principles are now available. Still, the inherent difficulties related to measuring and analysing directional wave spectra have not been completely solved yet. Standard techniques provide partial information on the directional spectrum, but they do not provide a robust estimate of the full directional spectrum. In particular, measurements from standard directional wave buoys allow the calculation of the directional spectrum if additional assumptions are made, which in turn are based on specific mathematical models for the directional distribution. These assumptions can significantly influence the resulting wave spectrum and its derived quantities, such as TF in the present case.

In this section the results of the the seakeeping trials will be presented, by means of the proposed integrated analysis used to process the data. Due to time constraints, the focus of the seakeeping trials has been to get as many head sea measurements as possible. Consequently, the results here presented are relative to the case of head-sea. Head sea state has been a prioritized because it is the most demanding condition for this type of craft, and also because model data is available only for this condition.

The aim of this procedure is to compute realistic full scale heave and pitch transfer functions TF using the proposed general integrated analysis. A focal point in the consistency of the results is found in the influence of the quality of the reconstructed directional wave spectrum derived from the output data of a directional wave buoy.

3.7.2 Method overview

The integrated analysis that leads from the measurements of the sea state and vessel's motions to the estimation of the TF is sketched in Fig. 3.20. The proposed methodology combines multiple sources of data into a single framework, specifically a wave buoy, onboard IMU and a bathymetry grid. In Fig.3.20, wave-related info are marked in blue whereas ship motion-related info are marked in red.

Starting from standard output of the directional wave buoy (wave energy, mean direction, directional spreading, skewness and kurtosis), the directional wave spectral density $S_\zeta(f, \varphi)$ is computed first, using specific models that take into account the frequency-dependent directional spreading and reconstruct the whole directional wave spectrum. On the other hand, mean values of ship course, speed and water depth along the run are calculated from the ship motion data . Those values are then used in combination with the reconstructed directional wave spectum to compute the directional encounter frequency wave spectrum.

Once the directional encounter frequency wave spectrum is computed, the heave and pitch forcing spectra can be obtained by means of simple integration. Heave and pitch response spectra can also be computed, using the data provided by the IMU. Finally TF of heave and pitch in head sea can be computed for every run. As a last step, the final TF are obtained averaging the results of each run.

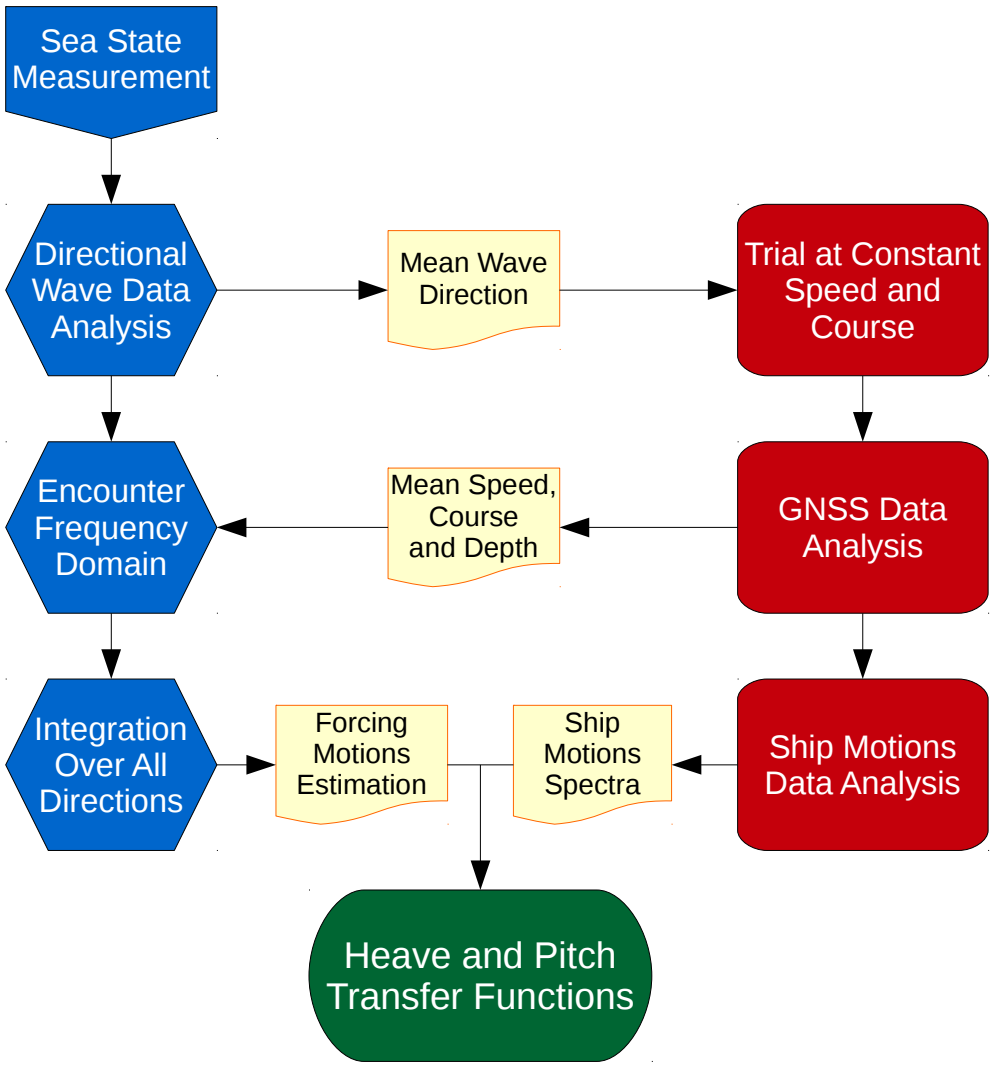

Figure 3.20: Basic flow chart of the proposed integrated analysis.

3.7.3 Mean speed course and depth

Since Xsens proprietary sensor fusion algorithm interpolates also GNSS data, the GNSS fix status flag was used in order to extract non-interpolated location information in order to avoid interpolation issues. For each run, ship mean speed and course are calculated using non-interpolated GNSS data. Once the run is concluded, the GNSS data subset is extracted from the IMU dataset.

Ship speed over ground (SOG) is computed by first order approximation, as the ratio between

the distance along a great circle calculated using the haversine (Sinnott [86]) formula:

$$a = sin^2\left(\frac{d}{2R}\right) = sin^2\left(\frac{\Delta\phi}{2}\right)\sin(\phi_1)\cos(\phi_2)sin^2\left(\frac{\Delta\lambda}{2}\right) \tag{3.5}$$

the great circle is then:

$$d = 2R\arctan\left(\sqrt{a}, \sqrt{1-a}\right) \tag{3.6}$$

Ship course over ground Θ is computed as the initial bearing for a great-circle route between two consecutive points:

$$\Theta = \arctan\frac{\sin(\Delta\lambda)\cos(\Delta\lambda)}{\cos(\phi_1)\sin(\phi_2) - \sin(\phi_1)\cos(\phi_2)\cos(\Delta\lambda)} \tag{3.7}$$

where ϕ_1 and ϕ_2 are initial and final latitude, $\Delta\lambda = (\lambda_2 - \lambda_1)$ is the difference in longitude, $\Delta\phi = (\phi_2 - \phi_1)$ the difference in latitude and $\Delta t = (\phi_2 - \phi_1)$ the difference in latitude. SOG and Θ are derived at the GNSS sample rate (4 Hz). The last parameter required by the procedure is the mean water depth d along the run. The North Adriatic basin bathymetry (the same used by HyMOLab for wave modelling and forecasts) with a grid resolution of 0.01° (lat/long) is here used and interpolated along the track of every run. Water depth changes induced by tides (of order of 10^{-1} m) are here neglected.

Averaged values of SOG, Θ and d for each run are then ready to be used for the computation of the actual encounter spectra. Fig. 3.21 shows a typical time series of boat course, speed and depth resulting from the above procedure, along with the data window detail (vertical lines).

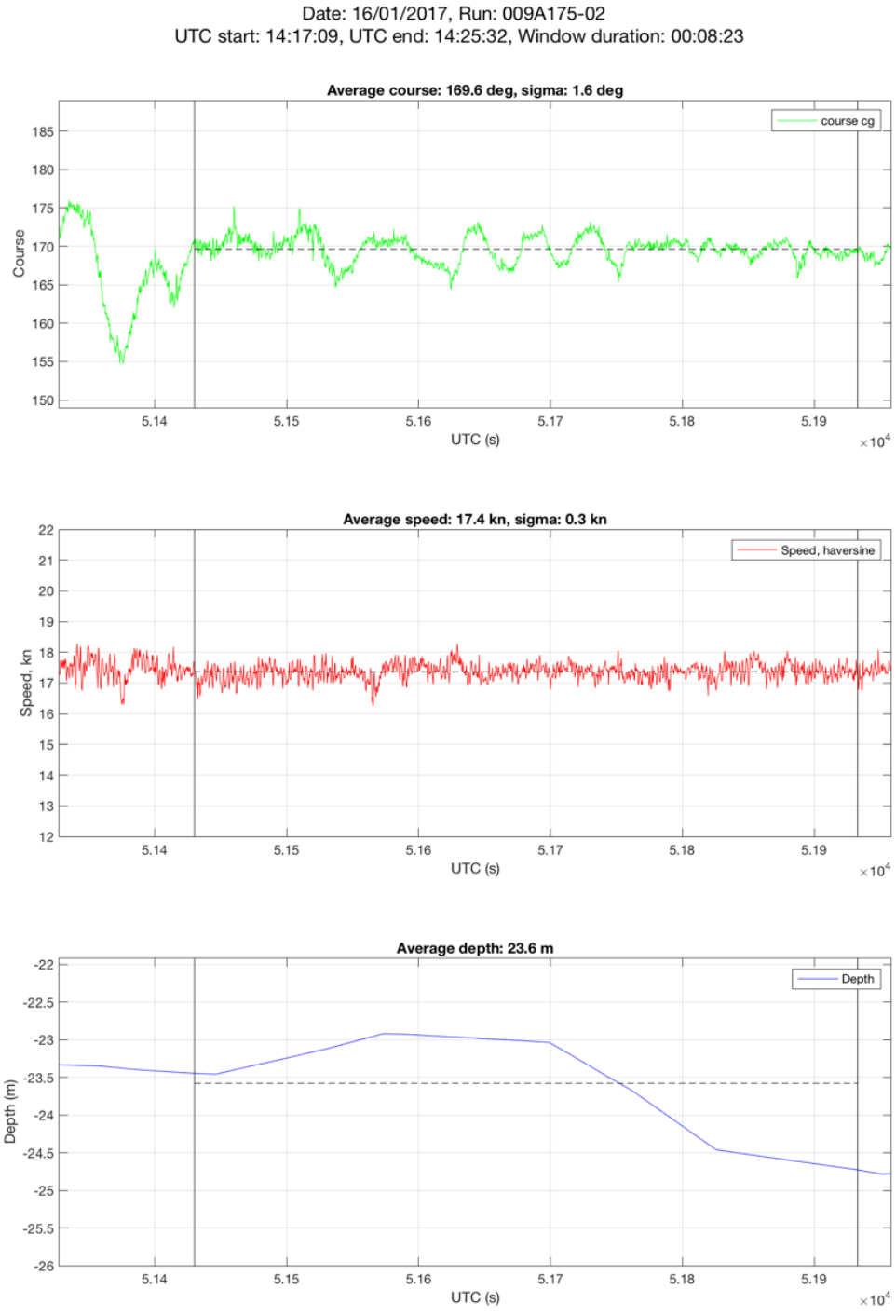

Figure 3.21: Example of SOG, Θ and d time series

3.7.4 Bottom effect

Since both the depth at the wavebuoy mooring position is known (see Fig.3.22a) and the main water depth at the actual test site can be interpolated on the bathymetry grid (see Fig.3.22b), the wave spectra at the test site $S_\zeta^{(t)}$ is calculated from the one measured by the buoy $S_\zeta^{(b)}$ in order to take into account bottom effects:

$$S_\zeta^{(t)}(f,\varphi) = B_S(f) \cdot S_\zeta^{(b)}(f,\varphi) \tag{3.8}$$

where:

$$B_S(f) = \frac{\tanh(k_w^{(b)} d^{(b)}) \cdot \left(1 + \dfrac{2k_w^{(b)} d^{(b)}}{\sinh(2k_w^{(b)} d^{(b)})}\right)}{\tanh(k_w^{(t)} d^{(t)}) \cdot \left(1 + \dfrac{2k_w^{(t)} d^{(t)}}{\sinh(2k_w^{(t)} d^{(t)})}\right)} \tag{3.9}$$

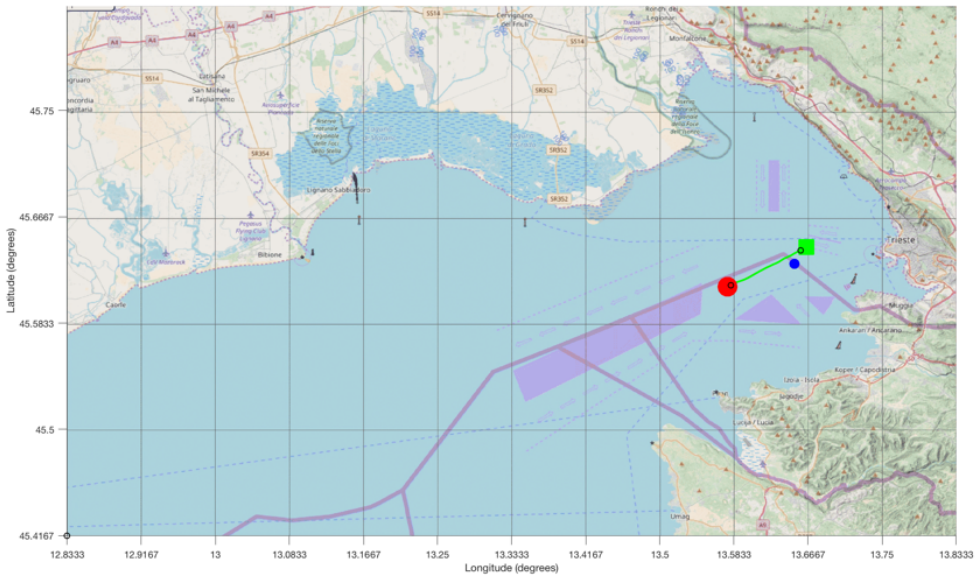

(a) Test track (green) and buoy position (blue)

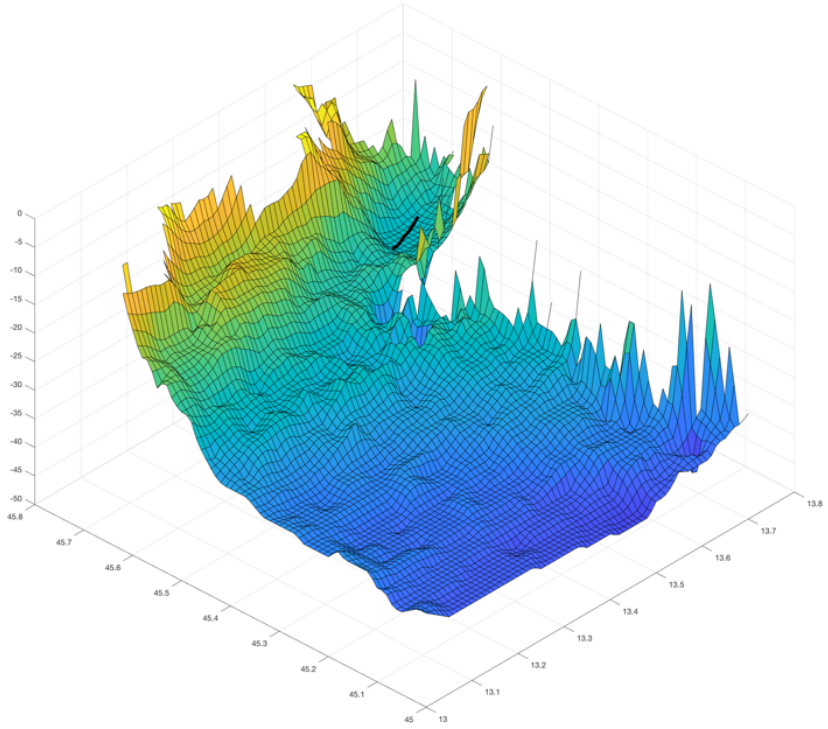

(b) Test depth interpolation (black line) and interpolation grid

Figure 3.22: Depth interpolation

3.7.5 Directional Wave Spectrum

In the representation of the sea state in terms of directional wave spectrum, significant advances in measurement techniques were made during the last two decades and a number of devices working on different principles are now available. Still, the inherent difficulties related to measuring and analysing directional wave spectra have not been completely solved yet. Standard techniques provide partial information on the directional spectrum, but they do not provide a robust estimate of the full directional spectrum. In particular, measurements from standard directional wave buoys allow the calculation of the directional spectrum if additional assumptions are made, which in turn are based on specific mathematical models for the directional distribution. These assumptions can significantly influence the look of the wave spectrum and of derived quantities, such as TF in the present case. The directional (2D) wave spectrum is commonly defined as:

$$S_\zeta(f,\varphi) = S_\zeta(f) \cdot D(f,\varphi) \tag{3.10}$$

where the angular dependent part $D(f,\varphi)$ is the directional spreading function (or directional distribution) that must fulfill the following condition:

$$\int_{-\pi}^{\pi} D(f,\varphi)\, d\varphi = 1 \tag{3.11}$$

The way $D(f,\varphi)$ is derived from specific models plays a key role in the entire process and on the accuracy of the final results (TF). A specific discussion on the models available and their use is given in subsection 3.7.6.

In Fig. 3.23 a possible single-peak directional spectral density $S_\zeta(f,\varphi)$ is shown for the modal frequency f^*, defined as:

$$f^* = f\Big|_{S_\zeta(f)=\max(S_\zeta(f))} \tag{3.12}$$

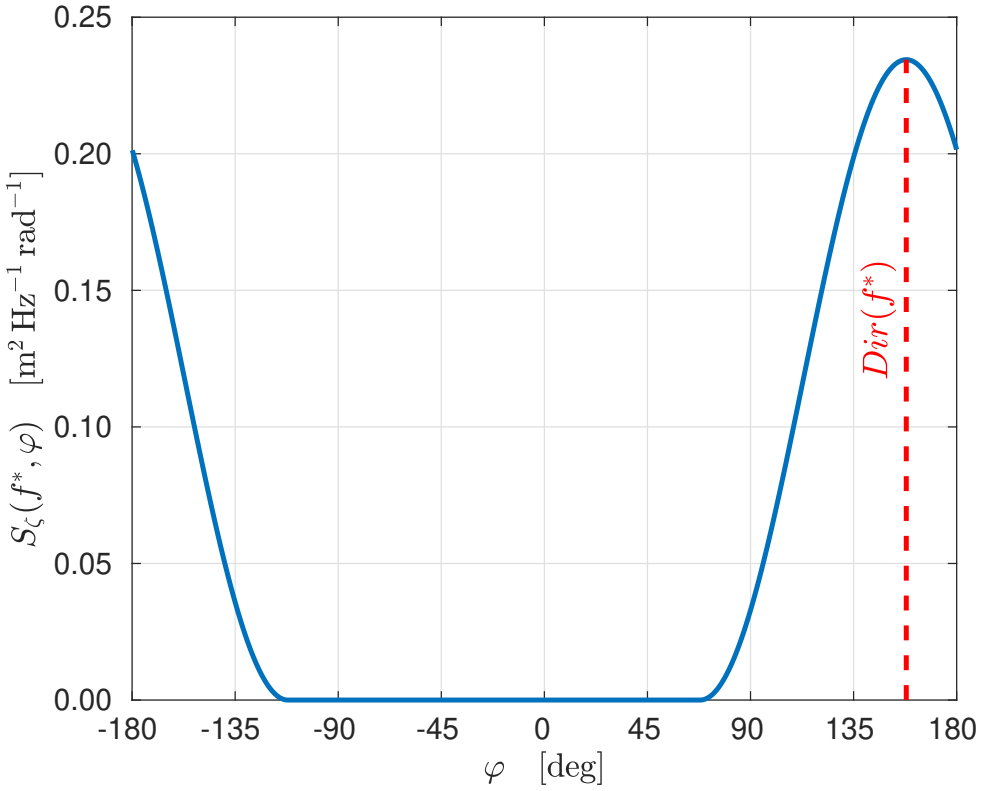

Figure 3.23: Directional spectrum for the modal frequency f^*.

Fig. 3.24 shows the surface $S_\zeta(f,\varphi)$ in terms of contour polar plot (after reconstruction using a simple cosine-squared directional distribution) where the radial distance and the angle from the *North* in clockwise direction represent frequencies and geographical directions respectively. Peak PWD and mean MWD wave directions are computed with the following standard formulas:

$$PWD = \varphi\Big|_{S_\zeta(f,\varphi)=\max(S_\zeta(f,\varphi))} \tag{3.13}$$

$$MWD = \arctan\left(\frac{\int_0^{2\pi}\int_0^{\infty}\sin(\varphi)\cdot S_\zeta(f,\varphi)\,df\,d\varphi}{\int_0^{2\pi}\int_0^{\infty}\cos(\varphi)\cdot S_\zeta(f,\varphi)\,df\,d\varphi}\right) \tag{3.14}$$

These directions, computed in quasi-real time during the sea-trials, are also shown in Fig. 3.24. Indeed, as head seas were the target condition of the project, the course of each run was manually aligned as soon as the last measurement of PWD and MWD available from the wave buoy were avalaible.

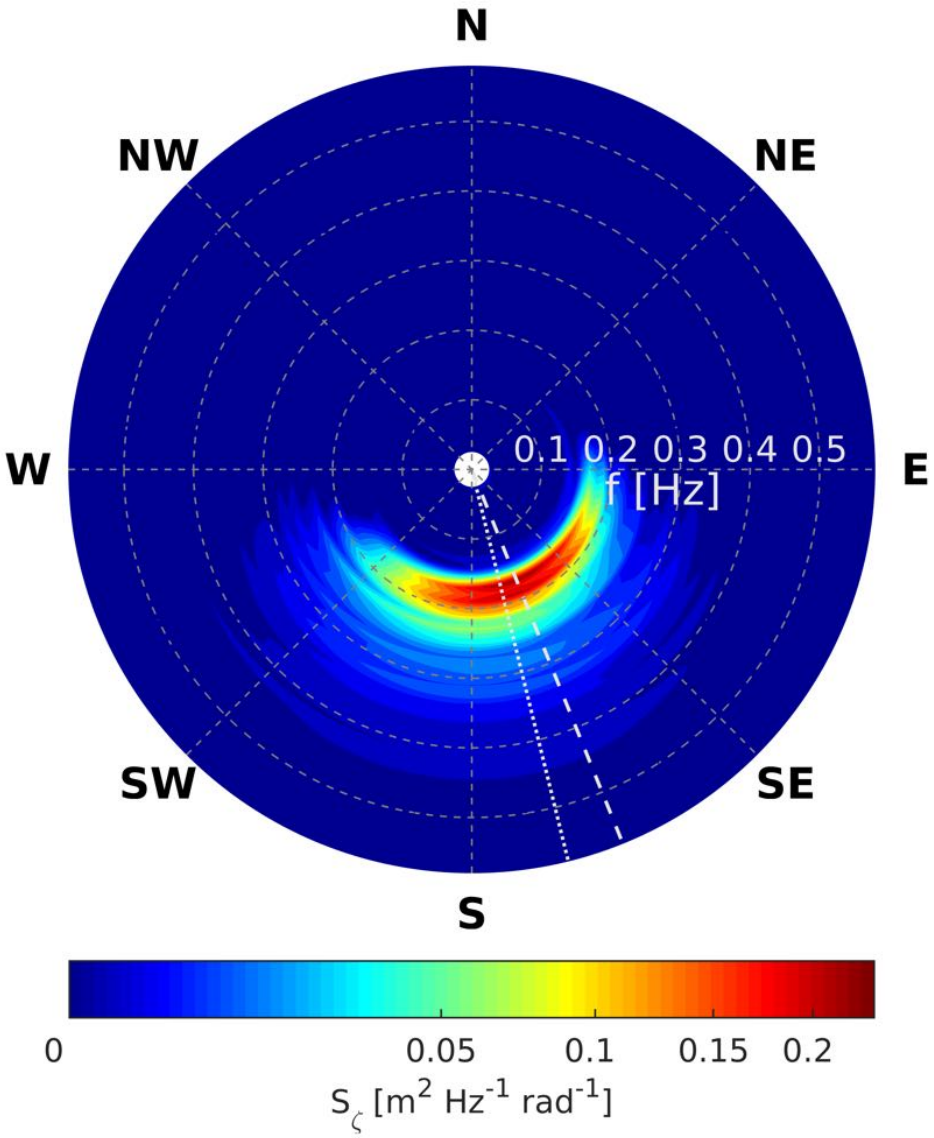

Figure 3.24: Directional spectrum (MWD=dotted ; PWD=dashed).

Starting from the definition of wave slope $\alpha = k_w A_w$, with k_w being the wave number and A_w the wave amplitude, the wave slope spectra $S_\alpha(f, \varphi)$ is then obtained:

$$S_\alpha(f, \varphi) = k_w(f)^2 \cdot S_\zeta(f, \varphi) \tag{3.15}$$

3.7.6 Directional Spreading Functions

The way $D(f, \varphi)$ in eq. 3.10 can be derived comes after specific assumptions that then lead to corresponding models. A tentative classification was given by Benoit et al. [87]. Four standard main models are here considered and compared:

1. *Unidirectional Sea* The unidirectional or long-crested sea is here considered first, although its application can safely be defined obsolete. Within this method, the whole wave energy detected by the buoy is associated with the single direction $Dir(f^*)$:

$$\varphi_0 = Dir(f^*) \tag{3.16}$$

where f^* is the modal frequency (eq. 3.12). The unidirectional distribution is then obtained:

$$D(f, \varphi) = \begin{cases} \dfrac{1}{\delta\varphi} & \text{if } \varphi = \varphi_0 \\ 0 & \text{if } \varphi \neq \varphi_0 \end{cases} \tag{3.17}$$

2. *Cosine-Squared* The Cosine-Squared distribution is perhaps the simplest and most widely used directional distribution for design applications as it is considered appropriate for common sea-state conditions in the open ocean. The following formulation has been employed:

$$\varphi_0(f) = \frac{Dir(f) \cdot \pi}{180} \tag{3.18}$$

$$D(f, \varphi) = \begin{cases} \dfrac{2}{\pi} \cos^2\left(\varphi - \varphi_0(f)\right) & \text{if } (\varphi_0 - \pi) < \varphi < (\varphi_0 + \pi) \\ 0 & \text{if } \varphi < (\varphi_0 - \pi) \vee (\varphi_0 + \pi) < \varphi \end{cases} \tag{3.19}$$

3. *Maximum Entropy Method (MEM I)* A first definition for the entropy was first proposed by Barnard [88] and then adapted to single-point systems by Lygre and Krogstad [89]. This method searches for an estimate that maximizes the entropy, defined as:

$$H_1(D) = -\int_0^{2\pi} \ln(D)\, d\varphi \tag{3.20}$$

and whose first two harmonics of the Fourier series decomposition coincide with the ones obtained from the measured co- and quad-spectra. Lygre and Krogstad (1986) found that the spreading function satisfying these conditions had the form:

$$D(f, \varphi) = \frac{\sigma_e^2}{2\pi \cdot (A_0 + 2C_1 \cos(\gamma) + 2D_1 \sin(\gamma) + 2\rho_2 \cos(2\gamma))} \tag{3.21}$$

where $\gamma = (\varphi - \varphi_0(f) - \varepsilon)$.

According to Benoit et al., the main advantage of this method lies in its high computational efficiency, although it consistently overestimates the height of the directional peaks. In addition, it sometimes predicts double peaks even in unimodal spectra cases. Thus, even when the model gives a double-peak distribution, it is not possible to conclude that the sea-state is bimodal. This represents the biggest limitation of this method.

4. *Maximum Entropy Principle (MEP; MEM II)* This method is based on the Shannon definition for the entropy and it was applied to directional wave analysis by Kobune and Hashimoto [90] and Nwogu et al. [91] for single-point systems. The entropy that has to be maximized is thus defined by:

$$H_2(D) = -\int_0^{2\pi} D \cdot \ln(D)\, d\varphi \tag{3.22}$$

and whose first four harmonics of the Fourier series decomposition coincide with the ones obtained from the measured co- and quad-spectra. Kobune and Hashimoto [90] found that the spreading function satisfying these conditions has the form:

$$D(f,\varphi) = \exp\left(-\sum_{j=0}^{4} L_j(f)\cdot c_j(\varphi)\right) \tag{3.23}$$

where the $c_j(\varphi)$ functions are defined as combinations of sines and cosines of phi:

$$c_j(\varphi) = \begin{cases} 1 & \text{if } j=0 \\ \cos(\varphi) & \text{if } j=1 \\ \sin(\varphi) & \text{if } j=2 \\ \cos(2\varphi) & \text{if } j=3 \\ \sin(2\varphi) & \text{if } j=4 \end{cases} \tag{3.24}$$

whereas $L_j(f)$ are the Lagrange's multipliers, determined by iteration method solving a set of nonlinear equations:

$$\int_0^{2\pi} (\beta_i(f) - c_i(\varphi)) \cdot \exp\left(-\sum_{j=1}^{4} L_j(f)\cdot c_j(\varphi)\right)\, d\varphi = 0 \tag{3.25}$$

for $i = 1, 2, 3, 4$.

with:

$$L_0 = \ln\left(\int_{-\pi}^{\pi} \exp\left(\sum_{j=1}^{4} L_j(f)\cdot c_j(\varphi)\right)\, d\varphi\right) \tag{3.26}$$

while:

$$\beta_i(f) = \begin{cases} A_1(f)/A_0(f) & \text{if } i=1 \\ B_1(f)/A_0(f) & \text{if } i=2 \\ A_2(f)/A_0(f) & \text{if } i=3 \\ B_2(f)/A_0(f) & \text{if } i=4 \end{cases} \tag{3.27}$$

where A_0, A_1, B_1, A_2 and B_2 are the first five Fourier coefficients.

In general, while there are no computational issues in the directional wave spectra given by the previous model *MEM I*, when *MEM II* is applied nonconvergence issues may occur. However, this drawback may be overcome by using some approximation schemes for solving the Lagrange's multipliers, as follows:

- *MEM II - AP2* Kim et al. [92] showed that by expanding the exponential term appearing in the nonlinear equations to the second order, an approximation of solution of the Lagrange's multipliers can be obtained as:

$$L_i(f) = \begin{cases} 2\beta_1\beta_3 + 2\beta_2\beta_4 - 2\beta_1\left(1+\sum_{j=1}^{4}\beta_j^2\right) & \text{if } i=1 \\ 2\beta_1\beta_4 - 2\beta_2\beta_3 - 2\beta_2\left(1+\sum_{j=1}^{4}\beta_j^2\right) & \text{if } i=2 \\ \beta_1^2 - \beta_2^2 - 2\beta_3\left(1+\sum_{j=1}^{4}\beta_j^2\right) & \text{if } i=3 \\ 2\beta_1\beta_2 - 2\beta_4\left(1+\sum_{j=1}^{4}\beta_j^2\right) & \text{if } i=4 \end{cases} \tag{3.28}$$

  Although this approximation scheme is not really identical to the original MEM II, it generally gives good results for unimodal, bimodal and asymmetric spectra.

- *MEM II - AP3* This extension of the *MEM 2* is based on the five Fourier coefficients measured and the spreading function is given by:

$$D(f,\varphi) = \exp\begin{pmatrix} -L_0(f) - L_1(f)\cos(\varphi) - L_2(f)\sin(\varphi) \\ -L_5(f)\cos(3\varphi) - L_6(f)\sin(3\varphi) \end{pmatrix} \tag{3.29}$$

  The solution of the multipliers from the above equation can be obtained either by iteration method or by an aproximation scheme as follows:

$$L_i(f) = \begin{cases} \beta_1 \dfrac{2\sum_{j=1}^{4}\beta_j^2 + 2.5\left(\sum_{j=1}^{4}\beta_j^2 - \left(\sum_{j=1}^{4}\beta_j^2\right)^2\right)^2}{\beta_1^2 + \beta_2^2 + 2\beta_1\beta_2\beta_4 + \beta_1^2\beta_3 - \beta_2^2\beta_3} & \text{if } i = 1 \\ \dfrac{L_1\beta_2}{\beta_1} & \text{if } i = 2 \\ \dfrac{L_1(3\beta_2^2 - \beta_1^2) - 4(\beta_1\beta_3 - \beta_2\beta_4)}{2(\beta_1^2 + \beta_2^2)} & \text{if } i = 5 \\ \dfrac{L_2(\beta_2^2 - 3\beta_1^2) - 4(\beta_3\beta_2 + \beta_1\beta_4)}{2(\beta_1^2 + \beta_2^2)} & \text{if } i = 6 \end{cases} \tag{3.30}$$

This method can still generate good estimates to the target spectrum and sometimes shows better results than *MEM II*, depending on the spectrum. However, in a similar way to the *MEM II*, this extension model can give false, although small, side lobes.

A comparison between the different formulations applied to the peak frequency is shown in Fig. 3.25. There are very large differences and double-peak against single peak distributions. This effect will be discussed in the results below.

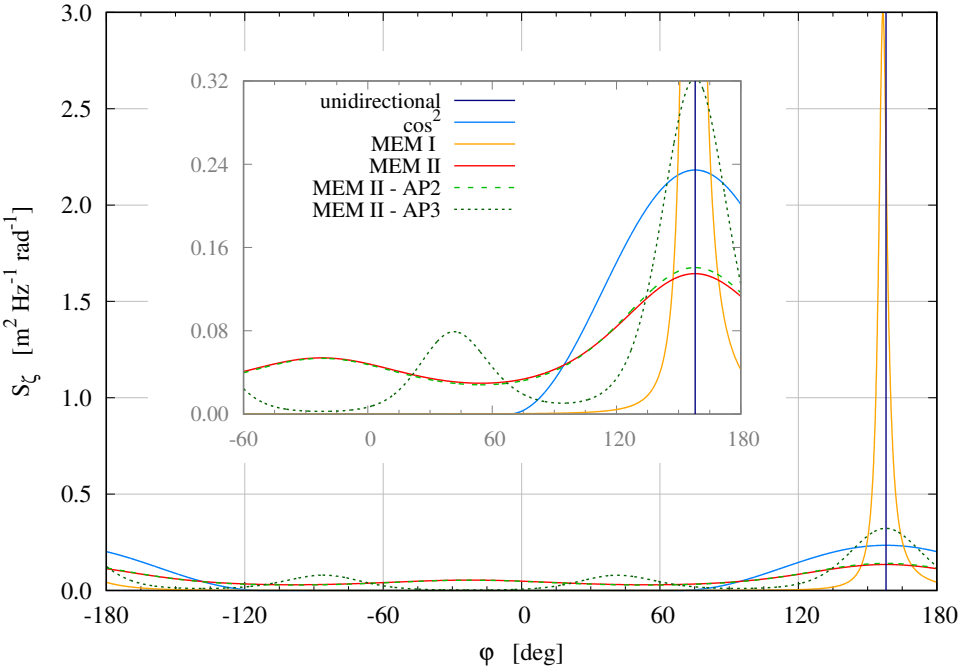

Figure 3.25: Directional spreading models comparison

3.7.7 Encounter Directional Wave Spectrum

Given the averaged yacht course over ground $\overline{\Theta}$, the heading angle χ is defined as the angle between $\overline{\Theta}$ and the direction of wave propagation φ as follows:

$$\chi(\varphi) = \overline{\Theta} - \varphi - \pi \tag{3.31}$$

Given the averaged yacht speed over ground $\overline{V}$, encouter frequencies are then computed using the well known formula (Lloyd, 1989):

$$f_e(f, \varphi) = f - \frac{\overline{V}}{\lambda_w(f, d)} \cdot \cos(\chi(\varphi)) \tag{3.32}$$

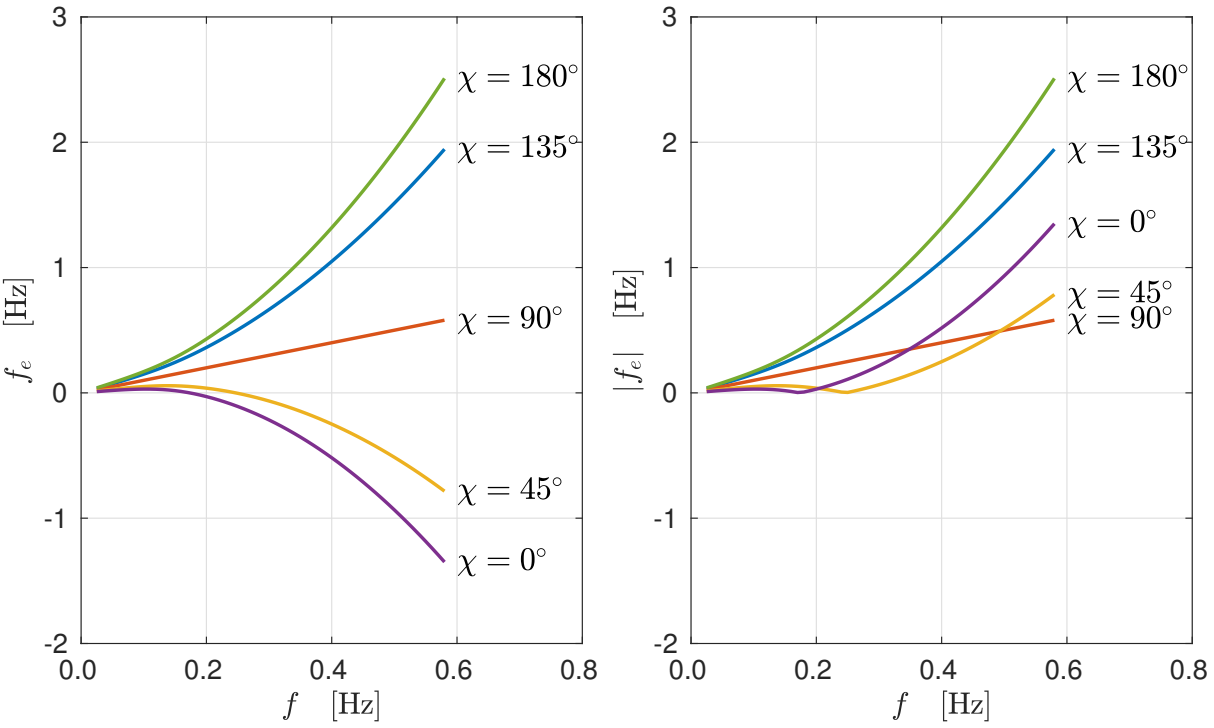

Figure 3.26: Encounter frequency f_e and $|f_e|$

Once the $f_e(f, \varphi)$ matrix is known, encounter frequency intervals Δf_e are calculated:

$$\begin{aligned} |\Delta f_e|_{i,j} = \max &\left[(f_e^{[\mathrm{lo}]})_{i,j} \, , \, (f_e)_{i,j} \, , \, (f_e^{[\mathrm{up}]})_{i,j} \right] + \\ - \min &\left[(f_e^{[\mathrm{lo}]})_{i,j} \, , \, (f_e)_{i,j} \, , \, (f_e^{[\mathrm{up}]})_{i,j} \right] \end{aligned} \tag{3.33}$$

where $(f_e^{[\mathrm{lo}]})_{i,j}$ and $(f_e^{[\mathrm{up}]})_{i,j}$ are the upper and lower bounds of the i-th encounter frequency bin and the j-th direction. The example in Fig. 3.27 shows a graphical representation of the computation of Δf_e in the case following sea conditions.

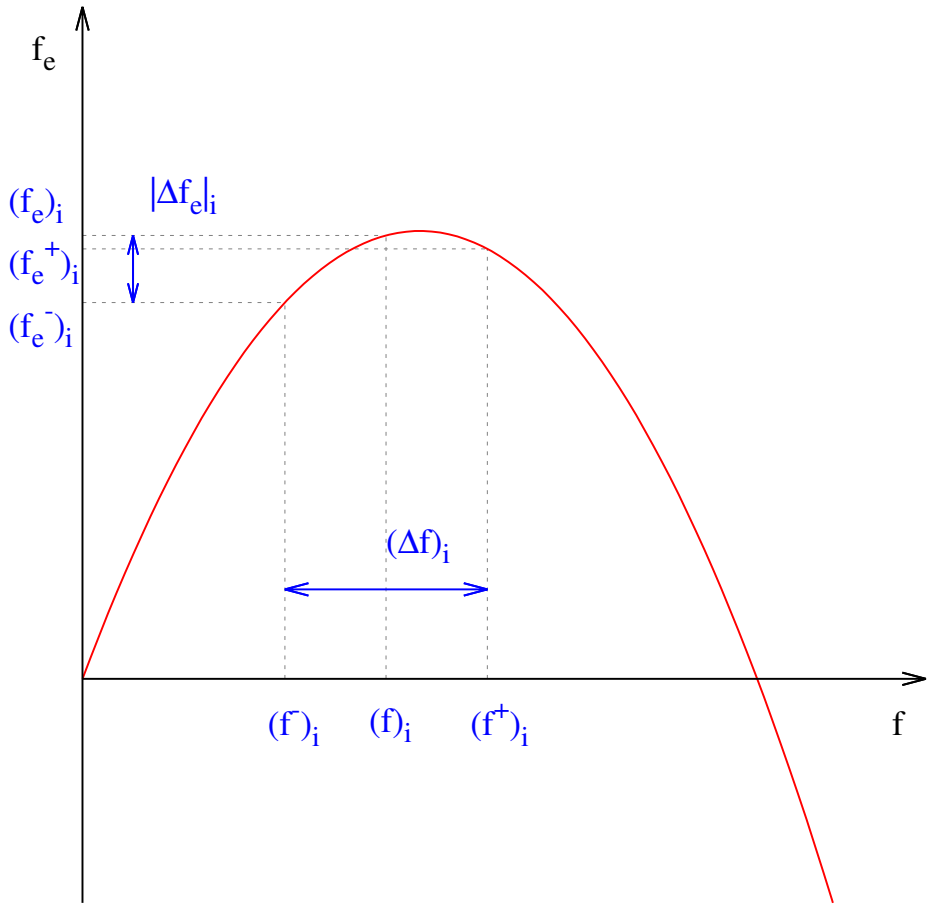

Figure 3.27: Encounter frequency interval in following sea

Then the encounter frequency directional spectrum is computed:

$$S_{\zeta,0}^{(e)}(f_e, \varphi) = S_\zeta(f, \varphi) \cdot \frac{\Delta f}{|\Delta f_e|} \tag{3.34}$$

The resulting spectrum is shown in Fig. 3.28, where the red dashed line represents the average yacht course. The white contour line represents the maximum measured wave frequency in the encounter frequency domain.

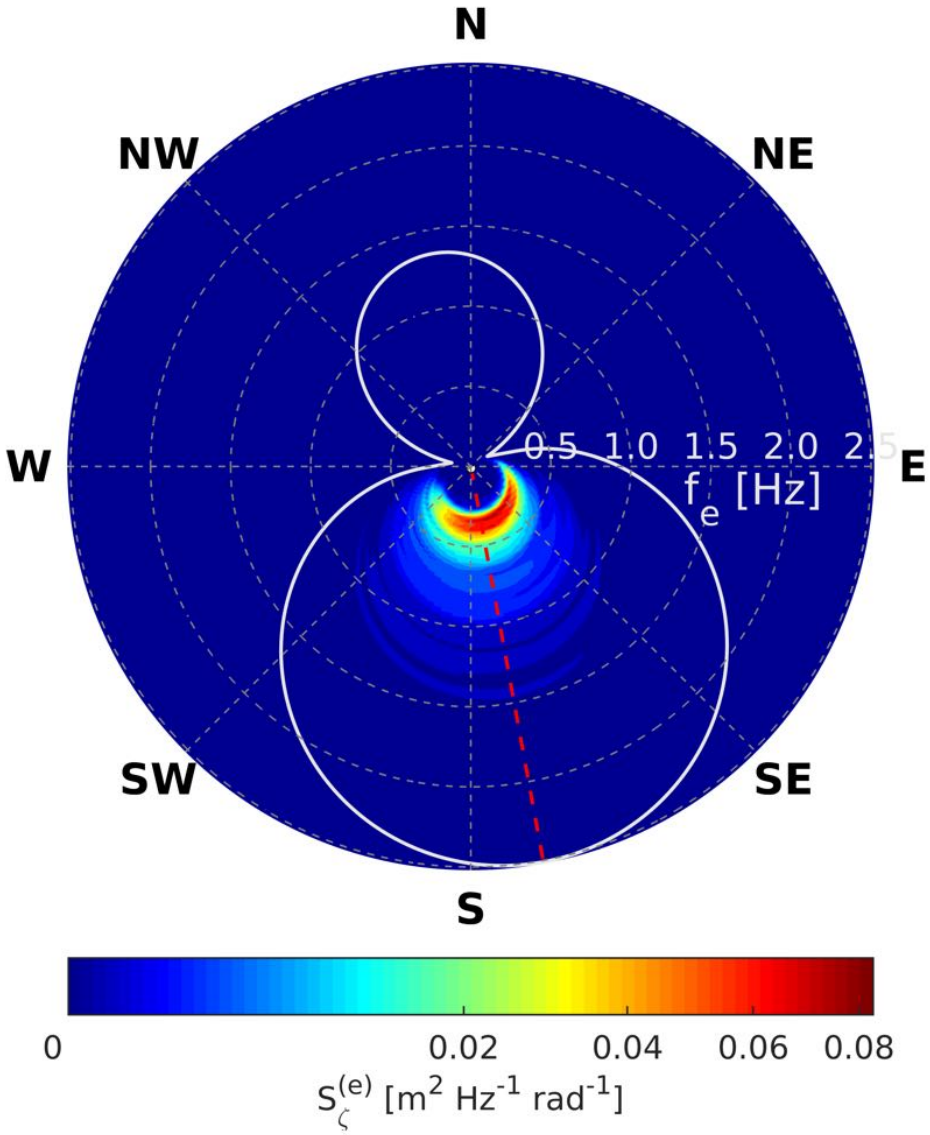

Figure 3.28: Encounter frequency directional wave spetrum.

The encounter frequency spectrum is then resampled at a constant frequency width so that $\Delta f_e^{(new)} = 0.02\,\text{Hz}$.

$$\left(S_\zeta^{(e)}\right)_{i,j} = \sum_{n=1}^{N_f} \left[\left(S_{\zeta,0}^{(e)}\right)_{n,j} \frac{(int)_{i,j,n} \cdot \delta_{i,j,n}}{\Delta f_e^{(new)}} \right] \tag{3.35}$$

where N_f is the number of new frequency bins, $\left(S^{(e)}_{\zeta,0}\right)_{n,j}$ is the encounter spectrum matrix having non-homogeneus Δf_e bin width, calculated using eq. 3.34. The $(int)_{i,j,n}$ variable is the $\left(S^{(e)}_{\zeta,0}\right)_{n,j}$ spectrum content inside the new frequency bins delimited by $(f_e^-)^{(new)}_{i,j}$ and $(f_e^+)_{n,j^{(new)}}$:

$$(int)_{i,j,n} = \min\left[(f_e^+)^{(new)}_{i,j}\,,\,|f_e^+|_{n,j}\right] - \max\left[(f_e^-)^{(new)}_{i,j}\,,\,|f_e^-|_{n,j}\right] \tag{3.36}$$

and $\delta_{i,j,n}$ is defined as:

$$\delta_{i,j,n} = \begin{cases} 1 & \text{if } (int)_{i,j,n} > 0 \\ 0 & \text{if } (int)_{i,j,n} \leq 0 \end{cases} \tag{3.37}$$

The four different combinations of frequency bins overlap $(int)_{i,n}$ are shown in Fig. 3.29.

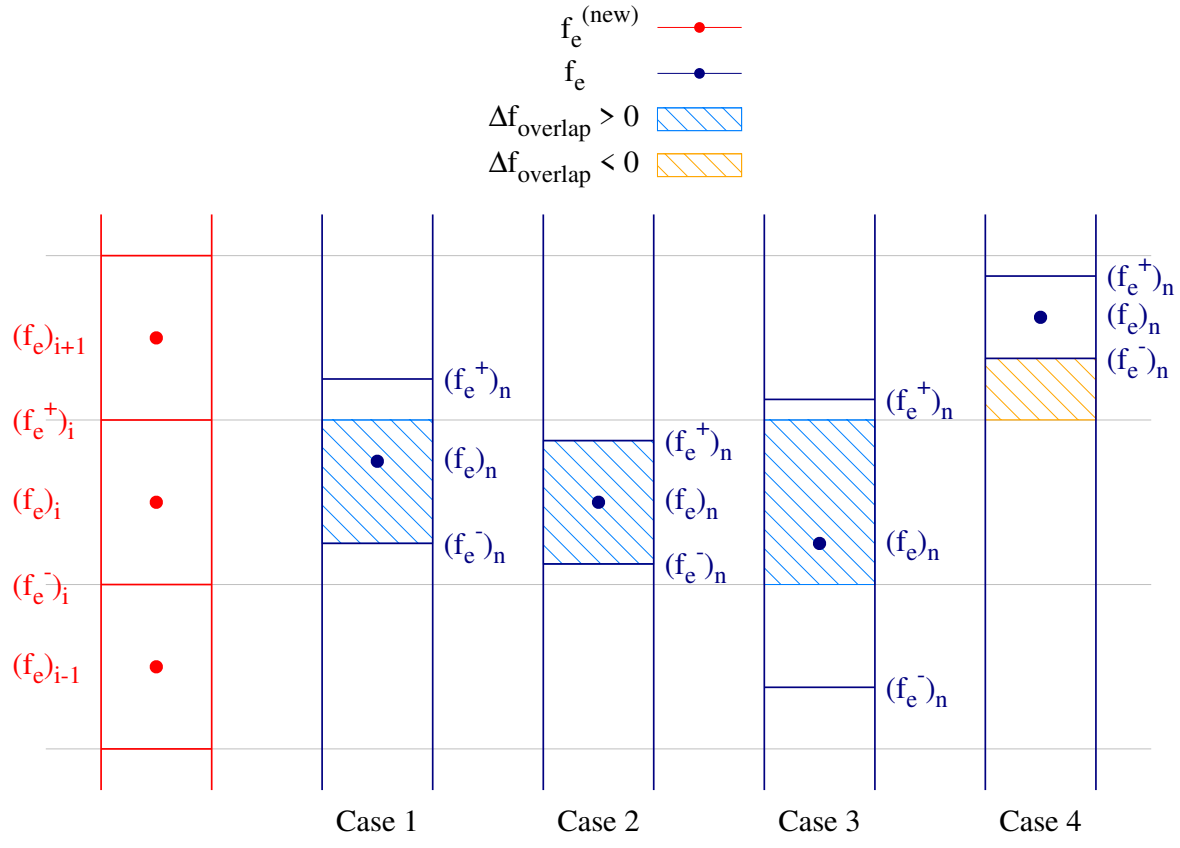

Figure 3.29: Frequency bins overlap cases

At this point, multiple transfomations and a directional spreading function has been applied to the initial 1D wave spectrum measured by the buoy: To ensure that every operation has been

carried out correctly, the total spectrum energy is evaluated to be equal to the original:

$$\int\int_{-\pi}^{+\pi} S_{\zeta}^{(e)}(f_e,\varphi)\,d\varphi df_e = \int\int_{-\pi}^{+\pi} S_{\zeta}^{b}(f,\varphi)\,d\varphi df \tag{3.38}$$

In order to evaluate heave and pitch forcing spectra, the directional encounter frequency spectrum is integrated over all directions φ. The heave forcing spectrum is obtained as follows:

$$S_{F_H}(f_e) = \int_{-\pi}^{+\pi} W_H(\varphi)^2 \cdot S_{\zeta}^{(e)}(f_e,\varphi)\,d\varphi \tag{3.39}$$

where $W_H(\varphi) = 1$ is the directional weight function for heave motion. The pitch motion forcing term, differently from the case of heave, is affected by the incoming wave direction, since the effective wave length (see Fig. 3.30) is:

$$\lambda_{eff} = \frac{\lambda}{cos(\chi)} \tag{3.40}$$

And so the effective wave steepness is:

$$\alpha_{eff} = \alpha cos(\chi) \tag{3.41}$$

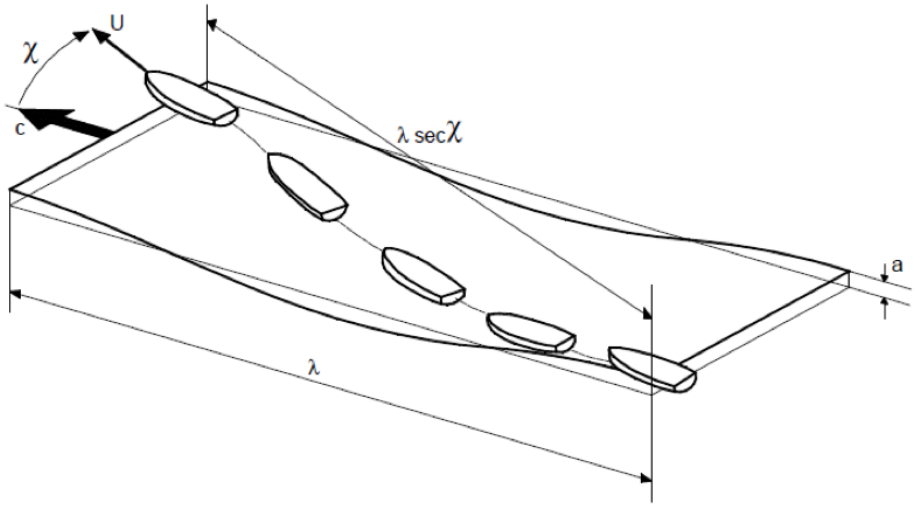

Figure 3.30: Effective wavelength for oblique waves, from [74]

The pitch forcing spectrum is obtained as follows:

$$S_{F_P}(f_e) = \int_{-\pi}^{+\pi} W_P(\varphi)^2 \cdot S_{\alpha}^{(e)}(f_e,\varphi)\,d\varphi \tag{3.42}$$

where $W_P(\varphi) = \cos(\chi(\varphi))$ is the directional weight function for pitch motion (eq: 3.41).

From the definition of power spectral density, forcing amplitude spectra are then obtained:

$$A_F(f_e) = \sqrt{S_F(f_e) \cdot 2 \cdot \Delta f_e^{(new)}} \tag{3.43}$$

Resulting spectra are shown in Fig. 3.31.

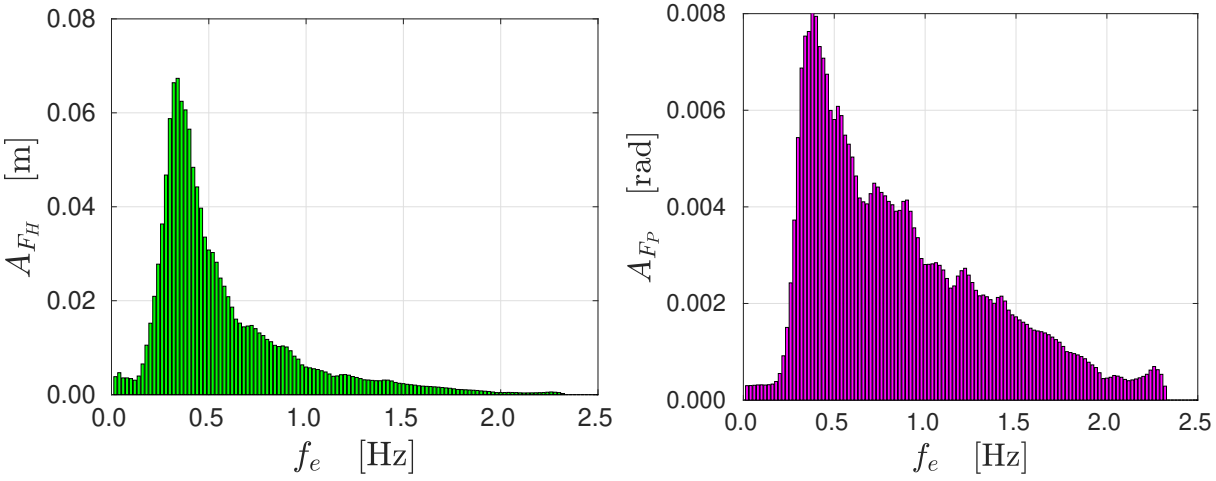

Figure 3.31: Heave (left) and pitch (right) forcing amplitudes.

3.7.8 Directional Wave Spreading

Fig. 3.32a shows the ratio between the wave energy included in the main angular sector [$PWD \pm 90°$] and the total energy in terms of significant wave heights. This value is given for each run of Table 3.1 and for each model used for the reconstruction of the directional spectrum. It is worth remembering that *Run* 2 and 3 belong to the second day of sea-trials when, according to on-board visual observations, the observed sea state was close to being unidirectional. On the contrary, for *Run* 1, 4 and 5 the sea direction was much more complex, due to a moderate wind rotation during the day and possible slight refraction effects. In any case, observed waves spreading and wind shifts were limited to a sector much narrower than 180°. In other words, the values of $H_{S\pm 90°}/H_S$ in Fig. 3.32a for the observed sea are equal to 1 for every run.

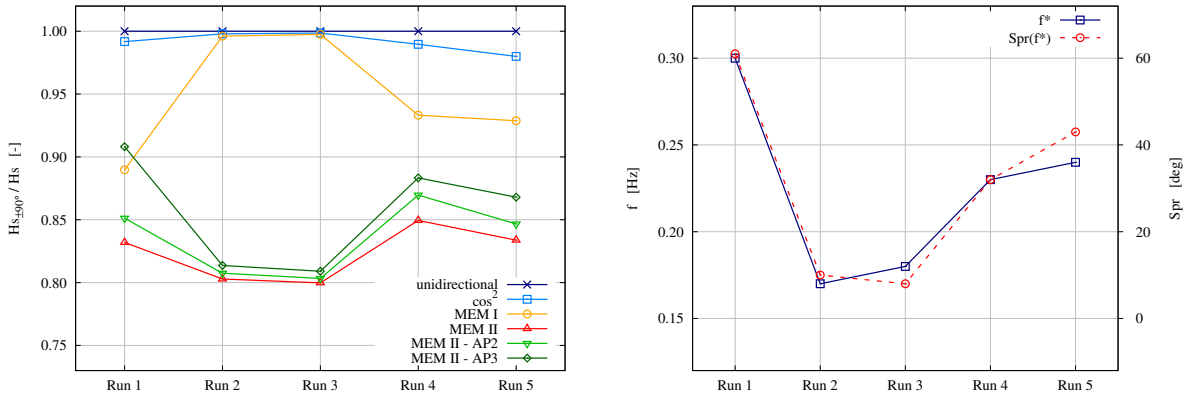

(a) Wave energy distribution.

(b) Peak frequency and its directional spreading.

Figure 3.32: Waves characteristics during the sea trials

As expected, cosine squared model keeps 98% of energy in the main sector for all runs. *MEM I* keeps the entire energy in the main sector for *Run* 2 and 3 only, whereas approximately from 5% to 10% of wave energy is distributed outside the main sector for the other runs. *MEM II*, in any version tested, underperforms for *Run* 2 and 3, with an energy loss from the main sector of approximately 20%. For *Run* 1, 4 and 5 the energy is distributed outside the main sector ranges between 10% and 20% approximately. Despite what said in the "Directional Wave Spreading" section, in our case *MEM I* shows better estimation of secondary peaks respect to *MEM II*. As shown by Kim et. al (1995), *MEM II* distributions are more suitable for sea states that present double peaks on the same frequency component.

A further insight comes from Fig. 3.32b. It shows two standard outputs of the wave buoy (Table 3.4), i.e. the modal frequency f^* (blue) and its spreading $Spr(f^*)$ (red). *Run* 2 and 3 show a very low spreading (less than 15 deg) and simultaneously a low modal frequency for the geographic area (around 0.17 Hz). On the contrary, *Run* 1, 4 and 5 show realtively higher modal frequencies (above 0.23 Hz) and mostly large spreading (above 35 deg). A common trend between Spr and f^* is evident, this suggest that, in this case, the spread value is influenced by frequency. The different performances of the models *MEM I* and *MEM II* reported in Fig. 3.32a are clearly related to the different sea state conditions during the runs.

3.7.9 Forcing Spectra

Fig. 3.33 shows heave forcing spectra in the encounter frequency domain. In this case, the curves represent a spectrum obtained from averaging the amplitude spectra from *Run* 2 and 3 only. This average is allowed because the sea state remained almost unvaried during both runs, as reported in Table 3.1. Moreover, each curve in the plot represents the results obtained with different directional spreading functions. There are two distinct features that can be observed. First of all, for $f_e \geq 0.3\,\text{Hz}$, *MEM II* models show lower amplitudes than the other models, *MEM I* included. For $f_e \leq 0.3\,\text{Hz}$, *MEM II* shows a large amount of energy in the lowest frequency range that comes from the secondary peaks introduced by the model outside the main sector. This effect

has evident consequencies on the results of the *TF* because of the exaggerated wave energy in the lowest frequency range where, in this case (site, day, wind conditions, fetch), there was no energy at all.

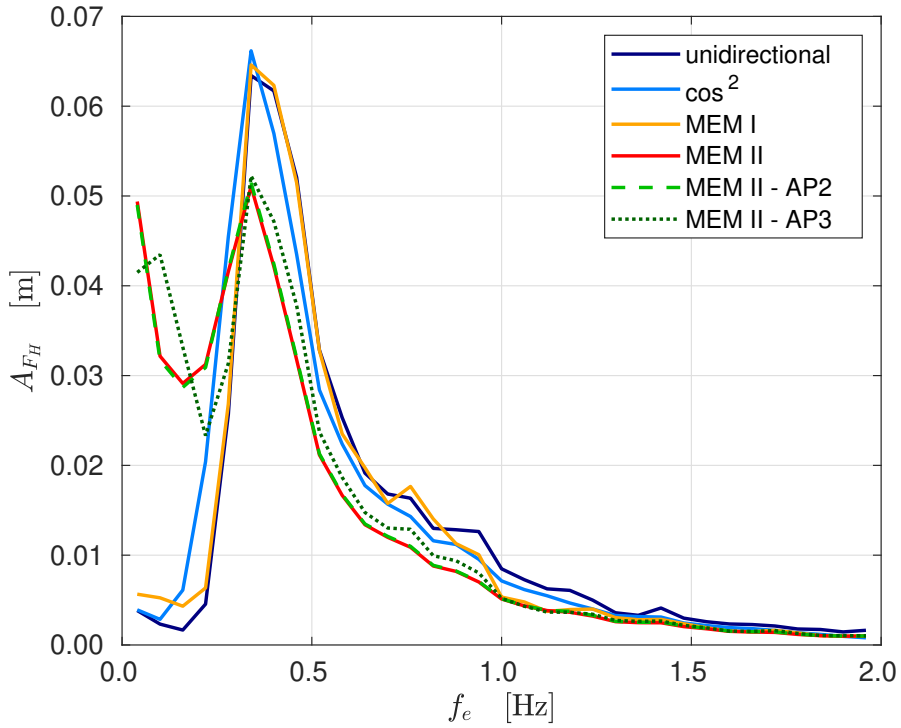

Figure 3.33: Heave forcing spectrum.

3.7.10 Transfer Functions

In this section, the results of this analysis are presented in the form of linear transfer functions (*TF*). The latter are evaluated frequency-by-frequency, that is dividing every motion spectral component with the equivalent component of the forcing spectra. The pitch *TF* is defined as:

$$A_\Theta / A_{F_P} \tag{3.44}$$

where A_Θ is the pitch motion amplitude spectrum, and A_{F_P} is the pitch forcing spectra (eq. 3.42 and 3.43). Pitch *TF* is shown in Fig. 3.34 along with the results obtained at model scale in towing tank experiments. The full scale results obtained from the procedure described earlier in this section are shown for each directional distribution model. The model scale data refer to two different loading conditions that embrace the loading condition tested at sea and were obtained in regular waves with small wave steepness.

It is important to point out that regular waves model scale data are not to be taken as a true benchmark for full scale irregular sea data since both the forcing term (monochromatic

vs. spectrum) and restraint conditions (2 DoF towing vs. 6 DoF self propelled) are different. Moreover, it is known that nonlinear effects in motion response are inevitably present.

Model scale results are here meant as comparison data, obtained under controlled conditions.

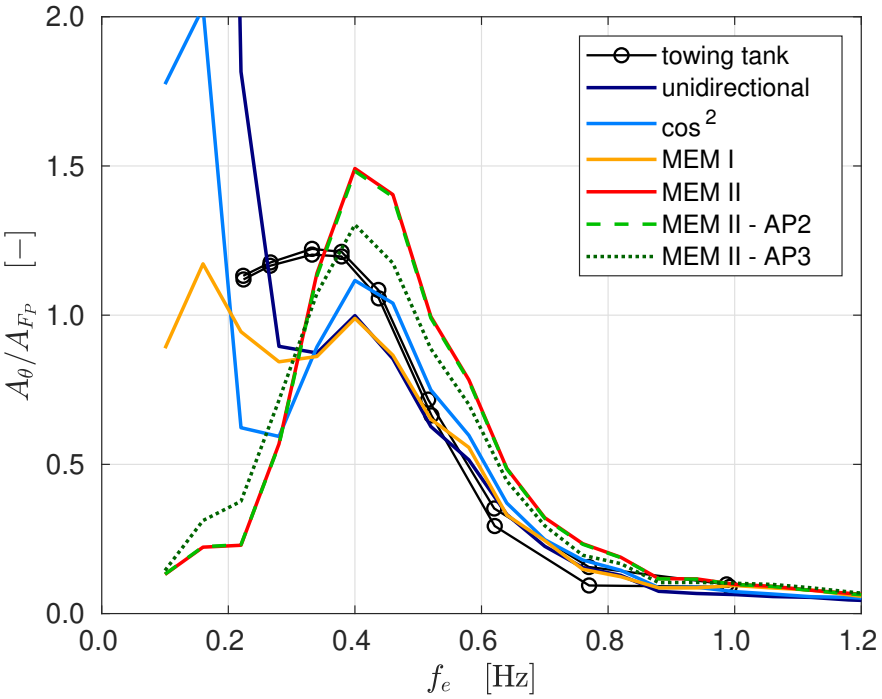

Figure 3.34: Pitch transfer function.

As expected, pitch *TF* based on *MEM II* model overestimate reference (model scale) data for $f_e \geq 0.35\,\text{Hz}$ and largely underestimate them for $f_e \leq 0.35\,\text{Hz}$. *TF* computed with *MEM I* show remarkable agreement instead, in particular for $f_e \geq 0.5\text{Hz}$. *MEM I* shows lower values of *TF* respect to model data in the peak region, this can be expected as irregular sea response is tipically lower than the one measured in regular waves. For low frequencies the *TF* obtained with *MEM I* assumes values around 1, coherently with a typical pitch *TF*.

Considering heave motion, since IMUs and accelerometers cannot detect vertical displacements, the only option is to rely on vertical acceleration at the CG ($\ddot{\zeta}_g$) measurements. Heave response spectrum components $(A_{\zeta_g})_i$ are obtained from the vertical acceleration amplitude spectrum components $(A_{\ddot{\zeta}_g})_i$ as follows:

$$(A_{\zeta_g})_i = \frac{(A_{\ddot{\zeta}_g})_i}{\omega_i^2} \tag{3.45}$$

The Heave *TF* is defined as:

$$A_{\zeta_g}/A_{F_H} \tag{3.46}$$

where A_{ζ_g} is the heave motion amplitude spectrum, and A_{F_H} is the heave forcing spectra (eq. 3.39 and 3.43).

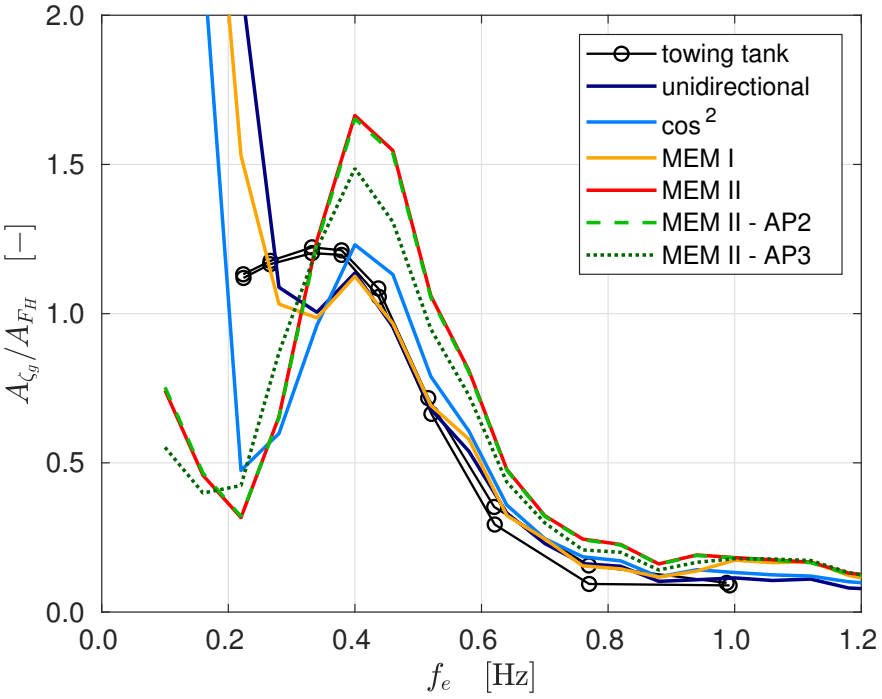

Figure 3.35: Heave transfer function.

Heave *TF* shows similar behavior as the case of pitch for $f_e \geq 0.35$ Hz if not a better match to the reference data in the case of *MEM I*. For $f_e \leq 0.35$ Hz the effect of both low forcing spectra and low frequency values dividing the acceleration spectra (see Fig. 3.36a) results in unrealistic values.

Next, vertical (heave) and angular (pitch) acceleration *TF* are discussed. In particular, vertical accelerations come from direct measurement whereas pitch acceleration come from double derivative of the measured pitch angle.

Fig. 3.36a and 3.36b show heave and pitch acceleration *TF*, averaged from *Run* 2 and 3. These parameters are now more closely related to the comfort on-board and to the sea-kindliness of the vessel. Once again, the results obtained with different directional spreading models applied to the wave buoy data, highlight the importance of the proper use of the directional spreading function.

In this specific case, i.e. narrow frequency band and extremely reduced spreading in *Run* 2 and 3, *TF* based on *MEM I* shows the best results against model scale data. In particular, the agreement with model scale data is good even in the low frequency range.

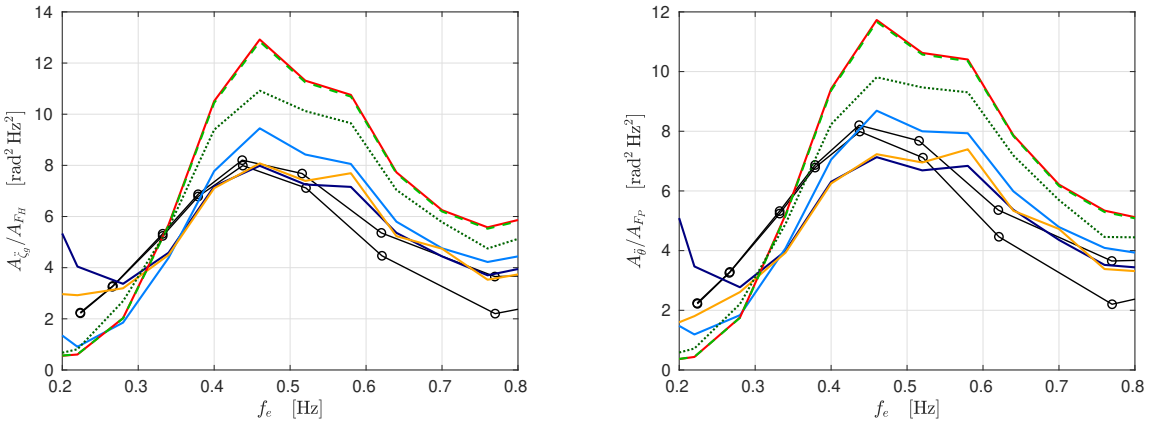

(a) Heave acceleration transfer function

(b) Pitch acceleration transfer function

Figure 3.36: Acceleration transfer function

The results of the integrated approach here presented are applied to data from concurrent measurements of the sea-state and of ship-motions collected during full-scale seakeeping trials of a planing pleasure boat has been presented. However, the procedure is completely general and could be applied to any kind of ship and weather condition.

Multiple sources of data are combined into the proposed integrated analysis, leading from the measurements of the sea state and vessels motions to the estimation of full-scale heave and pitch transfer functions (TF).

For the case considered, i.e. a relatively high frequency sea-state and a corresponding low significant wave height, it is found that the models play a fundamental role in the accuracy of the final results (TF). In particular, for the case considered, relatively less sophisticated models such as *MEM I* and cosine-squared gave very good agreement with controlled model scale results respect to more modern and complex wave directional distribution models.

3.8 Propulsion data analysis

Being the propulsion characteristics not the main focus of the experimental work carried out in this thesis, the propulsion data analysis only started in the last part of the Ph.D. program and it is in progress as of the writing of this thesis. The results that will be presented will calm water runs and some analysis on rough water.

3.8.1 Calm water

The results of the propulsion data analysis covers two days of testing where the engine rpm was increased by 200 rpm step until full throttle. Propeller shafts rpm and torque measurement are then properly windowed so that a in order to isolate the most appropriate data subset (constant value). The propulsion data is analysed in cojunction with the hull motion data from the onboard IMUs.

Since the two datasets (propulsion and motion) did not share the same acquisition system, they are not synchronized, although they share the same sample rate of 100 Hz. In order to facilitate the windowing process and later in depth analysis, the propulsion data has been synchronized to the motion data. The synchronization has been possible thanks to the fact that IMU1 and ACC2 were mounted on top of the other. Slightly after every acquisition, the IMU1/ACC2 assembly has been manually knocked three times in order to be able to later recognize the three peas in raw vertical acceleration. The method of manually align the signals in post-processing using the peaks has been replaced by the use of the signal cross-correlation technique, that has been proven to be much less time consuming and very accurate, also for calm water results, where vertical motions were very limited. The averaged values speed, torque and rpm and stored into a nested structured array ready for post-processing, in this case plotting one against each other. In Fig. 3.37, an overview of the calm water tests is presented, where both engine rpm (fixed) is compared to the yacht speed. Data from both starboard (SB) and port side (PS) propeller shafts is plotted, including multiple measurements from the two days of test.

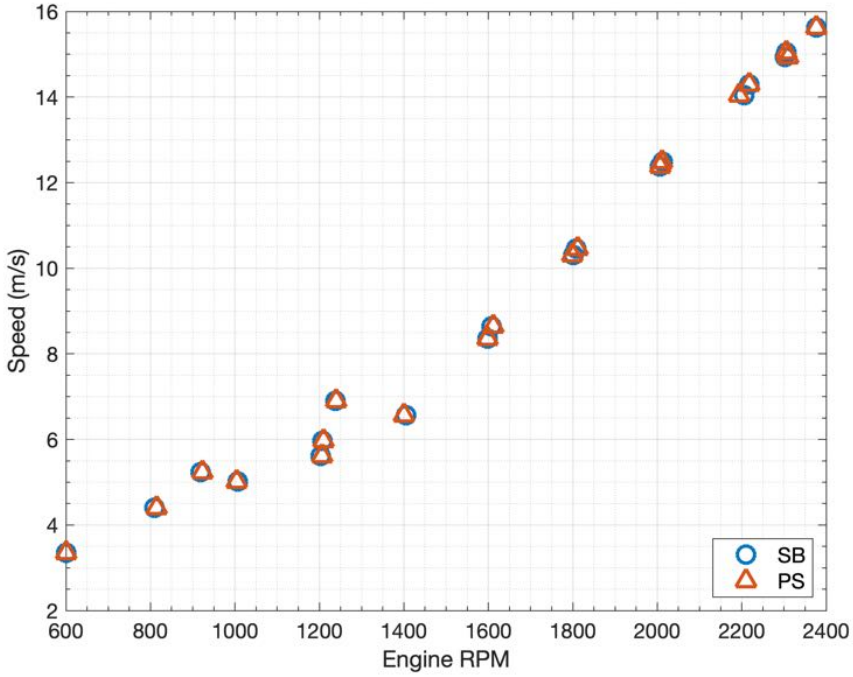

Figure 3.37: Calm water tests

The plots in Fig. 3.38 show the calculated shaft torque and power outptut along with the engine limit curves. Shaft strain has been measured by the strain gauges rosette and torque has been computed using 3.3 and 3.4, using the young modulus from the "Acqualoy 17" datasheet from the manufacturer and the poisson modulus has been estimated. The repetibility of the results is very clear from one day to the next, and also the fact that for higher speeds, the starboard shaft

always experienced slightly higher torque respect to the port side one. The same is not valid for lower speed where torque values are almost identical (as expected).

The fact that the starboard shaft shows higher torque is explained by the fact that the yacht started to heel at higher speed. In particular, positive heel angle is observed in fig 3.39b, and according to the IMU reference system (see 3.12a), it means that the yacht is heeled to starboard. This means that the starboard propeller is more immersed than the port side one and that results in a bigger load.

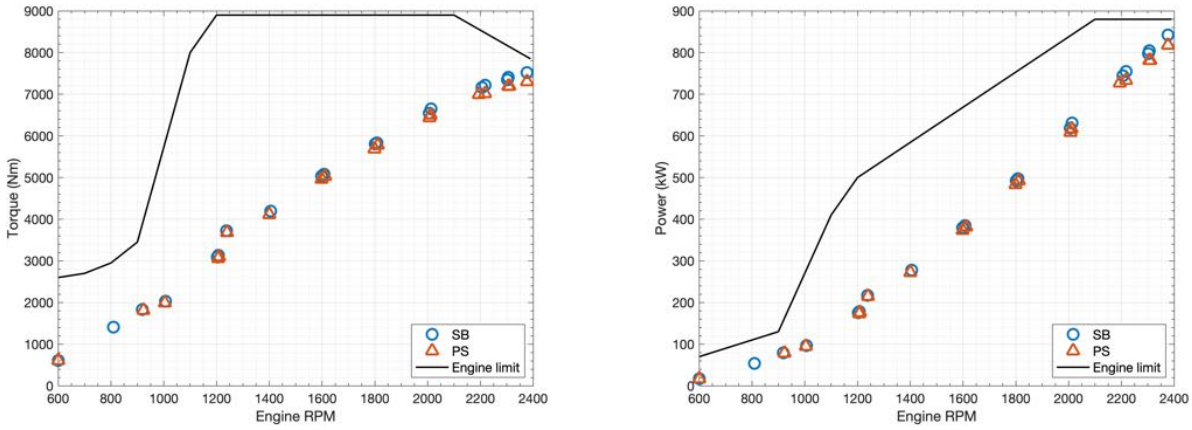

(a) Shaft torque

(b) Power output

Figure 3.38: Torque and power vs engine rpm

The yacht's trim is plotted in Fig. 3.39a, along with model data, it is clear that the full scale hull shows higher trim angle than the model tests. Comparing the full scale trim to the model at the design loading condition (LC1) it is however clear that the trend with speed is similar, and both show maximum values of trim for the same speed. The main difference between full scale and model scale test condition is that while in the case of model scale tests, the towing force is horizontal and applied near the center of gravity and the case of the yacht thrust is delivered to the lower-placed thrust bearing along the shaft direction. The thrust force in full scale could therefore generate an additional pitching moment and lead to higher running pitch values.

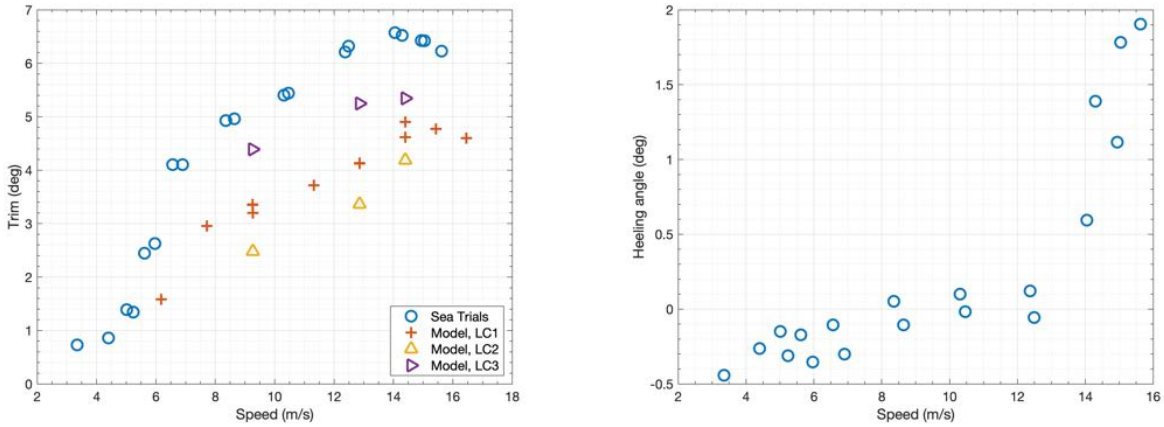

(a) Trim in calm water

(b) Heeling angle

Figure 3.39: Full-scale trim and heeling angles vs speed

In Fig. 3.40, the heeling angle at higher rpm/speed can be observed looking at the angle between the flybridge ceiling and the horizon. Moreover, the effect of heel angle on the wake is also easily observed, as it becomes asymmetric. Under operational cruising condition, two interceptors are installed, along with two adjustable flaps, ensuring zero heel and much lower trim angle at speed.

(a) 1200 rpm - no heel

(b) 1400 rpm - no heel

(c) 1600 rpm - no heel

(d) 1800 rpm - no heel

(e) 2000 rpm - no heel

(f) 2200 rpm - 0.5° heel

(g) 2300 rpm - 1.5° heel

(h) 2370 rpm - 1.7° heel

Figure 3.40: Yacht wake and heel angle during calm water sea trials

3.8.2 Head sea

In the the following subsection, some preliminary studies of the effects of the boat motion (Pitch) on the propulsion characteristics measured during seakeeping trials in head seas ($\chi = 180°$) will be presented. The signals of pitch, shaft torque and rpm have been analysed both in the time and frequency domain in order to highlight the their main relationships.

Frequency response

The first analysis of the three signals has been carried out in the frequency domain, comparing the frequency response of pitch with shaft torque and rpm. This simple analysis has been implemented using FFT Fourier transform algorithm to compute the single-sided amplitude spectra of the three signals and then compared. The comparison of normalized pitch, torque and rps values are plotted in Fig. 3.41, it is clear that all three measurements share a similar frequency response, in particular around the encounter frequency value of 0.4 Hz. As expected, that shaft torque and rpm response are related to the pitch motion, and ultimately to the wave excitation.

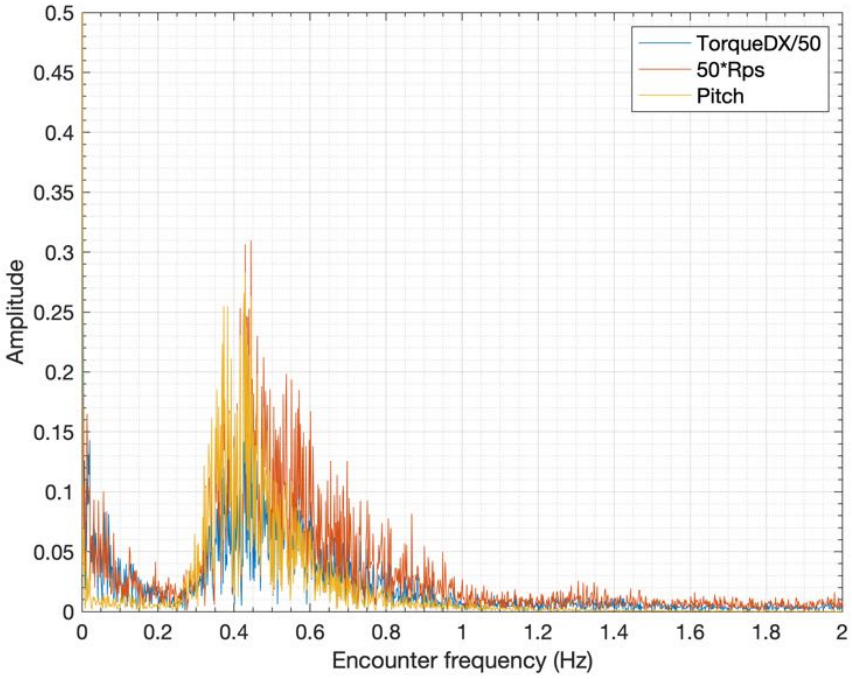

Figure 3.41: Normalized amplitude spectra of pitch, shaft torque and rps comparison

Time domain analysis

In the case of analysing the time series of the signals, the synchronization of the acceleration signals from IMU1 and ACC2 at the CoG is of paramount importance for phase analysis. An

example of the result of synchronization by means of the cross correlation is shown in fig: 3.42. The plot shows the synchronized timeseries of vertical acceleration, measured with IMU1 and ACC2. The signals of both motion and propulsion datasets, once synchronized, share the same UTC timestamp, provided by the GNSS system. This has been possible thanks to te fact that both datasets have the same sampling frequency.

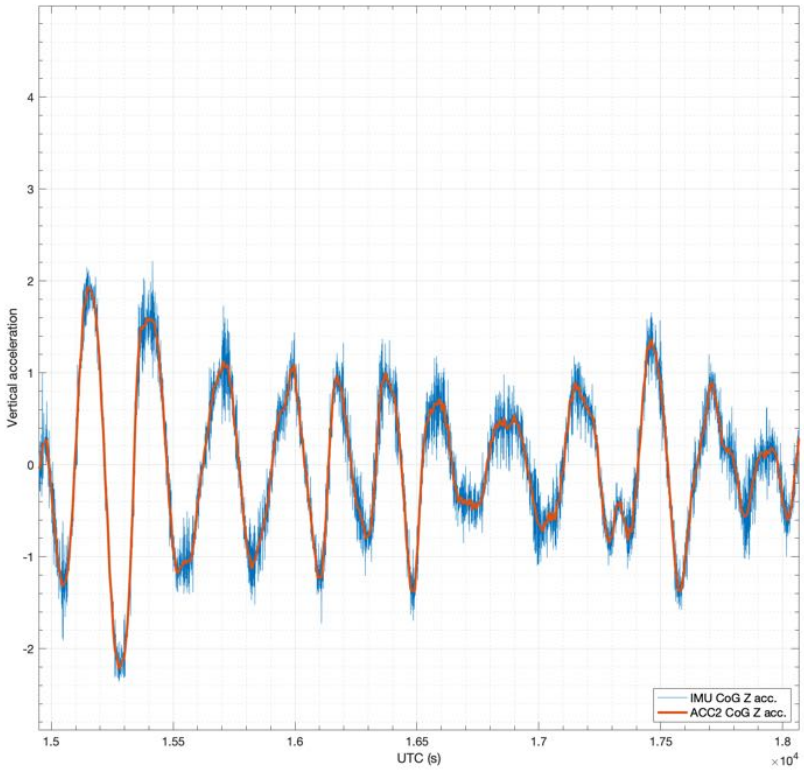

Figure 3.42: Example of acceleration timeseries from IMU1 and ACC2

The synchronized datasets allow for an analysis of the phase between pitch, shaft torque and rotation signals. Since the signals are not monochromatic, the (average) phase delay has been computed using the delay value found using the cross correlation technique. In Fig. 3.43

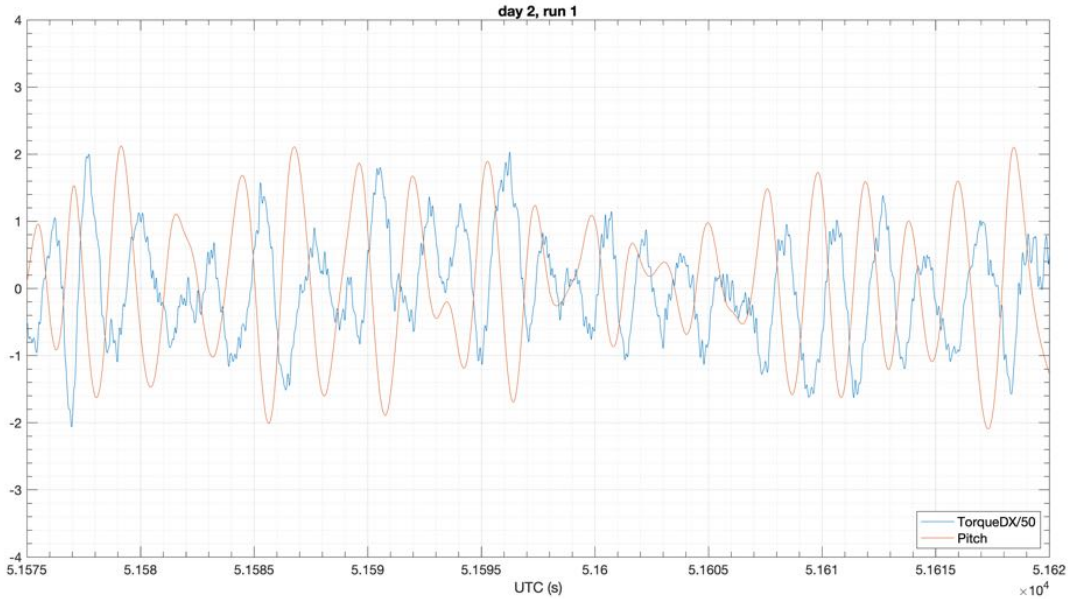

(a)

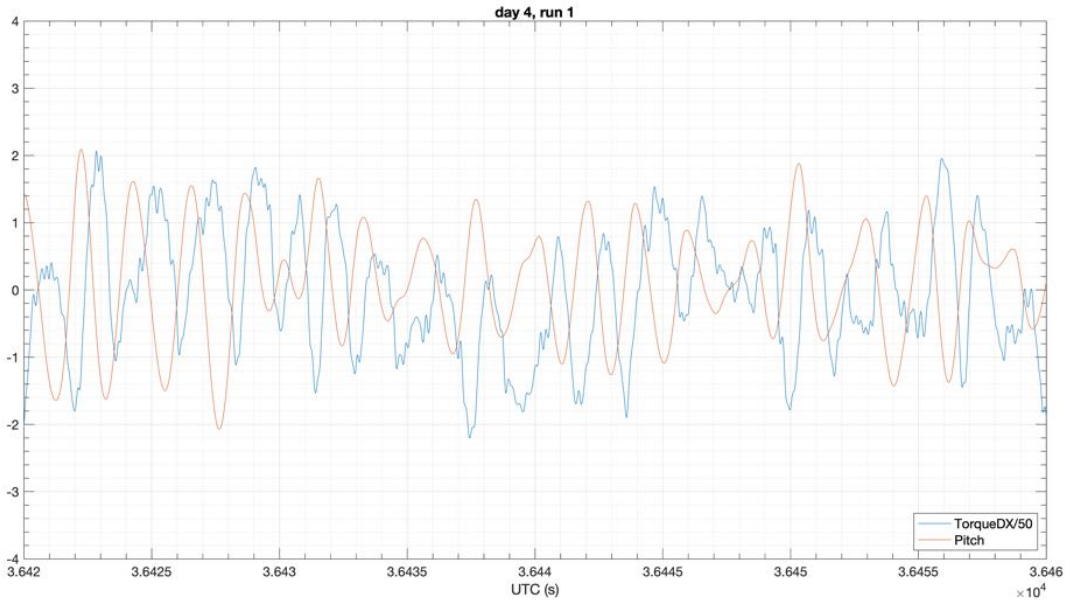

(b)

Figure 3.43: Pitch and torque timeseries comparison at 18kn

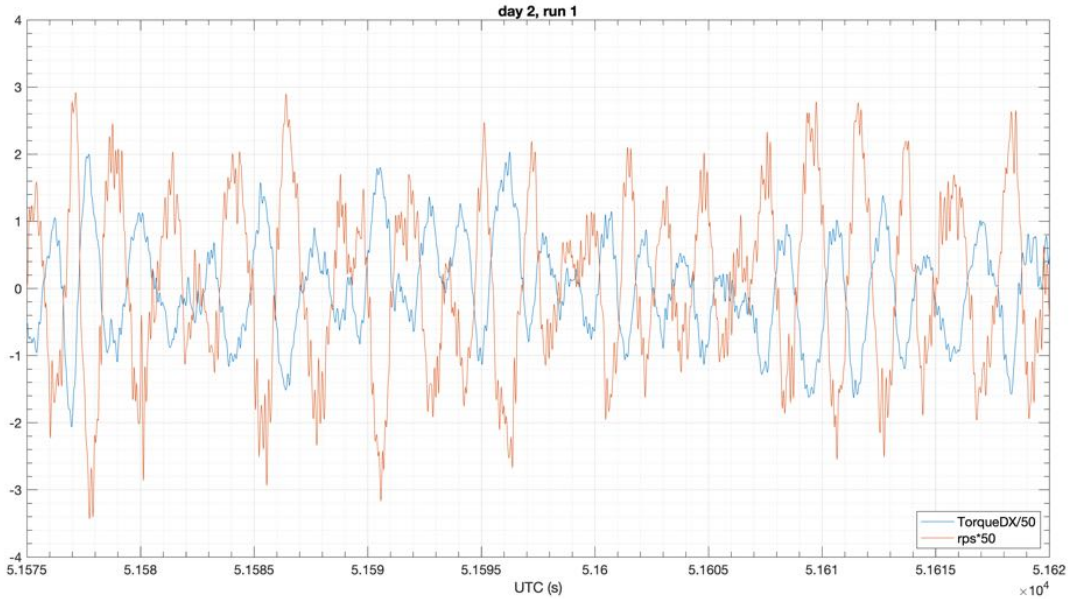

(a)

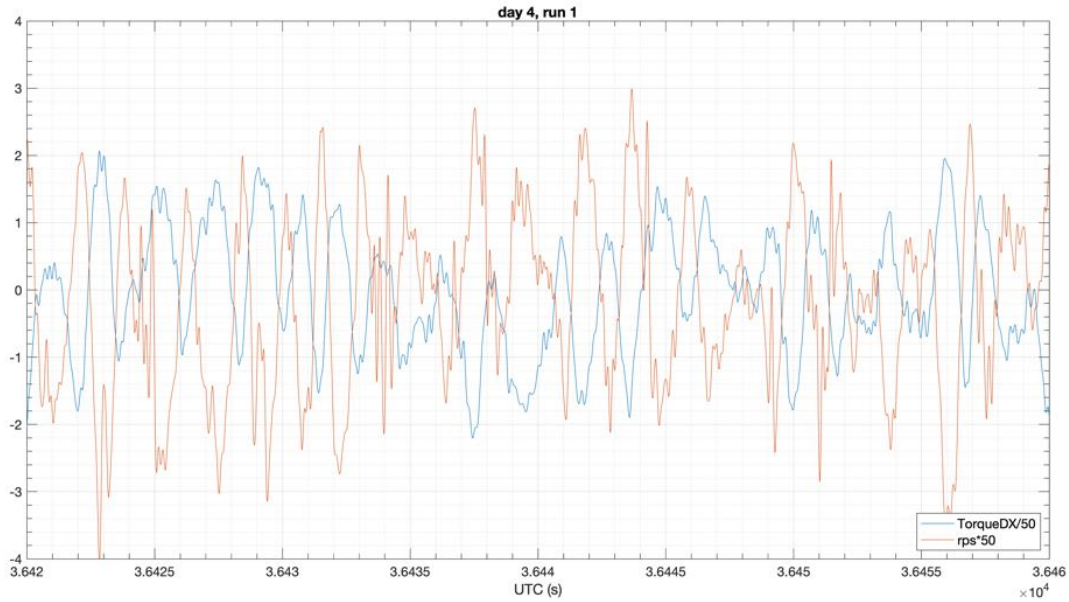

(b)

Figure 3.44: Torque and rotation speed timeseries comparison at 18kn

The data presented in Fig. 3.43 and 3.44 is relative to head sea runs at 18 kn from day 2 and 4. The analysis of the pitch and torque timeseries revealed that the torque response has a phase

lag of 115° respect to pitch motion. As expected, the analysis of torque and rpm signals revealed that torque and shaft rotation speed are in antiphase, this is easily visible in fig 3.44.

In terms of mean power output, no substantial differences were noted during seakeeping trials respect to what has been measured in calm water (figure 3.45).

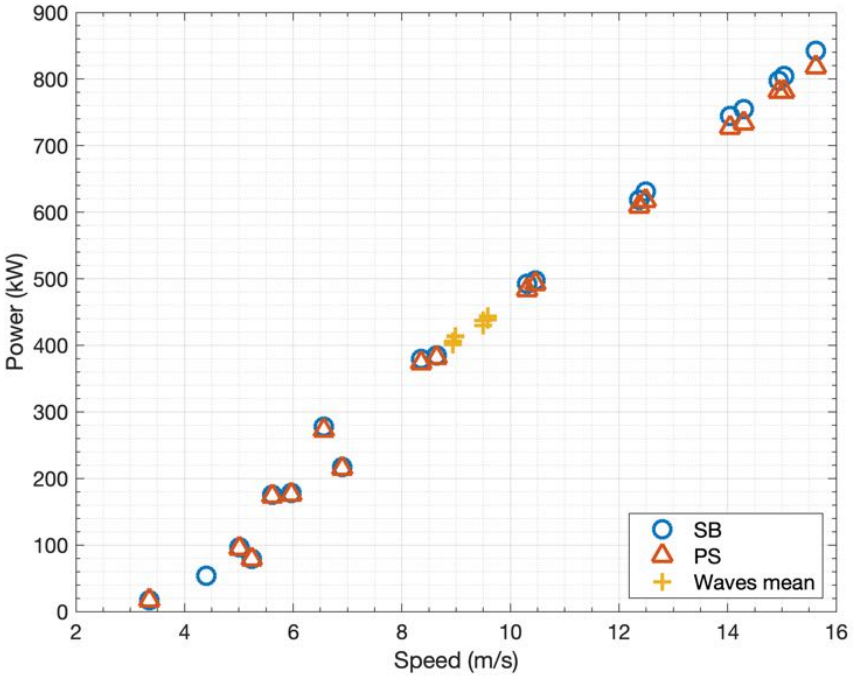

Figure 3.45: Power output in waves compared to calm water

The results shown so far in this section shows that the propulsive system is affected when cruising through mild head sea conditions. Nonetheless, although the engine response is clearly correlated to the boat motions, average values of power output did not show any significant increase respect to the case of calm water.

3.9 Closure

In this chapter, the process of planning, executing and analysis of full-scale seakeeping trials of a pleasure planing hull yacht has been presented.

A careful planning of the trials has been carried out in order to obtain a tentative scheduling long before the actual tests to maximize the number of measurements that could be made. A customized test course sequence has been devised in order to minimize the distance from the wave buoy. The ship motion and propulsion measurement systems have been tested and installed on board so that both could share a common measure and seakeeping trials have been carried out during four days.

A detailed analysis of the sea state and hull motions has been developed with the aim of improving the quality of the final result. This analysis resulted in the presented integrated approach for the analysis of data from concurrent measurements of the sea-state and of ship-motions. Multiple sources of data are combined into the proposed integrated analysis, leading from the measurements of the sea state and vessels motions to the estimation of full-scale heave and pitch (TF).

The main novelty of the proposed approach stands in its capability to compute a realistic encounter wave spectra using standard wave buoy data and directional distribution models in combination with vessel track and local bathymetry data. It is worth noting that although the integrated analysis has been here used in the particular case of a planing hull, the procedure is completely general and could be applied to any kind of ship and weather condition.

Preliminary analysis of the propulsion system measurements has been carried out and it appears that the yacht propulsion characteristics in terms of mean delivered power were not affected by the mild target sea conditions at the cruising speed. On the other side, a clear correlation between hull motions and shaft torque and rpm is found.

Some of the results of this sections have been presented at the 29th International Ocean and Polar Engineering Conference (ISOPE) in Honolulu, HI, USA with a paper entitled "Full-Scale Seakeeping Trials: An Integrated Analysis of Sea State and On-Board Data".

Chapter 4

Numerical simulations

4.1 Introduction

One of the main goals of the SOPHYA project is to use the large amount of experimental data gathered during towing tank tests and full scale sea trials in order to validate open-source simulation methodologies in the field of planing hulls.

Numerical simulations of the MCY65 planing hull in both calm water and regular waves have been carried out in collaboration with the Faculty of Mechanical Engineering and Naval Architecture of the University of Zagreb.

The collaboration is focused at the implementation and testing of the methodologies aimed at predicting hydrodynamic characteristics of planning hull in waves. In particular, the methodologies have been developed and tested within the framework of the foam-extend 4.0 software, and the Naval Hydro Pack software library [93, 94], developed by the research group at University of Zagreb, lead by Prof. Hrvoje Jasak.

With the aim of streamlining simulation workflow, an open-source fully-automated pre-processing procedure for planing hull CFD simulations has been developed. The procedure deals both with the meshing and the case folder setup, reducing the number of setup files, commands and parameters that the user have to deal. In order to correctly replicate established towing tank experimental procedures, new tools have been implemented in the solver. Further solver tools have been implemented in an effort to mitigate numerical issues related to planing hull simulations.

The results of CFD simulations have been analysed using the same procedure procedure used for experimental data, with only minor modifications due to the input file formats. This allows, especially for the seakeeping cases, a fair comparison between experimental data and CFD results.

Further regular waves simulations are then carried out on eight hull variants in order to assess the effect of geometrical parameters on the seakeeping abilities of the hull. A model of the best performing hull is then tested in the towing tank in order to validate the CFD results.

4.2 Computational facilities

The simulations carried out in this study have been performed on the cluster HyMO*lab* laboratory at the University of Trieste. The cluster has 24 computational nodes, each one having 12-core

3.07GHz xeon X5675 processors. Usually, calm water and seakeeping simulations have been carriead out using four nodes, a total of 48 process in parallel.

4.3 Automated pre-processing

4.3.1 Introduction

Pursuing the industrial goals of the project SOPHYA (Seakeeping Of Planing Hull YAchts), in particular those related to simplifying open source CFD simulations, a fully automated pre-processing procedure has been developed and tested. The procedure is based on open-source tools available in the OpenFOAM library [67]. The pre-processing time is drastically reduced making the procedure fully-automated and user friendly, still making it robust and accurate. The main feature of the procedure is the reduced number of parameters the user is required to provide in order to generate meshes for complicated geometries and set up the case easily. The proposed procedure can be employed on all hull forms and speeds, albeit tailored for planing hulls for the purposes of the present project. The procedure generates an octree based mesh with non-isotropic refinements around selected areas of interest, it allows to obtain meshes with reduced number of cells if compared to those obtained through standard octree based refinement regions having similar resolution. Hence, the smaller grid allows a further reduction of the time-to-results through reduction of the computational cost. In addition to the mesh generation, the developed procedure provides a ready to run foam-extend case for planing hull simulations.

4.3.2 Method and tools

In the next sections, the four main phases of the procedure is presented in the same chronological order of the operational procedure. The flow chart of the procedure, shown in Fig. 4.1, starts with a template case folder containing all the configuration files needed by the procedure. The only additional file the user is required to provide is a full scale geometry of the hull in *.stl* format. In the first phase, the user is expected to provide the main system parameters, i.e. hull model characteristics, domain dimensions, physical properties of water. Since the procedure creates several meshes in order to be able to choose the best quality one, in this phase the alternatives mesh case folders are created. The second phase deals with the actual meshing of the geometry, according to the input data. The third phase allows the user to easily check the quality of the generated meshes and select the best one. The ready-to-run case folder, containing the selected mesh, is then generated.

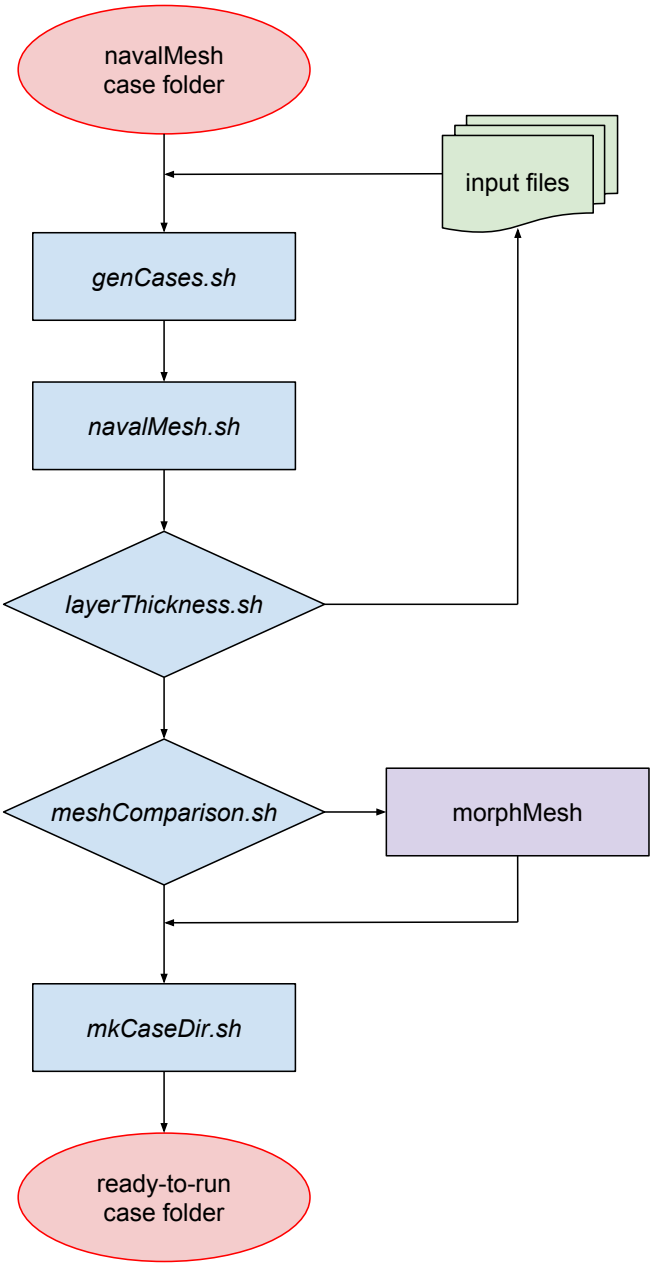

Figure 4.1: Procedure flowchart

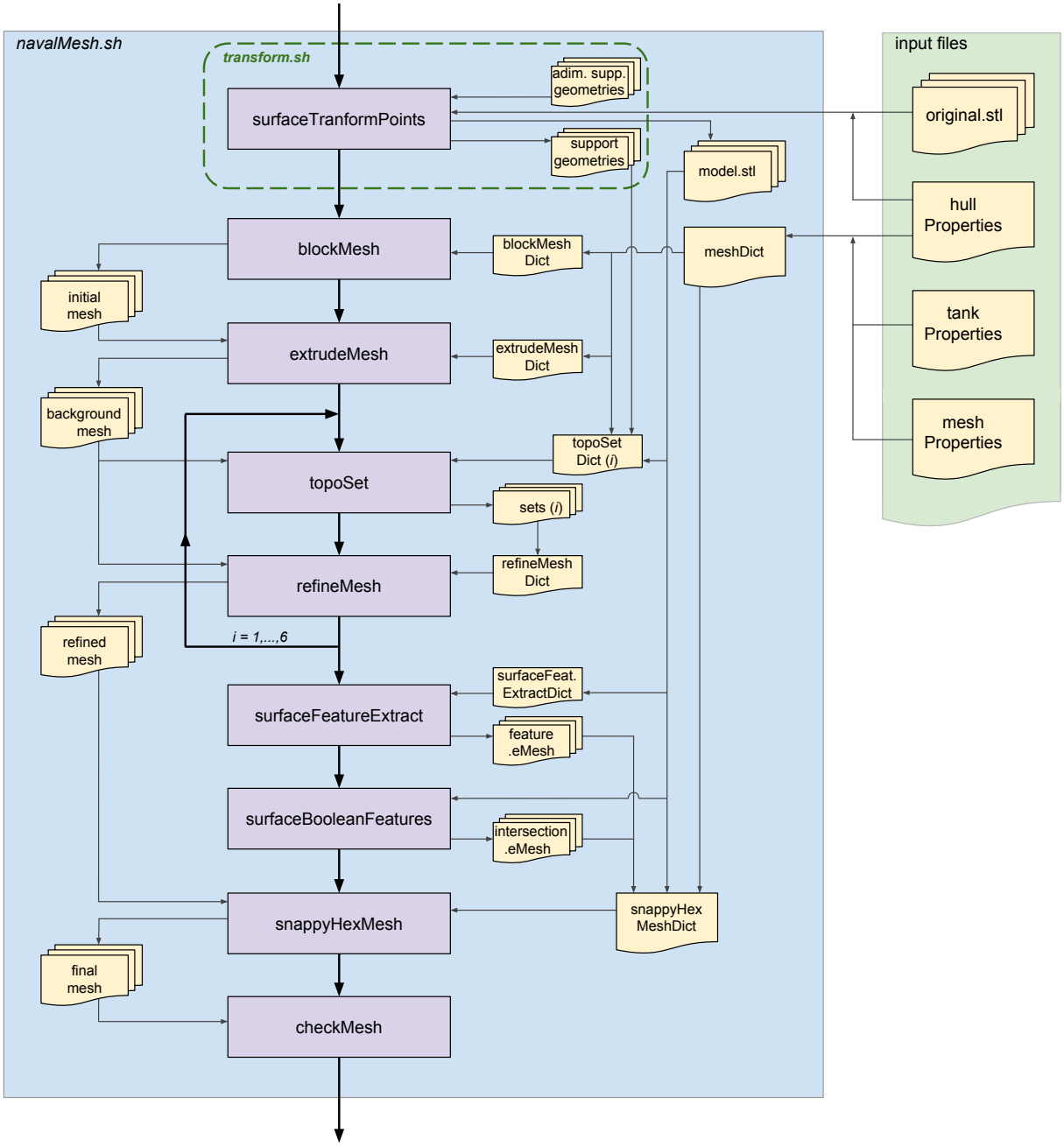

Figure 4.2: *navalMesh.sh* flow chart and file dependencies

4.3.3 Automatic grid generation

Pursuing the industrial goals of the project SOPHYA, in particular those related to the reduction of the pre-processing time-to-simulation, an automatic grid generation procedure has been developed and tested. The procedure is based on open-source tools available in OpenFOAM library. Octree

non-isotropic meshes with wall layer cells of prescribed thickness, are generated. The generation is based on very simple inputs, i.e. ship length, attitude, speed and transverse size of the basin. The grid resolution, and consequently the number of cells, is set using few simple non-dimensional parameters that depend on y^+ and Froude number. Fig. 4.3 shows a sample case.

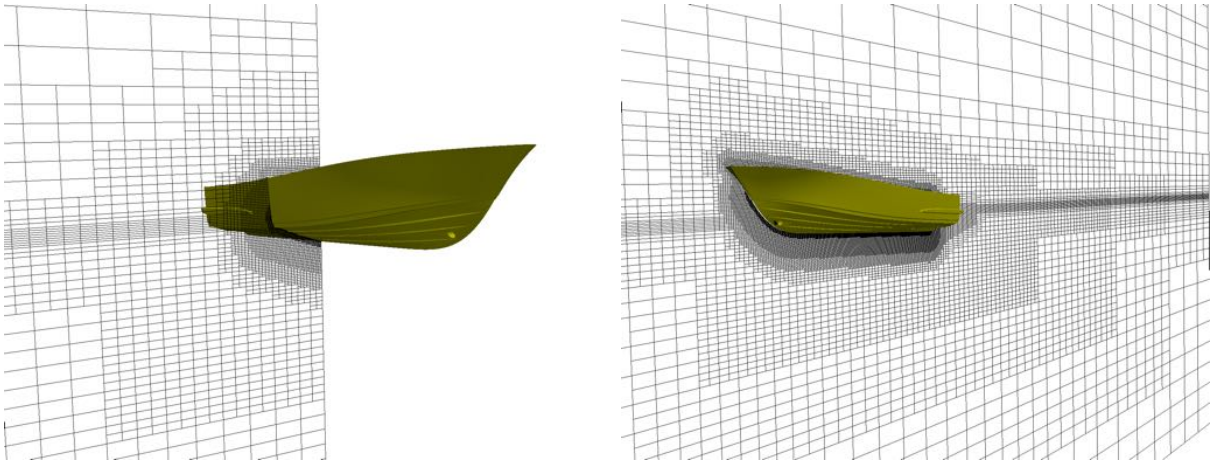

(a) (b)

Figure 4.3: Sample grid obtained with the home-developed automatic mesh generation procedure.

4.3.4 Configuration

The setup files for the proposed procedure are based on simulations of towing tank tests on a scaled model of the original Hull. The configuration phase provides for the only user input during the entire procedure, where the specified test parameters should be provided. The mandatory input parameters have been reduced to the minimum and divided into two dictionary files. In particular, the first file in which the user needs to specify data is called *hullProperties* (Fig.4.4), in this simple file the main geometrical and mechanical properties of the hull are entered, such as:

- Model length, breadth, draft, and scale;
- Model mass, centre of gravity and its moments of inertia;
- Expected model equilibrium/mean sinkage and trim at speed.

```
/* * * * * * * * * *
 *   MCY - 65feet   *
 * * * * * * * * * */

Lpp          2.46;        // [m]
B            0.74;        // [m]
T            0.18;        // [m]

vel          3.632;       // [m/s]

hullMass     143.51;      // [kg] // f(lc)
modelScale   6.5;

// Moment of inertia (CoG)
hullIxx      12.859;      // [kg m^2]
hullIyy      67.331;      // [kg m^2]
hullIzz      $hullIyy;    // [kg m^2]

// Center of Gravity (CAD frame of reference)
hullXg       1.039;       // [m]  // f(lc)
hullZg       0.302;       // [m]  // f(lc)

// Towing Point (CAD frame of reference)
towingX      1.043;       // [m]  // fixed
towingZ      0.270;       // [m]  // fixed
towZfs0      -0.0920;     // [m]  // f(lc)    // Initial Towing Point Immersion

// Trim and Sinkage (functions of LC and velocity)
trim         3.252;       // [deg]    // Positive: bow up
sinkage      -0.0014;     // [m]      // Positive: submersion
```

Figure 4.4: *hullProperties* input file

In a second file, named *tankProperties* (Fig.4.5), the size of the basin and water physical properties are specified. In case of open water simulations, the user can easily choose to avoid bottom effects using built in minimum depth formula using on the Froude number based on depth. In addition, wave properties are also specified in this dictionary to perform seakeeping simulations. A third file called *meshProperties* is also available for advanced mesh control, but it can be ignored if the results are satisfying. When the user input files have been set up, the first script *genCases.sh* generates four additional mesh folders (trimmed mesh folders) having slight trim difference respect to the actual hull position (main mesh folder). The procedure creates five different mesh folders: the main folder, containing the mesh with the actual expected hull position, and four additional folders containing meshes with slight trim variations. In particular, the hull trim values are $\tau_0 \pm 0.1$ and $\tau_0 \pm 0.2$ degrees, where τ_0 is the trim value of the main folder (expected equilibrium position). Trim value has been chosen as the parameter in this procedure since mesh quality is much more sensible to its variation respect to sinkage. This is due to the angle between the background mesh and the hull bottom.

```
nuWater      .00000092156;   // [m^2/s]  //  ITTC Fresh Water 23.6°C
rhoWater     997.3974;       // [kg/m^3] //  ITTC Fresh Water 23.6°C
grav         -9.8025;        // [m/s^2]  // Napoli

Fn              0.3; // Froude DEEP-WATER
d               4.0; // #calc "-($vel*$vel)/($Fn*$Fn*$grav)";
tankB           9.0; // #calc "$Lpp*4";
waveAmplitude   0.080; // max wave amplitude during the whole test series

waveHeight      0.0; // [m] waveHeight<2*waveAmplitude
wavePeriod      0.0; // [s]
```

Figure 4.5: *tankProperties* input file

4.3.5 Meshing - *navalMesh.sh*

The actual meshing procedure that is run for each of the five cases can be divided into eight different stages so that it is easier to understand. The following subsections will outline the tools used in the *navalMesh.sh* automated meshing procedure script, in the same order of execution. The meshing procedure flow chart, along with simplified file dependencies is shown in Fig. 4.2.

surfaceTransformPoints

The surfaceTransformPoints step is employed in order to correctly scale and translate/rotate the hull into its expected equilibrium position. The same process is applied to the support geometries in order to maintain their relative size and position respect to the hull.

The following command sequence serves to move the hull geometry from the original position to the running equilibrium position specific loading condition and speed. The new frame of reference has its origin at the towing point longitudinal position and the calm water height. The horizontal x-axis is positive towards the bow. The vertical z-axis is positive upwards.

```
surfaceTransformPoints  fullScale.stl   model.stl   -scale          "(  -1/scale 1/scale 1/scale )"
surfaceTransformPoints  model.stl       towing.stl  -translate      "(  -Xtow   0       -Ztow   )"
surfaceTransformPoints  towing.stl      trim.stl    -rollPitchYaw   "(  0       -Trim       0   )"
surfaceTransformPoints  trim.stl        sink.stl    -translate      "(  0       0       -Sinkage)"
surfaceTransformPoints  trim.stl        initial.stl -translate      "(  0       0       -Zfs0   )"
```

The variables (in blue) used in this specific step are read from the *hullProperties* file. The same procedure can be used to place the new geometry corresponding to the model attitude at rest, if trim is set to the static trim and sinkage to zero. After the transformations, the new coordinates of towing point and center of gravity are listed in Table 4.1 and 4.2.

Towing Point	
x	0
y	0
z	$-(Z_{fs,0} + Sinkage)$

Table 4.1: Towing point coordinates in final equilibrium for steady simulations.

Center of gravity for running attitude.	
x	$(X_G - X_{TOW}) \cdot \cos Trim - (Z_G - Z_{TOW}) \cdot \sin Trim$
y	0
z	$[(X_G - X_{TOW}) \cdot \sin Trim + (Z_G - Z_{TOW}) \cdot \cos Trim] - (Z_{fs,0} + Sinkage)$

Table 4.2: Center of gravity coordinates for running attitude.

blockMesh

The blockMesh tool creates the basic hexahedron-based mesh, filling the domain from the bottom boundary to the free surface (Fig. 4.7a). The cell size of the resulting grid can be customized via the correction factor `nCellsCoeffs` in the *meshProperties* file (Fig.4.6).

```
// Mesh size settings

hullRefLevel     1; // number of refinement levels in snappyHexMesh
nCellsCoeff      1; // background adimentional number of cells

// Boundary layer properties

nBoundLayers     5; // number of prismatic wall cells
growRate         1.3; // boundary layers growing rate
```

Figure 4.6: *meshProperties* input file

extrudeMesh

The existing mesh is extruded from the free surface (Fig. 4.7a) to the top boundary to fill the entire domain (Fig. 4.7b). This step ensures that cell faces lie on the still water free surface (z=0), an important mesh characteristic for free surface computations [95, 96]. In particular, if cell faces intersect the free surface upstream from the bow stagnation point, volume fraction smearing can occur, enhancing numerical ventilation[97].

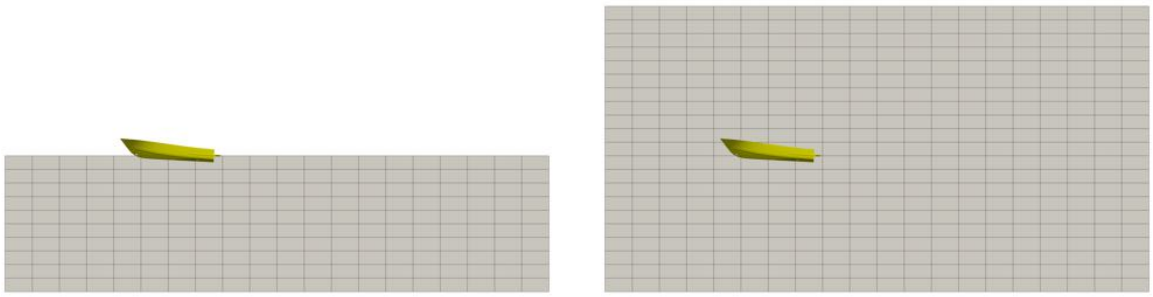

(a) Initial mesh to extrude

(b) Extruded background mesh

Figure 4.7: Background Mesh

topoSet

This step creates the necessary cells sets (mesh regions) that will be used later in order to selectively refine the existing uniform mesh. The topoSet tool uses hull and support geometries (Fig. 4.8) along with primitive box and distance-based regions (Fig. 4.9a) to achieve tvery targeted refinements.

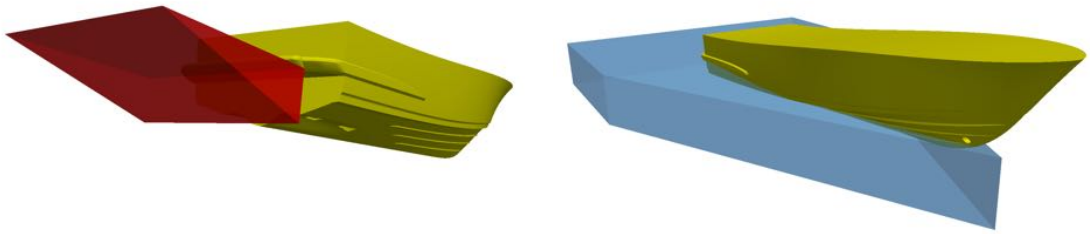

(a) Wake region

(b) Kelvin angle

Figure 4.8: Stern and Kelvin angle support geometries

In particular, free surface, hull contour and hull containing boxes are defined in the dictionary itself, where the wake and Kelvin prismatic regions are defined via additional stl geometries.

RefineMesh

The *refineMesh* stage is where the refinements are created in the previously selected regions. The sets from the previous step (Fig. 4.9a) are used to refine the mesh with three different methods: standard octree, vertical-only near the free surface and horizontal only near the hull. The combination of this three different approaches is aimed at conserving cell height along the whole free surface and having cubic cells near the hull surface. The refinements specific to the planing hull case carried out using the support geometries are shown in figure 4.10.

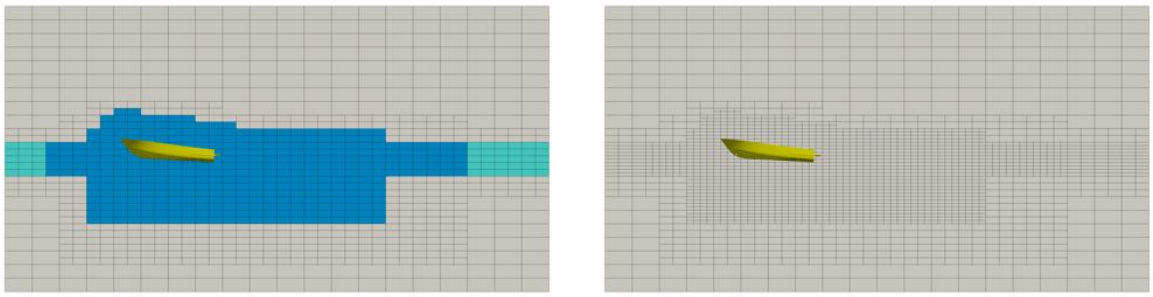

(a) Primitive box and distance-based regions

(b) Refined background mesh

Figure 4.9: Primitive regions based refinements

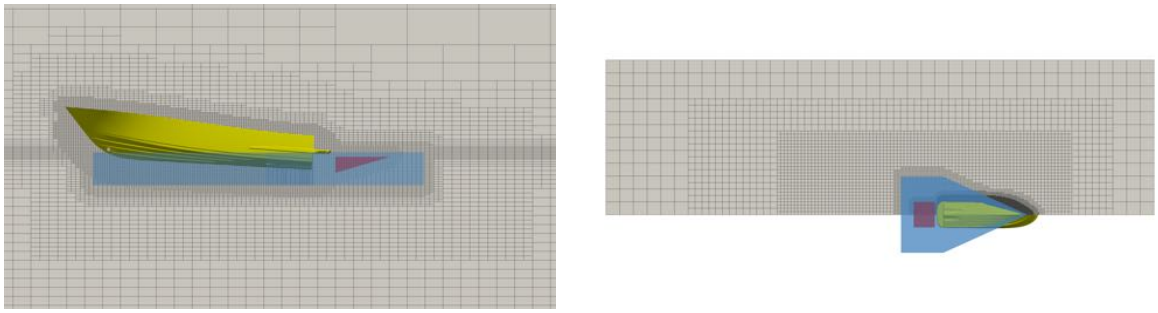

(a) Stern wake refinement

(b) Kelvin angle refinement

Figure 4.10: Support geometries based refinements

surfaceFeatureExtract

This step allows to extract important features of the hull related geometries, such as sharp corners within the surface that normally characterize spray-rails, lifting strakes and hard chines.

surfaceBooleanFeatures

The second to last step extracts important features regarding the whole hull geometry, comprised of different stl files combined. In particular, here the join lines between hull, deck, transom and appendages (Fig. 4.11a) will be extracted to achieve better results in the last meshing step.

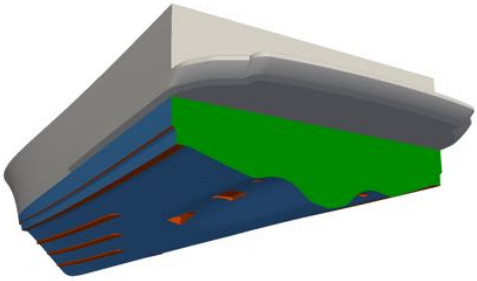

(a) Hull features

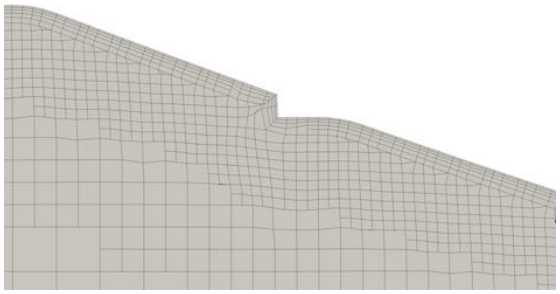

(b) Lifting strake layers detail

Figure 4.11

snappyHexMesh

The last step towards the final mesh is done through the snappyHexMesh tool, where additional refinements on and around the hull are added along with boundary layer cells addition (Fig. 4.11b). The boundary layer cells are added as the last sub-step, cell thickness at the wall is computed according to the preset y^+ value.

checkMesh

The checkMesh tool generates the mesh quality data needed in the last section of the procedure for all the five meshes. Relevant data is extracted from the resulting files and presented summarized in both tabular (Fig. 4.14) and graphical (Fig. 4.13). This step concludes the meshing phase of the procedure.

4.3.6 Mesh quality checks

Once the automated meshing procedure is completed, five slightly different meshes are created,. In order to choose which the best mesh among them, the user is provided with two different mesh quality checks, the first one concern the boundary layer cells and the second one is a direct quality comparison between the five meshes.

layerThickness.sh

This tool provides a graphical summary of the boundary cells thickness compared to the outer cell size. This representation (Fig. 4.12) provides a simpler view of the near wall structure of the grid that has been generated in the previous phase. In particular, thicknesses of both boundary cells and outer refinement region are given in millimeters, and the size comparison between the last boundary cell and the first outer cell is highlighted. This comparison is helpful to the user since boundary and outer cell size is computed independently. The boundary cell size is computed according to the preset y^+value, whereas the outer region cell size is the result of the octree refinement steps based on the hull length. For this reason, the cells size difference could be too disproportionate.

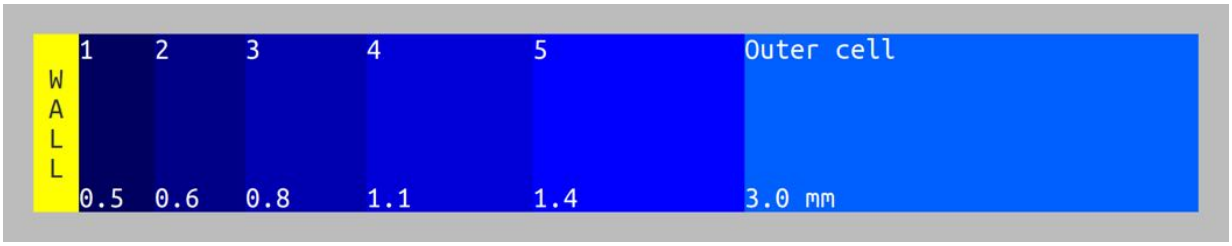

Figure 4.12: Boundary layer cells thickness and outer cell size

meshComparison.sh

The meshComparison.sh script enables the user to easily compare important mesh quality parameters between the five generated meshes. This tool will output data in two different modes. The first mode is a graphical representation of maximum values of non-orthogonality and skewness, where for both values and every mesh generated, rainbow gradient bars are displayed (Fig. 4.13). The color scale is set so that if the checkMesh step doesn't output any warning, only shades of green are visible.

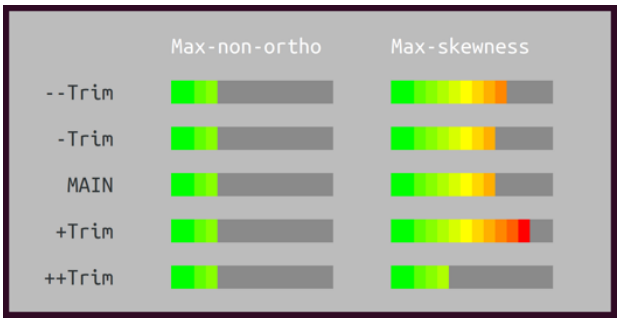

Figure 4.13: Graphical mesh quality comparison

In addition to the first simplified graphical representation, a tabular summary of maximum values of non-orthogonality and skewness, along with average boundary layer cells total thickness on both hull and appendages is shown (Fig. 4.14). In addition to the actual values of the mesh quality parameters, the check mesh warning message is color coded and reported in the first column.

	Ceck-mesh	Max-non-ortho	Max-skewness	Layer-thickness	
--Trim	Failed 1 mesh checks.	69.955 ()	4.930 (1)	80.6	(53.6)
-Trim	Failed 1 mesh checks.	69.955 ()	4.747 (2)	80.9	(54.3)
MAIN	Failed 1 mesh checks.	69.955 ()	4.674 (2)	80.5	(54.5)
+Trim	Failed 1 mesh checks.	69.955 ()	5.313 (1)	80.4	(52.7)
++Trim	Mesh OK.	69.954 ()	3.917 ()	80.7	(54.3)

Figure 4.14: Mesh quality parameters table

Mesh morphing configuration

Since the procedure provides five meshes each with a different hull position, if the best mesh is not the main one, it will need a re-positioning step to correct the trim angle. order to move each hull back to its original position. At this point, the user is expected only to execute the *morphMesh* application. The *morphMesh* application rotate the hull to the original (main case) trim angle from the best mesh case. In order to do so, the mesh around the hull is morphed using the same technique employed for dynamic meshes. Being the morphing minimal, it poses no particular issues in terms of added skewness.

Case folder preparation

Once the best mesh is selected (in case also morphed), the last step of the procedure creates a ready-to-run folder to be used with NavaHydro Pack solvers, based on foam-extend [98] library. Initial and boundary conditions for the $k-\omega$ SST model (according to Menter [99]), pressure and velocity are computed and written into the corresponding *initialConditionsDict* dictionary.

The dimensions of the relaxation zones are also set to mitigate wave reflections. Hull mass and inertia are halved, the coordinates of the center of gravity are updated according to the simulation frame of reference and mass inertia moments are calculated respect to the towing point (restrained). Ready-to-run folders for both VoF and Level Set method are created, along with optional seakeeping dictionaries in case of non-zero wave height in the *tankProperties* file. The proposed pre-processing procedure proved successful in producing highly detailed meshes used in the study of planing hull. The automated process ensures minimal user effort in the pre-processing phase, virtually eliminating the risk of user errors. The comparison between the number of manual operations that would be required by the user in order to do the same process and the manual operations needed with the present procedure is shown in Fig. 4.15. The operations are divided into three categories: commands (on terminal), file edits (dictionaries) and calculations (gradings, cell size, turbulence model initial conditions etc.). It is important to note that the red columns reported in the figure refers only to the generation of a single mesh, where the procedure (blue columns) is relative to the five (or more) alternative meshes that are automatically produced. Since the number of required user operations can be easily related to both time-to-simulations and number of possible user induced errors, the large advantages of the proposed method are evident.

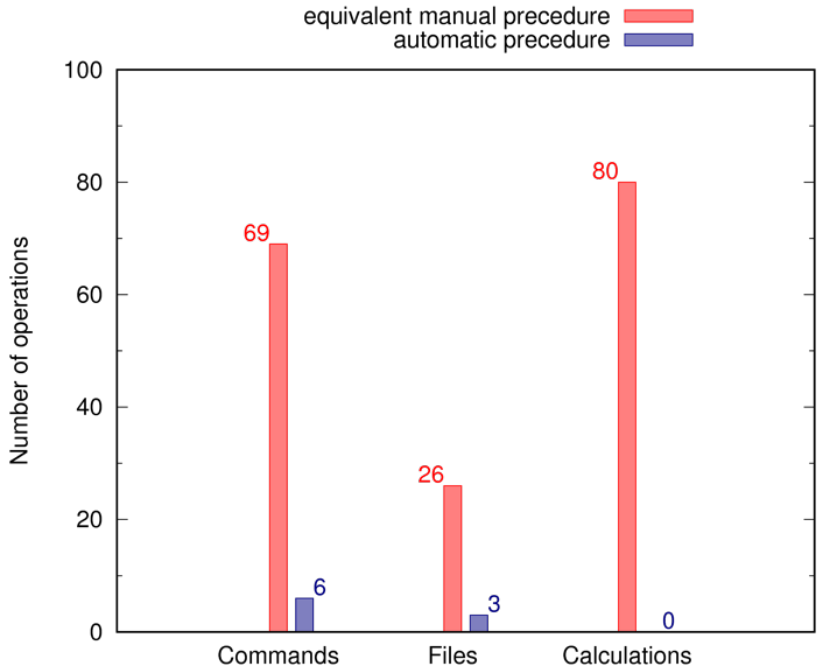

Figure 4.15: Required user operations comparison

In Fig. 4.16 the free surface elevation in the stern wake region is shown. The role of the wake region refinement in better resolving the wake free surface can be clearly seen.

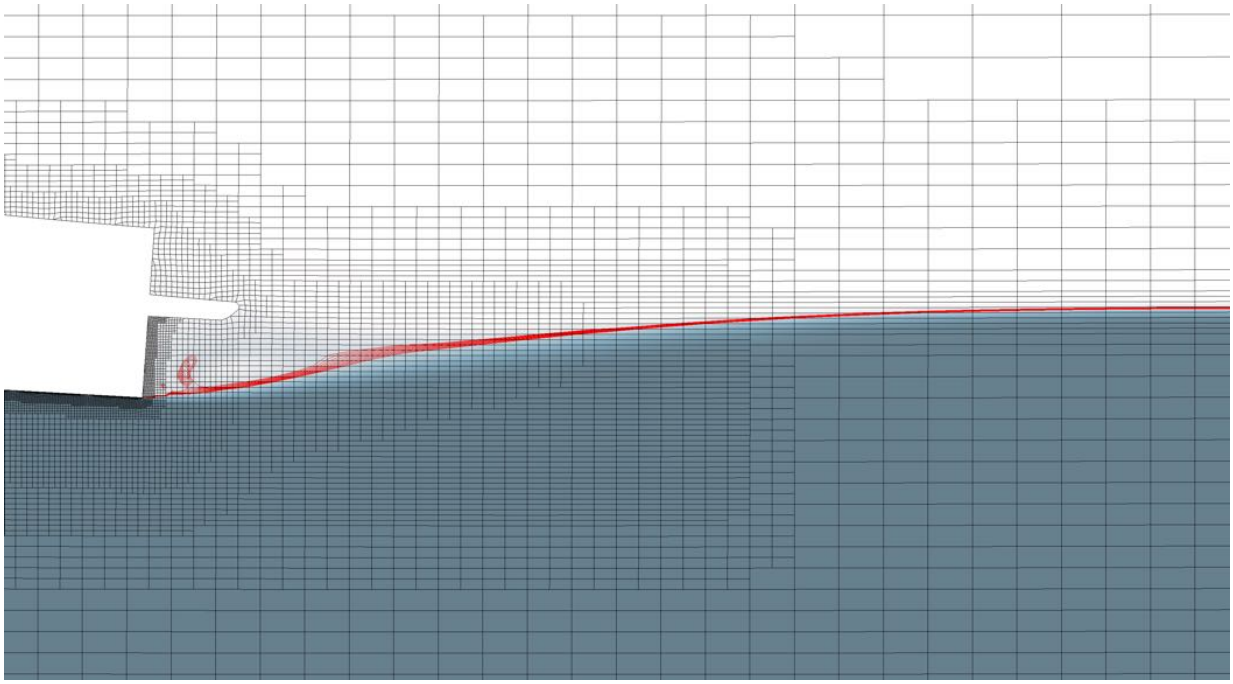

Figure 4.16: Stern wake free surface elevation inside the refinement regions

In conclusion,the procedure is capable of reducing the time-to-results of open source CFD simulations, both reducing time-to-simulation with an automated meshing procedure and case folder generation and computational time thanks to a high quality mesh with reduced number of cells. The procedure greatly reduces the number of file edits and user input files, it is also open source and easily to customize. The proposed workflow is able to generate meshes with complex refinement details and outputs quality reports that are compact and easier to read.

4.4 Calm water simulations

4.4.1 Introduction

For the calm water simulations, the *Navalfoam* two-phase, incompressible, viscous and turbulent flow transient solver, included in the Naval Hydro Pack software library has been employed. The Two free surface modeling techniques have been tested in preliminary simulations: the Level Set (LS) approach as described in Vukčević et al. [100, 101], and the Volume of Fluid (VoF) method [102].

Issues related to numerical ventilation (NV) are discussed according to the results of VoF and Level Set interface capturing methods. In order to deal with NV using the VOF method, a special, ventilation suppression method has been implemented following Viola [103].

Results of calm water simulations are then compared with experimental results and the main differences discussed.

4.4.2 Mathematical Model

The equations are discretised using collocated Finite Volume (FV) method implemented within foam–extend open-source software. Software library called Naval Hydro Pack based on foam-extend is used, specialized for large-scale two-phase flows encountered in naval hydrodynamics. A thorough validation study of the library solvers on full-scale naval hydrodynamic case can be found by Jasak et al. [104]. The two-phase, incompressible, turbulent and viscous flow model is employed, governed by the continuity and Navier-Stokes equations:

$$\nabla_{\bullet}\mathbf{u} = 0\,, \tag{4.1}$$

$$\frac{\partial \mathbf{u}}{\partial t} + \nabla_{\bullet}((\mathbf{u} - \mathbf{u}_M)\,\mathbf{u}) - \nabla_{\bullet}(\nu_e \nabla \mathbf{u}) = -\frac{1}{\rho}\nabla p_d\,, \tag{4.2}$$

where $\mathbf{u}$ stands for the velocity field, $\mathbf{u}_M$ is the grid velocity acconuting for the Space Conservation Law [105], ν_e is the effective kinematic viscosity allowing eddy viscosity turbulent modelling, and ρ stands for the discontinuous density field. p_d is the dynamic pressure calculated as: $p_d = p - \rho \mathbf{g}_{\bullet}\mathbf{x}$, where $\mathbf{g}$ denotes the gravitational acceleration and $\mathbf{x}$ the radii vector. In order to properly resolve the discontinuity of density and dynamic pressure at the free surface, interface-corrected discretisation schemes based on the Ghost Fluid Method (GFM) are employed [94]. This approach removes the problem of spurious air velocities occurring in the air phase next to the interface.

The present GFM takes into account only the normal stress balance, while the tangential stress balance is approximated by blending the dynamic viscosity using the volume fraction variable α:

$$\nu = \alpha \nu_{water} + (1 - \alpha)\,\nu_{air}\,, \tag{4.3}$$

where ν presents the dynamic viscosity of the mixture, while ν_{water} and ν_{air} denote dynamic viscosities of water and air, respectively.

Two free surface capturing methods are used and compared in this work: the Volume of Fluid (VoF) method and the Level Set (LS) approach. In VoF method the volume fraction variable α is transported using the following equation:

$$\frac{\partial \alpha}{\partial t} + \nabla_{\bullet}(\mathbf{u}\alpha) + \nabla_{\bullet}(\mathbf{u}_r \alpha(1 - \alpha)) = 0\,, \tag{4.4}$$

where the third term presents the interface compression using the compression velocity $\mathbf{u}_r$ following [106]. In the LS approach, implicit redistancing is used to maintain the sign distance characteristic of the field [100]:

$$\frac{\partial \Psi}{\partial t} + \nabla_{\bullet}(\mathbf{c}\Psi) - \Psi \nabla_{\bullet}\mathbf{c} - b\nabla_{\bullet}\left(\nabla \Psi\right) = b\frac{\sqrt{2}}{\epsilon}\tanh\left(\frac{\Psi}{\epsilon\sqrt{2}}\right)\,, \tag{4.5}$$

where Ψ stands for the Level Set field, while b and ϵ stand for diffusion coefficient and width parameter, respectively. $\mathbf{c}$ is the modified convective velocity. For further details regarding LS interface capturing method the reader is referred to Vukčević et al. [94].

For the simulations where dynamic sinkage and trim is calculated, a geometric method is used to integrate the rigid body motion equations [107]. Surge, sway, yaw and roll degrees of freedom

are constrained using Lagrange multipliers. The numerical model has proved accurate and robust and it has been employed in the recent past in variety of applications related to fluid-structure interaction, with or without free surface [96, 108, 109].

4.4.3 Simulations setup

The calm water simulations are carried out in model scale ($\lambda = 6.5$), the hull is free to translate vertically (heave) and rotate around the towing point (trim).

Since in the model experiments the towing point was not in the centre of gravity and the rigid body motion solver allowed constraints to be applied only to it a new constrain method has been implemented. In order to correctly replicate established towing tank experimental procedures, the new constraining method allows for rotational and translational restraint to be applied on an arbitrary point.

Once the towing point coordinates respect to the center of gravity are specified in the *dynamicMeshDict* dictionary, the moments of inertia respect to the towing point are computed internally and so the additional pitching moment due the model mass respect to the towing point.

The mesh has been has been generated with the *navalMesh* open-source fully-automated meshing tool presented in 4.3. The domain width and depth are set according to the towing tank measures specified in 2.1 and it spans $2L_{PP}$ in front of the hull and $5L_{PP}$ aft. The final mesh has approximately 1.58 million cells (see fig 4.3, 4.11b and 4.16 for some mesh refinement details).

The simulation time step is dinamically adjusted in order to keep the Courant number $Co < 1.0$ and the simulation is carried on so that that the hull attitude and resistance converge.

Initial and boundary conditions

Uniform distributed velocity equal to the carriage mean speed is set at the inlet and outlet boundary,

Uniform static pressure is set to zero on the whole domain. For k and ω, uniform values are also set across the domain and their values have been computed following the Menter [99] approach.

Relaxation zones

A particural issue that can easily interfere with the solution of computational naval hydrodynamic is due to wave reflections inside the domain. In order to avoid that the waves generated by the hull could be partially reflected back into the domain by the far-field boundary, the domain decomposition using relaxation zones proposed by Vukčević [100] has been adopted.

The decomposition method splits the fluid field into a perturbed and incident components:

$$\vartheta = \vartheta_I + \vartheta_P \tag{4.6}$$

The scope of the relaxation zones is to make the perturbed component vanish by prescribing the incident component at the boundary.

Given the transport equation of a variable ϑ, the transport operator Tr is defined as:

$$Tr(\vartheta) = \frac{\partial \vartheta}{\partial t} + \nabla_\bullet(\rho \mathbf{u} \vartheta) - \nabla_\bullet(\nu \nabla \vartheta) - S = 0 \tag{4.7}$$

where **u** is the convecting field, ν the diffusion coefficient and S the source term.

A relaxation zone operator $Rz(\vartheta_P)$ is defined here as a function of the perturbed component only.

The relaxation zones have been applied along the inlet, outlet and side of the domain, and between them and the CFD region lies a blending zone, where the two operator are smoothly blended using a weight field w:

$$(1-w)Tr(\vartheta) + wRz(\vartheta_P) = 0 \tag{4.8}$$

This methods requires the domain to be decomposed in two regions:

1. **CFD region**, where $w = 0$ and fields are computed via the transport operator Tr.
2. **Relaxation zone**, where $0 < w < 1$ and the perturbed field is forced to vanish.

At the boundary, $w = 1$ and fields are prescribed so that they match the boundary conditions (uniform flow, calm water).

The weight field follows an exponential law inside the blending zone of length λ. In Fig. 4.17, the blending zones, along with the weight field trend is shown for regular waves case.

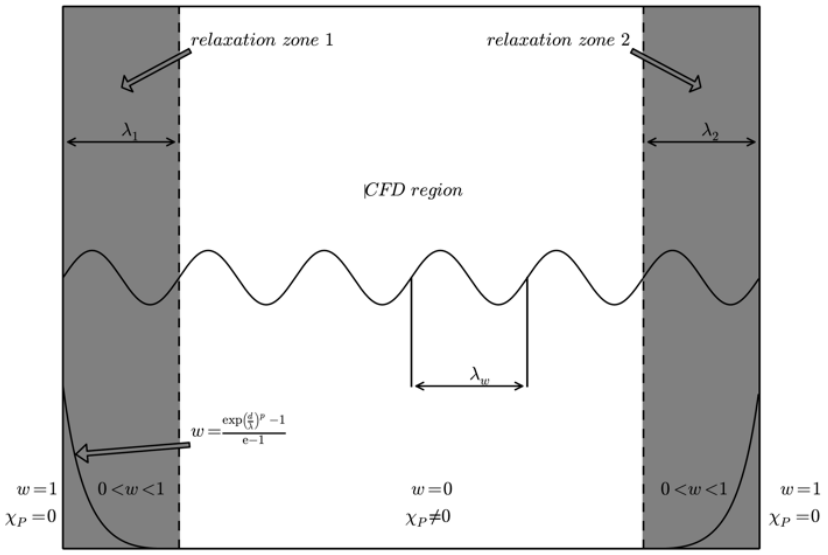

Figure 4.17: Relaxation zones and wheight field, from [100]

4.4.4 Preliminary simulations

In the following, the preliminary results obtained by means of the two different interface capturing methods described in Section 4.4.2, namely VoF and LS, are discussed. The investigation is carried out in model scale. Fixed sinkage and trim conditions are enforced, corresponding to the position of the hull as measured in model scale experiments. Preliminary simulations were focused at

highlighting the differences between the two interface capturing methods and eventual issues arising in the particular case of a planing hull. From the first tests it was clear that LS results were closer to the experimental results, and the most obvious difference between the two solutions was the presence of air-rich mixture under the hull for VoF simulations.

It is well known from the literature that numerical ventilation (NV) issues may be encountered in VoF-based numerical simulations of yacht hydrodynamics. NV manifests itself when volume fraction smearing is transported along the whole wetted hull, leading (among other effects) to lower viscous stresses [110]. In order to limit this effect, different approches [103] have been adopted, among all, the artificial suppression method is the most used. This method consist basically in adding a negative source term to the volume fraction transport equation if the volume fraction is above 0.5 and and the wall distance is lower than an arbitrary distance. Other methods aim at solving the problem using a different advection schemes, such as modified HRIC [111]. This method aims at reducing volume fraction smearing at the interface in order to limit NV.

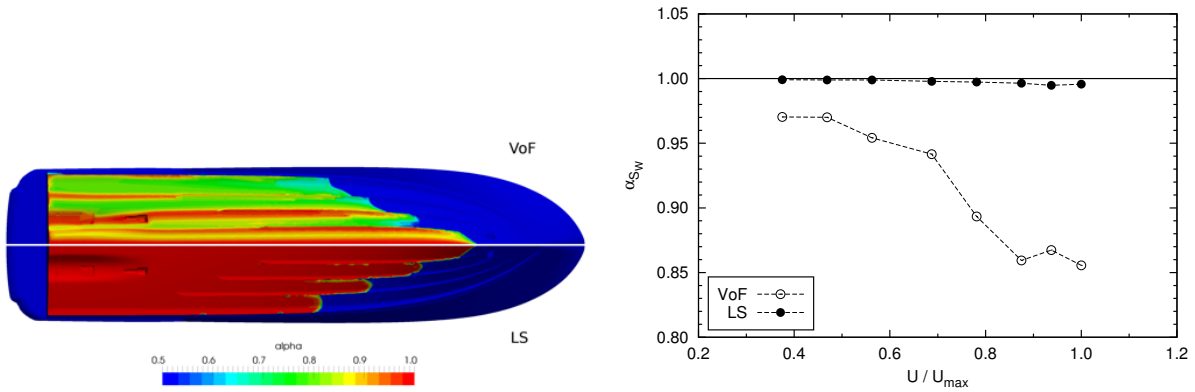

(a) (b)

Figure 4.18: (a) Bottom view of the volume fraction on the wetted hull surface using VoF (upper) and LS (lower) at the highest design speed. (b) Volume fraction on the wetted hull surface, both with VoF (○) and LS (●), as function of hull speed.

The way NV in the VoF method influences the results is the following. Since the dynamic viscosity is calculated using Eq. 4.3, the mixture viscosity on a considerable portion of the wetted surface is significantly lower than the actual viscosity of water.

Fig. 4.18a shows the volume fraction on the wetted hull surface. The geometry of the wetted surface at the bow is significantly different: in LS simulation, the wetted surface exhibits a step-like behaviour caused by spray-rails, while the smearing of the VoF field partially diminishes the effect of the spray-rails, increasing the overall wetted surface. In Fig. 4.18b the effect of hull speed on NV in highlighted. The benefits of using LS method are clearly visible, especially at high speed.

Consequences of NV are clearly observed on the pressure distribution along the hull. Fig. 4.19 shows the non-dimensional dynamic pressure along three longitudinal cuts on the hull surface for both VoF and LS simulations. Going the bow stagnation point toward the stern, an increasing

difference between VoF and the LS pressure is found. The smaller viscosity (due to NV) causes smaller pressure drop along the hull with respect to the simulation with LS. As a consequence of VoF field smearing at the bow, the pressure peak in Fig. 4.19b is also smeared, while the peak in Fig. 4.19c is shifted towards the bow.

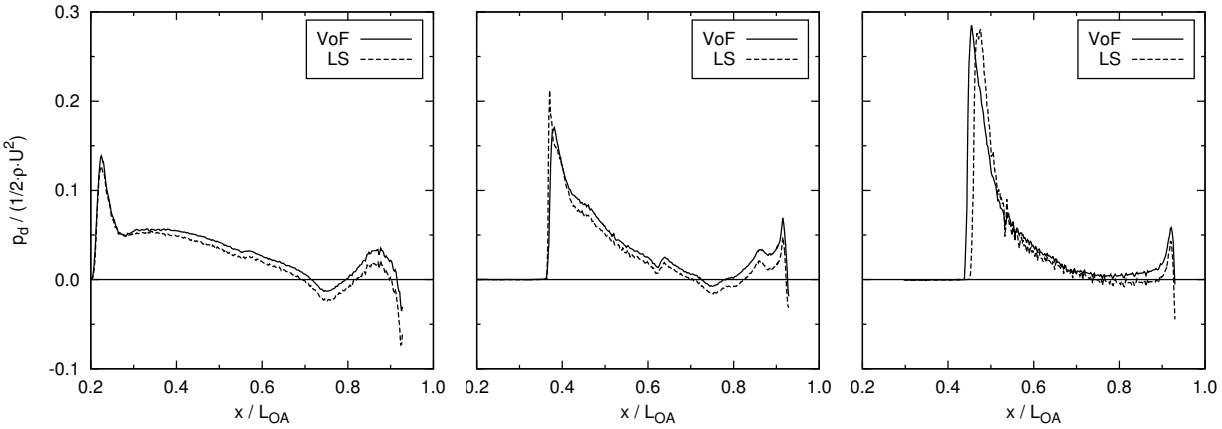

(a) (b) (c)

Figure 4.19: Non-dimensional dynamic pressure along three longitudinal cuts (10% (a), 50% (b) and 80% (c) of the hull half-width) on the hull surface at the highest design speed. Solid line: VoF; dashed line: LS.

The smaller pressure drop in turn influences the integral vertical pressure force and the pitching moment as shown in Fig. 4.20. The Figure shows the non-dimensional error in the vertical force and in the pitching moment with respect to the towing point.

Hence, since the geometry of the interface-hull intersection is of paramount importance for performance of planning crafts, LS method presents a better option for interface capturing.

Finally, the consequences of NV on the pressure distribution along the hull, can be easily observed in free trim and sinkage simulations. Fig. 4.21 shows the time series of the non-dimensional sinkage (a) and trim (b) during the 2-DoF simulation (VoF and LS) at the highest design speed. The largest differences between VoF and LS are found in the trim angle.

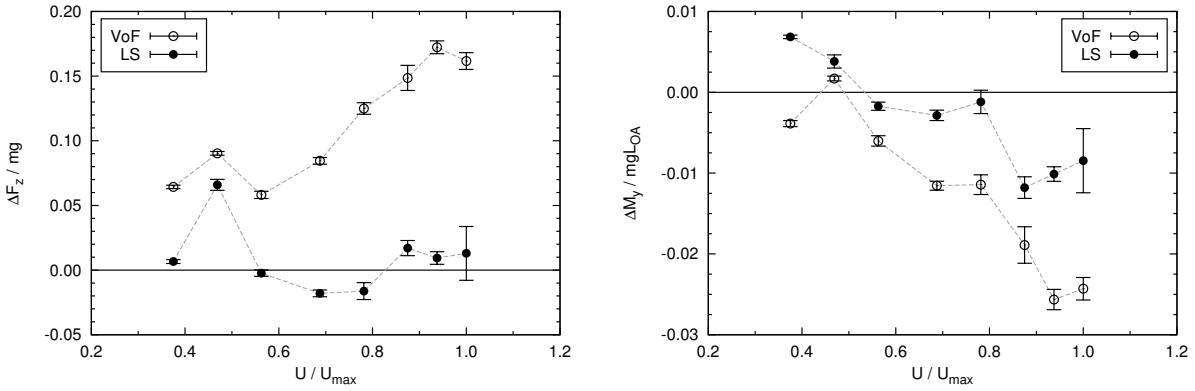

Figure 4.20: Non-dimensional error in the vertical force (a) and in the pitching moment (b) with respect to the towing point. VoF (○) and LS (●) simulations.

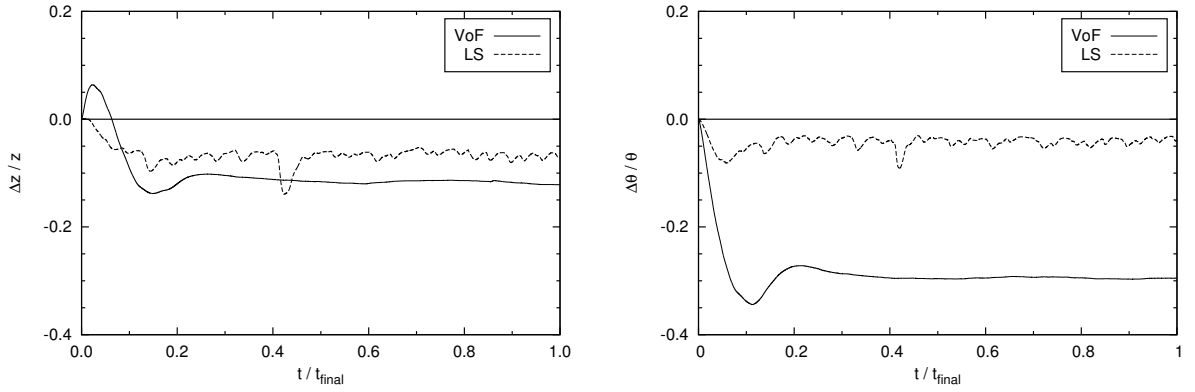

Figure 4.21: Time series of the non-dimensional sinkage (a) and trim (b) during the simulation at the highest design speed. Solid line: VoF; dashed line: LS.

4.4.5 Simulations and results

The preliminary simulations in calm water clearly showed the advantages of the Level Set method over the volume of fluid, first of all it essentially eliminate the known problem of numerical ventilation. This method lead to smaller errors in the estimation of the hull attitude and in term also its total resistance, making it a natural choice moving forward with the simulations.

The calm water simulations for the model were carried out for the design loading condition (LC1) using the *navalFoamLeveSet* solver. A calm water simulation on 48 cores usually take around 1 hour per run, the 8 runs taking approximately 7 hours of computation time.

In Fig. 4.22, the wake formation at v=5.044 m/s is highligthed, bow wave, near transom wake and rooster tail are clearly visible. The effect of the relaxation zones on the sides and on the

outlet could be seen as the wake flattens out.

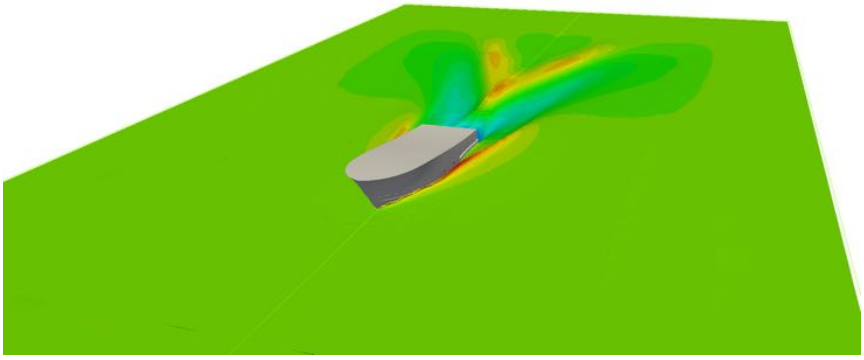

(a) Front view

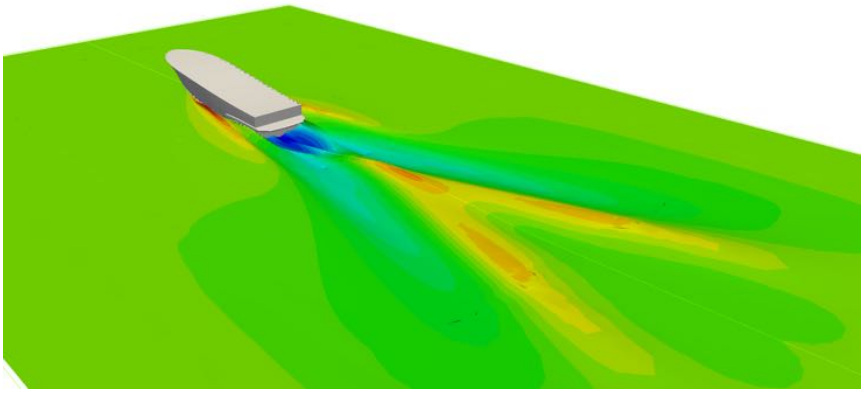

(b) Stern view

Figure 4.22: Free surface elevation in calm water, v=5.04 m/s

In the next plots, total resistance, trim and sinkage results are shown and compared to model experiments. The plots show error bars for the 2σ values of resistance, in the case of trim and sinkage, maximum and minimum values of the windowed time series are used. The data analysis of the simulation results shows that apart from the lowest speed case, the total resistance (Fig. 4.23) of the simulated cases is lower than the experimental measurements. The general trend of the resistance is more or less similar, the differences are more pronounced between 4.45 and 5.65 m/s. The fact that the total resistance is underestimated in the simulations is consistent with the results of running trim. Lower running trim leads to less total resistance since the aft-oriented horizontal component of the total lift force is smaller.

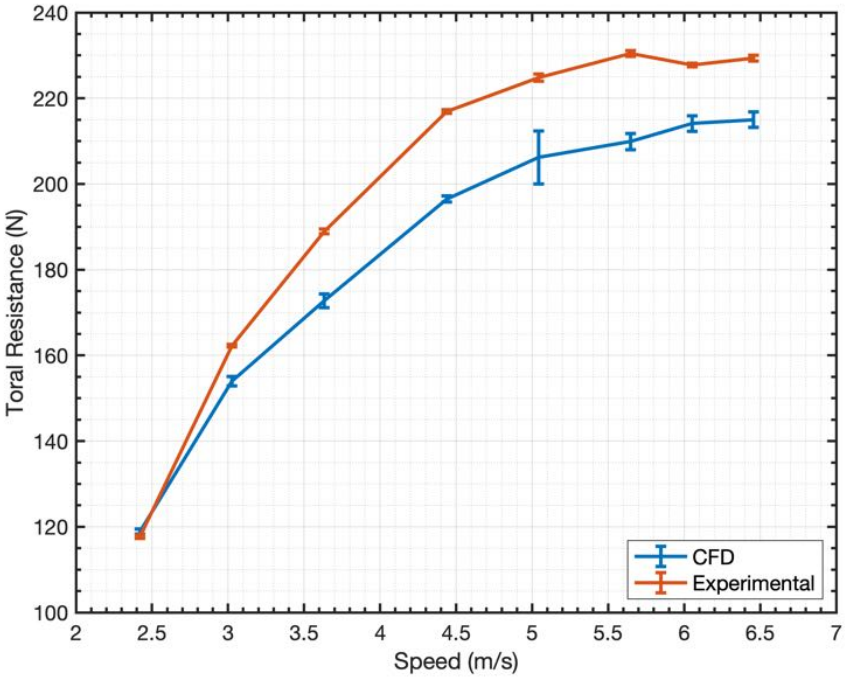

Figure 4.23: Calm water resistance results comparison

Looking at the results of the running trim, it is obvious that, apart from the lowest speed case, the simulations underestimate the running trim. The differences between experimental and simulations are much more pronounced, especially at higher speeds. Comparing trim and resistance results it is clear that a better estimation of the running trim at low speed (2.4 to 3.0 m/s)leads to resistance values that are closer to the experimental measurements, and the greater the gap between experimental and CFD results, the greater the difference between measured and CFD resistance. Nonetheless, bth CFD and experimental results show a decrease of the trim angle for the two highest speeds, and that coincides with a flattening of the resistance curves.

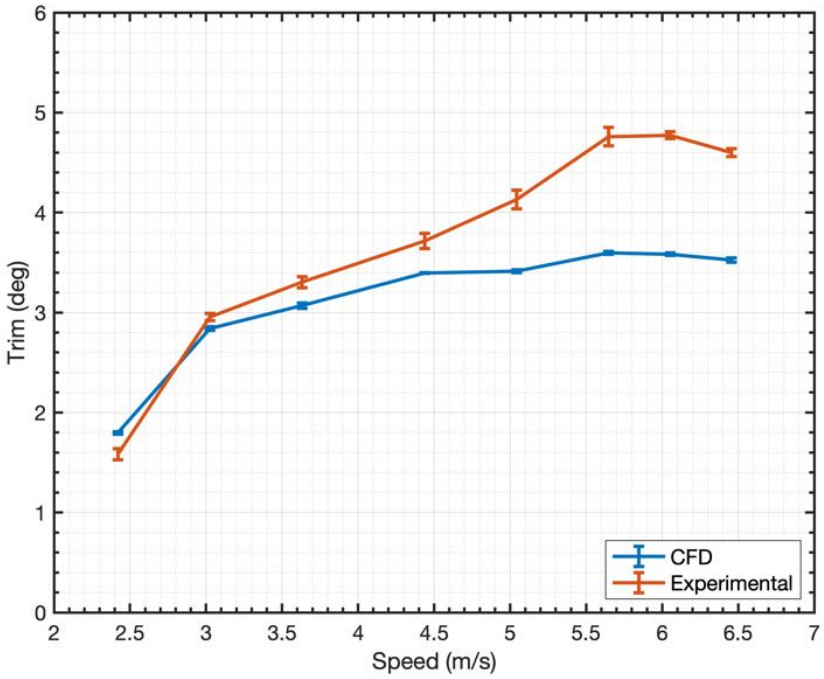

Figure 4.24: Calm water trim results comparison

The comparison between experimental and computational sinkage values shows that the two curves are closer respect to the case of trim. in particular, the computational results overestimate experimental values only for speeds greater than 3.63 m/s. at lower speeds (where also the trim shows better estimation) sinkage is underestimated. The the fact that sinkage is more overestimated for higher speeds could also be linked with the underestimation of the trim value. Lower trim values lead to lower total lift force and hence the hull is have to be more immersed to balance its weight. It is important to point out that trim and sinkage values are tightly dependent on each other, so it is not possible to draw definitive observations since trim values at higher speeds show a large discrepancy.

Further work towards better estimation of the running attitude of a hard chine warped hull planing hull could see the use of overset (chimera) mesh instead of mesh morphing, De Marco et al. [70] showed that the overset method lead to better estimation of the running attitude of a stepped planing hull in calm water.

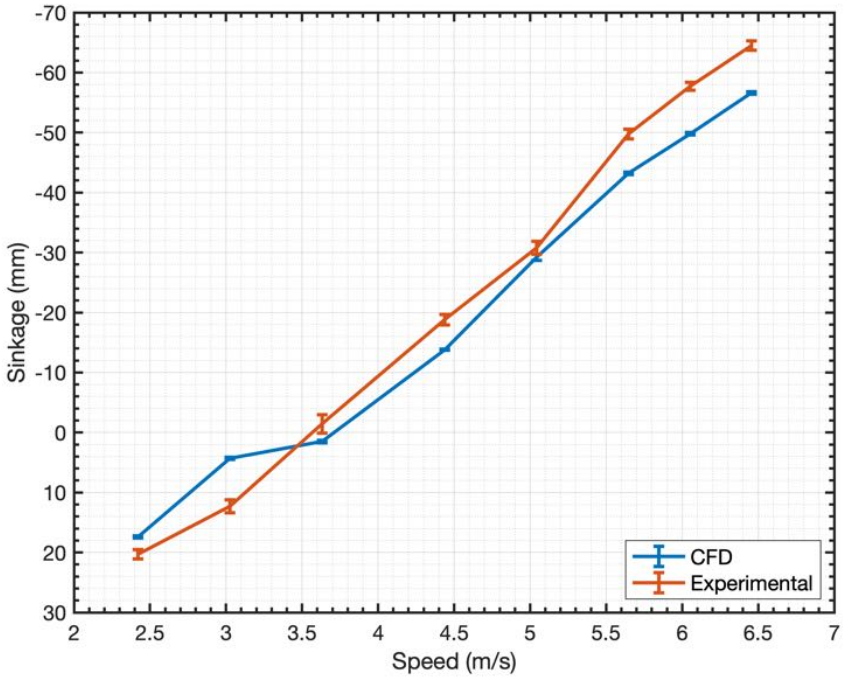

Figure 4.25: Calm water sinkage results comparison

4.5 Regular waves

4.5.1 Introduction

Numerical simulations of the MCY hull in regular waves have been carried out following the previous calm water simulations with the aim of comparing CFD and experimental transfer functions. This investigation is an important part of the SOPHYA project as it allowed to verify that the Naval Hydro Pack transient solver was able to estimate planing hull motions in waves with a satisfactory accuracy. Due to time and resources constraints, only the design speed of 18 kn (full scale) has been tested.

4.5.2 Simulations setup

The seakeeping simulations are carried out in model scale ($\lambda = 6.5$), the hull is free to translate vertically (heave) and rotate around the towing point (pitch). The same constraining method as in the case of calm water has been employed.

In order to log linear acceleration on the same places where accelerometers were placed during towing tank seakeeping tests, a simple tool has been implemented to the Naval Hydro Pack suite. The tool use rotational and linear acceleration data already computed by 6-DOF [112] solver to compute the linear acceleration in arbitrary points whose coordinates are specified in a dictionary

file entry.

Numerical wave probes have been used in order to check wave characteristics near the hull. In order to account wave amplitude losses inside the CFD region, preliminary simulations of wave propagation without the hull have been performed. The amplitude measurements at the same coordinate of the hull center of gravity were compared with the prescribed (desired) value. The ratio between the measurements has been then used as a "numerical wavemaker" transfer function in order to correct input amplitudes for every wave amplitude tested so that the wave amplitude at the hull CoG coincides with the desired ones.

The *navalFoamLeveSet* transient solver has been used, the same as in the case of calm water simulations. The simulation time step is dinamically adjusted in order to keep the Courant number $Co < 5.0$ and a maximum of $1/300$ of the wave period. The simulation is carried on until a periodic convergence of the hull motions is achieved.

The mesh has been has been generated with the *navalMesh* open-source fully-automated meshing tool presented in 4.3. The calm water trim value is used in the meshing procedure so that mesh deformations are symmetrical and minimized. The domain width and depth are set according to the towing tank measures specified in 2.1 and its length is defined by:

$$L = 4L_{WL} + 2\lambda_w^{max} \tag{4.9}$$

where λ_w^{max} is the maximum wavelength tested in the series. The final mesh has approximately 2.7 million cells. A typical simulation of 14 seconds took around 70 hours on 48 cores.

Initial and boundary conditions

Uniform static pressure is set to zero on the whole domain. For k and ω, uniform values are also set across the domain and their values have been computed following the Menter [99] approach.

For the seakeeping simulations relaxation zones are also employed, in this case, the prescribed fields at the inlet, side and outlet corresponds to a regular wave of given frequency and amplitude. The wave field, computed according to Stoke's second order wave theory is then superposed to the uniform velocity field. The inlet relaxation zone is $3.5L_{WL}$ long, the side and outlet are $1L_{WL}$ and $3L_{WL}$ long respectively. In Fig. 4.26, the effect of the relaxation zone is clearly visible.

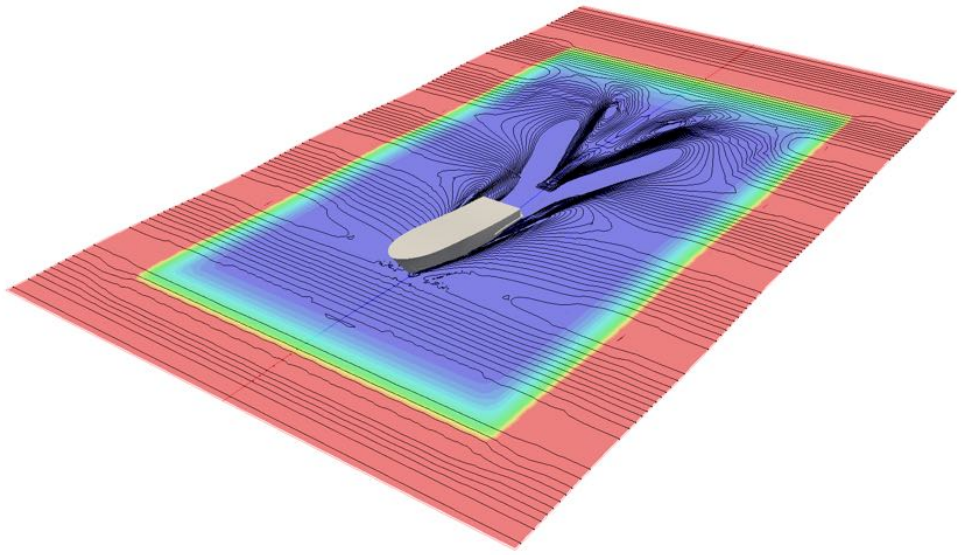

Figure 4.26: Weight function and relaxation zones

The regular waves seakeeping simulations were carried out using the same boundary conditions for the $k-\omega$ SST turbulence model as in the case of calm water simulations.

4.5.3 Data analysis

The results of regular waves seakeeping simulations were analysed with the same tools used for experimental data. One of the main differences respect to the experimental data is that in the case of CFD, data is logged according to the simulation timestep. This means that since the timestep is dynamically adjusted throughout the simulation, the data is logged at a variable rate. In order for the discrete Fourier transform to work, the data is re-sampled at 100 Hz using linear interpolation. Another notable difference is that CFD data did not present significant trends due to carriage rail curvature and residual standing waves. In Fig. 4.27, an example of CFD timeseries and analysis results for a specific wave is shown.

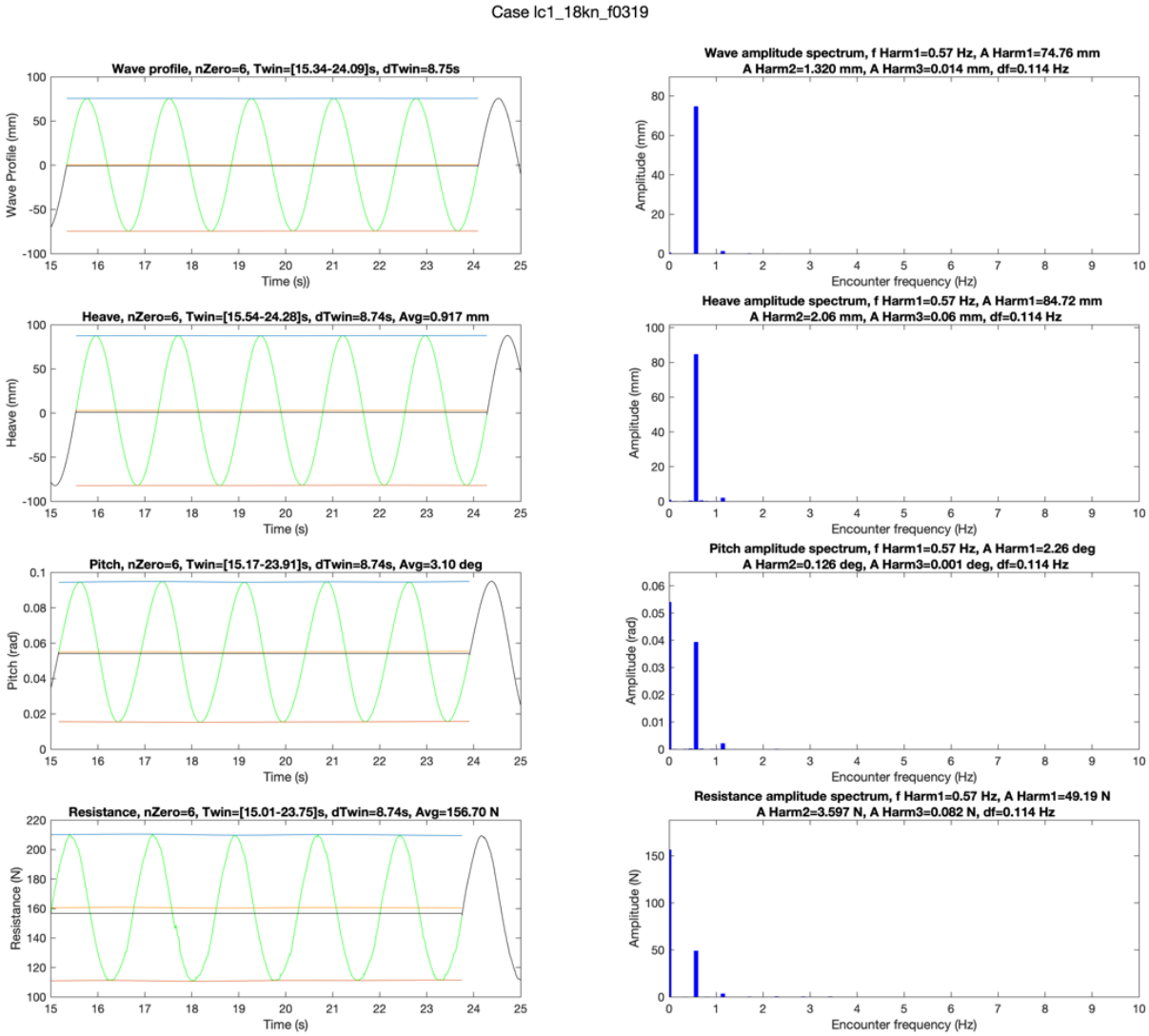

Figure 4.27: Example of CFD seakeeping data analysis results

4.5.4 Results and discussion

Regular waves seakeeping simulations carried out using the same wave frequency and amplitudes specified in the experimental program for the design speed of 3.63 m/s (18 kn in full scale). The results of the simulations are presented using both heave and pitch transfer functions, as in the case of model and full scale results.

In Fig. 4.28, eight snapshots of a simulated wave encounter period are shown. Note that also in these images, the relaxation zone effect on the side can be seen as the perturbated field (bow and stern waves) are dissipated.

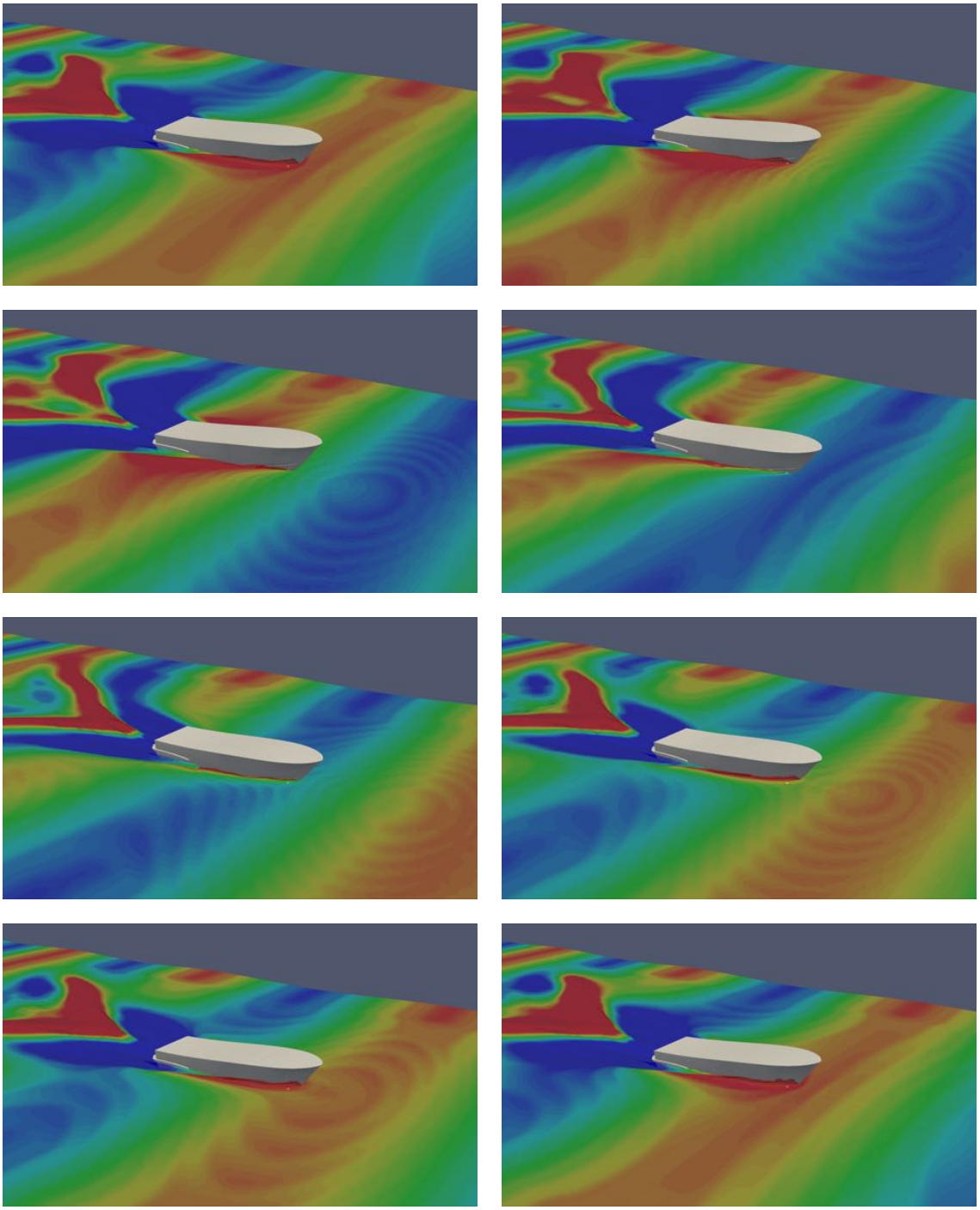

Figure 4.28: Snapshots of a regular wave simulation, V=3.632 m/s, $\lambda/L_{WL} = 2.4$

Taking the heave transfer function comparison in consideration, the simulation results show a remarkable agreement with model scale experimental results for all the tested wavelengths. The transfer functions are indistinguishable if only for the two wavelengths corresponding to the peak response, where the simulation results slightly underestimate the heave motion.

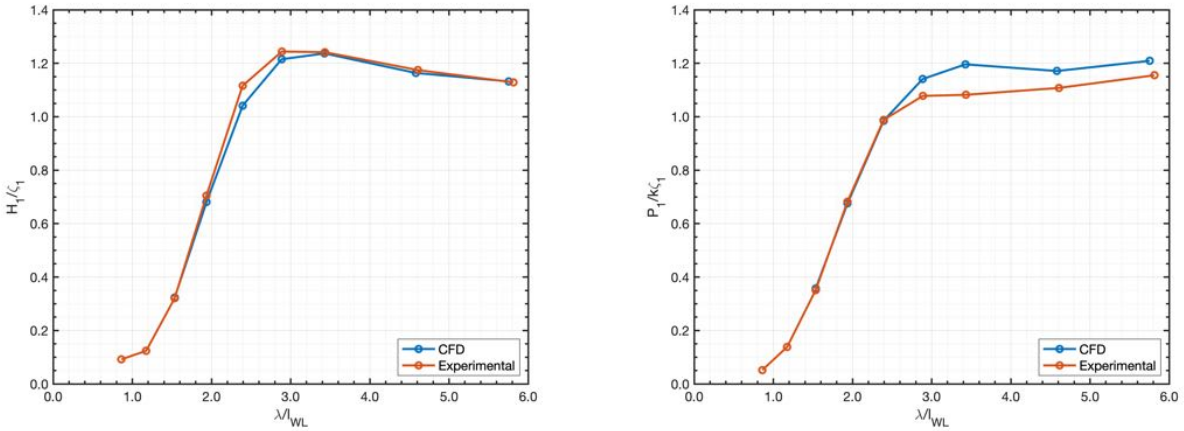

(a) Heave transfer function comparison

(b) Pitch transfer function comparison

Figure 4.29: LC1 transfer functions comparison

The comparison between experimental and numerical and experimental pitch transfer function shows excellent agreement until the critical wavelengths, here the CFD results overestimate the response by a maximum of 8% . A better agreement is shown for longer wavelengths, where the response is overestimated by around 4%. The fact that simulations reach higher pitch values when near to the peak response could be due to lower damping factors acting on the bow region, where large spray formations are present.

In Fig. 4.30, a general comparison between numerical simulations, towing tank and full scale seakeeping results is presented. Full scale results are from the integrated analysys procedure using the directional distribution model based on MEM I method.

In general, it can be observed that regular waves simulation results show a better agreement with experimental results respect to the calm water simulations. Although the physical phenomena involved in the motion response of a planing hull in waves is more complex than steady planing, part of the reason why seakeeping results are more accurate could lie in the amplitude of dominant forces respect to their estimation error. As discussed in section 4.4, small changes in steady pressure distribution along the hull's bottom could drastically change its running attitude and thus its total resistance.

In the case of regular waves, it is reasonable to assume that such inaccuracies (and other ones) are still present, but the hydrodynamic and hydrostatic forces coming from the waves exciting the hull are much larger due to hull inertia, and so the relative error are smaller than in the calm water case. Smaller forcing term relative errors have much smaller effect on the hull motion, and in terms in its transfer function.

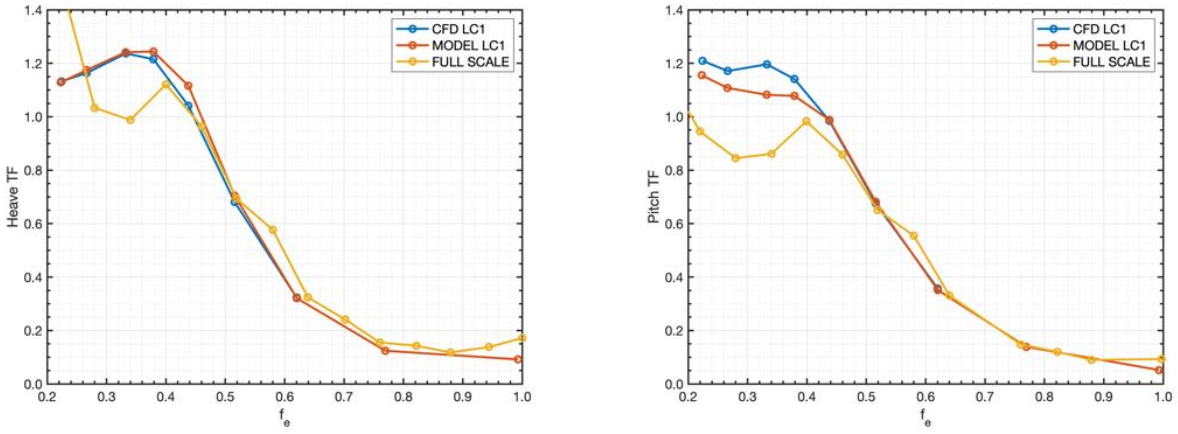

(a) Heave transfer function comparison

(b) Pitch transfer function comparison

Figure 4.30: CFD, model and full scale transfer functions comparison

4.6 Effect of hull shape

4.6.1 Introduction

The main objective of the seakeeping simulations was to verify that the computational framework based on the Naval Hydro Pack was able to predict seakeeping abilities of the model tested in the towing tank. The first intended application of such framework was to estimate the effect of the variation of specific geometrical parameters on the seakeeping behavior of the hull.

In accordance with the SOPHYA project leaders, a set of three wavelengths have been chosen as representatives of the worst possible condition in terms of motion and acceleration response, namely $\lambda = 1.75L_{PP}$, $\lambda = 2.25L_{PP}$ and $\lambda = 2.75L_{PP}$.

Eight alternative hullforms have been generated using two geometrical parameters and their seakeeping responses have been compared with the original hull. A scale model of the best performing hull alternative has been manufactured and tested in the towing tank in order to verify if the same differences are encountered in the towing tank tests.

The eight hullforms have been obtained through free form deformation techniques [113, 114] applied directly on the original hull grid in order to maintain mesh topology. The wave height has also been kept constant for all three wavelength in order to use the same vertical grid resolution respect to the wave amplitude.

4.6.2 Alternative hull shapes

Two geometrical parameters have been selected as the most significant for the seakeeping performances of the hull:

Initial deadrise angle β : Defined as the initial deadrise angle between the vertical plane and the lower hull surface. it has the effect of controlling the concavity/convexity of the hull

between the keel and the chine. A β value will result in a more convex hull and vice versa. The values of β used are $-5°$, $0°$ (original) and $+5°$.

Chine lateral displacement y_c :Defined as the lateral displacement of the chine as a percentage of the initial value. The values of β used are -40%, 0% (original) and +40%.

In Fig. 4.31, two hull variations corresponding by opposite values of both geometrical parameters are compared to the original hull. The front view shows both the effect of chine transversal displacement and initial deadrise angle affecting hull concavity/convexity below the chine.

Since the bow geometry is affecting seakeeping behavior the most, the deformations associated to the two geometrical parameters have been not applied along the whole hull length. Moreover, from a design point of view, the aft sections where the machinery resides are less suitable for large variation of the hull bottom. The bounds of the geometrical parameters value have been chose following some guidelines of the boatyard, since interior spaces are an important factor for Yacht design.

In order to deform only the bow region, weight functions $w(x)$ have been applied to the parameters as a function of the longitudinal coordinate x:

$$\beta(x) = \beta w_\beta(x) \tag{4.10}$$

$$y_c(x) = y_c w_c(x) \tag{4.11}$$

The weight function for β is:

$$w_\beta = 0 \qquad \text{if} \quad 0 \leq x \leq 0.25L \tag{4.12}$$

$$w_\beta = [1 - cos(pi * (x - 0.25L)/(0.5L))]/2 \qquad \text{if} \quad 0.25L \leq x \leq 0.75L \tag{4.13}$$

$$w_\beta = 1 \qquad \text{if} \quad 0.75L \leq x \leq L \tag{4.14}$$

The weight function for y_c is:

$$w_c = 0 \qquad \text{if} \quad 0 \leq x \leq 0.4L \tag{4.15}$$

$$w_c = [(x - 0.4L)/(0.6L)]^4 \qquad \text{if} \quad 0.4L \leq x \leq L \tag{4.16}$$

The $0.4L$ weight function bound for y_c has been set in order to avoid deformations in aft section of the hull where the hull and sides are prismatic. In Fig. 4.32, the effect of the chine lateral displacement weight function can be observed.

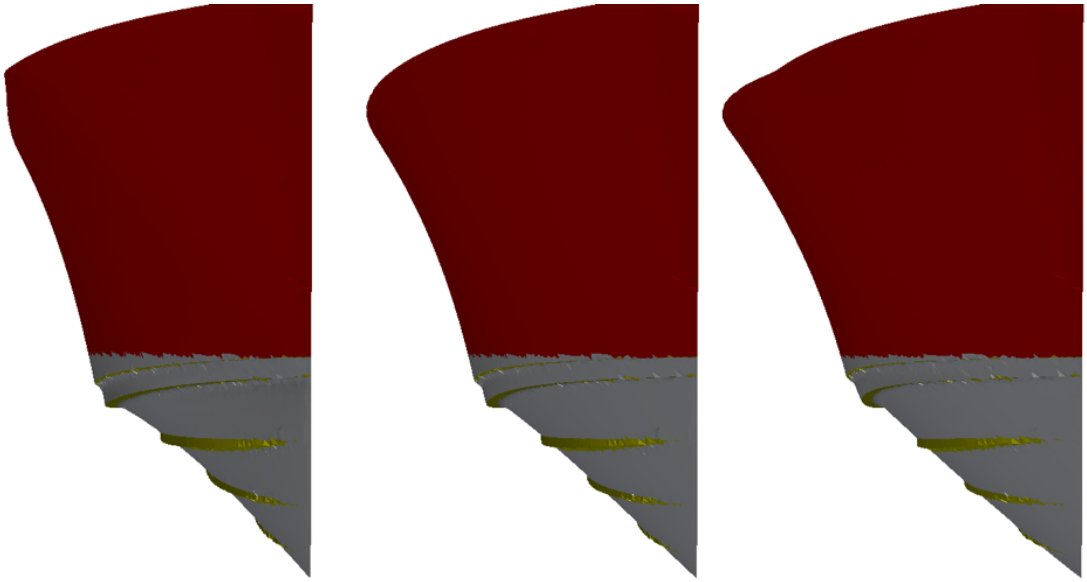

(a) Hull1, $y_c = -40\%$, $\beta = -5°$ (b) Hull0 (original), $y_c = 0\%$, $y\beta = 0°$ (c) Hull8, $y_c = +40\%$, $\beta = +5°$

Figure 4.31: Hull shape comparison, front view

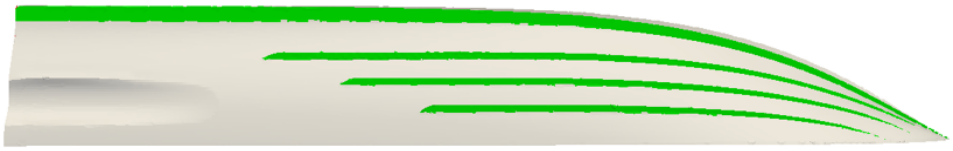

(a) Hull1, $y_c = -40\%$, $\beta = -5°$

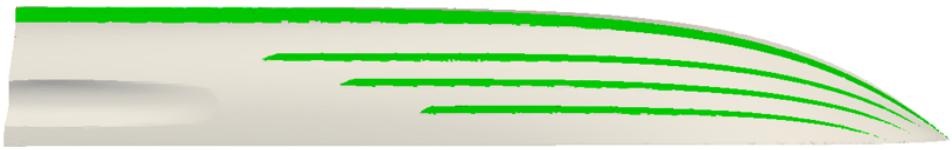

(b) Hull0 (original), $y_c = 0\%$, $y\beta = 0°$

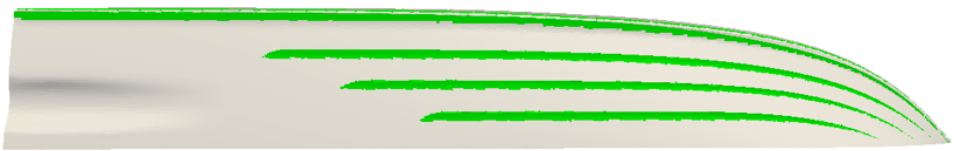

(c) Hull8, $y_c = +40\%$, $\beta = +5°$

Figure 4.32: Hull shape comparison, front view

4.6.3 Results

The eight hull variants have been simulated each for the three wavelengths using the same solver, initial and boundary conditions described in section . The data analysis method is also the same as earlier simulations.

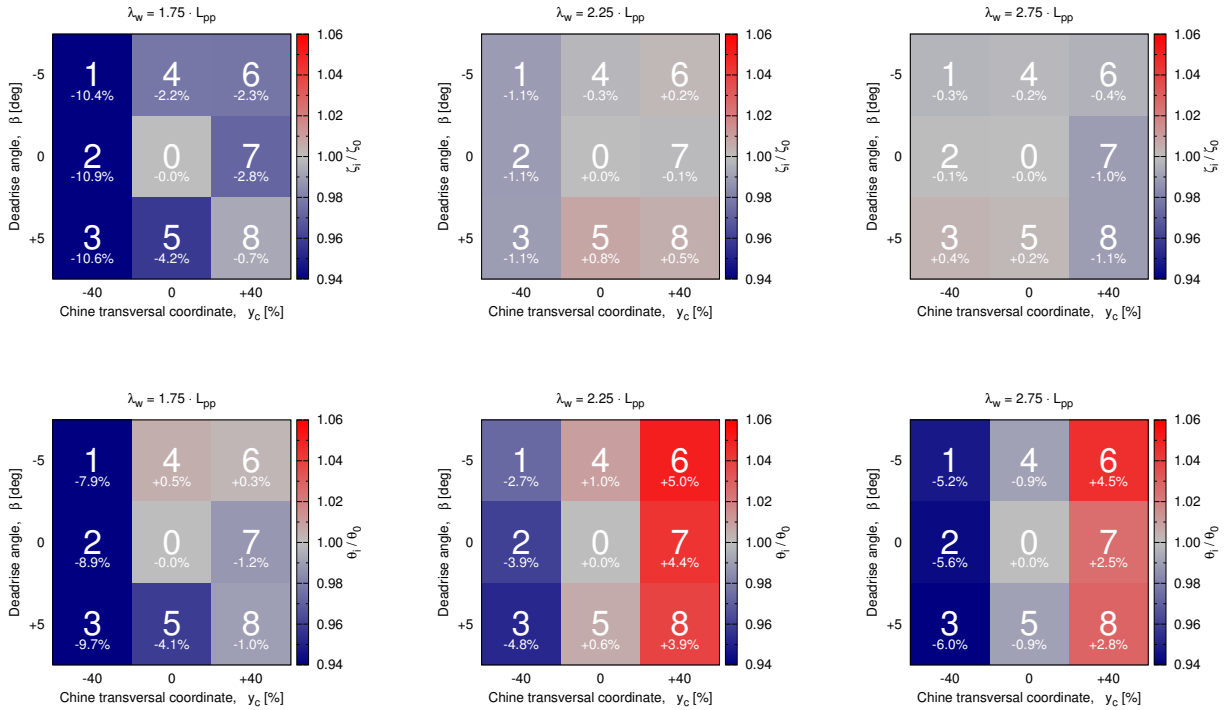

Figure 4.33: Comparison of heave and pitch response between the alternative hullforms

In Fig.4.33, the comparison of both heave (first row) and pitch (second row) Transfer functions (TF) are given as the ratio between the TF of the original hull and the TF of every other hull variant. The TF ratio percentages are plotted inside the hull test matrix for every wavelengths, and they are color coded for easier interpretation.

The resulting matrices allow for an easier assesment of the effect of a parameter on both TF and at different wavelengths. The main observations on the results of the simulations of the eight different hulls are:

- The effect of both initial deadrise angle and lateral chine displacement have a stronger effect on the pitch TF than on the heave TF.
- In general, the chine lateral displacement parameter has a bigger effect on hull responses than the initial deadrise angle.
- Apart for the case of heave for longer waves, both higher initial deadrise angle and smaller lateral chine displacements lead to smaller hull motion response.

The fact that steeper hull sections are affecting pitch response the most is expected since hydrodynamics forces are reduced away from the pivot point, and so affecting pitching moment the most. A similar trend has been also experienced by Kim et al.[115].

It is important to point out that these conclusion are valid only for the variables chosen in this study, as well as their implementation into the free-form mesh deformation algorithm.

In Fig.4.34, the analysis of bow acceleration data is presented using the same technique as the previous image. In addition, acceleration values as a function of wavelength are plotted for each hull alternative. Accelerations are not adimensionalized since wave amplitude is constant across the three wavelength.

Also in the case of bow acceleration, the same observations as in the case of pitch *TF* are true, although the differences here are bigger for the first two wavelenghts. Vertical acceleration has been chosen as an important factor as it is closely related to the on-board comfort.

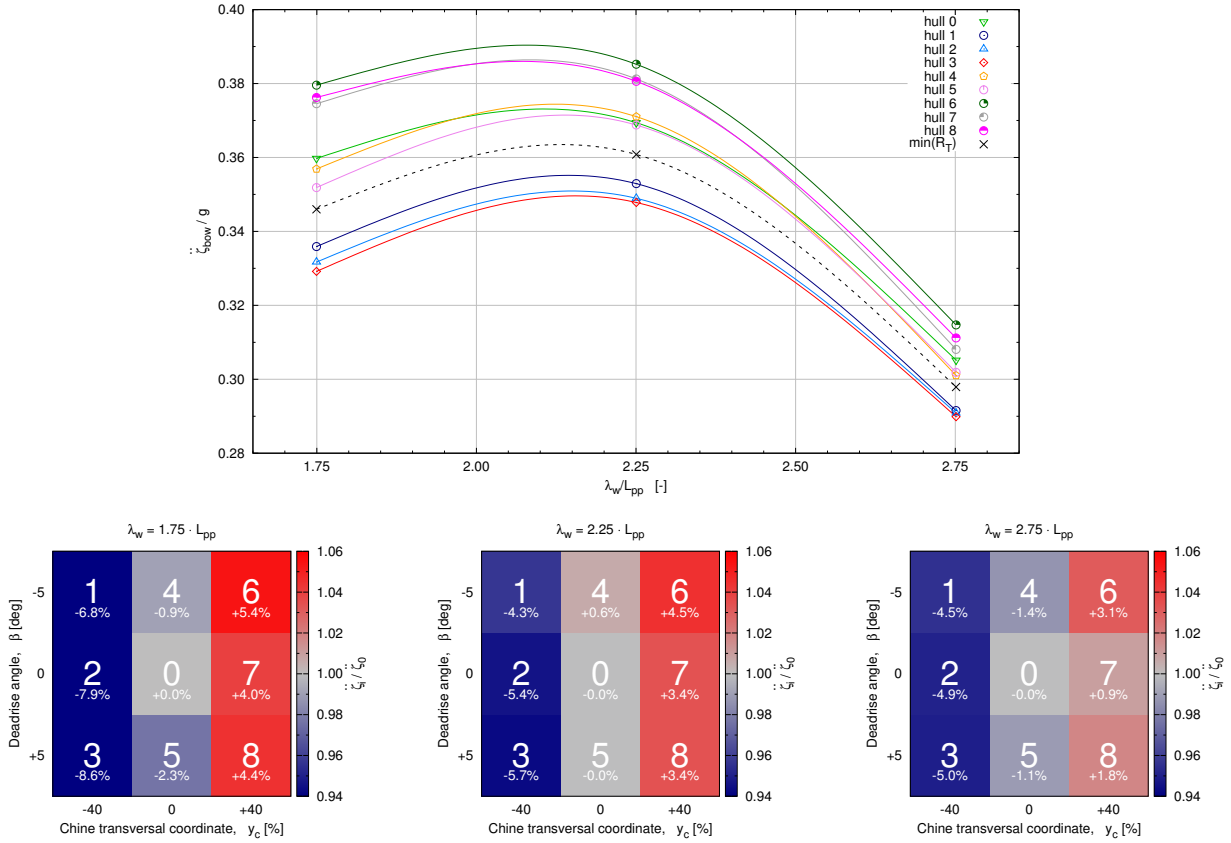

Figure 4.34: Comparison of bow accelerations between the alternative hullforms

In conclusion, given the results showed in the previous plots, "Hull3" alternative has been selected as the optimal hull for for seakeeping as it presented lowest motion and acceleration response.

4.6.4 Experimental results

Following the results of the simulations on the eight hull variants, a twing tank model of the chosen "Hull3" design has been manufactured and tested in the Towing tank of the University of Naples "Federico II".

The experimental setup was identical to the one used for the original model. Since the model construction was different from the original, ad-hoc modifications were necessary in order to place accelerometers in the same coordinates of the original model (Fig.4.35). Both center of gravity and moments of inertia were matched to the old model using the inertial balance. At the end, the model was floated and the design waterline was checked.

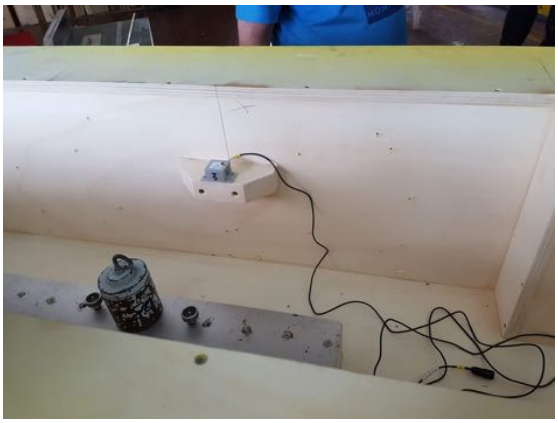

(a) CG accelerometer placement

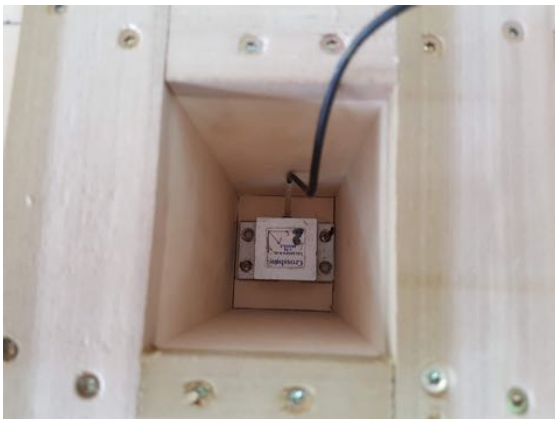

(b) Bow accelerometer placement

(c) Model on inertial balance, LCG check

(d) Model on inertial balance, waterline check

Figure 4.35: Optimal hull setup

Also in this case, the same data analysis procedure used in previous experimental results was used.

The results of the experimental data of both original and "Hull3" are plotted in Fig. 4.36a in terms of vertical acceleration response at the bow.

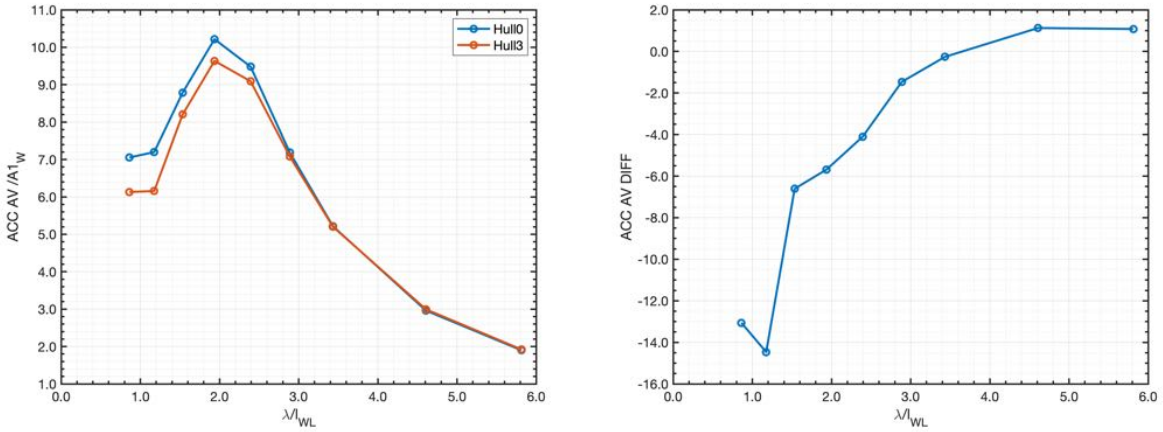

(a) Comparison of bow vertical accelerations between hull0 and Hull3

(b) Bow vertical accelerations difference between hull0 and Hull3

Figure 4.36: Bow vertical accelerations comparison

It is clear that "Hull3" shows lower values of vertical acceleration response respect to the original hull, as it was in the case of the case of seakeeping simulations. In particular, Fig. 4.34, shows that simulations estimate 8 to 5 percent decrease in vertical acceleration between $\lambda = 1.75L_{PP}$ and $\lambda = 2.75L_{PP}$.

In Fig. 4.36b, the difference in bow vertical acceleration response between hull0 and hull3 is plotted in terms of percentage, as in Fig. 4.34. Looking at the percentages between $\lambda = 1.75L_{PP}$ and $\lambda = 2.75L_{PP}$, it can be observed that hull3 shows 6 to 2 percent decrease in vertical acceleration.

The experimental data shows that the effect of the hull shape variations on acceleration response predicted using the Naval Hydro solver, in combinations with the developed procedures and tools, are observed also in towing tank test results. Quantitatively, the results show a reasonable agreement for the critical wavelengths.

4.7 Closure

In this chapter, the methods and tools used for the simulations of planing hulls in calm water and regular waves are presented. An open-source automatic grid generation procedure has been presented. A significant reduction of the pre-processing time-to-simulation, along with higher mesh quality, has been achieved. The procedure has been used for the pre-processing of all the calm water and seakeeping cases, allowing for a drastic reduction of the time-to-simulation, thanks also to the automation of the case folder preparation.

Preliminary calm water simulations using two different interface capturing methods show that the numerical ventilation (NV)phenomenon is occurring when using the Volume-of-Fluid method. The effects of the he well known problem of (NV) have been investigated, and the use of the Level Set (LS) method proved to be a better option. Significant reduction in residual force and moment have been achieved in captive simulations, leading to better estimation of the running attitude in 2-DOF simulations.

The calm water simulations showed that the main issue is the underestimation of the running trim, especially at the highest speeds. This in terms leads to an underestimation of the total resistance.

Regular waves simulations were carried out making use of the previously developed pre-processing procedures. The results of the simulations, in terms of transfer functions, show excellent agreement with experimental results in terms of heave response and good agreement for pitch response, where CFD results overestimate the response by a maximum of 8% at the peak response. In general, the simulated motions corresponding to critical wavelengths are less accurate respect to shorter and longer wavelengths.

In order to assess the effect of two geometrical parameters on the seakeeping behaviour, regular waves simulations were carried out on eight hull variants. The simulations results were used to chose the best candidate in terms of seakeeping performances.

The selected optimal hull has been then tested in the towing tank and the results confirmed the predicted lower vertical accelerations respect to the original hull.

Chapter 5

Conclusions

This thesis work present an experimental and numerical assesment of the seakeeping behavior of planing hulls in rough sea. The Ph.D. work has been carried out under the frame of the SOPHYA project. SOPHYA (Seakeeping Of Planing Hull YAchts) is a research and development project in maritime technologies aimed at the investigation of the performances of planing pleasure-boats in terms of sea-kindliness, safety and powering in mild weather conditions. The investigation is carried out via three main activities that are reflected in the chapters of the present work : model scale experiments, full scale sea trials and numerical simulations. Relevant conclusions and main contributions of each chapter are hereafter summarized:

Model experiments

An extensive description of both calm water and regular waves tests is presented, along with the data analysis procedure and results. The results of both experimental campaigns are essential to the other project phases, where model results will be used for comparison and as reference. Analysis of the results of seakeeping tests in regular waves highlighted that although hull motions response was near to monochromatic, vertical accelerations responses showed higher harmonics content.

In order to further investigate nonlinear behavior of planing hulls in regular waves, an extensive experimental campaign on two Naples Systematic Series (NSS) models in regular waves with varying steepness and frequency has been carried out. The results of over a hundred seakeeping tests have been analyzed and results are discussed in terms of transfer functions, second and third harmonic responses of motions and accelerations as a function of both wave frequency and steepness. The shift in critical wavelength is observed when speed is increased inside the planing regime and that the same shift is also observed in the second harmonic response, in particular for vertical accelerations. Slenderness ratio is found to have a notable effect only on pitch motion at higher speeds. As reported by other authors, first harmonic response (transfer function) decreases with increasing steepness, the study also shows that increasing wave steepness and speed lead to increased second harmonic response in motions and both second and third harmonic response in accelerations. In particular, it is observed that the dependency of the second harmonic response with respect to wave steepness is close to linear, third harmonic response is instead closer to quadratic.

The main contribution of the work on model experiments is represented by the extensive analysis regarding nonlinearities of a systematic series of planing hull in regular waves. In particular the aspects concerning higher harmonics and their trends with respect to speed, wave and geometrical characteristics. In addition, data gathered during the experiments makes for a considerable addition to the NSS dataset.

Full scale sea trials

The process of planning, executing and analysis of full scale sea trials in calm water and rough sea has been presented. A customized test course sequence has been devised in order to maximize the number of measurements in head sea and minimize the distance from the wave buoy. The ship motion and propulsion measurement systems has been tested and installed on board to ensure that both motion and propulsion measurements could be later synchronized.

An integrated approach for the analysis of on-board motion and directional wave buoy measurements has been developed with the aim of providing a better estimation of the full scale motion transfer functions. The method make use of directional sea-state information from the wave buoy, combined with wave directional distribution models to generate directional wave spectra. Data from on board positioning system and local bathymetry are then used to compute the directional encounter spectra, motions forcing spectra and ultimately transfer functions. The effect of wave directional distribution models on the estimation of the yacht transfer function are discussed and it is found that, for the case considered here, relatively simple wave distribution models led to a good agreement with model scale transfer functions. The integrated analysis procedure is completely general and could be applied to any kind of ship type and weather condition, where other directional models could be more appropriate.

Preliminary analysis of the propulsion propeller shafts sensors has been carried out. Given the mild sea condition during the seakeeping tests, mean delivered power was not affected at the cruising speed. A clear correlation between hull motions and shaft torque and rpm is found phase lags could be computed using cross-correlation technique.

The main contribution of the work carried out for the full scale sea trials is the integrated analysis of sea state and on-board data procedure, also presented at the 29th International Ocean and Polar Engineering Conference (ISOPE).

Numerical simulations

As a first step towards a reliable computational framework for seakeeping simulations of a planing hull, an open-source automatic grid generation script has been developed. The meshing procedure is based on OpenFOAM built-in meshing tools and generate an ad-hoc grid suitable for planing hull simulations using multiple refinements techniques. The grid generation script is part of an automated procedure that provide the user with graphical mesh quality reports and ready-to-run folder, dramatically reducing user inputs and time-to-simulation.

Preliminary calm water simulations using two different interface capturing methods showed numerical ventilation (NV) when using the Volume of Fluid method. The phenomenon has been investigated and comparing the results with the Level Set simulations showed how the latter method was able to essentially avoid NVwithout the need of ventilation suppression methods providing better estimation of the running attitude in 2-DOF simulations.

Results of calm water simulations show running trim underestimation at the highest speeds, and in terms underestimation of the total resistance respect to towing tank data. Sinkage show a better agreement with experimental results.

After some preliminary simulations on the wave generation and propagation, regular waves seakeeeping simulations have been carried out. In order to correctly reproduce towing tank conditions and restraints, virtual accelerometers and new restraint method have been implemented. The results of seakeeping simulations in terms of transfer functions, are in excellent agreement with experimental data for heave and good agreement for pitch response, where a maximum of 8% overestimation at the peak response is seen.

The simulation framework has been used to investigate eight alternative hullform variations based on two geometric parameters on the seakeeping performances. The most capable hullform has been tested in the towing tank and the estimated changes in vertical acceleration were comparable with simulation results.

The main contributions of the work done on numerical simulations is the open-source fully-automated pre-processing procedure for planing hull CFD simulations, presented at the 23th Symposium on Theory and Practice of Shipbuilding, and the tools implemented in foam-extend with the help of foam-extend code developers.

5.1 Future work

Due to the large amount of experimental data gathered during the experiments, model self propulsion and full scale propulsion data in calm water could not be analysed by the author due to time constraints. Further studies on self-propelled planing hull both in model and full scale are planned. The collected data could then be used as benchmark for future self-propulsion planing hull simulations using the tools developed in this work. In particular, model scale experiments in irregular sea, using a wave spectrum matching the one measured at sea could deliver more appropriate comparison data for the proposed integrated analysis results.

Simulations using the artificial ventilation suppression tool for VOF simulations could be carried out and compared with the current ones. Simulations involving self-propelled model using actuator disks and propellers are planned and reference data is avalaible from self-propulsion experiments.

The experimental data from the investigation of nonlinear behavior of planing hulls in regular waves makes for an extensive benchmark database for future numerical investigations on this interesting topic.

The hope of the author is that Ph.D. students and researchers could use the present work as a starting point for further advancements in experimental and numerical studies on the subject of planing hull crafts.

Funding

The Ph.D. scholarship has been financed by "PO FRIULI VENEZIA GIULIA - FONDO SOCIALE EUROPEO 2014/2020" (European Social Found).

The Regional Program *POR FESR 2014 2020 - 1.3.b - Ricerca e sviluppo - Aree tecnologie marittime e smart health* of Regione Friuli-Venezia Giulia is acknowledged for providing the financial support of the SOPHYA Project.

Acknowledgements

I would like to offer special thanks to my professor Giorgio Contento, who sadly is no longer with us but will forever be remembered for his great dedication toward the teaching profession. Thank you Giorgio for all the fruitful discussion we had, from difficult ('toxic' as you called them) topics to woodworking, and many other things.

My sincere gratitude goes to my Supervisor Amedeo Migali, that although the logistic difficulties has always managed to be present, and my co-Supervisor Prof. Alberto Francescutto with whom I shared my passion for rare and old books, for his kindness. It has been a pleasure to share this experience with you.

I would also extend my thanks to the researchers and professors in Naples. Thanks to Fabio De Luca, a colleague and friend with shared passions. Thank you for allowing me to pursue my interest in the experimental research with you. Thanks to Prof. Ermina Begovic, for your kindness and clear explanations. My thanks goes also to the team at the University of Zagreb, Inno, Vuko and Prof. Jasak for their professionalism and collaborative spirit. Thank you for your precious collaboration and helping our team reaching our goals.

Ringraziamenti

Questa breve parte del presente lavoro di tesi, pur essendo scorrelata dagli aspetti scientifici della stessa, rappresenta una sezione particolarmente significativa in quanto mi permette di parlare delle persone che mi hanno permesso di arrivare a questo traguardo.

Voglio quindi ringraziare in primis i miei genitori, Nadia e Louis, ai quali dedico questo lavoro. Siete le fondamenta e l'armatura della mia vita, il vostro affetto e impegno nel crescermi e sostenermi, così come il mio riconoscimento, è senza misura.

Un ringraziamento particolare ad Elisa, compagna di vita e molte avventure. Sono fiero di averti accanto, grazie per la dolcezza e l'impegno che mi dedichi ogni giorno.

Grazie ad Annamaria a Roberto per avermi accolto con tanto affetto ed entusiasmo nella loro famiglia. Un ringraziamento particolare anche alla nonna "Toti" e alla zia Francesca per avermi sempre riservato un accoglienza e gentilezza fuori dal comune.

Voglio ringraziare il mio tutore Ing. Amedeo Migali, che nonostante la logistica impegnativa è stato presente e attento al mio percorso. Un grazie anche al mio Co-tutore, Prof. Alberto Francescutto, con il quale ho avuto il piacere di condividere questa esperienza (e la passione per i libri rari).

Un ricordo e ringraziamento speciale va al mio professore Giorgio Contento, che tragicamente è venuto a mancare poco prima che questo lavoro si potesse concludere. Grazie per le lunghe discussioni nelle quali mi hai fatto apprezzare la bellezza della ricerca e per avermi dato la possibilità di fare questa esperienza indimenticabile.

Voglio ringraziare l'amico e collega Thomas Puzzer, con il quale ho condiviso il lavoro del progetto SOPHYA e molto altro. Grazie per le vivaci e profique discussioni tecniche, è stato un piacere condividere l'esperienza del dottorato con una persona tanto preparata. Un ringraziamento va anche all'amico e collega Marco De Santis per gli interessanti scambi tecnici e l'aiuto datomi durante la stesura di questo lavoro.

Una buona parte di questo lavoro di tesi è incentrata sull'analisi sperimentale svolta presso la vasca navale dell'università di Napoli. Durante le settimane passate in vasca ho avuto il piacere di lavorare con professori e tecnici ai quali vorrei rivolgere un ringraziamento in quanto mi hanno riservato sempre un accoglienza particolare.

Ringrazio Fabio De Luca, amico e collega per avermi permesso ed aiutato a coltivare la passione per la sperimentazione. Ringrazio la Prof. Ermina Begovich per la sua collaborazione e per le sue spiegazioni sempre molto chiare. Un ringraziamento va anche ai tecnici Biagio, Andrea e Antonio per l'accoglienza e la collaborazione.

List of Figures

List of Tables

Bibliography

[1] *Boating market monitor: Yachting market monitor in the luxury world*. Tech. rep. Deloitte Italy Spa, 2019.

[2] Christian Sparre. *Norges sjøforsvar, 1814-1914*. H. Aschehoug & Company (W. Nygaard), 1914.

[3] Donaldson. In: *Scientific American Supplement* (1877).

[4] Daniel Savitsky and Jerry L Gore. "Re-evaluation of the planing hull form". In: *Journal of Hydronautics* 14.2 (1980), pp. 34–47.

[5] Daniel Savitsky. "On the subject of high-speed monohulls". In: *Society of Naval Architects and Marine Engineers, Greece* (2003).

[6] Daniel Savitsky. "On the seakeeping of planing hulls". In: *Marine Technology* 5.2 (1968), pp. 164–174.

[7] Th Von Karman. "The impact on seaplane floats during landing". In: (1929).

[8] Herbrt Wagner. "Über Stoß-und Gleitvorgänge an der Oberfläche von Flüssigkeiten". In: *ZAMM-Journal of Applied Mathematics and Mechanics/Zeitschrift für Angewandte Mathematik und Mechanik* 12.4 (1932), pp. 193–215.

[9] W Sottorf. *Experiments with planing surfaces*. Tech. rep. NACA-TM-661. National Advisory Committee for Aeronautics, 1932.

[10] W Sottorf. *Experiments with planing surfaces*. Tech. rep. 1934.

[11] A Sambraus. "Planing-Surface Tests at Large Froude Numbers-Airfoil Comparison". In: (1938).

[12] FWS Locke Jr. "Tests of a flat bottom planing surface to determine the inception of planing". In: *Navy Department, BuAer, Research Division Report* 1096 (1948).

[13] L Sedov. "Scale effect and optimum relations for sea surface planning". In: (1947).

[14] James M Shoemaker. "Tank tests of flat and v-bottom planning surfaces". In: (1934).

[15] W Sottorf. *The Design of Floats*. Tech. rep. NACA-TM-661. National Advisory Committee for Aeronautics, 1938.

[16] Daniel Savitsky, RE Prowse, and DH Lueders. "High-speed hydrodynamic characteristics of a flat plate and 20 degrees dead-rise surface in unsymmetrical planing conditions". In: (1958).

[17] K Davidson and A Suarez. "Tests of twenty related models of V-bottom motor boats". In: *EMB Series* 50 (1948).

[18] Eugene P Clement. "Resistance Test of a Systematic Series of Planing Hull Forms". In: *Trans. SNAME* 71 (1963), pp. 491–579.

[19] JA Keuning and J Gerritsma. "Resistance tests of a series of planing hull forms with 25 degrees deadrise angle". In: *Int. Shipbuilding Progress* 29.337 (1982).

[20] Jan Alexander Keuning, PF Terwisga, et al. "Resistance Tests Of A Series Planing Hull Forms With 30O Deadrise Angle, And A Calculation Model Based On This And Similar Systematic Series". In: *Int. Shipbuilding Progress* 40.424 (1993).

[21] Gerald Fridsma. *A systematic study of the rough-water performance of planing boats*. Tech. rep. STEVENS INST OF TECH HOBOKEN NJ DAVIDSON LAB, 1969.

[22] E Nadine Hubble. *Resistance of Hard-Chine, Stepless Planing Craft with Systematic Variation of Hull Form, Longitudinal Center of Gravity, and Loading*. Tech. rep. Naval Surface Warfare Center Carderock Div Bethesda, 1974.

[23] Henry D Holling and E Nadine Hubble. *Model resistance data of Series 65 hull forms applicable to hydrofoils and planing craft*. Tech. rep. Naval Surface Warfare Center Carderock Div Bethesda, 1974.

[24] GJ Grigoropoulos and TA Loukakis. "Resistance of double-chine, large, high-speed craft". In: *Bulletin de L'Association Technique Maritime et Aeronautique ATMA* 99 (1999).

[25] GJ Grigoropoulos and TA Loukakis. "Resistance and seakeeping characteristics of a systematic series in the pre-planing condition (Part I)". In: *Trans. SNAME* 110 (2002), pp. 77–113.

[26] Bryson J Metcalf et al. *Resistance tests of a systematic series of US Coast Guard planing hulls*. Tech. rep. Naval Surface Warfare Center Carderock Div Bethesda Md, 2005.

[27] DH Kowalyshyn and B Metcalf. "A USCG systematic series of high speed planing hulls". In: *Trans. SNAME* 114 (2006).

[28] DJ Taunton, DA Hudson, and RA Shenoi. "Characteristics of a series of high speed hard chine planing hulls-part 1: performance in calm water". In: *International Journal of Small Craft Technology* 152 (2010), pp. 55–75.

[29] E Begovic and C Bertorello. "Resistance assessment of warped hullform". In: *Ocean Engineering* 56 (2012), pp. 28–42.

[30] F De Luca and C Pensa. "The Naples warped hard chine hulls systematic series". In: *Ocean Engineering* 139 (2017), pp. 205–236.

[31] Gerard Fridsma. *A systematic study of the rough-water performance of planing boats–Part 2 irregular waves*. Tech. rep. 1971.

[32] Ernest E Zarnick and CR Turner. *Rough water performance of high length to beam ratio planing boats*. Tech. rep. David W Taylor Naval Ship Research And Development Center Bethesda, 1981.

[33] DJ Taunton, DA Hudson, and RA Shenoi. "Characteristics of a series of high speed hard chine planing hulls-part II: performance in waves". In: *International Journal of Small Craft Technology* 153 (2011), B1–B22.

[34] Ermina Begovic, C Bertorello, and S Pennino. "Experimental seakeeping assessment of a warped planing hull model series". In: *Ocean Engineering* 83 (2014), pp. 1–15.

[35] E Begovic et al. "Statistical analysis of planing hull motions and accelerations in irregular head sea". In: *Ocean Engineering* 112 (2016), pp. 253–264.

[36] Raymond G Allen, Robert R Jones, and DW Taylor. "A simplified method for determining structural design-limit pressures on high performance marine vehicles". In: *Advanced Marine Vehicles Conference*. 1978, p. 754.

[37] James A Kallio. *Results of Full Scale Trials on Two High Speed Planing Craft (KUDU 2 and KAAMA)*. Tech. rep. David W Taylor Naval Ship Research And Development Center Bethesda, 1978.

[38] J Ooms and Jan Alexander Keuning. "Comparative full scale trials of two fast rescue vessels". In: *TUDelft, Faculty of Marine Technology, Ship Hydromechanics Laboratory Report 1100-P, International Conference SURV IV, Surveillance, Pilot & Rescue Craft for the 21st Century, Gothenburg, Sweden*. 1997.

[39] AFJ van Deyzen, JA Keuning, and RHM Huijsmans. "Smart control of fast ships–Part 1: A setup for automated proactive control of the thrust used to increase the operability of a small planing monohull sailing in head seas". In: *International Shipbuilding Progress* 59.1-2 (2012), pp. 1–19.

[40] AFJ van Deyzen, JA Keuning, and RHM Huijsmans. "Smart control of fast ships–Part 2: A conceptual model of automated proactive thrust control". In: *International Shipbuilding Progress* 59.1-2 (2012), pp. 21–54.

[41] Richard H Akers et al. "Predicted vs. measured vertical-plane dynamics of a planing boat". In: *FAST*. Vol. 99. 1999, pp. 91–105.

[42] Karl Garme and Anders Rosén. "Time-domain simulations and full-scale trials on planing craft in waves". In: *International Shipbuilding Progress* 50.3 (2003), pp. 177–208.

[43] Hans Jorgen B Morch and Ole A Hermundstad. "Planing craft in waves-Full scale measurements". In: *Proceedings of the International Conference on Fast Sea Transportation, FAST'2005, June 2005, St. Petersburg, Russia, Paper: P2005-2 Proceedings.* 2005.

[44] JA Keuning, F Van Walree, et al. "The comparison of the hydrodynamic behaviour of three fast patrol boats with special hull geometries". In: *HIPER 06: 5th International Conference on High-performance Marine Vehicles*. Australian Maritime College. 2006, p. 137.

[45] NC Townsend, PA Wilson, and S Austen. "What influences rigid inflatable boat motions?" In: *Proceedings of the Institution of Mechanical Engineers, Part M: Journal of Engineering for the Maritime Environment* 222.4 (2008), pp. 207–217.

[46] F Prini et al. "Full-Scale Seakeeping Trials of an All-Weather Lifeboat". In: *SURV 9 Conference: Surveillance, Pilot & Rescue Craft, London, UK: The Royal Institution of Naval Architects*. 2018.

[47] Josef Camilleri, DJ Taunton, and Pandeli Temarel. "Full-scale measurements of slamming loads and responses on high-speed planing craft in waves". In: *Journal of Fluids and Structures* 81 (2018), pp. 201–229.

[48] M Caponnetto. "Numerical simulation of planing hulls". In: *Proceeding of the 3 rd Numerical Towing Tank Symposium*. 2000, pp. 9–13.

[49] Mario Caponnetto. "Practical CFD simulations for planing hulls". In: *Process of Second International EuroConference on High Performance Marine Vehicles, HIPER'01* (2001), pp. 128–138.

[50] Daniel Savitsky. "Hydrodynamic design of planing hulls". In: *Marine technology* 1.1 (1964).

[51] Rodrigo Azcueta. "Steady and unsteady RANSE simulations for planing crafts". In: *FAST Sea Transportation, Ischia, Italy* (2003).

[52] Rodrigo Azcueta. "Computation of turbulent free-surface flows around ships and floating bodies". In: *PhD Thesis, University of Hambourg* (2001).

[53] Toru Katayama, Takashige Hinami, and Yoshiho Ikeda. "Longitudinal motion of a super high-speed planing craft in regular head waves". In: *Proc. 4th Osaka Colloquium on Seakeeping Performance of Ships*. 2000, pp. 214–220.

[54] Mario Caponnetto et al. "Motion simulations for planing boats in waves". In: *Ship Technology Research* 50.4 (2003), pp. 182–198.

[55] E Thornhill et al. "Planing hull performance evaluation using a general purpose CFD code". In: Twenty-Fourth Symposium on Naval Hydrodynamics. Washington, DC. 2003.

[56] Eric Thornhill et al. "Planing hull model tests for cfd validation". In: *6th Canadian Marine Hydromechanics and Structures Conference*. 2010.

[57] Stefano Brizzolara and Francesco Serra. "Accuracy of CFD codes in the prediction of planing surfaces hydrodynamic characteristics". In: *2nd International Conference on Marine Research and Transportation*. 2007, pp. 147–159.

[58] Derrill B Chambliss and George M Boyd Jr. "The Planing Characteristics of Two V-shaped Prismatic Surfaces Having Angles of Dead Rise of 20 Degrees and 40 Degrees". In: (1953).

[59] Charles L Shuford Jr. "A theoretical and experimental study of planing surfaces including effects of cross section and plan form". In: (1958).

[60] Stefano Brizzolara and Diego Villa. "CFD simulation of planing hulls". In: *Proceedings of the 7th International conference on High-Performance Marine Vehicles, Melbourne, Florida, USA*. 2010.

[61] Stefano Brizzolara and A Federici. "CFD modeling of planning hulls with partially ventilated bottom". In: *The William Froude Conference: Advances in Theoretical and Applied Hydrodynamics–Past and Future. Portsmouth*. 2010, pp. 24–25.

[62] Reza Yousefi, Rouzbeh Shafaghat, and Mostafa Shakeri. "Hydrodynamic analysis techniques for high-speed planing hulls". In: *Applied ocean research* 42 (2013), pp. 105–113.

[63] TC Fu et al. "An assessment of computational fluid dynamics predictions of the hydrodynamics of high-speed planing craft in calm water and waves". In: *Proceedings*. 2014, pp. 2–7.

[64] Eric G Paterson, Robert V Wilson, and Fred Stern. *General-purpose parallel unsteady RANS ship hydrodynamics code: CFDSHIP-IOWA*. Tech. rep. IOWA INST OF HYDRAULIC RESEARCH IOWA CITY, 2003.

[65] Thomas C Fu et al. "A detailed assessment of numerical flow analysis (NFA) to predict the hydrodynamics of a deep-V planing hull". In: *International Shipbuilding Progress* 60.1-4 (2013), pp. 143–169.

[66] Stefano Gaggero, Diego Villa, and Marco Ferrando. "An OpenSource Approach for the Prediction of Planning Hull Resistance". In: 10th Symposium on High Speed Marine Vehicles, HSMV2014, Naples. 2014.

[67] Hrvoje Jasak, Aleksandar Jemcov, Zeljko Tukovic, et al. "OpenFOAM: A C++ library for complex physics simulations". In: *International workshop on coupled methods in numerical dynamics*. Vol. 1000. IUC Dubrovnik Croatia. 2007, pp. 1–20.

[68] Fabio De Luca et al. "An extended verification and validation study of CFD simulations for planing hulls". In: *Journal of Ship Research* 60.2 (2016), pp. 101–118.

[69] Simone Mancini et al. "Three - Dimensional Pressure Distribution on Planing Hulls". In: ed. by CRC Press. Vol. 3. 3rd International Conference on Maritime Technology and Engineering, Lisbon. July 2016, pp. 353–360.

[70] Agostino De Marco et al. "Experimental and numerical hydrodynamic analysis of a stepped planing hull". In: *Applied Ocean Research* 64 (2017), pp. 135 –154. ISSN: 0141-1187. DOI: https://doi.org/10.1016/j.apor.2017.02.004. URL: http://www.sciencedirect.com/science/article/pii/S0141118716302620.

[71] Rasul Niazmand Bilandi et al. "A Numerical And Analytical Way For Double-Stepped Planing Hull In Regular Wave". In: VIII International Conference on Computational Methods in Marine Engineering, MARINE 2019. 2019, pp. 417 –427.

[72] S Desogus, A Germak, and C Origlia. *Misure assolute dell'accelerazione di gravità a Napoli, Ischia, Pozzuoli ed Ercolano*. Tech. rep. 102. IMGC-CNR, May 2003.

[73] Manley St Denis and Willard J Pierson Jr. *On the motions of ships in confused seas*. Tech. rep. NEW YORK UNIV BRONX SCHOOL OF ENGINEERING and SCIENCE, 1953.

[74] ARJM Lloyd. *Seakeeping: ship behaviour in rough weather*. E. Horwood, 1989.

[75] JJ Van den Bosch. "Tests with two planing boat models in waves". In: *TU Delft, Faculty of Marine Technology, Ship Hydromechanics Laboratory, Report No. 266* (1970).

[76] Bessho Masatoshi. "Motions of a High Speed Planing Boat in Regular Head Sea". In: *Bulletin of the Society of Naval Architects of Korea* 14.4 (1977), pp. 36–44.

[77] Forng-chen Chiu and M Fujino. "Nonlinear prediction of vertical motions and wave loads of high-speed crafts in head sea". In: *International shipbuilding progress* 36.406 (1989).

[78] Forng-Chen Chiu, Wen-Chuan Tiao, and Jenhwa Guo. "Experimental study on the nonlinear pressure acting on a high-speed vessel in regular waves". In: *Journal of marine science and technology* 12.4 (2007), pp. 203–217.

[79] Wen-Chuan Tiao. "Experimental investigation of nonlinearities of ship responses in head waves". In: *Applied Ocean Research* 33.1 (2011), pp. 60–68.

[80] F De Luca and C Pensa. "The Naples Systematic Series–Second part: Irregular waves, seakeeping in head sea". In: *Ocean Engineering* 194 (2019), p. 106620.

[81] JA Keuning. "The nonlinear behaviour of fast monohulls in head waves". PhD thesis. Technische Universiteit Delft, Delft, The Netherlands, 1994.

[82] Dong-Jin Kim et al. "An experimental study on the motion response of a high-speed planing craft in regular head waves". In: *Journal of the Society of Naval Architects of Korea* 46.4 (2009), pp. 373–381.

[83] Lauro Giorgio et al. *The Specialist committe on Trials and Monitoring*. 1999.

[84] Luca Donatini et al. "MWM: A 35 years wind&wave high resolution hindcast dataset and an operational forecast service for the mediterranean sea". In: *18th International Conference on Ships and Shipping Research*. 2015, pp. 185–195.

[85] John Carlton. *Marine propellers and propulsion*. Butterworth-Heinemann, 2018.

[86] Roger W. Sinnott. "Virtues of the Haversine". In: *Sky Telesc.* 68 (1984), p. 159.

[87] Michel Benoit, Peter Frigaard, and Hemming A Schäffer. "Analysing multidirectional wave spectra: a tentative classification of available methods". In: *Proc. seminar on multidirectional waves and their interaction with structures*. 1997, pp. 131–158.

[88] Thomas E Barnard. *Analytical Studies of Techniques for the Computation of High-Resolution Wavenumber Spectra.* Tech. rep. TEXAS INSTRUMENTS INC DALLAS SCIENCE SERVICES DIV, 1969.

[89] Asle Lygre and Harald E Krogstad. "Maximum entropy estimation of the directional distribution in ocean wave spectra". In: *Journal of Physical Oceanography* 16.12 (1986), pp. 2052–2060.

[90] K Kobune. "Estimation of directional spectra from the maximum entropy principle?" In: *Proc. 5th Int. Offshore Mechanics and Arctic Eng. Symp., Tokyo, 1986*. Vol. 1. 1986, pp. 80–85.

[91] OD Nwogu. "Directional wave spectra by the maximum entropy method". In: *IAHR Seminar, Maritime Hydraulics Section, Lausanne, Switzerland, 1987*. 1987.

[92] Taerim Kim, Li-Hwa Lin, and Hsiang Wang. "Application of maximum entropy method to the real sea data". In: *Coastal Engineering 1994*. 1995, pp. 340–355.

[93] Hrvoje Jasak, Inno Gatin, and V Vukčević. "Accurate green water loads calculation using naval hydro pack". In: *IOP Conference Series: Materials Science and Engineering*. Vol. 276. 1. IOP Publishing. 2017, p. 012011.

[94] Vuko Vukčević, Hrvoje Jasak, and Inno Gatin. "Implementation of the Ghost Fluid Method for free surface flows in polyhedral Finite Volume framework". In: *Computers & fluids* 153 (2017), pp. 1–19.

[95] Guido Lupieri, Thomas Puzzer, and Giorgio Contento. "Numerical Study of the Wave-Wave Interaction by Viscous Flow Simulations with OpenFOAM®". In: *21st Symposium on Theory and Practice of Shipbuilding, In Memoriam prof. Leopold Sorta*. Vol. 1. University Of Rijeka. 2014, pp. 257–266.

[96] Guido Lupieri and Giorgio Contento. "Numerical simulations of 2-D steady and unsteady breaking waves". In: *Ocean Engineering* 106 (2015), pp. 298–316.

[97] Riccardo Pigazzini et al. "Experimental and Numerical Prediction of the Hydrodynamic Performances of a 65 ft Planing Hull in Calm Water". In: *NAV2018-Technology and Science for the Ships of the Future*. Vol. 1. IOS Press. 2018, pp. 480–487.

[98] H Jasak et al. *Release Notes for FOAM-Extend-3.2*. 2015.

[99] Florian R Menter. "Two-equation eddy-viscosity turbulence models for engineering applications". In: *AIAA journal* 32.8 (1994), pp. 1598–1605.

[100] Vuko Vukčević, Hrvoje Jasak, and Šime Malenica. "Decomposition model for naval hydrodynamic applications, Part I: Computational method". In: *Ocean Engineering* 121 (2016), pp. 37–46.

[101] Vuko Vukčević, Hrvoje Jasak, and Šime Malenica. "Decomposition model for naval hydrodynamic applications, Part II: Verification and validation". In: *Ocean engineering* 121 (2016), pp. 76–88.

[102] O Ubbink and RI Issa. "A method for capturing sharp fluid interfaces on arbitrary meshes". In: *Journal of computational physics* 153.1 (1999), pp. 26–50.

[103] IM Viola, RGJ Flay, and R Ponzini. "CFD analysis of the hydrodynamic performance of two candidate America's Cup AC33 hulls". In: *International Journal of Small Craft Technology, Trans. RINA* 154 (2012), B1.

[104] Hrvoje Jasak et al. "CFD validation and grid sensitivity studies of full scale ship self propulsion". In: *International Journal of Naval Architecture and Ocean Engineering* 11.1 (2019), pp. 33–43.

[105] I Demirdžić and Milovan Perić. "Space conservation law in finite volume calculations of fluid flow". In: *International journal for numerical methods in fluids* 8.9 (1988), pp. 1037–1050.

[106] Henrik Rusche. "Computational fluid dynamics of dispersed two-phase flows at high phase fractions". PhD thesis. Imperial College London (University of London), 2003.

[107] Andreas Müller and Zdravko Terze. "Geometric methods and formulations in computational multibody system dynamics". In: *Acta mechanica* 227.12 (2016), pp. 3327–3350.

[108] Guido Lupieri and Giorgio Contento. "On the wavy flow past a weakly submerged horizontal circular cylinder at low Keulegan–Carpenter numbers". In: *Journal of Marine Science and Technology* 22.4 (2017), pp. 673–693.

[109] Riccardo Pigazzini et al. "VIV analysis of a single elastically-mounted 2D cylinder: Parameter Identification of a single-degree-of-freedom multi-frequency model". In: *Journal of Fluids and Structures* 78 (2018), pp. 299–313.

[110] Mario Caponnetto et al. "Simulation of Flow and Motion of High-Speed Vessels". In: *Proceedings of the 12th International Conference on Fast Sea Transportation*. 2013.

[111] Christoph Böhm and Kai Graf. "Advancements in free surface RANSE simulations for sailing yacht applications". In: *Ocean Engineering* 90 (2014), pp. 11–20.

[112] Inno Gatin et al. "Enhanced coupling of solid body motion and fluid flow in finite volume framework". In: *Ocean engineering* 143 (2017), pp. 295–304.

[113] Nicola Demo et al. "An efficient shape parametrisation by free-form deformation enhanced by active subspace for hull hydrodynamic ship design problems in open source environment". In: *arXiv preprint arXiv:1801.06369* (2018).

[114] Marco Tezzele et al. "Model order reduction by means of active subspaces and dynamic mode decomposition for parametric hull shape design hydrodynamics". In: *arXiv preprint arXiv:1803.07377* (2018).

[115] Dong Jin Kim et al. "Design of high-speed planing hulls for the improvement of resistance and seakeeping performance". In: *International Journal of Naval Architecture and Ocean Engineering* 5.1 (2013), pp. 161–177.